

High-precision Study of Parity-violation in ^{133}Cs

A thesis submitted in partial fulfilment of
the requirements for the degree of

Doctor of Philosophy

by

Arup Chakraborty

Roll No: 20330003

Under the guidance of

Prof. Bijaya Kumar Sahoo

Physical Research Laboratory

Ahmedabad 380009, Gujarat, India



Department of Physics

Indian Institute of Technology, Gandhinagar

2024

THESIS APPROVAL

Certified that the thesis titled

High-precision Study of Parity-violation in ^{133}Cs ,

submitted by **Arup Chakraborty** (Roll No. **20330003**) to the **Indian Institute of Technology Gandhinagar**, is approved for the degree of *Doctor of Philosophy*.

Date: 23rd December 2024

Place: Gujarat, India



23/12/2024

Prof. Sonjoy Majumder
External Examiner
IIT Kharagpur, West Bengal



23/12/2024

Prof. Vinod Chandra
FDC member
IIT Gandhinagar, Gujarat



23-Dec-24

Prof. B. Sivaraman
DSC and FDC member
PRL, Gujarat



Dr. Ketan M. Patel
DSC and FDC member
PRL, Gujarat



Dr. Narendra Ojha
DSC and FDC member
PRL, Gujarat



23/12/2024

Prof. B. K. Sahoo
PhD Supervisor and FDC member
PRL, Gujarat

Declaration

I hereby declare that this PhD thesis titled “**High-precision study of parity-violation in ^{133}Cs** ” is carried out by me to fulfil the requirement of PhD degree at *Atomic, Molecular and Optical Physics Division* of Physical Research Laboratory (PRL) under the supervision of Prof. Bijaya Kumar Sahoo. All information and facts provided in this thesis are correct to the best of my knowledge. I also declare that wherever I have borrowed any ideas or results of someone else, I have properly cited to the original sources.

Signature:

Arup Chakraborty

Certificate

It is certified that the work contained in this thesis titled “**High-precision study of parity-violation in ^{133}Cs** ”, submitted by Arup Chakraborty (Roll No. 20330003) to the Indian Institute of Technology Gandhinagar, is a record of bonafide research work carried out under my supervision and has not been submitted elsewhere for a degree.

Signature:

Prof. Bijaya Kumar Sahoo

Atomic, Molecular and Optical Physics Division

Physical Research laboratory (PRL)

Ahmedabad-380009, India

Acknowledgements

I would like to express my deepest and heartfelt gratitude to my PhD supervisor, Prof. Bijaya Kumar Sahoo. His exceptional vision, expertise, and guidance have been pivotal in shaping the trajectory of my research. His unwavering support has not only inspired me but has also been a constant source of motivation throughout my graduate journey.

I am sincerely grateful to my DSC members, Prof. Bhalamurugan Sivaraman, Dr. Ketan M. Patel, and Dr. Narendra Ojha. Their invaluable suggestions and insightful feedback during the DSC seminars have greatly enriched my research, allowing me to approach my work from diverse and broader perspectives.

I extend my heartfelt thanks to Prof. R. P. Singh, Dr. Rajesh Kushawaha, Dr. Naveen Chauhan, Prof. Goutam K. Samanta, Prof. Srubabati Goswami, Dr. Satyajit Seth, Dr. Aveek Sarkar, and Prof. Varun Sheel for their teachings and the enlightening discussions during the coursework and projects. Their contributions have been instrumental in deepening my understanding and advancing my research. I also deeply appreciate Prof. Namit Mahajan for his kind behavior and support throughout this journey. A special acknowledgment is due to Dr. Bhushit Vaishnav, Head of PRL Academic Services, whose unwavering assistance and encouragement from my very first day at PRL have been indispensable. My heartfelt thanks also go to Mr. Jigar Raval for his prompt assistance and swift resolution of issues related to the Vikram-100 and Param Vikram-1000 high performance computing cluster. His kindness and approachability have been a great comfort during my PhD tenure.

A PhD life would not be complete without crossing paths with some truly unforgettable colleagues. Let me begin by expressing my gratitude to my amazing friends Wafikul, Debashis, Guru Vai, Trinesh, Dharmendra, Kamran, the other Arup, Aditya and Sanjay for being the ideal subjects of my jokes. You guys were always there when I needed you. Wafikul, thanks to you, I am now the proud and ‘official’ owner of a DSLR. Dharmendra, your contributions are beyond words, so I’ll say, “Thanks for everything,”

and leave it at that. Wafikul, Debashis, and Trinesh, your patience and support deserve a standing ovation. Seriously, take a bow! Now, onto my two incredible bosses, Ananya and Malika. Thank you for entrusting me with the vital role of supplying you two with all the juicy gossip from PRL. Keeping you guys updated has been both a duty and a delight. A huge shoutout to Rithvik, who has been the go-to person for chats about everything from physics to Indian culture to the mysteries of spirituality. Thanks for keeping things interesting! Ramanuj da, your help and advice have been nothing short of life-saving- thank you! Saurabh vai, your witty humor has been like a breath of fresh air amidst the chaos of this PhD journey. A big thank you to Bharathi vai and Supriya da. I have also met with an amazing junior, Vaibhav. Lastly, to my college crew, Puranjoy, Gourav, Gope, Koustav, and Urmi-you guys made this journey a whole lot more fun!

I would like to express my heartfelt gratitude to my beloved grandmother, parents, and family for their unwavering love, constant encouragement, tireless support, and the countless sacrifices they have made for me. Their prayers have been my rock, giving me the strength to push through every challenge along this journey. It's because of their hard work, dedication, and prayers that I am here today, writing my doctoral thesis.

To my grandfather
Shri Abani Bhushan Chakraborty

List of publications

A. Included in thesis:

1. “*Relativistic normal coupled-cluster theory analysis of second- and third-order electric polarizabilities of Zn I*”, **A. Chakraborty**, S.K. Rithvik and B. K. Sahoo. Phys. Rev. A **105**, 062815 (2022).
2. “*Deciphering core, valence and double-core-polarization contributions to parity violating amplitudes in ^{133}Cs using different many-body methods*”, **A. Chakraborty** and B. K. Sahoo, J. Phys. Chem. A **127**, 7518 (2023).
3. “*High-precision electric dipole polarizabilities of the clock states in ^{133}Cs* ”, **A. Chakraborty** and B. K. Sahoo, Phys Rev. A **108**, 042818 (2023).
4. “*High-accuracy Nuclear-Spin-Dependent Parity-Violating Amplitudes in ^{133}Cs* ”, **A. Chakraborty** and B. K. Sahoo, Phys. Rev. A **110**, 022812 (2024).

B. Not included in thesis:

1. “*Zr $^{3+}$ ion as a prospective terahertz atomic clock*”, Jyoti, **A. Chakraborty**, Yanmei Yu, Jingbiao Chen, Bindiya Arora and B. K. Sahoo, Phys. Rev. A **108**, 023115 (2023).

Contents

1	Introduction	1
1.1	Parity transformation	2
1.2	Origin of PV in atoms	4
1.3	Parity violating electric dipole transition	5
1.4	Parity violating Hamiltonian	6
1.5	Probing new physics	10
1.6	Theoretical procedure to calculate $E1_{PV}$	11
1.7	A brief history of PV in atomic systems	13
1.8	Current status of APV and motivation	16
1.9	Objective of the thesis	19
1.10	Outline of the thesis	19
2	Essential Tools and Techniques in Atomic Many-Body Methods	29
2.1	Atomic Hamiltonian	30
2.2	Electronic wave function and second quantization	34
2.3	Challenges with multi-electron atomic system	36
2.4	Variational method	38
2.5	Mean-field model	40
2.6	The DHF method	44
2.7	Basis function expansion	45
2.8	Diagrammatic representations of orbitals and interactions	47

2.9	Electron correlation effects	50
2.10	Summary	52
3	Many-Body Methods: Integrating Electronic Correlation Effects	55
3.1	The RMBPT method	56
3.1.1	Calculation of transition matrix element	59
3.2	RPA	61
3.2.1	Formulation of RPA	62
3.2.2	Correlation from BO	66
3.2.3	Correlation from SR	67
3.2.4	Normalization correction	70
3.3	The RCC Theory	71
3.3.1	Calculation of transition matrix element	75
3.4	Summary	77
4	Electric Dipole Polarizability of Closed-Shell Atomic Systems	83
4.1	Theory of static polarizability	84
4.2	Methodology	85
4.3	Results and Discussion	90
4.4	Summary	94
5	Unraveling NSI PV Amplitude Calculation in ^{133}Cs	99
5.1	Evaluation Procedures of $E1_{PV}^{NSI}$	100
5.1.1	Sum-over-states approach	103
5.1.2	First-principle approach	107
5.2	Many-body methods of $E1_{PV}^{NSI}$	114
5.2.1	DHF method	115
5.2.2	RMBPT method	116
5.2.3	CPDF method	119
5.2.4	RPA method	122

5.2.5	CPDF-RPA method	124
5.2.6	RCC method	130
5.3	Results and Discussions	136
5.3.1	Excitation energies and matrix elements	137
5.3.2	Results for $E1_{PV}^{NSI}$ amplitude	138
5.4	Summary	148
6	Hyperfine Interaction Induced Electric Dipole Polarizability in ^{133}Cs	155
6.1	Prelude of earlier calculations	157
6.2	Theory of dynamic polarizability	158
6.3	Approaches for calculation	167
6.4	Results and Discussion	173
6.5	Summary	179
7	RCC calculations of NSD PV in ^{133}Cs	185
7.1	Theory	186
7.2	Results and Discussions	191
7.2.1	Calculation for vector polarizability	204
7.3	Summary	206
8	Summary and Future Directions	211
8.1	Thesis summary	211
8.2	Novelty of the thesis	214
8.3	Future directions	215

List of Figures

1.1	Right-handed (RH) and Left-handed (LH) coordinate systems.	2
1.2	Diagrammatic representation of electro-weak interactions among the elementary particles in the SM. Here q, q' denote the quarks; e^- and ν represent electron and neutrino respectively.	4
1.3	Diagrammatic representations of electro-weak interactions between nucleons and electrons present in an atomic system. Here, p and n denote proton and neutron, respectively.	5
1.4	A flowchart describing the history and current status of PV studies in atomic systems.	13
2.1	Electronic coordinate system taking nucleus as the origin. \vec{r}_i and \vec{r}_j are the position vectors for i and j^{th} electrons (e^-) respectively and r_{ij} denotes the distance between them.	31
2.2	Flowchart for the iterative scheme used in the DHF method.	45
2.3	Graphical representation of particle and core states separated by Fermi vacuum. The black balls represent occupied states and the white balls represent unoccupied states. We have also shown a single electron excitation from core states to particle states by the arrow.	48
2.4	Diagrammatic representation of hole and particle creation and annihilation. Hole lines are denoted with downward arrows, and particle lines are denoted with upward arrows.	49

2.5	Graphical representations of normal-ordered one-body and two-body interactions operator.	50
3.1	A flowchart depicting the procedure of atomic many-body calculation. .	56
3.2	Diagrammatic representations of the $\Omega_{2c}^{(1)}$ and $\Omega_{2v}^{(1)}$ operators. The dotted line represents the V_{res} interaction term. The double arrow represents the valence orbital v	59
3.3	Zeroth-order transition matrix element of a general one-body operator \mathcal{O} . .	60
3.4	Diagrammatic representation of the second-order matrix element correction to the calculation of property denoted by a one-body operator \mathcal{O} . .	62
3.5	Diagrammatic representation of the RPA wave operator Ω_{pa}^{RPA} . The double line in the diagram implies that through the iterative scheme, the CP effects are included to all-orders.	63
3.6	Diagrammatic representation of the all-order RPA diagrams. One can note the strong resemblance between the RPA and RMBPT(2) diagrams. .	64
3.7	Equivalence between RPA and RMBPT: the shown RPA diagram effectively corresponds to two RMBPT(3) diagrams.	65
3.8	Equivalence between RPA and RMBPT: This particular RPA diagram corresponds to one RMBPT(3) diagram.	66
3.9	Direct diagrams of BO corrections to the transition matrix element. Diagrams (i) and (ii) correspond to the $\mathcal{O}\Omega_{1i}^{(2)}$ term, whereas (iii) and (iv) correspond to the $\Omega_{1f}^{(2)\dagger}\mathcal{O}$ term.	67
3.10	Direct diagrams of the SR correlations that appear via $\langle\Phi_f \mathcal{O}\Omega_{2i}^{(2)} \Phi_i\rangle$. .	69
3.11	Direct diagrams of the SR correlations that correspond to the $\langle\Phi_f \Omega_{2f}^{(2)\dagger}\mathcal{O} \Phi_i\rangle$ term.	70
3.12	Direct diagrams of the SR correlation that appear through $\langle\Phi_f \Omega_{2f}^{(1)\dagger}\mathcal{O}\Omega_{2i}^{(1)\dagger} \Phi_i\rangle$ and $\langle\Phi_f \Omega_{2c}^{(1)\dagger}\mathcal{O}\Omega_{2c}^{(1)\dagger} \Phi_i\rangle$ terms. The first three diagrams correspond to the first term and the last three diagrams correspond to the later term. .	71
3.13	Goldstone diagrammatic representations of the T_1 and T_2 operators. . .	73

3.14	Goldstone diagrammatic representation of the S_{1v} and S_{2v} operators. . .	74
3.15	A few important matrix elements evaluating diagrams at the RCCSD level. . .	76
3.16	Breakdown of a few RCCSD property diagrams in terms of RMBPT diagrams. Below each diagram, the corresponding RMBPT terms have been mentioned.	77
4.1	Ratios of dipole polarizability value of Zn and Cs^+ from different many-body methods and their DHF values.	91
5.1	Goldstone diagrams representing Core (a and b) and Valence (c and d) contributions to $E1_{PV}^{NSI}$ in the V^{N_e-1} DHF potential of a one-valence atomic system. The operator D is shown with a curly line and H_W is shown in a line with a bullet point.	101
5.2	A few important electron correlation contributing diagrams to $E1_{PV}^{NSI}$ in the RMBPT(3) method.	104
5.3	A few representative DCP diagrams from the RMBPT(3) method. . . .	107
5.4	A few typical Goldstone diagrams of the RMBPT(3) method. It demonstrates how Valence contributions through $\Omega_v^{(1,1)\dagger}D$ in the RMBPT(3) ^W method correspond to Core contributions through (a) $\Omega_c^{(1,0)\dagger}H_W\tilde{\Omega}_c^{(0,1)}$ and (b) $H_W\tilde{\Omega}_c^{(1,1)}$ in the RMBPT(3) ^D method.	112
5.5	Goldstone diagrams contributing to amplitude determining equation of Ω_c^{CPDF} . Through an iterative scheme, these effects are included to all-orders.	114
5.6	Diagrams denoting amplitude solving equation for Ω_v^{CPDF} . These core-polarization effects are included to all-orders in the CPDF method. . .	117
5.7	Property diagrams of the CPDF method. These diagrams are similar to the DHF method, but the H_W operators of the DHF diagrams are replaced by Ω_c^{CPDF} and Ω_v^{CPDF}	117
5.8	Graphical representation of Ω_c^\pm and its expansion in terms of lower-order perturbative method.	119

5.9	Graphical representation of Ω_v^\pm and its expansion in terms of lower-order perturbative method.	122
5.10	Property contributing diagrams of the RPA. These diagrams are similar to the CPDF diagrams, but the core-polarization effects are included through the D operator instead of H_W	124
5.11	Goldstone diagrams representing terms of Eq. (5.66) representing the $u^{PV\pm}$ term that gives rise to DCP contributions in the CPDF-RPA method. Diagrams from (ix) to (xvi) along with their exchanges are coming due to the implementation of the orthogonalization condition. .	128
5.12	Goldstone diagrams contributing to the $E1_{pV}^{NSI}$ amplitude in the CPDF-RPA method.	129
5.13	Goldstone diagrams showing breakdown of the $T^{(1)}$ operators in terms of lower-order perturbative excitations.	130
5.14	Goldstone diagrams showing breakdown of the $S_v^{(1)}$ operators in terms of lower-order perturbative excitations.	131
5.15	A few important $E1_{pV}^{NSI}$ evaluating diagrams in the RCCSD method. .	133
5.16	Breakdown of few RCCSD property diagrams in terms of lower-order RMBPT diagrams.	134
5.17	Relating Core contributing diagrams from (i) $D\Omega_c^{(1,1)}$ of the RMBPT(3) ^W method and (ii) $H_W\tilde{\Omega}_c^{(1,1)}$ of the RMBPT(3) ^D method to the Core contributing diagrams in the CPDF-RPA method. The former remains as a Core contributing diagram while the later turns out to be a Valence contributing diagram in the RCCSD method.	135
6.1	Goldstone diagrams representing the DHF contributions to the second-order E1 polarizability. The horizontal line represents the E1 operator D	157

6.2	Diagrammatic representation of the top contribution to the third-order hyperfine interaction induced E1 polarizability. In addition to two interactions by the E1 operator D (represented by a horizontal line), each diagram includes a hyperfine interaction $\mathbf{T}_{\mathbf{J}}^{(1)}$ (represented by a curly line).	159
6.3	Diagrammatic representation of the center part of the third-order hyperfine interaction induced E1 polarizability. All notations are the same as the previous figure.	160
6.4	Diagrammatic representation of the normalization part of the third-order hyperfine interaction induced E1 polarizability.	162
6.5	Demonstration of contributions from two different combinations of intermediate states (J' and J'') to the (a) top, (b) center and (c) normalization parts of the static $\alpha_F^{S(2,1)}$ value of the $F = 3$ level of ^{133}Cs . States with subscript $-$ symbol in the figure represent the lower angular momentum state of a fine-structure partner; i.e. P_- means $P_{1/2}$ and D_- denotes $D_{3/2}$, while P and D stand for the $P_{3/2}$ and $D_{5/2}$ states respectively.	172
6.6	Contributions from different combinations of intermediate states (J' and J'') to the (a) top and (b) center parts of the static $\alpha_F^{T(2,1)}$ value of the $F = 3$ level of ^{133}Cs . The notation is same as in the previous figure.	173
7.1	\mathcal{X}_{PV}^{NSD} values for the $F_f - F_i$ transitions of the $7s\ ^2S_{1/2}(F_f)$ and $6s\ ^2S_{1/2}(F_i)$ states in ^{133}Cs from different methods. The plotted values are presented in the same units as in Table 7.1.	192
7.2	Ratios of the calculated \mathcal{X}_{PV}^{NSD} values for the $F_f - F_i$ transitions of the $7s\ ^2S_{1/2}$ and $6s\ ^2S_{1/2}$ states, respectively, in ^{133}Cs from different methods with respect to their DHF values.	196
7.3	Contributions from different intermediate states to the \mathcal{X}_{PV}^{NSD} values for different $7s\ ^2S_{1/2}(F_f) - 6s\ ^2S_{1/2}(F_i)$ transitions in ^{133}Cs . P_- denotes $P_{1/2}$, and P denotes the $P_{3/2}$ state.	202

List of Tables

1.1	Accuracy in measurements and calculations of PV effects in various atomic systems.	14
1.2	Contribution to $E1_{PV}^{NSI}$ for the $6S_{1/2}-7S_{1/2}$ transition in ^{133}Cs in $10^{-11}i(-Q_W/N) e a_0$, a_0 being Bohr radius. The Core contribution has been color-coded blue, whereas the Main contribution from Ref. [38] has been shown in red.	18
3.1	A comparative description of the RMBPT method formalism for the closed-shell and one-valence open-shell atomic systems. $ \Psi_c\rangle$ and $ \Psi_v\rangle$ are the exact wave function of the total Hamiltonian H . Ω_c represents the wave operator accounting for electron correlations only from the core orbitals, while Ω_v takes care of correlations from all electrons, including the valence electron. The subscript ‘linked’ means that only the linked diagrams will contribute to the wave operator [1]. The subscript ‘2’ in $\Omega_{2c}^{(1)}$ and $\Omega_{2v}^{(1)}$ corresponds to double excitation. a, b, p, q, r and v are the single electron orbitals (i.e., $ a\rangle \equiv \phi_a\rangle$, $ p\rangle \equiv \phi_p\rangle$, and so on) and $\epsilon_a, \epsilon_b, \epsilon_p, \epsilon_q, \epsilon_r$ and ϵ_v are the corresponding single particle orbital energies, respectively.	57
3.2	A description of the SR terms in terms of their corresponding wave operators. There are a total of 36 terms contributing to the SR correlation, including both direct and exchange terms.	68

3.3	A comparative description of the RCCSD method formalism for closed-shell and one-valence atomic systems. The operator, T , is applied only to excite the core electrons, and S_v corresponds to excitations that include the valence sector. The subscripts ('1' and '2') in T and S_v operators correspond to the level of excitation. H_N is the normal ordered Hamiltonian. Here, 'conn' stands for the connected terms and 'op' corresponds to the open part in $H_N e^T$ contraction. The term ΔE_v is known as the electron attachment energy or the electron affinity of the valence electron v . '*' denotes excited configuration with respect to $ \Phi_c\rangle$ or $ \Phi_v\rangle$ for closed-shell or one-valence atomic system respectively.	72
3.4	Reduced E1 matrix elements in a.u. of ^{133}Cs atom from various many-body methods. We also compare our values with the experimental results.	78
4.1	Calculated static dipole (α_d) polarizability values (in a.u.) of Zn and Cs^+ using different many-body methods in the relativistic framework. .	90
4.2	Comparison of contributions to α_d (in a.u.) of Zn and Cs^+ from various RCCSD terms. We also compare the corresponding contributions from previously reported calculations using the RCCSD method for α_d of the Zn atom. Here, Norm denotes the difference between the contributions after and before normalizing the wave function with a normalization factor. NA stands for not applicable and Nonlin corresponds to the contributions from nonlinear terms.	92
4.3	Comparative table for α_d value (in a.u.) from different calculations using various many-body methods, experiments and scaling procedures. . . .	93
5.1	Excitation energies (in cm^{-1}) of the low-lying states of ^{133}Cs from the RCCSD method. Energies are compared with the experimental values. We also present H_W (in units of $10^{-11}i(-Q_W/N) e a_0)$ matrix elements from various many-body method. N is the neutron number.	137

5.2	$E1_{PV}^{NSI}$ values, in units $10^{-11}i(-Q_W/N) e a_0$, of the $6s\ ^2S_{1/2} - 7s\ ^2S_{1/2}$ and $6s\ ^2S_{1/2} - 5d\ ^2D_{3/2}$ transitions in ^{133}Cs from DC Hamiltonian reported by various works. The methods labeled as ‘Sum-over’ and ‘Mixed’ are derived using the sum-over-states approach and mixed many-body methods, respectively. Results highlighted in bold font are asserted to have an accuracy within 0.5% accuracy.	139
5.3	Estimated ‘Main’ contributions to the $E1_{PV}^{NSI}$ values, in units $10^{-11}i(-Q_W/N) e a_0$, of the $6s\ ^2S_{1/2} - 7s\ ^2S_{1/2}$ transition in ^{133}Cs using matrix elements involving $np\ ^2P_{1/2}$ intermediate states in the sum-over-states approach. Four cases are being considered: (a) <i>ab initio</i> result in which calculated values from Table 5.1 and 3.4 are used; (b) replacing calculated E1 matrix elements by their experimental values; (c) retaining calculated E1 matrix elements and using experimental energies; and (d) using experimental values for both E1 matrix elements and energies.	140
5.4	Core and Valence correlation contributions to the $E1_{PV}^{NSI}$ values, in units $10^{-11}i(-Q_W/N) e a_0$, for the $6s\ ^2S_{1/2} - 7s\ ^2S_{1/2}$ and $6s\ ^2S_{1/2} - 5d\ ^2D_{3/2}$ transitions in ^{133}Cs from the RMBPT(3) ^W and RMBPT(3) ^D approaches. Results (a) considering H_{eff} effect due to V^{N_e-1} potential and (b) using DHF orbital energies are shown for comparison.	141
5.5	<i>Ab initio</i> contributions to Core and Valence parts of the $E1_{PV}^{NSI}$ values, in units $10^{-11}i(-Q_W/N) e a_0$, for the $6s\ ^2S_{1/2} - 7s\ ^2S_{1/2}$ and $6s\ ^2S_{1/2} - 5d\ ^2D_{3/2}$ transitions in ^{133}Cs from different methods considered in this work using the DC Hamiltonian. Available results from previous calculations are also given for comparison.	142
5.6	Comparison of contributions from the initial and final perturbed states to $E1_{PV}^{NSI}$ of the $6s\ ^2S_{1/2} - 7s\ ^2S_{1/2}$ transition of ^{133}Cs , in units $10^{-11}i(-Q_W/N) e a_0$, at different levels of approximation between the present work and that are reported in Refs. [14, 25].	143

5.7	Contributions to Core and Valence parts from different terms to $E1_{PV}^{NSI}$ of the $6s\ ^2S_{1/2} - 7s\ ^2S_{1/2}$ and $6s\ ^2S_{1/2} - 5d\ ^2D_{3/2}$ transitions in ^{133}Cs , in units $10^{-11}i(-Q_W/N) e a_0$ from Eqs. 5.69 and 5.70 of the CPDF-RPA method, which are quoted under ‘Expression a’ and ‘Expression b’ respectively. Results are given using the calculated ω value, ω^{ex} and ω^{ex} with the experimental energies of the initial and final states (denoted by $E_{i,f}^{expt}$).	149
5.8	First-principle calculated $E1_{PV}^{NSI}$ values (in $-i(Q_W/N) e a_0 \times 10^{-11}$) of the $6s\ ^2S_{1/2} - 7s\ ^2S_{1/2}$ and $6s\ ^2S_{1/2} - 5d\ ^2D_{3/2}$ transitions in ^{133}Cs from different terms of the RCCSD method. Both <i>ab initio</i> and scaled values are given for comparison. We have used two different types of scaling: (a) only scaling amplitudes of the unperturbed $S_v^{(0)}$ operators and (b) scaling amplitudes of both the $S_v^{(0)}$ and $S_v^{(1)}$ operators. Here, contributions under ‘Norm’ represents the difference between the contributions after and before normalizing the RCCSD wave functions. ‘Others’ denotes contributions from those RCCSD terms that are not shown explicitly in this table.	150
6.1	Calculated values of the second-order static and dynamic E1 polarizabilities (in a.u.) of the ground state of the Cs atom. Wavelengths are in nm.	163
6.2	Magnetic dipole hyperfine interaction induced E1 polarizabilities (in 10^{-10} Hz/(V/m) ²) of the hyperfine levels of the ground state of ^{133}Cs at various wavelengths (λ). Wavelengths are in nm. The unit Hz/(V/m) ² can be converted into a.u. by multiplying 0.401878046×10^8	164

6.3	The presently calculated the second-order static and dynamic atomic E1 polarizabilities (in a.u.) of the ground state of Cs atom. E1 matrix elements used in the estimation of ‘Main’ contributions are given explicitly, where values shown with superscript ‘ <i>a</i> ’ are calculated using the RCCSDT method.	168
6.4	Some of the important matrix elements (in a.u.) of the $\mathbf{T}_{\mathbf{J}}^{(1)}$ operator of ^{133}Cs . Numbers appearing as $a[b]$ mean $a \times 10^b$. See the text for explanation of how the experimental values for the off-diagonal matrix elements are inferred.	170
6.5	Breakdown of our calculated $\alpha_F^{S(2,1)}$, $\alpha_F^{A(2,1)}$ and $\alpha_F^{T(2,1)}$ values for the $F = 3$ and $F = 4$ levels of ^{133}Cs in terms of the valence, valence-core, core-valence, core-core and core contributions. Results are given for both the static and dynamic E1 polarizabilities (in $10^{-10} \text{ Hz}/(\text{V}/\text{m})^2$). . . .	171
6.6	The ‘Main’ contributions of $T(\omega)$, $C(\omega)$ and $R(\omega)$ to the $\alpha_F^{S(2,1)}$, $\alpha_F^{A(2,1)}$, $\alpha_F^{T(2,1)}$ values of the $F = 3$ and $F = 4$ hyperfine levels of the ground state of ^{133}Cs at different wavelengths. All values are in a.u..	175
6.7	Summary of the k_s value from different theoretical and experimental works in units of $10^{-10} \text{ Hz}/(\text{V}/\text{m})^2$	179
7.1	Estimated \mathcal{X}_{PV}^{NSD} values of the hyperfine transitions ($F_f - F_i$) among all possible hyperfine levels F_f and F_i of the $7s \ ^2S_{1/2}$ and $6s \ ^2S_{1/2}$ states, respectively, in ^{133}Cs from different methods. All the values are given in the units of $iea_0 K_W \times 10^{-12}$. We also compare these values with the values reported in previous works at different levels of approximation in the many-body method.	191
7.2	The Core and Valence contributions to the \mathcal{X}_{PV}^{NSD} values in all the considered transitions among all possible hyperfine levels F_f and F_i of the $7s \ ^2S_{1/2}$ and $6s \ ^2S_{1/2}$ states, respectively, in ^{133}Cs from different methods. Same units as in Table 7.1 are used here.	194

7.3	Comparison of contributions from the initial and final perturbed states to \mathcal{X}_{PV}^{NSD} among all possible hyperfine levels of the $7s\ ^2S_{1/2}(F_f) - 6s\ ^2S_{1/2}(F_i)$ transition in ^{133}Cs at different methods, in units of $iea_0K_W \times 10^{-12}$. . .	197
7.4	Contributions from different RCC terms to the \mathcal{X}_{PV}^{NSD} values (in units $iea_0K_W \times 10^{-12}$) of the $7s\ ^2S_{1/2}(F_f) - 6s\ ^2S_{1/2}(F_i)$ transitions in ^{133}Cs . Here, contributions given under ‘Norm’ represent the corrections to results due to normalization factors of the wave functions. In this table \overline{D} denotes only the effective one-body part of $e^{T^{(0)\dagger}}De^{T^{(0)}}$. Contributions from other non-linear terms of the RCCSD method are given together under “Others”.	199
7.5	Calculated reduced $K^{(1)}$ matrix elements (in $iK_W \times 10^{-12}$) of the low-lying states of ^{133}Cs using the RCCSD method. These values have been used to estimate the ‘Main’ contributions to the \mathcal{X}_{PV}^{NSD} amplitudes. . .	200
7.6	Estimated ‘Main’ Contributions to the \mathcal{X}_{PV}^{NSD} values, in units of $iea_0K_W \times 10^{-12}$, of the $7s\ ^2S_{1/2}(F_f) - 6s\ ^2S_{1/2}(F_i)$ transitions in ^{133}Cs using matrix elements involving the $np\ ^2P_{1/2,3/2}$ ($n = 6 - 9$) intermediate states from the RCCSD method in the sum-over-states approach. The values given by <i>ab initio</i> results. These values obtained after replacing some of the calculated E1 matrix elements and energies by their precisely known experimental values are given under semi-empirical results. These values are estimated for the initial perturbed and final perturbed states separately, then the final values are given after adding both the contributions.	201
7.7	The final recommended Main, Core, DCP+Tail, Breit and QED contributions to the \mathcal{X}_{PV}^{NSD} values (in units of $iea_0K_W \times 10^{-12}$) of the $7s\ ^2S_{1/2}(F_f) - 6s\ ^2S_{1/2}(F_i)$ transitions in ^{133}Cs . Uncertainties are quoted within the parentheses.	203

7.8	Numerical results for α and β values for 6S-7S transition in ^{133}Cs in a.u. We have used the experimental value of $\frac{\alpha}{\beta} = 9.905(11)$ from Ref. [21]. The error in the results is calculated from the uncertainty in the E1 matrix elements.	204
7.9	Breakdown of the semi-empirical results for α and β in terms of individual contribution. The results are in a.u.	206
8.1	Calculated static α_d value in a.u. of Zn using the RNCCSD method. . .	216

Abstract

In an atomic system, parity-violation (PV) arises from two primary sources. The first source is the neutral weak interactions between the atomic nucleus and electrons. The second source is the electromagnetic interaction between electrons and a potentially existing parity-violating nuclear anapole moment (NAM) within the nucleus. While the concept of NAM is fundamental, its existence remains a subject of debate. The weak interactions, mediated by the Z_0 boson (and Z_0 -like bosons, if exist), are classified into nuclear spin-independent (NSI) and nuclear spin-dependent (NSD) interactions, based on whether the axial-vector and vector currents originate from the electron and nuclear sectors, respectively, or vice versa.

To probe new physics, the study of PV in atomic systems has been one of the principal tools over the past few decades. By combining high-precision measurements with atomic many-body calculations of NSI PV observables, one can determine the nuclear weak charge and compare it to the value predicted by the Standard Model (SM) of particle physics. Any discrepancy between these values could indicate potential new physics beyond the SM. The most precise data on atomic PV is currently derived from the $6s\ ^2S_{1/2} \rightarrow 7s\ ^2S_{1/2}$ transition in cesium (^{133}Cs), with experimental and theoretical accuracies reported at 0.35% [C. S. Wood *et al.*, *Science* **275**, 1759 (1997)] and 0.3% [S. G. Porsev *et al.*, *Phys. Rev. D* **82**, 036008 (2010); V. A. Dzuba *et al.*, *Phys. Rev. Lett.* **109**, 203003 (2012); B. K. Sahoo *et al.*, *Phys. Rev. D* **103**, L111303 (2021)], respectively. Despite theoretical accuracies being claimed within 0.3%, the final values show a 1% discrepancy across these studies. Moreover, the Core contribution due to the occupied orbitals among these theoretical results varies by 200%. In this scenario a detailed analysis is much needed to find out the reason behind such discrepancies among various theoretical results. On the other hand, the primary goal of the NSD PV study is to probe NAM. Unlike NSI PV, a few theoretical studies have been conducted for NSD PV in atomic systems. One such system is ^{133}Cs atom, in which NSD PV amplitudes

among various hyperfine levels for the $6s\ ^2S_{1/2} \rightarrow 7s\ ^2S_{1/2}$ transition have been studied [W. C. Haxton *et al.*, *Ann. Rev. Nuc. Part. Sc.* **51**, 261 (2001), V. V. Flambaum *et al.*, *Phys. Rev. C* **56**, 1641 (1997), W. R. Johnson *et al.*, *Phys. Rev. A* **67**, 062106 (2003)]. The atomic parameter corresponding to NAM, K_a , extracted from atomic calculations by combining with the experiment is at 4σ variance with the nuclear calculations and experiments. One of the possible reasons for the variance may be due to incomplete inclusion of the electron correlation effects in the atomic many-body calculations.

In this thesis, we address these disparities regarding the NSI and NSD PV studies from the point of view of atomic many-body calculations. We have applied various many-body methods such as coupled-perturbed Dirac-Fock (CPDF), random phase approximation (RPA), combined CPDF-RPA and relativistic coupled-cluster (RCC) to study the NSI and NSD PV amplitudes in ^{133}Cs . We analyze the connections among these methods and how they incorporate electron correlation effects into the calculation. There is a significant difference between the RCC result and the result calculated using other methods mentioned above for the PV amplitudes. The reason is that the RCC method incorporates all the correlation effects up to all-order, including those which were neglected in other methods. We explain that the reason behind the mismatch of the Core contributions among different NSI PV studies is due to improper classification of Core and Valence contributions across different many-body methods. We also revise the K_a value based on our RCC calculation for the NSD PV amplitudes in ^{133}Cs . Our study suggests that the reason for discrepancy between atomic and nuclear physics results is not because of uncertainties associated with different many-body calculations, but it could be either due to unknown systematic effects present in the experiment or inappropriate approximations made in the nuclear calculations.

Chapter 1

Introduction

SYMMETRY or invariance of the Hamiltonian describing a physical system is an important concept in physics [1, 2, 3]. In general, symmetry exists when an operation preserves certain properties of the system. If a given process remains unchanged under a particular operation, it is termed invariant under the associated symmetry transformation. Symmetry transformations in physical systems can be categorized as either continuous or discrete. For each symmetry transformation, there exists a unitary operator [1], which carries all the information of the symmetry operation. Continuous symmetries are associated with operations that have the concept of infinitesimal transformation. For continuous symmetry transformation, the unitary operator corresponding to the symmetry is written as the exponential function. As an example of continuous symmetry that differs infinitesimally from the identity transformation, the operator \mathcal{R} can be written as

$$\mathcal{R} = \mathcal{I} - \frac{i\epsilon}{\hbar}G, \quad (1.1)$$

where G is the hermitian generator of the symmetry operator and ϵ denotes an infinitesimal transformation. If the Hamiltonian of the system, H , is invariant under \mathcal{R} , one can write

$$\mathcal{R}^\dagger H \mathcal{R} = H. \quad (1.2)$$

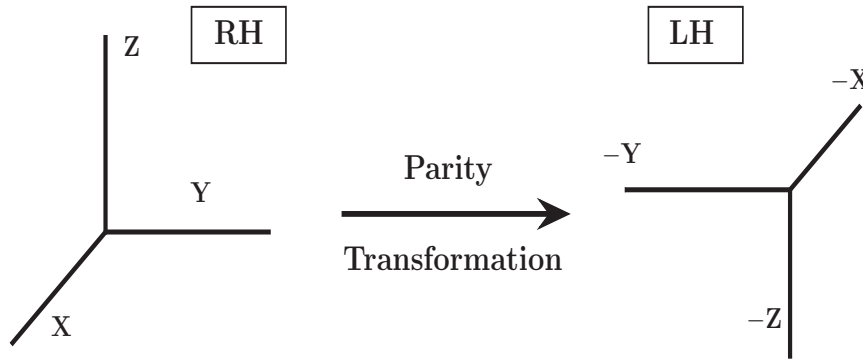


Figure 1.1: Right-handed (RH) and Left-handed (LH) coordinate systems.

It is equivalent to

$$[G, H] = 0. \quad (1.3)$$

This suggests that if the Hamiltonian of a system is invariant under continuous symmetry operation, then the generator of the operation is constant of the motion. This remarkable theorem was discovered by the German mathematician Emmy Noether. It states *Every conservation principle corresponds to symmetry in nature* [4]. For example, translational symmetry results in the conservation of linear momentum, rotational symmetry gives conservation of the angular momentum, and so on [5].

For discrete symmetries, there is no concept of infinitesimal transformation. The transformation parameters are allowed to have only discrete finite values. Discrete symmetries take the physical system from one distinct state to another. The three discrete symmetries in physical studies are charge conjugation (C), parity (P), and time-reversal (T). Some of these symmetries are violated in certain natural processes [6]. In this thesis work, we focus on the violation of one such discrete symmetry: P-symmetry.

1.1 Parity transformation

The parity operator \hat{P} , when applied to the coordinate system, changes the right-handed (RH) system to the left-handed (LH) system as shown in Fig. 1.1. So the

position vector under this transformation changes as

$$\vec{r} \xrightarrow{\hat{P}} -\vec{r}. \quad (1.4)$$

Considering this, the effect of P operation on the wave function of the system is

$$\hat{P}|\Psi(\vec{r})\rangle = |\Psi(-\vec{r})\rangle. \quad (1.5)$$

Operating \hat{P} two times, the wave function reverts to its original state $|\Psi(\vec{r})\rangle$; i.e.

$$\hat{P}\hat{P}|\Psi(\vec{r})\rangle = \hat{P}^2|\Psi(\vec{r})\rangle = \hat{P}|\Psi(-\vec{r})\rangle = |\Psi(\vec{r})\rangle. \quad (1.6)$$

This implies that \hat{P} has two eigenvalues ± 1 ; i.e.

$$\begin{aligned} \hat{P}|\Psi(\vec{r})\rangle &= |\Psi(-\vec{r})\rangle \\ &= \pm |\Psi(\vec{r})\rangle. \end{aligned} \quad (1.7)$$

The wave function with positive sign is known as even parity state and the one with a negative sign is odd parity state. \hat{P} is a Hermitian operator since it has real eigenvalue, i.e. $\hat{P}^\dagger = \hat{P}$. Also, $\hat{P}^2 = \mathcal{I}$, this implies \hat{P} is a unitary operator. So under P operation any operator \mathcal{O} transforms as

$$\mathcal{O} \rightarrow \hat{P}^{-1}\mathcal{O}\hat{P}.$$

If the system is invariant under parity transformation, then one can write that

$$\hat{P}^{-1}H\hat{P} = H. \quad (1.8)$$

This gives

$$[H, \hat{P}] = 0. \quad (1.9)$$

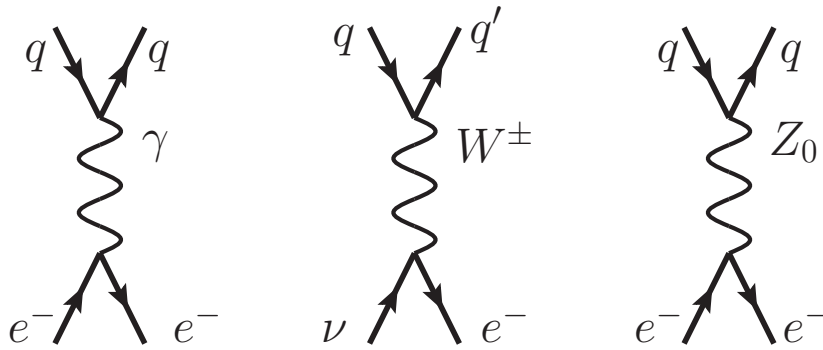


Figure 1.2: Diagrammatic representation of electro-weak interactions among the elementary particles in the SM. Here q , q' denote the quarks; e^- and ν represent electron and neutrino respectively.

As \hat{P} commutes with H , they can have a set of common eigenfunctions. This also clearly implies that for the parity violation (PV), H does not commute with \hat{P} .

1.2 Origin of PV in atoms

According to the Standard Model (SM) of particle physics, matter consists of quarks (q) and leptons. Their interactions are primarily governed by electromagnetic (em) and weak forces. Photons (γ) mediate the em interaction, while the weak interaction involves the exchange of heavy intermediate particles W^\pm and Z_0 . The weak interaction mediated by W^\pm induces a change in charge among interacting particles, as W^\pm are charged particles. Feynman diagrams, illustrated in Fig. 1.2, depict these interactions graphically. Within atoms or molecules, electrons and nucleons (proton and neutron) can engage in interactions through the em and weak forces. The em interaction between an electron and a proton, facilitated by photons, dominates and conserves parity. The resulting wave functions in an atom possess specific angular momentum and parity. Nevertheless, the weak interaction, propagated by the neutral Z_0 boson, can also occur between the nucleus and electron in an atom. Along with Z_0 boson, there can be other intermediate particles, namely Z_d and Z' , which can give rise to beyond the SM (BSM) physics, which is shown in Fig. 1.3 [7, 8]. This weak interaction leads to mixing

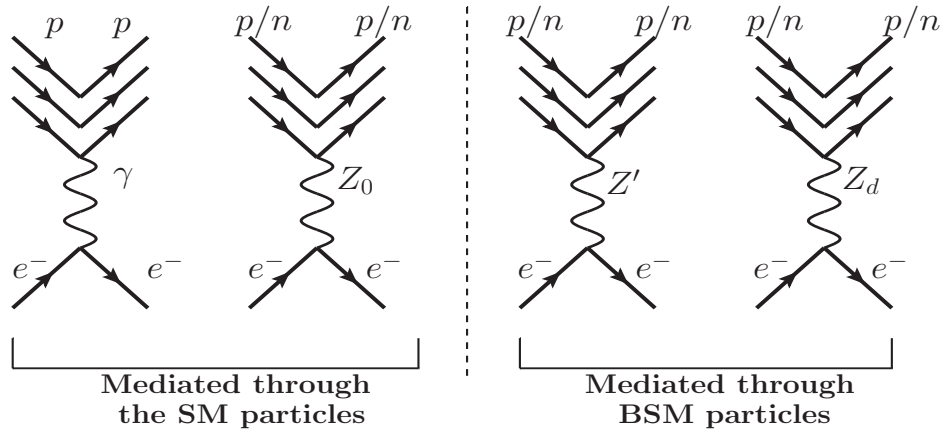


Figure 1.3: Diagrammatic representations of electro-weak interactions between nucleons and electrons present in an atomic system. Here, p and n denote proton and neutron, respectively.

between states of opposite parity. Since the magnitude of this effect is relatively small, it can be treated perturbatively. The experimental observation of these consequences poses significant challenges, but after years of concerted efforts, several groups have successfully detected this phenomenon [9, 10, 11, 12, 13].

Another source of PV in atomic systems is from the nuclear anapole moment (NAM) [14, 15]. The notion of the NAM was introduced by the Soviet physicist Yakov B. Zel'dovich. This P-odd, T-even moment of the nucleus arises due to the presence of weak interactions between nucleons. It interacts with atomic electrons close to the nucleus and gives rise to PV. Although the effect of NAM is smaller than that of neutral weak current interaction, atomic experiments probing PV are sensitive to both effects [14].

1.3 Parity violating electric dipole transition

To understand PV in atomic systems, it is imperative to know about the parity selection rules. For two parity eigenstates $|\Psi_\alpha\rangle$ and $|\Psi_\beta\rangle$ with eigenvalues being ε_α and ε_β

($\varepsilon_{\alpha,\beta} = \pm 1$), respectively, it can be shown that

$$\langle \Psi_\alpha | \vec{r} | \Psi_\beta \rangle = 0 \quad (1.10)$$

unless $\varepsilon_\alpha = -\varepsilon_\beta$. In other words, the P-odd operator \vec{r} connects states of opposite parities. So, according to the parity selection rules, electric dipole transition (E1) is forbidden between two atomic states with the same parity. However, because of the weak interaction present in the atoms, states with opposite parities mix with each other, resulting in finite transition amplitude between states with the same parity. The magnitude of this transition is typically of the order of 1 part in 10^{12} [14, 16]. One can measure this parity violating electric dipole amplitude ($E1_{PV}$) by taking interference between $E1_{PV}$ amplitude with another em transition amplitude, namely electric quadrupole (E2) and magnetic dipole (M1) or induced electric dipole ($E1^{induced}$) [9, 10, 13].

1.4 Parity violating Hamiltonian

As mentioned earlier, PV in an atom arises mainly due to the weak interactions between the electrons and the nucleus. The corresponding PV Hamiltonian in an atomic system can be constructed using bilinear covariants

$$H_{PV} = \frac{G_F}{2\sqrt{2}} \sum_{i=p,n} \left[\vec{J}_{\mu V}^i \cdot \vec{J}_{eA}^\mu + \vec{J}_{\mu A}^i \cdot \vec{J}_{eV}^\mu \right] \quad (1.11)$$

$$= H_{PV}^{NSI} + H_{PV}^{NSD}, \quad (1.12)$$

where G_F ($= 2.22 \times 10^{-14}$ atomic units (a.u.)) is the Fermi coupling constant. ‘ i ’ can be either p or n denoting proton or neutron respectively. $\vec{J}_\mu^i, \vec{J}_e^\mu$ are the nucleon and electron current respectively. As the weak interaction violates P but conserves T symmetry, the Hamiltonian has to be written as the product of axial and vector currents. H_{PV} can be further written as the sum of nuclear spin-independent (NSI) and nuclear spin-dependent (NSD) Hamiltonians.

For the NSI component, the Hamiltonian takes the form [17, 18, 19]

$$H_{PV}^{NSI} = \frac{G_F}{2\sqrt{2}} \int d^3r_e 2 \sum_{i=p,n} \int d^3r_i [C_{1i} \bar{\psi}_i \gamma_\mu \psi_i \cdot \bar{\psi}_e \gamma_\mu \gamma_5 \psi_e] \delta(\vec{r}_i - \vec{r}_e), \quad (1.13)$$

where C_{1i} is the electron-nucleon coupling co-efficient for the NSI component. \vec{r}_e and \vec{r}_i denote the electronic and nuclear coordinates respectively. ψ_e and ψ_i correspond to the electronic and nuclear wave functions respectively. Since $\bar{\psi} = \psi^\dagger \gamma_0$, we get

$$H_{PV}^{NSI} = \frac{G_F}{2\sqrt{2}} \int d^3r_e 2 \sum_{i=p,n} \int d^3r_i [C_{1i} \psi_i^\dagger \gamma_0 \gamma_\mu \psi_i \cdot \psi_e^\dagger \gamma_0 \gamma_\mu \gamma_5 \psi_e] \delta(\vec{r}_i - \vec{r}_e). \quad (1.14)$$

Neglecting the off-diagonal terms from the above summation whose contributions would be very small [19], we get

$$H_{PV}^{NSI} = \frac{G_F}{2\sqrt{2}} \int d^3r_e \psi_e^\dagger \gamma_5 \psi_e 2 \sum_{i=p,n} \int d^3r_i C_{1i} \psi_i^\dagger \psi_i \delta(\vec{r}_i - \vec{r}_e). \quad (1.15)$$

The summation over the nuclear wave functions yields the number densities of the proton and neutron, which are given by

$$\sum_p \psi_p^\dagger \psi_p = Z \rho_p(r), \quad (1.16)$$

and

$$\sum_n \psi_n^\dagger \psi_n = N \rho_n(r), \quad (1.17)$$

where Z and N denote the number of protons and neutrons respectively. ρ_p and ρ_n are the nucleon densities for protons and neutrons respectively which are normalized; i.e.

$$\int dr \rho_{p,n} 4\pi r^2 = 1. \quad (1.18)$$

So one can write

$$\begin{aligned}
 H_{PV}^{NSI} = \frac{G_F}{2\sqrt{2}} \int d^3r_e \psi_e^\dagger \gamma_5 \psi_e \sum_{i=p,n} \int d^3r_i 2 [C_{1p} \psi_p^\dagger \psi_p] \delta(\vec{r}_p - \vec{r}_e) \\
 + C_{1n} \psi_n^\dagger \psi_n] \delta(\vec{r}_n - \vec{r}_e)]. \quad (1.19)
 \end{aligned}$$

Assuming the nucleon densities coincide; i.e. $\rho_p = \rho_n = \rho$, the above equation gives

$$\begin{aligned}
 H_{PV}^{NSI} &= \frac{G_F}{2\sqrt{2}} \int d^3r_e \psi_e^\dagger \gamma_5 \psi_e 2 [C_{1p}Z + C_{1n}N] \rho(r) \\
 &= \frac{G_F}{2\sqrt{2}} Q_W \gamma_5 \rho(r), \quad (1.20)
 \end{aligned}$$

where we define $Q_W = 2 [C_{1p}Z + C_{1n}N]$ and is known as nuclear weak charge. In similar fashion H_{PV}^{NSD} can be written as

$$\begin{aligned}
 H_{PV}^{NSD} &= \frac{G_F}{2\sqrt{2}} \int d^3r_e 2 \sum_{i=p,n} \int d^3r_i [C_{2i} \bar{\psi}_i \gamma_\mu \gamma_5 \psi_i \cdot \bar{\psi}_e \gamma_\mu \psi_e] \delta(\vec{r}_i - \vec{r}_e) \\
 &= \frac{G_F}{2\sqrt{2}} \int d^3r_e 2 \sum_{i=p,n} \int d^3r_i C_{2i} [\bar{\psi}_i \gamma_0 \gamma_5 \psi_i \bar{\psi}_e \gamma_0 \psi_e \\
 &\quad + \bar{\psi}_i \gamma_r \gamma_5 \psi_i \cdot \bar{\psi}_e \gamma_r \psi_e] \delta(\vec{r}_i - \vec{r}_e). \quad (1.21)
 \end{aligned}$$

Here C_{2i} is the electron-nucleon coupling co-efficient for the NSD component. Substituting $\bar{\psi} = \psi^\dagger \gamma_0$ and using properties of gamma matrices the above equation reduces to

$$\begin{aligned}
 H_{PV}^{NSD} &= \frac{G_F}{2\sqrt{2}} \int d^3r_e \sum_{i=p,n} \int d^3r_i 2 C_{2i} [\psi_i^\dagger \gamma_5 \psi_i \psi_e^\dagger \psi_e \\
 &\quad + \psi_i^\dagger \vec{\alpha}^D \gamma_5 \psi_i \cdot \psi_e^\dagger \vec{\alpha}^D \psi_e] \delta(\vec{r}_i - \vec{r}_e). \quad (1.22)
 \end{aligned}$$

Here $\vec{\alpha}^D$ is the Dirac matrix. Since γ_5 is of the order of v/c and can be neglected, the

above equation yields

$$H_{PV}^{NSD} = \frac{G_F}{2\sqrt{2}} \int d^3r_e \sum_{i=p,n} \int d^3r_i 2C_{2i} \psi_i^\dagger \vec{\Sigma} \psi_i \cdot \psi_e^\dagger \vec{\alpha}^D \psi_e \delta(\vec{r}_i - \vec{r}_e), \quad (1.23)$$

where we have used the relation $\vec{\alpha}^D \gamma_5 = \vec{\Sigma}$; $\vec{\Sigma}$ is the four component spinor. Now integrating over nuclear coordinates, we get a quantity that is proportional to the nuclear spin \vec{I} . A constant of proportionality can be defined such that

$$\sum_{i=p,n} C_{2i} |\vec{\Sigma}| \delta(\vec{r}_i - \vec{r}_e) = K_{NSD} \rho(r),$$

where K_{NSD} is called the weak magnetic moment of the nucleus for the neutral weak current. Therefore, the NSD component of the PV Hamiltonian yields the form

$$H_{PV}^{NSD} = \frac{G_F}{\sqrt{2}} K_{NSD} \vec{\alpha}^D \cdot \vec{I} \rho(r). \quad (1.24)$$

As NAM arises because of weak interaction among nucleons, it contributes to the NSD PV. So using the same notation for the total NSD PV Hamiltonian, which arises from NAM and neutral current, we can write

$$H_{PV}^{NSD} = \frac{G_F}{\sqrt{2}} K_W \vec{\alpha}^D \cdot \vec{I} \rho(r) = \frac{G_F}{\sqrt{2}} K_W \vec{I}^{(1)} \cdot \vec{K}^{(1)}. \quad (1.25)$$

Here $\vec{K}^{(1)}$ is the electronic component of H_{PV}^{NSD} and K_W is the total weak magnetic moment. K_W depends on the contributions from both NAM and NSD components of electron-nucleus weak interaction, which can be expressed as

$$K_W = K_a + K_{NSD}, \quad (1.26)$$

where K_a denotes contribution from the NAM interaction.

1.5 Probing new physics

With progress in high-precision experimental techniques and theoretical methodologies, atomic physics assumes a crucial role in the exploration of new physics. Precision in both atomic and high-energy experiments yields distinct sensitivities to new physics models, thus offering complementary testing approaches. Atomic measurements explore energies surpassing the presently attainable in high-energy facilities. For example, the study of PV or electric dipole moment in atoms puts limits on the BSM models such as supersymmetry, multi-Higgs model, etc. [14]. As mentioned earlier, it is only possible to measure the interference of $E1_{PV}$ and some other forbidden em transition amplitude (E2, M1 or $E1^{induced}$). The measured quantity can be represented as

$$\frac{(E1_{PV} \otimes X^{em})^{expt}}{X^{em}} = A \left(\frac{E1_{PV}}{A} \right)^{theory}, \quad (1.27)$$

where X^{em} denotes E2, M1 or $E1^{induced}$ and A denotes either Q_W or K_W values. X^{em} has to be measured or calculated. To extract precise values of Q_W or K_W from the Eq. 1.27, one needs to know all the factors $(E1_{PV} \otimes X^{em})^{expt}$, X^{em} and $\left(\frac{E1_{PV}}{A}\right)^{theory}$ very accurately. The combination of experimental measurements and theoretical computations of atomic PV enables the extraction of Q_W, K_W values, which characterize NSI and NSD interactions.

The extraction of Q_W has important implications for BSM physics. One can express the deviation of this quantity from its SM value as

$$\Delta Q_W = Q_W - Q_W^{SM}, \quad (1.28)$$

where the SM value of Q_W at the tree level is given by

$$Q_W^{SM} = -N + Z(1 - 4\sin^2\theta_W). \quad (1.29)$$

Here θ_W is the Weinberg mixing angle. After the inclusion of radiative corrections [20]

$$Q_W^{SM} = -0.9793N + (0.9793 - 3.8968 \sin^2\theta_W)Z. \quad (1.30)$$

From this ΔQ_W one can put limit to the mass of an extra heavy Z' boson using the following equation [21, 22]

$$\Delta Q_W \approx 0.4(Z + 2N) \frac{M_{Z_0}^2 \cos^2\theta_W}{M_{Z'}^2}. \quad (1.31)$$

It is possible to parameterize ΔQ_W in terms of isospin conserving (\mathcal{S}) and breaking (\mathcal{T}) parameters as follows [22]

$$\Delta Q_W = Z(-0.0145 \mathcal{S} + 0.011 \mathcal{T}) - N (0.00782 \mathcal{T}). \quad (1.32)$$

One can use the above equation to constrain the \mathcal{S} parameter by taking $\mathcal{T} = 0$ [14, 22]. Essentially, the collective precision of the experiment and the associated theory must reach at least sub-one percent to scrutinize BSM physics effectively. One can also probe new physics from the NSD PV studies. For example, NAM can be used to probe hadronic PV inside the nucleus and also put a limit to the nucleon-meson coupling coefficients [23]. Although NAM is a fundamental property of the nucleus, its existence is still under debate. By combining experiment and theory one can extract K_W and then K_a to probe NAM.

1.6 Theoretical procedure to calculate $E1_{PV}$

From a theoretical point of view, it is important to calculate $E1_{PV}$ accurately to probe BSM physics. We explain the procedure for calculating this quantity below. The atomic Hamiltonian of the system will contain in addition the PV Hamiltonian H_{PV} and hence

the eigenfunctions will become states of mixed parities given by

$$|\Psi_n^F\rangle = |\Psi_n^{(0),F}\rangle + |\Psi_n^{(1),F}\rangle, \quad (1.33)$$

where $|\Psi_n^{(0),F}\rangle$ is the zeroth-order wave function in the hyperfine coordinate and can be expressed as $|\Psi_n^{(0),F}\rangle = |(IJ)FM_F\rangle$. $|\Psi_n^{(1),F}\rangle$ is the first-order perturbed wave function and can be written as sum-over zeroth-order unperturbed eigenfunctions as

$$|\Psi_n^{(1),F}\rangle = \sum_{n \neq n'} |\Psi_{n'}^{(0),F}\rangle \frac{\langle \Psi_{n'}^{(0),F} | H_{PV} | \Psi_n^{(0),F} \rangle}{E_n^{(0),F} - E_{n'}^{(0),F}}. \quad (1.34)$$

As H_{PV} is odd parity operator, the perturbed $|\Psi_n^{(1),F}\rangle$ and the unperturbed wave function $|\Psi_n^{(0),F}\rangle$ are of opposite parities. These PV admixtures allow non-zero E1 transition between states originally of the same parity ($|\Psi_i\rangle$ and $|\Psi_f\rangle$) given by

$$\begin{aligned} E1_{PV} &= \frac{\langle \Psi_f^F | D | \Psi_i^F \rangle}{\sqrt{\langle \Psi_f^F | \Psi_f^F \rangle \langle \Psi_i^F | \Psi_i^F \rangle}} \\ &\simeq \frac{\langle \Psi_f^{(0),F} | D | \Psi_i^{(1),F} \rangle + \langle \Psi_f^{(1),F} | D | \Psi_i^{(0),F} \rangle}{\sqrt{\langle \Psi_f^{(0),F} | \Psi_f^{(0),F} \rangle \langle \Psi_i^{(0),F} | \Psi_i^{(0),F} \rangle}}, \end{aligned} \quad (1.35)$$

where D is the E1 operator. $E1_{PV}$ can be written in terms of parity eigenstates as

$$\begin{aligned} E1_{PV} &= \frac{1}{\sqrt{\langle \Psi_f^{(0),F} | \Psi_f^{(0),F} \rangle \langle \Psi_i^{(0),F} | \Psi_i^{(0),F} \rangle}} \left[\sum_{n \neq i} \frac{\langle \Psi_f^{(0),F} | D | \Psi_n^{(0),F} \rangle \langle \Psi_n^{(0),F} | H_{PV} | \Psi_i^{(0),F} \rangle}{(E_i^{(0),F} - E_n^{(0),F})} \right. \\ &\quad \left. + \sum_{m \neq f} \frac{\langle \Psi_f^{(0),F} | H_{PV} | \Psi_m^{(0),F} \rangle \langle \Psi_m^{(0),F} | D | \Psi_i^{(0),F} \rangle}{(E_f^{(0),F} - E_m^{(0),F})} \right], \end{aligned} \quad (1.36)$$

where n and m are the intermediate states. Dealing with wave functions of hyperfine levels is quite challenging. To consider only the electronic coordinates, We make an approximation that the electronic and nuclear coordinates are decoupled, i.e., $|(IJ)FM_F\rangle = |IM_I; JM_J\rangle$. As the NSI PV Hamiltonian does not depend on nuclear

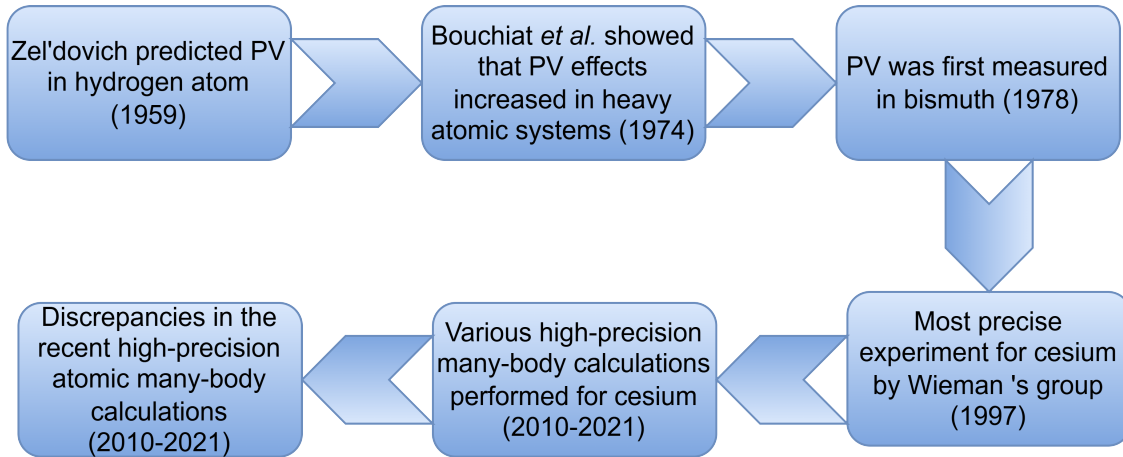


Figure 1.4: A flowchart describing the history and current status of PV studies in atomic systems.

spin, the decoupling of electronic and nuclear coordinates is quite easy in comparison to the NSD PV Hamiltonian, as H_{PV}^{NSD} depends on nuclear spin. Later in the thesis, we discuss in detail the decoupling procedure for PV calculation.

1.7 A brief history of PV in atomic systems

In this section, we discuss the historical trajectory of PV study in atomic systems. Illustrated in Figure 1.4, we present a timeline outlining the evolution of this phenomenon. Understanding PV proved challenging initially. The first inkling that parity conservation might not hold universally emerged in the early 1950s with the perplexing behavior of kaons, identified today as spin-0 particles and viewed as bound quark-antiquark states. This puzzle arose when the kaon decayed into either two pions or three pions, resulting in two distinct final states with opposite parities [16]. In a groundbreaking analysis in 1956, Lee and Yang proposed that the resolution to this puzzle lay in recognizing that P-symmetry is not conserved in this process [24]. Subsequent to the discovery of PV in nuclear beta decay [25], Yakov B. Zel'dovich proposed optical rotation experiments in atoms to measure atomic PV (APV) as a low-energy test for the SM [26]. Unfortunately, his focus was primarily on hydrogen atom, where PV effects

Table 1.1: Accuracy in measurements and calculations of PV effects in various atomic systems.

Atomic System	Transition	Accuracy in Experiment	Accuracy in Theory
^{133}Cs	$[5p^6]6S_{1/2} \rightarrow [5p^6]7S_{1/2}$	0.35% [13]	$\sim 0.3\%$ [38, 39]
^{205}Tl	$[6s^2]6P_{1/2} \rightarrow [6s^2]6P_{3/2}$	$\sim 1\%$ [10]	$\sim 3\%$ [40, 41]
^{205}Tl	$[6s^2]6P_{1/2} \rightarrow [6s^2]7P_{1/2}$	–	$\sim 5\%$ [40]
^{208}Pb	$6p^2, J=0 \rightarrow 6p^2, J=1$	$\sim 1\%$ [11]	$\sim 8\%$ [42]
^{209}Bi	$6p^3, J=3/2 \rightarrow 6p^3, J=3/2$	$\sim 2\%$ [12]	$\sim 11\%$ [42]
^{209}Bi	$6p^3, J=3/2 \rightarrow 6p^3, J=5/2$	$\sim 9\%$ [34]	$\sim 15\%$ [44]
$^{137}\text{Ba}^+$	$[5p^6]6S_{1/2} \rightarrow [4d^{10}]5D_{3/2}$	–	$\sim 1\%$ [45]
^{174}Yb	$[6s^2] \rightarrow [6s5d], J=1$	$\sim 0.5\%$ [37]	$\sim 10\%$ [46]
$^{171}\text{Yb}^+$	$[4f^{14}]6S_{1/2} \rightarrow [4f^{14}]5D_{3/2}$	–	$\sim 5\%$ [47]
^{223}Fr	$[6p^6]7S_{1/2} \rightarrow [6p^6]8S_{1/2}$	–	$\sim 1\%$ [48]
$^{226}\text{Ra}^+$	$7s^2 S_{1/2} \rightarrow 6d^2 D_{3/2}$	–	$\sim 1\%$ [49]

are very small. However, Bouchiat *et al.* later demonstrated that PV effects increase proportionally to Z^3 [27, 28]. This revelation catalyzed the study of PV, reigniting physicists' interest in exploring PV effects in heavy atoms. The first signal of PV in atoms was observed in 1978 at Novosibirsk in an optical rotation experiment with bismuth (Bi). Presently, APV has been measured in cesium (^{133}Cs) [13, 29, 30, 31, 32], bismuth (^{209}Bi) [12, 33, 34], lead (^{208}Pb) [11, 35, 36], thallium ($^{205,203}\text{Tl}$) [9, 10], and ytterbium (^{174}Yb) [37].

As previously mentioned, we need experimental measurements and atomic structure calculations to extract new physics from the PV studies. Currently, ^{133}Cs holds the best theoretical accuracy at about 0.3% [38, 39]. The theoretical uncertainty associated with ^{205}Tl stands at approximately 3% for the $6P_{1/2} - 6P_{3/2}$ transition [40, 41] and is even higher, around 5%, for the $6P_{1/2} - 7P_{1/2}$ transition [40]. Moving on to other elements, the theoretical accuracy reaches approximately 8% for ^{208}Pb [42], 11% to 15% for ^{209}Bi

[42, 43, 44], 1% for singly charged barium ion ($^{137}\text{Ba}^+$) [45], 10% for ^{174}Yb [46], 5% for $^{171}\text{Yb}^+$ [47], 1% for Francium (^{223}Fr) [48] and about 1% for singly charge radium ion ($^{226}\text{Ra}^+$) [49]. In Table 1.1, the accuracy of various measurements and calculations has been presented. This table clearly shows that ^{133}Cs has the most precise experimental value for the APV amplitude. Since high-precision experimental results are essential for making predictions about BSM physics, ^{133}Cs is the ideal choice. The remarkable precision in determining the Q_W from the ^{133}Cs atom positions it as a crucial system for low-energy tests of the SM, rendering it one of the most effective tools for exploring new physics. Furthermore, the measurements of PV in ^{133}Cs have introduced a novel avenue for investigating PV within the nucleus, specifically the NAM.

There is a rich history of calculating the $E1_{PV}^{NSI}$ amplitude for the $6s\ ^2S_{1/2} - 7s\ ^2S_{1/2}$ transition in ^{133}Cs , employing various state-of-the-art relativistic atomic many-body theories at different levels of approximation. In the early stages, Dzuba *et al.* [50, 51] utilized the time-dependent Hartree-Fock (TDHF) method in their calculations. Simultaneously, Mårtensson [52] applied the combined coupled-perturbed Dirac-Hartree-Fock (CPDF) method and random-phase approximation (RPA), collectively known as the CPDF-RPA method, to explore the impact of core-polarization (CP) effects on $E1_{PV}^{NSI}$. While technically equivalent, Mårtensson also presented intermediate-level results using approximations at the Dirac-Hartree-Fock (DHF), CPDF, and RPA methods, explicitly detailing contributions from double-core-polarization (DCP) effects.

Blundell *et al.* [53] subsequently utilized a linearized version of the relativistic coupled-cluster (RCC) method in the singles and doubles excitation approximation (SD method) to estimate the $E1_{PV}^{NSI}$ amplitude for the mentioned transition. They employed a sum-over-states approach, assessing matrix elements of the E1 operator and the PV interaction Hamiltonian for transitions involving $np\ ^2P_{1/2}$ intermediate states (referred to as the “Main” contribution) with the principal quantum number $n = 6 - 9$. Additionally, the method used the E1 matrix elements and magnetic dipole hyperfine structure constants to evaluate the uncertainty of $E1_{PV}^{NSI}$. Uncertainties from energies were addressed using experimental values, while contributions from core orbitals (the

“Core” contribution) and higher $np\ ^2P_{1/2}$ intermediate states (the “Tail” contribution) were estimated through lower-order methods.

Following these efforts, Dzuba *et al.* [54] refined their TDHF method calculation by including correlation contributions through Brückner orbitals (BO), terming the approach RPA+BO method. Subsequent works introduced higher-order contributions from the Breit, lower-order QED, and neutron skin effects through various studies, aiming for a more precise $E1_{PV}^{NSI}$ value to extract the BSM physics [43, 55, 56, 57, 58, 59, 60]. It is important to note that these higher-order effects were estimated through different many-body methods without considering correlations among themselves. Shortly after these theoretical results, RCC theory with singles and doubles approximation (RCCSD method) was employed to treat both em and PV interactions on an equal footing [48, 61].

For the NSD PV study, experiments had been conducted only for ^{133}Cs and ^{205}Tl among different hyperfine levels of the $6S_{1/2}-7S_{1/2}$ and $6P_{1/2}-6P_{3/2}$ transitions respectively [9, 10, 13]. The accuracy of the ^{133}Cs experiment was about 15% but for ^{205}Tl , the uncertainty of the experimental result was greater than the central value itself. Similarly, for the theoretical calculation, very little effort had been put in. In one of the early calculations, Flambaum and Dzuba *et al.* [40, 62] had used the DHF+BO method to estimate the $E1_{PV}^{NSD}$ values between different hyperfine levels of the $6s\ ^2S_{1/2} \rightarrow 7s\ ^2S_{1/2}$ transition of ^{133}Cs . Subsequently, Johnson *et al.* [63] employed RPA to calculate these amplitudes by incorporating electron correlation effects due to CP effects to all-order. However, they neglected the effects of DCP. Later Safronova employed the SD method to estimate $E1_{PV}^{NSD}$ for the above transition in ^{133}Cs [64].

1.8 Current status of APV and motivation

Since the early 2000s, the predominant source of theoretical uncertainty in determining the $E1_{PV}^{NSI}$ amplitude of ^{133}Cs has been the inherent challenge of solving the fundamental many-body problem in atomic structure. A decade ago, Porsev *et al.* [38] improved

the sum-over-states result of Blundell *et al.* by incorporating non-linear terms from the RCCSD method into their SD method and introducing valence triple excitations (CCSDvT method). They claimed an accuracy of approximately 0.27% for the $E1_{PV}^{NSI}$ amplitude of the $6s\ ^2S_{1/2} - 7s\ ^2S_{1/2}$ transition in ^{133}Cs . However, the estimation of Core and Tail contributions still involved a combination of many-body methods without explicit specification of the considered physical effects.

In a subsequent attempt to refine the calculated $E1_{PV}^{NSI}$ value, Dzuba *et al.* [65] determined the Core and Tail contributions using their TDHF approach, excluding DCP contributions, following a similar approach to their earlier works [50, 51]. They used the Main contribution from the calculation of Porsev *et al.* This calculation yielded a Core contribution with an opposite sign compared to that reported by Porsev *et al.* In 2013, Roberts *et al.* [66] separately reported the DCP contribution, presenting results slightly different from Mårtensson [52]. The discrepancy in the sign of the Core contribution between Dzuba *et al.* and Porsev *et al.* prompted criticism in two papers [67, 68], leading to a call for further investigation into different correlation contributions to $E1_{PV}^{NSI}$ from a first-principle approach.

In 2021, Sahoo *et al.* [39] improved their calculation of the $E1_{PV}^{NSI}$ amplitude by implementing the singles, doubles, and triples approximation (RCCSDT method) to both the unperturbed and perturbed wave functions and utilizing a substantially larger set of basis functions. They explicitly presented the Core and Valence (Main and Tail combined) contributions. The Core contribution in this approach aligned with their earlier RCCSD results [48, 61], and was close to the reported values of Blundell *et al.* [53] and Porsev *et al.* [38]. However, in a Comment, Roberts and Ginges advocated for an opposite sign of the Core contribution, providing intermediate results from their RPA+BO method [69]. Additionally, Tan *et al.* [70] estimated the combined Core and Tail contributions to the $E1_{PV}^{NSI}$ amplitude using mixed-parity orbitals through RPA and supported the value reported in Ref. [38]. This sign issue has been demonstrated in Table 1.2 quantitatively.

Addressing the issue of the sign problem with the Core contribution to the $E1_{PV}^{NSI}$

Table 1.2: Contribution to $E1_{PV}^{NSI}$ for the $6S_{1/2} - 7S_{1/2}$ transition in ^{133}Cs in $10^{-11}i(-Q_W/N)|e|a_0$, a_0 being Bohr radius. The Core contribution has been color-coded blue, whereas the Main contribution from Ref. [38] has been shown in red.

Reference	Core	Main	Tail	Total	Method
Porsev <i>et al.</i> , 2010	-0.0020	0.8823	0.0195	0.8998	CCSD _v T, sum-over state method, “Blend of many-body methods”
Dzuba <i>et al.</i> , 2012	0.0018	0.8711	0.0238	0.8967	TDHF+BO
	0.0018	0.8823	0.0238	0.9079	Main from Porsev <i>et al.</i> , 2010
Sahoo <i>et al.</i> , 2021	-0.0018	0.8594*	0.0391	0.8967	RCCSDT
Tan <i>et al.</i> , 2022	-	-	-	0.89034	P-mixed RPA

*Contribution from $9P_{1/2}$ state included in Tail part.

amplitude in ^{133}Cs is crucial. Furthermore, the basis for dividing the net $E1_{PV}^{NSI}$ result into Core, Main, Tail, DCP, etc., contributions in an approach should be precisely defined. Understanding missing physical effects in a method compared to others is essential, particularly when a combination of methods is employed to estimate these contributions individually. Misinterpretation or misrepresentation of these contributions can have repercussions when used to infer BSM physics.

As mentioned in the earlier section one of the main reasons to study NSD PV is to probe NAM. Unlike NSI PV studies, very little effort has been put into exploring the NSD PV effects in atomic systems. Though a finite value of NAM in ^{133}Cs has been inferred by combining the measured $E1_{PV}^{NSD}$ amplitude with the earlier calculations, the inferred value is at variance with the results of the shell model and the nucleon-nucleon scattering experiments [71, 72]. The value of NAM for ^{133}Cs extracted from atomic calculation is about 4σ away from nuclear result [14]. Furthermore, the nuclear parameter extracted from this value is inconsistent with that of ^{205}Tl [14]. There could be various reasons for this discrepancy like incomplete correlation in the atomic calculations, error in the atomic experiment, or incomplete nuclear model. In order to probe NAM, it is crucial to address the inconsistency between atomic and nuclear

results.

1.9 Objective of the thesis

One of the primary focuses of this study is to resolve the sign discrepancy associated with the Core contributions to the $E1_{PV}^{NSI}$ calculations of the $6s\ ^2S_{1/2} - 7s\ ^2S_{1/2}$ transition in ^{133}Cs . This work aims at highlighting the limitations of the sum-over-states approach and elucidate the reasons behind the discrepancies between the Core contributions of Porsev *et al.* [38] and Dzuba *et al.* [65]. By exploring different procedures within a general many-body framework for evaluating $E1_{PV}^{NSI}$ amplitudes in atomic systems, demonstrating how the definition of the Core contribution can vary across these procedures. This study also extends this analysis to the $E1_{PV}^{NSI}$ amplitude of the $6s\ ^2S_{1/2} - 5d\ ^2D_{3/2}$ transition in ^{133}Cs . The key motivation for including the $S - D_{3/2}$ transition of Cs in the discussion is that this analysis is expected to improve the precision of its $E1_{PV}^{NSI}$ amplitude, a crucial requirement for ongoing experiments [73, 74]. In this study we implement the *ab initio* RCCSD method to determine $E1_{PV}^{NSD}$ for ^{133}Cs . As mentioned above, the earlier calculations for NSD PV involve the use of lower-order many-body methods. Many contributions like DCP, wave function normalization, and contributions from non-linear terms have been neglected in those methods. Neglecting these correlation contributions can be a possible reason for the inconsistency between the atomic and nuclear results for estimating the NAM. This study focuses on and tries to validate the results and discover the reasons behind the discrepancies mentioned among the NAM values from different studies.

1.10 Outline of the thesis

Chapter 1: The initial chapter of this thesis explores various aspects of PV. It commences by exploring the discrete parity transformation and dives into the origins of PV in atoms. The chapter then explores the effective form of the PV Hamiltonian,

elucidating the crucial quantities, namely Q_W and K_W , which are to be extracted to investigate new physics. The chapter concludes with an exploration of the historical context of measurements and calculations related to PV, offering insights into the current status and challenges faced by the scientific community in this field. Finally, the motivation behind the theoretical work undertaken in this study is articulated.

Chapter 2: We explore essential tools aimed at simplifying the computational procedures for diverse physical properties in atomic systems. This chapter begins by discussing the challenges faced in multi-electron atomic systems. It then explores the scientific methods used to address these issues. In this context, we introduce mathematical formulations and a corresponding diagrammatic method, represented by Goldstone diagrams. This chapter serves as a foundational step towards comprehending the functioning of many-body methods.

Chapter 3: We present the relativistic many-body perturbation (RMBPT) theory for atomic systems. Then, we discuss the RPA method, illustrating its connection with the RMBPT method. The chapter explores the RCC method for closed-shell and one-valence atomic systems, detailing how RCC incorporates correlation effects into calculations up to all-orders. We also present the results for E1 matrix elements of Cs using the RMBPT, RPA, and RCC methods.

Chapter 4: In this chapter, we explore the electric dipole polarizability of closed-shell atomic systems Cs^+ and zinc as the case study. We examine the RMBPT, RPA, and RCCSD methods and their formulations for polarizability calculations. We then discuss the result for dipole polarizability using these many-body methods. We also compare our results with the available theoretical and experimental results to validate our calculations.

Chapter 5: We explore different many-body methods for evaluating the NSI PV amplitude. We begin by outlining the general methodology to calculate NSI PV amplitude using both the sum-over-state approach and the *ab initio* approach. Subsequently, we illustrate various equivalent expressions for the PV amplitude evaluation

and demonstrate how different methods use them. Additionally, we discuss how the definition of Core and Valence contributions are not unique and vary depending on the choice of perturbation procedure. Subsequently, we offer an explicit discussion regarding the contributions from Core and Valence correlations across varied many-body methodologies and elucidate their redistribution.

Chapter 6: In this chapter, we investigate the scalar, axial, and tensor polarizabilities of the hyperfine levels of the ground state of ^{133}Cs atom, examining both static and dynamic polarizabilities. We present contributions from all Core and Valence intermediate states, explaining their significance in improving the accuracy of calculations. Additionally, we discuss the underlying reasons for the discrepancies between theoretical and experimental results for polarizability.

Chapter 7: This chapter presents the calculation of the NSD PV amplitude among different hyperfine levels of $6S_{1/2} - 7S_{1/2}$ transition in ^{133}Cs atom. In this chapter, we have discussed an alternative formulation of the PV Hamiltonian to include the DCP effect in the calculation and also implement the RCCSD method to study the NSD PV. We also provide a revised value for the NAM in ^{133}Cs atom.

Chapter 8: In this chapter, we conclude the thesis. The chapter begins with summarizing the work. We also discuss the possible future works and their implications.

Bibliography

- [1] J. J. Sakurai, *Modern Quantum Mechanics*, Addison-Wesley Publishing Company, Inc, USA (1994).
- [2] A. Hosaka and H. Toki, *Quarks, Baryons and Chiral Symmetry*, World Scientific, Singapore (2001).
- [3] K. Huang, *Quarks, Leptons and Gauge Fields*, 2nd edition, World Scientific, Singapore (1992).
- [4] E. Noether, *Nachr. Ges. Wiss., Göttingen* **37**, 235 (1918).
- [5] E. L. Hill, *Rev. Mod. Phys.* **23**, 253 (1951).
- [6] W. Pauli, *Niels Bohr and the Development of Physics*, McGraw-Hill, New York (1955).
- [7] S. M. Barr, *Phys. Rev. D* **47**, 2025 (1993); *Phys. Rev. Lett.* **68**, 1822 (1992); *Phys. Rev. D* **45**, 4148 (1992).
- [8] I. Bars, *Phys. Lett.* **106B**, 105 (1981).
- [9] N. H. Edwards, S. J. Phipp, P. E. G. Baird and S. Nakayama, *Phys. Rev. Lett.* **74**, 2654 (1995).
- [10] P. A. Vetter, D. M. Meekhof, P. K. Majumder, S. K. Lamorcaux and E. N. Fortson, *Phys. Rev. Lett.* **74**, 2658 (1995).

- [11] D. M. Meekhof, P. Vetter, P. K. Majumder, S. K. Lamoreaux and E. N. Fortson, Phys. Rev. Lett. **71**, 3442 (1993).
- [12] M. J. D. Macpherson, K. P. Zetie, R. B. Warrington, D. N. Stacey and J. P. Hoare, Phys. Rev. Lett. **67**, 2784 (1991).
- [13] C. S. Wood, S. C. Bennett, D. Cho, B. P. Masterson, J. L. Roberts, C. E. Tanner and C. E. Wieman, Science **275**, 1759 (1997).
- [14] J. S. M. Ginges and V. V. Flambaum, Phys. Reports **397**, 63 (2004).
- [15] Ya. B. Zel'dovich, Zh. Eksp. Teor. Fiz. **33**, 1531 (1957).
- [16] M. A. Bouchiat and C. C. Bouchiat, Rep. Prog. Phys. **60**, 1351 (1997).
- [17] E. D. Commins, Phys. Scr. **36**, 468 (1987).
- [18] E. D. Commins, Phys. Scr. T46, 92 (1993).
- [19] I. B. Khriplovich, *Parity Nonconservation in Atomic Phenomena*, Gordon and Breach, Philadelphia (1991).
- [20] M. Peskin and T. Tachikawa, Phys. Rev. Lett. **65**, 964 (1990); Phys. Rev. D **46**, 381 (1992).
- [21] D. London and J. L. Rosner, Phys. Rev. D **34**, 1530 (1986).
- [22] W. J. Marciano and J. L. Rosner, Phys. Rev. Lett. **65**, 2963 (1990); **68**, 898(E) (1992).
- [23] W. C. Haxton, C. -P. Liu and M. J. Ramsey-Musolf, Phys. Rev. Lett. **86**, 5247 (2001).
- [24] T. D. Lee and C. N. Yang, Phys. Rev. **104**, 254 (1956).
- [25] C. S. Wu, E. Ambler, R. W. Hayward, D. D. Hoppes, and R. P. Hudson, Phys. Rev. **105**, 1413 (1957).

- [26] Ya. B. Zel'dovich, Zh. Eksp. Teor. Fiz. **36**, 964 (1959); Sov. Phys. JETP **9**, 682 (1959).
- [27] M. A. Bouchiat and C. C. Bouchiat, J. Phys. (Paris) **35**, 899 (1974); J. Phys. (Paris) **36**, 493 (1975).
- [28] M. A. Bouchiat and C. C. Bouchiat, Phys. Lett. B **48**, 111 (1974).
- [29] M. A. Bouchiat, J. Guena, L. Hunter, and L. Pottier, Phys. Lett. B **117**, 358 (1982).
- [30] J. Guéna, D. Chauvat, P. Jacquier, E. Jahier, M. Lintz, S. Sanguinetti, A. Wasan, M. A. Bouchiat, A. V. Papoyan, and D. Sarkisyan, Phys. Rev. Lett. **90**, 143001 (2003).
- [31] J. Guéna, M. Lintz, and M. A. Bouchiat, Phys. Rev. A **71**, 042108 (2005).
- [32] K. Tsigutkin, D. Dounas-Frazer, A. Family, J. E. Stalnaker, V. V. Yashchuk, and D. Budker, Phys. Rev. Lett. **103**, 071601 (2009).
- [33] J. D. Taylor, P. E. G. Baird, R. G. Hunt, M. J. D. Macpherson, G. Nowicki, P.G.H. Sandars, D. N. Stacey, J. Phys. B **20**, 5423 (1987).
- [34] R. B. Warrington, C. D. Thompson, D. N. Stacey, Europhys. Lett. **24**, 641 (1993).
- [35] S. J. Phipp, N. H. Edwards, P. E. G. Baird, and S. Nakayama, J. Phys. B: At., Mol. Opt. Phys. **29**, 1861 (1996).
- [36] T. P. Emmons, J. M. Reeves, E. N. Fortson, Phys. Rev. Lett. **51**, 2089 (1983).
- [37] D. Antypas, A. Fabricant, J. E. Stalnaker, K. Tsigutkin, V. Flambaum, and D. Budker, Nat. Phys. **15**, 120 (2019).
- [38] S. G. Porsev, K. Beloy and A. Derevianko, Phys. Rev. D **82**, 036008 (2010).
- [39] B. K. Sahoo, B. P. Das and H. Spiesberger, Phys. Rev. D **103**, L111303 (2021).

- [40] V. A. Dzuba, V. V. Flambaum, P. G. Silvestrov, O. P. Sushkov, *J. Phys. B* **20**, 3297 (1987).
- [41] M. G. Kozlov, S. G. Porsev, W. R. Johnson, *Phys. Rev. A* **64**, 052107 (2001).
- [42] V. A. Dzuba, V. V. Flambaum, P. G. Silvestrov, O. P. Sushkov, *Europhys. Lett.* **7**, 413 (1988).
- [43] V. A. Dzuba, V. V. Flambaum, O. P. Sushkov, *Phys. Lett. A* **141**, 147 (1989).
- [44] M. G. Kozlov, S. G. Porsev, V. V. Flambaum, *J. Phys. B* **29**, 689 (1996).
- [45] B. K. Sahoo, R. Chaudhuri, B. P. Das, and D. Mukherjee, *Phys. Rev. Lett.* **96**, 163003 (2006).
- [46] V. A. Dzuba and V. V. Flambaum, *Phys. Rev. A* **83**, 042514 (2011).
- [47] B. K. Sahoo and B. P. Das, *Phys. Rev. A* **84**, 010502(R) (2011).
- [48] B. K. Sahoo, *J. Phys. B* **43**, 085005 (2010).
- [49] L. W. Wansbeek, B. K. Sahoo, R. G. E. Timmermans, K. Jungmann, B. P. Das, and D. Mukherjee, *Phys. Rev. A* **78**, 050501(R) (2008).
- [50] V. A. Dzuba, V. V. Flambaum, P. G. Silvestrov and O. P. Sushkov, *Phys. Lett. A* **103**, 265 (1984).
- [51] V. A. Dzuba, V. V. Flambaum, P. G. Silvestrov and O. P. Sushkov, *J. Phys. B: Atom. Mol. Phys.* **18**, 597 (1985).
- [52] A. -M. Mårtensson-Pendrill, *J. Phys.* **46**, 11 (1985).
- [53] S. A. Blundell, J. Sapirstein and W. R. Johnson, *Phys. Rev. D* **45**, 5 (1992).
- [54] V. A. Dzuba, V. V. Flambaum and J. S. M. Ginges, *Phys. Rev. D* **63**, 062101 (2001).

- [55] A. I. Milstein, O. P. Sushkov and I. S. Terekhov, Phys. Rev. Lett. **89**, 283003 (2002).
- [56] B. A. Brown, A. Derevianko and V. V. Flambaum, Phys. Rev. C **79**, 035501 (2009).
- [57] A. Derevianko, Phys. Rev. Lett. **85**, 1618 (2000); Phys. Rev. A **65**, 012106 (2001).
- [58] M. G. Kozlov, S. G. Porsev and I. I. Tupitsyn, Phys. Rev. Lett. **86**, 3260 (2001).
- [59] V. M. Shabaev, K. Pachucki, I. I. Tupitsyn and V. A. Yerokhin, Phys. Rev. Lett. **94**, 213002 (2005).
- [60] V. A. Dzuba, V. V. Flambaum and J. S. M. Ginges, Phys. Rev. D **66**, 076013 (2002).
- [61] B. P. Das, B. K. Sahoo, G. Gopakumar, and R. K. Chaudhuri, J. Mol. Str. **768**, 141 (2006).
- [62] V. V. Flambaum and D. W. Murray, Phys. Rev. C **56**, 1641 (1997).
- [63] W. R. Johnson, M. S. Safronova and U. I. Safronova Phys. Rev. A **67**, 062106 (2003).
- [64] M. S. Safronova *et al.*, Nuc. Phys. A **827**, 411 (2009).
- [65] V. A. Dzuba, J. C. Berengut, V. V. Flambaum and B. Roberts, Phys. Rev. Lett. **109**, 203003 (2012).
- [66] B. M. Roberts, V. A. Dzuba and V. V. Flambaum, Phys. Rev. A **88**, 042507 (2013).
- [67] M. S. Safronova, D. Budker, D. DeMille, D. F. J. Kimball, A. Derevianko and C. W. Clark, Rev. Mod. Phys. **90**, 025008 (2018).
- [68] C. Wieman and A. Derevianko, arXiv:1904.00281 (Unpublished).

- [69] B. M. Roberts and J. S. M. Ginges, Phys. Rev. D **105**, 018301 (2022).
- [70] H. B. Tran Tan, D. Xiao and A. Derevianko, Phys. Rev. A **105**, 022803 (2022).
- [71] W. S. Wilburn and J. D. Bowman, Phys. Rev. C **57**, 3425 (1998).
- [72] W. C. Haxton and C. E. Wieman, Ann. Rev. Nuc. Part. Sc. **51**, 261 (2001).
- [73] J. Choi and D. S. Elliott, Phys. Rev. A **93**, 023432 (2016).
- [74] A. Kastberg, T. Aoki, B. K. Sahoo, Y. Sakemi and B. P. Das, Phys. Rev. A **100**, 050101(R) (2019).

Chapter 2

Essential Tools and Techniques in Atomic Many-Body Methods

APPPLICABILITY of quantum many-body methods spans across diverse branches of physics, such as atomic physics, molecular physics, nuclear physics, and condensed matter physics. This chapter focuses on quantum many-body methods within the context of atomic physics. When dealing with atoms containing two or more electrons, exact solutions to the Schrödinger equation become unattainable. Therefore, many-body methods become essential to obtain accurate wave functions for determining atomic properties [1, 2, 3]. Accurate calculations of atomic properties, particularly for studying phenomena like PV, lifetimes, and polarizabilities, necessitate the use of reliable many-body methods. To achieve precision in calculations, employing adequate quantum many-body methods within a relativistic framework is imperative. However, adopting a covariant form of the relativistic Hamiltonian for atomic property calculations proves impractical due to its complexity, making it unsolvable. Consequently, a pragmatic approach involves utilizing the Dirac Hamiltonian and a non-relativistic form for nuclear potential and electron-electron interactions in defining the total atomic Hamiltonian, facilitating the determination of atomic spectroscopic properties. Given the inherent complexity of solving the equation of motion (EOM) for a system with in-

interactions between two electrons, Coulomb interactions within an atomic system, pose a formidable challenge. Consequently, we resort to approximated many-body methods in our analyses. Starting with a mean-field approximation in the Hartree-Fock (HF) (referred to as DHF in the relativistic form) procedure, we treat Coulomb interactions among electrons as an average potential. Subsequently, residual interactions are addressed through many-body methods. In practical applications of many-body methods, essential tools are required to streamline the computational tasks involved in determining properties within atomic systems. The field theory widely acknowledges the efficacy of second quantized formulations, normal order forms, and Wick's theorem, among others, as they facilitate simplified calculations and improve the understanding of various physical processes [4]. Additionally, the use of Feynman-like diagrams provides a more straightforward and realistic approach to comprehending these processes [4, 5]. This chapter introduces and defines these mathematical tools along with a corresponding diagrammatic approach, known as the Goldstone diagrams [1, 2, 3], which applies to both occupied and unoccupied electron states. The interaction forces within atomic systems find expressions in terms of these mechanisms. We explore these tools for constructing single-particle wave functions, whereby the matrix elements of interaction operators can be expressed separately in radial integrals and angular factors of the single-particle orbitals [6, 7, 8, 9].

2.1 Atomic Hamiltonian

Let us consider an atom of N_e number of electrons. The total Hamiltonian of the atom can, then, be written as

$$\begin{aligned} H_{tot} &= T_N(\vec{R}) + T_e(\vec{r}) + V_{eN}(\vec{r}, \vec{R}) + V_{ee}(\vec{r}) \\ &= \frac{P^2}{2M} + \sum_{i=1}^{N_e} \frac{p_i^2}{2m_e} - \sum_i \frac{Ze^2}{|\vec{R} - \vec{r}_i|} + \frac{1}{2} \sum_{i \neq j} \frac{e^2}{|\vec{r}_i - \vec{r}_j|}, \end{aligned} \quad (2.1)$$

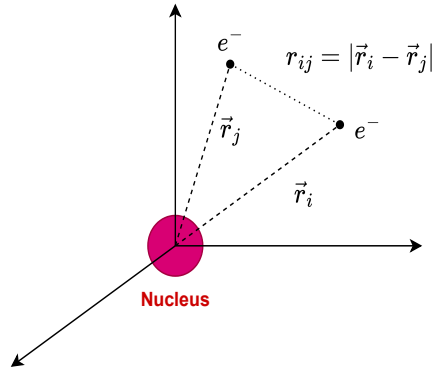


Figure 2.1: Electronic coordinate system taking nucleus as the origin. \vec{r}_i and \vec{r}_j are the position vectors for i and j^{th} electrons (e^-) respectively and r_{ij} denotes the distance between them.

where the first two terms are the kinetic energy operators of the nucleus and electrons, respectively, the third term corresponds to the electron-nucleus Coulomb interactions, and the last term involves the electron-electron repulsive Coulomb interactions. In Eq. 2.1, P and p_i denote the momentum operators of the nucleus and i^{th} electron, respectively, and M and m_e are the masses of nucleus and electron, respectively. Nuclear coordinates are defined as \vec{R} , and electronic coordinates are given as \vec{r} .

The Hamiltonian in Eq. 2.1 satisfies the Schrödinger equation

$$H_{tot}|\Psi(\vec{r}, \vec{R})\rangle = E_{tot}|\Psi(\vec{r}, \vec{R})\rangle, \quad (2.2)$$

where the wave function $|\Psi(\vec{r}, \vec{R})\rangle$ carries information about the nucleus and electrons of the atom. Since we are interested only in electronic properties in this study, we decouple electronic and nuclear wave functions. The basic idea behind this approximation lies in the fact that the nucleus is heavier than the electrons by three orders of magnitude. Consequently, we treat the nuclear positions as effectively fixed, and the nuclear wave functions are considered highly localized around the nuclear coordinate. This can be

utilized by using the quasi-separable ansatz

$$|\Psi\rangle = |\Psi_N(\vec{R})\rangle \otimes |\Psi_e(\vec{r})\rangle \equiv |\Psi_N(\vec{R})\rangle |\Psi_e(\vec{r})\rangle. \quad (2.3)$$

Under this approximation, the kinetic energy term $T_N(\vec{R})$ can be neglected as it is smaller than $T_e(\vec{r})$ by a factor $\frac{M}{m_e}$. Hence, after taking the atomic nucleus as our origin as shown in Fig. 2.1, the electronic Hamiltonian takes the form

$$\begin{aligned} H_e(\vec{r}) &= T_e(\vec{r}) + V_{eN}(\vec{r}) + V_{ee}(\vec{r}) \\ &= \sum_{i=1}^{N_e} \frac{p_i^2}{2m_e} - \sum_i \frac{Ze^2}{|\vec{r}_i|} + \frac{1}{2} \sum_{i \neq j} \frac{e^2}{|\vec{r}_i - \vec{r}_j|}, \end{aligned} \quad (2.4)$$

which follows the electronic Schrödinger equation

$$H_e |\Psi_e(\vec{r})\rangle = E_e |\Psi_e(\vec{r})\rangle, \quad (2.5)$$

where E_e is the eigenvalue of H_e . To incorporate relativistic effects, we have to consider the Dirac Hamiltonian. In 1928, Paul Dirac introduced the Dirac equation which is consistent with both quantum mechanics and special relativity. Dirac equation successfully describes the properties of spin 1/2 finite mass particles (electrons, quarks). The Dirac Hamiltonian for an atomic system under Coulomb potential (in a.u.) is

$$H_{DC} = \sum_i \left[c \vec{\alpha}_i^D \cdot \vec{p}_i + (\beta_i^D - 1)c^2 + V_i^{nuc} \right] + \frac{1}{2} \sum_{i \neq j} \frac{1}{r_{ij}}, \quad (2.6)$$

where H_{DC} is the Dirac-Coulomb (DC) Hamiltonian, c is the velocity of light, and β^D is another four component Dirac matrix. $\vec{\alpha}^D$ and β^D can be expressed in matrix form as

$$\vec{\alpha}_k^D = \begin{pmatrix} 0 & \vec{\sigma}_k \\ \vec{\sigma}_k & 0 \end{pmatrix} \quad \text{and} \quad \beta^D = \begin{pmatrix} \mathcal{I} & 0 \\ 0 & -\mathcal{I} \end{pmatrix}, \quad (2.7)$$

where σ_k is the k^{th} Pauli spin matrix. A single particle orbital $|\psi\rangle$ can be written as a four-component one-particle wave function [10]

$$\psi(\vec{r}) = \frac{1}{r} \begin{pmatrix} P_{n\kappa}(r)\chi_{\kappa m_j}(\theta, \phi) \\ iQ_{n\kappa}(r)\chi_{-\kappa m_j}(\theta, \phi) \end{pmatrix}, \quad (2.8)$$

where $P_{n\kappa}(r)$ and $Q_{n\kappa}(r)$ correspond to the large and small components of the single particle orbital wave function, respectively. $\kappa = -a(j + \frac{1}{2})$ is the relativistic quantum number, where $a = 2(j - l) = \pm 1$ serves as a sign factor. j and m_j are total and azimuthal angular momentum quantum numbers, respectively, and l is the orbital angular momentum quantum number. The spin angular function $\chi_{\kappa m}(\theta, \phi)$ is given by

$$\chi_{\kappa m_j}(\theta, \phi) = \frac{1}{\sqrt{2l+1}} \begin{pmatrix} a\sqrt{l + \frac{1}{2} + am_j} Y_l^{m_j-1/2}(\theta, \phi) \\ \sqrt{l + \frac{1}{2} - am_j} Y_l^{m_j+1/2}(\theta, \phi) \end{pmatrix}. \quad (2.9)$$

When $a = 1$, i.e., $j = l + 1/2$,

$$\chi_{\kappa m_j}(\theta, \phi) = \frac{1}{\sqrt{2l+1}} \begin{pmatrix} \sqrt{l + m_j + \frac{1}{2}} Y_l^{m_j-1/2}(\theta, \phi) \\ \sqrt{l - m_j + \frac{1}{2}} Y_l^{m_j+1/2}(\theta, \phi) \end{pmatrix}. \quad (2.10)$$

When $a = -1$, i.e., $j = l - 1/2$,

$$\chi_{\kappa m_j}(\theta, \phi) = \frac{1}{\sqrt{2l+1}} \begin{pmatrix} -\sqrt{l - m_j + \frac{1}{2}} Y_l^{m_j-1/2}(\theta, \phi) \\ \sqrt{l + m_j + \frac{1}{2}} Y_l^{m_j+1/2}(\theta, \phi) \end{pmatrix}. \quad (2.11)$$

2.2 Electronic wave function and second quantization

Electrons are fermions; they follow Fermi-Dirac statistics. For non-interacting electrons the total electronic wave function $|\Psi\rangle$ (dropping the subscript ‘e’) for an atom is a Slater determinant. In this case, the total electronic wave function is composed of different single electron orbital with dimension of the determinant as $N_e \times N_e$; i.e.

$$\Psi = \frac{1}{\sqrt{N_e!}} \begin{vmatrix} \psi_1(\vec{r}_1) & \psi_1(\vec{r}_2) & \cdots & \psi_1(\vec{r}_{N_e}) \\ \psi_2(\vec{r}_1) & \psi_2(\vec{r}_2) & \cdots & \psi_2(\vec{r}_{N_e}) \\ \vdots & \ddots & & \vdots \\ \psi_{N_e}(\vec{r}_1) & \psi_{N_e}(\vec{r}_2) & \cdots & \psi_{N_e}(\vec{r}_{N_e}) \end{vmatrix}. \quad (2.12)$$

The factor $\frac{1}{\sqrt{N_e!}}$ is the normalization factor. The above Slater determinant is denoted for convenient use by [1]

$$|\Psi\rangle = |\{abc \cdots \text{up to } N_e \text{ number of index}\}\rangle. \quad (2.13)$$

By treating $|\Psi\rangle$ as the reference state, an excited state can be defined as

$$\begin{aligned} |\Psi_{ab \cdots}^{pq \cdots}\rangle &= a_p^\dagger a_q^\dagger a_b a_a |\{abc \cdots \text{up to } N_e \text{ number of index}\}\rangle \\ &= |\{pqc \cdots \text{up to } N_e \text{ number of index}\}\rangle. \end{aligned} \quad (2.14)$$

a_i^\dagger represents the creation of electron i , whereas a_i represents the annihilation of electron i with respect $|\Psi\rangle$. Therefore in the above expression, $|\Psi_{a,b,\dots}^{p,q,\dots}\rangle$ denotes a determinant for which the single occupied orbital ‘a’ is replaced by the virtual orbital ‘p’ and so on. We categorize electrons within atomic systems based on their locations into three distinct types: occupied (referred to as holes or core), unoccupied (referred to as particles), and general electrons. This classification is facilitated by the second quantization form-

alism, allowing us to distinguish and perform algebraic operations on these different electron types. In our notation, we denote occupied electrons by subscripts with letters a, b, c, d, \dots , unoccupied (virtual) electrons by subscripts p, q, r, s, \dots , and general electrons by subscripts i, j, k, l, \dots , providing a clear representation for the various electron categories. We can express all physical operators in terms of these creation and annihilation operators [1, 3]. In the second quantization formalism, a one-body operator (F) can be expressed

$$F = \sum_i^{N_e} f(\vec{r}_i) = \sum_{j,l} \langle j|f|l \rangle a_j^\dagger a_l. \quad (2.15)$$

Similarly, a two-body operator (G) can take the form as

$$G = \sum_{i<j}^{N_e} g(\vec{r}_i, \vec{r}_j) = \frac{1}{2} \sum_{k,l,m,n} \langle kl|g|mn \rangle a_k^\dagger a_l^\dagger a_m a_n. \quad (2.16)$$

Let's discuss the matrix element of any general one and two-body operators, which encompass both radial and angular momentum factors. Given the computational challenges associated with handling the m_j components of the total angular momentum j , our approach involves isolating the m_j dependent factors during the calculation, focusing solely on the remaining magnitudes. Specific transitions to distinct m_j states can then be addressed in the final stages of the calculations. This can be done with the help of the Wigner-Eckart theorem, which tells a one-body operator of rank ' k ' (f_q^k) in a single particle representation can be expressed as [1, 6, 7, 10],

$$\langle j m_j | f_q^k | j' m_{j'} \rangle = (-1)^{j-m_j} \begin{pmatrix} j & k & j' \\ -m_j & q & m_{j'} \end{pmatrix} \langle j || f^k || j' \rangle, \quad (2.17)$$

where $\langle j || f^k || j' \rangle$ is called the reduced matrix element and is independent of m_j component and the quantity in $()$ is called 3j symbol. Similarly, one can use the Wigner-Eckart theorem for a two-body operator. Before using the Wigner-Eckart theorem, we use the coupling factor to write a two-body operator as a product of two spherical tensors as

follows [11, 12]

$$g(\vec{r}_1, \vec{r}_2) = \sum_k g_k(r_1, r_2) [T^k(1).U^k(2)]_0^0. \quad (2.18)$$

$g_k(r_1, r_2)$ is the radial part of the integral with rank k dependency. Now in terms of the reduced matrix element we can write [12, 13]

$$\begin{aligned} \langle j_a j_b | g(\vec{r}_1, \vec{r}_2) | j_c j_d \rangle = & \sum_k (-1)^{(j_a - m_a + j_b - m_b + k - q)} \begin{pmatrix} j_a & k & j_c \\ -m_a & q & m_c \end{pmatrix} \\ & \times \begin{pmatrix} j_b & k & j_d \\ -m_b & -q & m_d \end{pmatrix} R^k(j_a j_b j_c j_d), \end{aligned} \quad (2.19)$$

where R^k is given by

$$R^k(j_a j_b j_c j_d) = (-1)^k \langle j_a || T^k || j_c \rangle \langle j_b || U^k || j_d \rangle. \quad (2.20)$$

2.3 Challenges with multi-electron atomic system

Recalling from the earlier section the electronic Hamiltonian for an atom with N_e number of electrons can be written as (dropping the subscript)

$$\begin{aligned} H &= \sum_{i=1}^{N_e} \underbrace{\left[c \vec{\alpha}^D \cdot \vec{p} + (\beta^D - 1)c^2 + V_i^{nuc} \right]}_{h_1(\vec{r}_i)} + \frac{1}{2} \sum_{i \neq j} \underbrace{\frac{1}{r_{ij}}}_{h_2(\vec{r}_i, \vec{r}_j)} \\ &= \sum_{i=1}^{N_e} h_1(\vec{r}_i) + \frac{1}{2} \sum_{i \neq j} h_2(\vec{r}_i, \vec{r}_j), \end{aligned} \quad (2.21)$$

where h_1 and h_2 represent the one-body and two-body terms, respectively, with \vec{r}_i s being the generalised coordinates and r_{ij} is distance between two electrons. To calculate the energy due to the Hamiltonian in Eq. 2.21, we need to evaluate the following expectation

value

$$\langle \Psi | H | \Psi \rangle = \langle \Psi | \sum_i h_1(\vec{r}_i) | \Psi \rangle + \langle \Psi | \frac{1}{2} \sum_{i \neq j} h_2(\vec{r}_i, \vec{r}_j) | \Psi \rangle = E \langle \Psi | \Psi \rangle. \quad (2.22)$$

As mentioned earlier, electrons are fermions, for non-interacting electrons the total electronic wave function $|\Psi\rangle$ for an atom is a Slater determinant. To evaluate the one-body integral $\langle \Psi | \sum_i h_1(\vec{r}_i) | \Psi \rangle$ and the two-body integral $\langle \Psi | \frac{1}{2} \sum_{i \neq j} h_2(\vec{r}_i, \vec{r}_j) | \Psi \rangle$ in Eq. 2.22, there exists a convenient tool to simplify the integrals containing the Slater determinant wave functions to sum of integrals involving individual orbitals. These set of rules are called *Slater-Condon* (SC) rules [1, 14, 15] and are outlined below.

(i) For any general one-body operator F in an N particle system defined as a sum of individual operators, $F = \sum_{i=1}^N f(\vec{r}_i)$, it can follow

$$\begin{aligned} (a) \quad & \langle \Psi | \sum_i f(\vec{r}_i) | \Psi \rangle = \sum_a \langle \psi_a | f(\vec{r}_i) | \psi_a \rangle, \\ (b) \quad & \langle \Psi_a^p | \sum_i f(\vec{r}_i) | \Psi \rangle = \langle \psi_p | f(\vec{r}_i) | \psi_a \rangle \\ \text{and } (c) \quad & \langle \Psi_{a,b,\dots}^{p,q,\dots} | \sum_i f(\vec{r}_i) | \Psi \rangle = 0. \end{aligned} \quad (2.23)$$

(ii) For any general two-body operator G in an N particle system, defined as $G = \frac{1}{2} \sum_{i \neq j} g(\vec{r}_i, \vec{r}_j)$, we have

$$\begin{aligned} (a) \quad & \langle \Psi | \frac{1}{2} \sum_{i \neq j} g(\vec{r}_i, \vec{r}_j) | \Psi \rangle = \frac{1}{2} \sum_{a,b} \left[\langle \psi_a(1) \psi_b(2) | g(\vec{r}_1, \vec{r}_2) | \psi_a(1) \psi_b(2) \rangle \right. \\ & \quad \left. - \langle \psi_b(1) \psi_a(2) | g(\vec{r}_1, \vec{r}_2) | \psi_a(1) \psi_b(2) \rangle \right], \\ (b) \quad & \langle \Psi_a^p | \frac{1}{2} \sum_{i \neq j} g(\vec{r}_i, \vec{r}_j) | \Psi \rangle = \sum_b \left[\langle \psi_p(1) \psi_b(2) | g(\vec{r}_1, \vec{r}_2) | \psi_a(1) \psi_b(2) \rangle \right. \\ & \quad \left. - \langle \psi_b(1) \psi_p(2) | g(\vec{r}_1, \vec{r}_2) | \psi_a(1) \psi_b(2) \rangle \right], \\ (c) \quad & \langle \Psi_{a,b}^{p,q} | \frac{1}{2} \sum_{i \neq j} g(\vec{r}_i, \vec{r}_j) | \Psi \rangle = \langle \psi_p(1) \psi_q(2) | g(\vec{r}_1, \vec{r}_2) | \psi_a(1) \psi_b(2) \rangle \\ & \quad - \langle \psi_q(1) \psi_p(2) | g(\vec{r}_1, \vec{r}_2) | \psi_a(1) \psi_b(2) \rangle \end{aligned}$$

and (2.24)

$$(d) \quad \langle \Psi_{a,b,\dots}^{p,q,\dots} | \frac{1}{2} \sum_{i \neq j} g(\vec{r}_1, \vec{r}_2) | \Psi \rangle = 0. \quad (2.25)$$

Applying the SC rules in Eq. 2.22, the integral takes the form

$$\begin{aligned} \langle \Psi | \sum_i h_1(\vec{r}_i) + \frac{1}{2} \sum_{i \neq j} h_2(\vec{r}_i, \vec{r}_j) | \Psi \rangle &= \sum_i \langle \psi_i | h_1 | \psi_i \rangle + \frac{1}{2} \sum_{i,j} \left[\langle \psi_i \psi_j | h_2 | \psi_i \psi_j \rangle \right. \\ &\quad \left. - \langle \psi_j \psi_i | h_2 | \psi_i \psi_j \rangle \right] = \sum_i \epsilon_i \langle \psi_i | \psi_i \rangle, \end{aligned} \quad (2.26)$$

where ϵ_i is single particle orbital energy. For the i^{th} electron, the above equation takes the form

$$h_1 | \psi_i \rangle + \frac{1}{2} \sum_j \left[\langle \psi_j | h_2 | \psi_j \rangle | \psi_i \rangle - \langle \psi_i | h_2 | \psi_j \rangle | \psi_j \rangle \right] = \epsilon_i | \psi_i \rangle. \quad (2.27)$$

As can be inferred from the above equation, to solve for i^{th} electron we need to know orbital wave functions for all the other electrons. Further, solving Eq. 2.27 iteratively does not guarantee to yield the ground state energy. Here comes the necessity to apply the variational principle to Eq. 2.27 in order to obtain the ground state energy. In the next section, we shall introduce the variational principle and the variational method to obtain the ground state wave function and energy of the multi-electron atomic system.

2.4 Variational method

The variational method is useful for estimating the upper bound value for the ground state eigenenergy of a system whose Hamiltonian is known, but its eigenvalues and eigenstates are not known [16]. Assume that H is the Hamiltonian of a system and $|\Psi_0\rangle$ is its exact but unknown ground state wave function. Then

$$H | \Psi_0 \rangle = E_0 | \Psi_0 \rangle, \quad (2.28)$$

where E_0 is the exact ground state energy of the system and it is given by

$$E_0 = \frac{\langle \Psi_0 | H | \Psi_0 \rangle}{\langle \Psi_0 | \Psi_0 \rangle}. \quad (2.29)$$

If $|\Phi_0\rangle$ is an arbitrary wave function and E is the corresponding energy

$$E = \frac{\langle \Phi_0 | H | \Phi_0 \rangle}{\langle \Phi_0 | \Phi_0 \rangle}, \quad (2.30)$$

then the variational principle states that $E \geq E_0$.

Proof: As the exact unknown eigenfunctions ($|\Psi_n\rangle$) form a complete set, the approximate state can be written in terms of linear combination of them

$$|\Phi_0\rangle = \sum_n C_n |\Psi_n\rangle, \quad (2.31)$$

with $H|\Psi_n\rangle = E_n|\Psi_n\rangle$. Assume that the eigenfunctions are orthonormalized; i.e. $\langle \Psi_m | \Psi_n \rangle = \delta_{mn}$.

The normalization of $|\Phi_0\rangle$ leads to

$$\begin{aligned} \langle \Phi_0 | \Phi_0 \rangle &= 1 \\ \Rightarrow \sum_{m,n} C_m^* C_n \underbrace{\langle \Psi_m | \Psi_n \rangle}_{\delta_{mn}} &= 1 \\ \Rightarrow \sum_n |C_n|^2 &= 1. \end{aligned} \quad (2.32)$$

The expectation value of the Hamiltonian in the approximate state is

$$\begin{aligned} \langle \Phi_0 | H | \Phi_0 \rangle &= E = \sum_{m,n} C_m^* C_n \langle \Psi_m | H | \Psi_n \rangle \\ &= \sum_{m,n} C_m^* C_n E_n \underbrace{\langle \Psi_m | \Psi_n \rangle}_{\delta_{mn}} \\ &= \sum_n E_n |C_n|^2. \end{aligned} \quad (2.33)$$

But, by definition, the energy of the ground state (E_0) is the lowest. Therefore, $E_0 \leq E_n$. Using this in Eq. 2.33 we get

$$\begin{aligned} \langle \Phi_0 | H | \Phi_0 \rangle &= \sum_n E_n |C_n^2| \geq E_0 \underbrace{\sum_n |C_n^2|}_{=1} \\ \Rightarrow \langle \Phi_0 | H | \Phi_0 \rangle &\geq E_0. \end{aligned} \quad (2.34)$$

2.5 Mean-field model

The variational approach we follow differs from minimizing energy coefficients associated with wave functions; instead, we minimize with respect to the wave functions directly. We consider the total trial electronic wave function Φ_0 to be

$$\Phi_0 = \frac{1}{\sqrt{N_e!}} \begin{vmatrix} \phi_1(\vec{r}_1) & \phi_1(\vec{r}_2) & \cdots & \phi_1(\vec{r}_{N_e}) \\ \phi_2(\vec{r}_1) & \phi_2(\vec{r}_2) & \cdots & \phi_2(\vec{r}_{N_e}) \\ \vdots & \ddots & & \vdots \\ \phi_{N_e}(\vec{r}_1) & \phi_{N_e}(\vec{r}_2) & \cdots & \phi_{N_e}(\vec{r}_{N_e}) \end{vmatrix}. \quad (2.35)$$

In this approach, we assume that the functional differentiation of the expectation value of the Hamiltonian H due to any infinitesimal change in single particle orbital $|\phi\rangle$ is zero; i.e.,

$$\text{For } |\phi_k\rangle \rightarrow |\phi_k\rangle + \delta|\phi_k\rangle, \quad \delta\langle \Phi_0 | H | \Phi_0 \rangle = 0. \quad (2.36)$$

Moreover, we constraint that the $|\phi_i\rangle$'s would remain orthogonal throughout the process of minimization

$$\langle \phi_i | \phi_j \rangle = \delta_{ij}. \quad (2.37)$$

If both the conditions in Eqs. 2.36 and 2.37 are satisfied, we can connect the two

equations through Lagrange's undetermined multipliers (λ_{ij})

$$\delta F = \delta \left[\langle \Phi_0 | H | \Phi_0 \rangle - \sum_{ij} \lambda_{ij} (\langle \phi_i | \phi_j \rangle - \delta_{ij}) \right] = 0. \quad (2.38)$$

$$\Rightarrow \delta \left[\langle \Phi_0 | \sum_i h_1(\vec{r}_i) + \frac{1}{2} \sum_{i \neq j} h_2(\vec{r}_i, \vec{r}_j) | \Phi_0 \rangle - \sum_{ij} \lambda_{ij} (\langle \phi_i | \phi_j \rangle - \delta_{ij}) \right] = 0. \quad (2.39)$$

In Eq. 2.38, we set $F = \langle \Phi_0 | H | \Phi_0 \rangle - \sum_{ij} \lambda_{ij} (\langle \phi_i | \phi_j \rangle - \delta_{ij})$. It is evident from Eq. 2.39 that the number of Lagrange's undetermined multipliers is N_e^2 . We demand that the first-order derivatives of Eq. 2.39 with respect to all the λ_{ij} 's vanish. At first, we shall look at the variation of the one-body term in Eq. 2.39 due to any infinitesimal change in orbital $|\phi_k\rangle$; i.e.

$$\delta \langle \Phi_0 | \sum_i h_1(\vec{r}_i) | \Phi_0 \rangle = \delta \left[\sum_i \langle \phi_i | h_1(\vec{r}_i) | \phi_i \rangle \right] \quad (2.40)$$

$$= \langle \delta \phi_k | h_1(\vec{r}_i) | \phi_k \rangle + \langle \phi_k | h_1(\vec{r}_i) | \delta \phi_k \rangle \quad (2.41)$$

$$= \langle \delta \phi_k | h_1(\vec{r}_i) | \phi_k \rangle + \langle \delta \phi_k | h_1(\vec{r}_i) | \phi_k \rangle^*, \quad (2.42)$$

where the symbol '*' in the second term is used to denote hermitian conjugate (h.c.).

Similarly, the variation of the two-body term in Eq. 2.39 can also be simplified as

$$\begin{aligned} \delta \langle \Phi_0 | \frac{1}{2} \sum_{i \neq j} h_2(\vec{r}_i, \vec{r}_j) | \Phi_0 \rangle &= \delta \frac{1}{2} \sum_{i \neq j} \left[\langle \phi_i \phi_j | h_2 | \phi_i \phi_j \rangle - \langle \phi_j \phi_i | h_2 | \phi_i \phi_j \rangle \right] \\ &= \frac{1}{2} \sum_i \left[\langle \phi_i \delta \phi_k | h_2 | \phi_i \phi_k \rangle + \langle \phi_i \phi_k | h_2 | \phi_i \delta \phi_k \rangle - \langle \delta \phi_k \phi_i | h_2 | \phi_i \phi_k \rangle \right. \\ &\quad \left. - \langle \phi_k \phi_i | h_2 | \phi_i \delta \phi_k \rangle \right] + \frac{1}{2} \sum_j \left[\langle \delta \phi_k \phi_j | h_2 | \phi_k \phi_j \rangle + \langle \phi_k \phi_j | h_2 | \delta \phi_k \phi_j \rangle \right. \\ &\quad \left. - \langle \phi_j \delta \phi_k | h_2 | \phi_k \phi_j \rangle - \langle \phi_j \phi_k | h_2 | \delta \phi_k \phi_j \rangle \right]. \end{aligned} \quad (2.43)$$

Utilizing the following identity

$$\langle \phi_1 \phi_2 | \mathcal{O} | \phi_3 \phi_4 \rangle = \langle \phi_2 \phi_1 | \mathcal{O} | \phi_4 \phi_3 \rangle$$

in Eq 2.43 for any two-body hermitian operator \mathcal{O} , we get

$$\begin{aligned} \delta \langle \Phi_0 | \frac{1}{2} \sum_{i \neq j} h_2(\vec{r}_i, \vec{r}_j) | \Phi_0 \rangle &= \sum_i \left[\langle \phi_i \delta \phi_k | h_2 | \phi_i \phi_k \rangle + \langle \phi_i \delta \phi_k | h_2 | \phi_i \phi_k \rangle \right. \\ &\quad \left. - \langle \delta \phi_k \phi_i | h_2 | \phi_i \phi_k \rangle - \langle \delta \phi_k \phi_i | h_2 | \phi_k \phi_i \rangle \right], \end{aligned} \quad (2.44)$$

where we exploited the dummy nature of the indices i and j in Eq. 2.44. Combining Eqs. 2.42 and 2.44, we can write

$$\begin{aligned} \delta F &= \langle \delta \phi_k | h_1 | \phi_k \rangle + \langle \delta \phi_k | h_1 | \phi_k \rangle^* \\ &+ \sum_i \left[\langle \phi_i \delta \phi_k | h_2 | \phi_i \phi_k \rangle + \langle \phi_i \delta \phi_k | h_2 | \phi_i \phi_k \rangle^* - \langle \delta \phi_k \phi_i | h_2 | \phi_i \phi_k \rangle - \langle \delta \phi_k \phi_i | h_2 | \phi_i \phi_k \rangle^* \right] \\ &- \sum_i \left[\lambda_{ik} \langle \delta \phi_k | \phi_i \rangle^* + \lambda_{ki} \langle \delta \phi_k | \phi_i \rangle \right]. \end{aligned} \quad (2.45)$$

Now, we shall evaluate the variation of F with respect to ϕ_k^* ; i.e.

$$\begin{aligned} \frac{\delta F}{\delta \phi_k^*} &= h_1 | \phi_k(\vec{r}_1) \rangle + \sum_i \left[\langle \phi_i(\vec{r}_2) | h_2 | \phi_i(\vec{r}_2) \rangle | \phi_k(\vec{r}_1) \rangle \right. \\ &\quad \left. - \langle \phi_i(\vec{r}_2) | h_2 | \phi_k(\vec{r}_2) \rangle | \phi_i(\vec{r}_1) \rangle \right] - \sum_i \lambda_{ki} | \phi_i(\vec{r}_1) \rangle = 0, \end{aligned} \quad (2.46)$$

which can be written as

$$[h_1 + (J_k - K_k)] | \phi_k \rangle = \sum_i \lambda_{ki} | \phi_i \rangle, \quad (2.47)$$

where the J_i is the direct term and K_i is the exchange term and defined as

$$J_k | \phi_k(\vec{r}_1) \rangle = \sum_i \langle \phi_i(\vec{r}_2) | h_2 | \phi_i(\vec{r}_2) \rangle | \phi_k(\vec{r}_1) \rangle \quad (2.48)$$

and

$$K_k | \phi_k(\vec{r}_1) \rangle = \sum_i \langle \phi_i(\vec{r}_2) | h_2 | \phi_k(\vec{r}_2) \rangle | \phi_i(\vec{r}_1) \rangle. \quad (2.49)$$

From Eq. 2.48, it is evident that the direct term is the classical Coulomb interaction

averaged over ϕ_i and the exchange term is an integral operator with no classical analog and is a result of the antisymmetric nature of the wave function.

The left-hand side of Eq. 2.47 is called the Fock operator, $\mathcal{F}_k = h_1 + (J_k - K_k)$. Then Eq. 2.47 takes the form

$$\mathcal{F}_k \phi_k = \sum_i \lambda_{ki} \phi_i. \quad (2.50)$$

Several solutions to Eq. (2.50) are possible for different choices of λ_{ki} . However, we have the liberty to focus on those values of λ_{ki} which satisfy the following condition

$$\lambda_{ki} = \delta_{ki} \epsilon_k, \quad (2.51)$$

where ϵ_k is a new Lagrange's multiplier. With this special choice of λ_{ki} , Eq. 2.50 assumes the following form

$$\mathcal{F}_k \phi_k = \epsilon_k \phi_k. \quad (2.52)$$

Eq. 2.52 is called the HF equation where ϵ_k s are the eigenvalues of the Fock operator. Following the Dirac notation Eq. 2.52 can be written for i^{th} electron as

$$h_1 |\phi_i\rangle + \sum_j \left[\langle \phi_j | h_2 | \phi_j \rangle |\phi_i\rangle - \langle \phi_i | h_2 | \phi_j \rangle |\phi_j\rangle \right] = \epsilon_i |\phi_i\rangle. \quad (2.53)$$

A comparison between Eq. 2.27 and Eq. 2.53 reveals a similarity in mathematical form, differing only by a factor of 'half'. However, the fundamental distinction lies in their philosophical origins. Eq. 2.53 is derived using the variation principle, ensuring that the energy value obtained from this equation satisfies the variational condition.

2.6 The DHF method

As mentioned earlier, we have to consider the DC Hamiltonian to include relativistic effects. However, due to the presence of the two-body interaction term, it is not possible to exactly solve the eigenvalue equation. Therefore, we approximate this electron-electron interaction based on the earlier discussions. Using the variational principle and mean-field approach, we define a central potential $U_{DHF}(r)$, commonly known as the DHF potential. Following Eq. 2.53, the mean-field potential of the ground state; $U_{DHF} = \sum_i u_{DHF}(\vec{r}_i)$ is defined by

$$u_{DHF}|\phi_i\rangle = \sum_a \left[\langle \phi_a | h_2 | \phi_a \rangle |\phi_i\rangle - \langle \phi_a | h_2 | \phi_i \rangle |\phi_a\rangle \right]. \quad (2.54)$$

Introducing this mean-field potential allows us to decompose the total electronic Hamiltonian as

$$H = H_{DHF} + V_{res}, \quad (2.55)$$

where

$$H_{DHF} = \sum_i \left[c \vec{\alpha}_i^D \cdot \vec{p}_i + (\beta_i^D - 1)c^2 + V_i^{nuc} + u_{DHF}(\vec{r}_i) \right] \quad (2.56)$$

and the residual interaction is given by

$$V_{res} = \sum_{i>j} \frac{1}{r_{ij}} - \sum_i u_{DHF}(\vec{r}_i). \quad (2.57)$$

In a more compact form, the DHF Hamiltonian is expressed as

$$H_{DHF} = \sum_i \left[h_1(\vec{r}_i) + u_{DHF}(\vec{r}_i) \right] = \sum_i f_i, \quad (2.58)$$

where f_i is basically the single particle DHF operator. Since the DHF potential is effectively a one-body operator, so one can generate the single-particle orbitals by solving

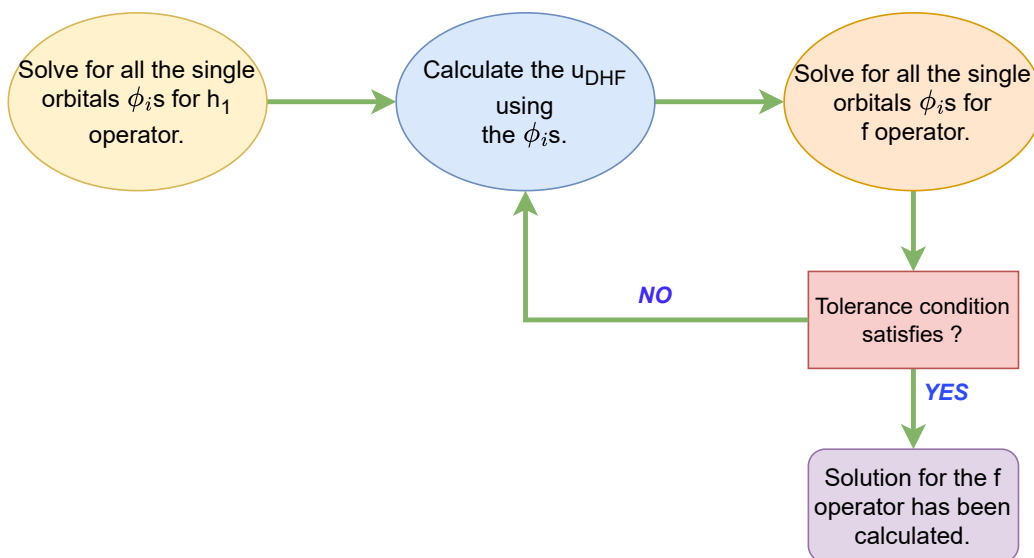


Figure 2.2: Flowchart for the iterative scheme used in the DHF method.

the following equation

$$f_i|\phi_i\rangle = [h_1(\vec{r}_i) + u_{DHF}(\vec{r}_i)]|\phi_i\rangle = \epsilon_i|\phi_i\rangle. \quad (2.59)$$

In solving the above equation, we first generate single particle orbitals for the h_1 operator and then use that to calculate the average field (U_{DHF}) and then solve the eigenvalue Eq. 2.59 way until self-consistency is reached. The flowchart of this procedure is shown pictorially in Fig. 2.2.

2.7 Basis function expansion

In atomic and molecular computations, the single-particle orbitals are typically constructed as linear combinations of known functions [17, 18]. Mathematically, any set of functions that satisfies the completeness theorem can be used as basis functions. In this current investigation, the computations are conducted using Gaussian-type orbitals

(GTOs)

$$\phi_i(r) = \sum_l \mathcal{C}_{l,i} \eta_{l,i}(r). \quad (2.60)$$

In this expression, the $\mathcal{C}_{l,i}$ coefficients correspond to the basis set expansion, and the radial part of the GTOs takes the form $\eta_{l,i}(r) = Nr^l e^{-\alpha_i r^2}$, where $l = 0, 1, 2, \dots$ denotes the symmetries s, p, d, \dots respectively and N is the normalization constant. The exponents α_i s are determined by the relation

$$\alpha_i = \alpha_0 \beta^{i-1}, \quad (2.61)$$

where α_0 and β serve as parameters determined by the basis size and the specific atomic system chosen. This parametric relation is known as the even-tempering condition in many-body calculations [19]. In the relativistic framework the large and small components of $\phi_i(\vec{r})$ are expressed in terms of the GTOs as

$$\phi_i(\vec{r}) = \frac{1}{r} \begin{pmatrix} P_i(r) \chi_{\kappa m}(\theta, \phi) \\ iQ_i(r) \chi_{-\kappa m}(\theta, \phi) \end{pmatrix} = \frac{1}{r} \begin{pmatrix} \sum_l \mathcal{C}_{l,i}^L \eta_{l,i}^L(r) \chi_{\kappa m}(\theta, \phi) \\ i \sum_l \mathcal{C}_{l,i}^S \eta_{l,i}^S(r) \chi_{-\kappa m}(\theta, \phi) \end{pmatrix}, \quad (2.62)$$

where $\mathcal{C}_{l,i}^L$ and $\mathcal{C}_{l,i}^S$ are the coefficient of expansion for large and small components of the DHF orbital. In our case, the GTOs are given by

$$\begin{aligned} \eta_{l,i}^L &= N^L r^l e^{-\alpha_i r^2}, \\ \text{and } \eta_{l,i}^S &= N^S \left[\frac{d}{dr} + \frac{\kappa}{r} \right] \eta_{l,i}^L. \end{aligned} \quad (2.63)$$

In general, one can express the eigenvalue equation for the DHF operator in terms of the GTOs as

$$\begin{aligned} \sum_l \langle \eta_{m,i} | h_1 | \eta_{l,i} \rangle \mathcal{C}_{l,i} &+ \sum_l \sum_a \mathcal{C}_{l,i} \left[\langle \eta_{m,i} \phi_a | h_2 | \eta_{l,i} \phi_a \rangle - \langle \eta_{m,i} \phi_a | h_2 | \phi_a \eta_{l,i} \rangle \right] \\ &= \epsilon_i \sum_l \mathcal{C}_{l,i} \langle \eta_{m,i} | \eta_{l,i} \rangle. \end{aligned}$$

$$\implies \sum_l F_{m,l} \mathcal{C}_{l,i} = \epsilon_i \sum_l \langle \eta_{m,i} | \eta_{l,i} \rangle \mathcal{C}_{l,i}, \quad (2.64)$$

where $F_{m,l}$ can be inferred from the left side of the above equation. In a compact notation, the above equation can be written as

$$FC = \epsilon SC, \quad (2.65)$$

where S is the overlap matrix whose elements are constructed by $\langle \eta_{m,i} | \eta_{l,i} \rangle$. The above equation can be transformed to a symmetric form [20]

$$\begin{aligned} FS^{-1/2}S^{1/2}\mathcal{C} &= \epsilon S^{-1/2}S^{1/2}\mathcal{C}. \\ \implies S^{-1/2}FS^{-1/2}S^{1/2}\mathcal{C} &= \epsilon S^{-1/2}S^{-1/2}S^{1/2}\mathcal{C}. \\ \implies \tilde{F}\tilde{\mathcal{C}} &= \epsilon\tilde{\mathcal{C}}. \end{aligned} \quad (2.66)$$

These are the transformed Roothaan equations which can be solved for $\tilde{\mathcal{C}}$ by diagonalizing \tilde{F} .

2.8 Diagrammatic representations of orbitals and interactions

In many-electron theory, it is more convenient to deal with N_e -electron reference state $|\Phi_0\rangle$, rather than the vacuum state $|0\rangle$ [1, 2, 3]. Consequently, we introduce the concept of normal ordering for a string of operators with respect to the reference state $|\Phi_0\rangle$, commonly known as the Fermi vacuum. The single-electron states occupied in $|\Phi_0\rangle$ are known as the hole or core states, and those unoccupied are referred to as particle states as shown pictorially in Fig. 2.3. When an annihilation operator a_a acts on $|\Phi_0\rangle$ then a hole is created, whereas when a creation operator a_p^\dagger acts on $|\Phi_0\rangle$, a particle is created. So the string of operators $a_p^\dagger a_a$ when acts on $|\Phi_0\rangle$, it gives a single electron excitation from core states to particle states. In order to include only those terms

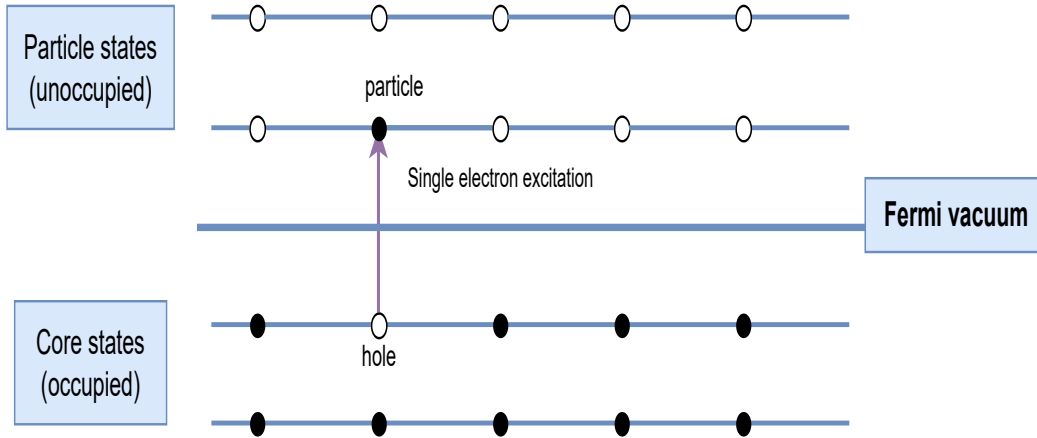


Figure 2.3: Graphical representation of particle and core states separated by Fermi vacuum. The black balls represent occupied states and the white balls represent unoccupied states. We have also shown a single electron excitation from core states to particle states by the arrow.

which correspond to real excitation, we use the normal ordering. A string of second quantized operators is said to be in normal ordered form if all the annihilation operators lie right to all creation operators. We represent the normal ordered form of the string of operators by the notation $\{\}$. Now, one can define the basic formula for the Wick's contraction between the creation and annihilation operators by adopting the normal ordering technique with respect to the reference $|\Phi_0\rangle$ [21]. The only non-zero contraction takes place only when the particle annihilation operator present left to the particle creation operators as follows

$$\overbrace{a_p a_q^\dagger} = a_p a_q^\dagger - \{a_p a_q^\dagger\} = a_p a_q^\dagger + a_q^\dagger a_p = \delta_{pq}. \quad (2.67)$$

Similarly, for the core orbitals, one can write the non-zero Wick's contraction as

$$\overbrace{a_a^\dagger a_b} = a_a^\dagger a_b - \{a_a^\dagger a_b\} = a_a^\dagger a_b + a_b a_a^\dagger = \delta_{ab}. \quad (2.68)$$

All the other combinations essentially will give rise to zero. Graphically, we can represent general operators in normal ordered form. Diagrammatically, orbitals are

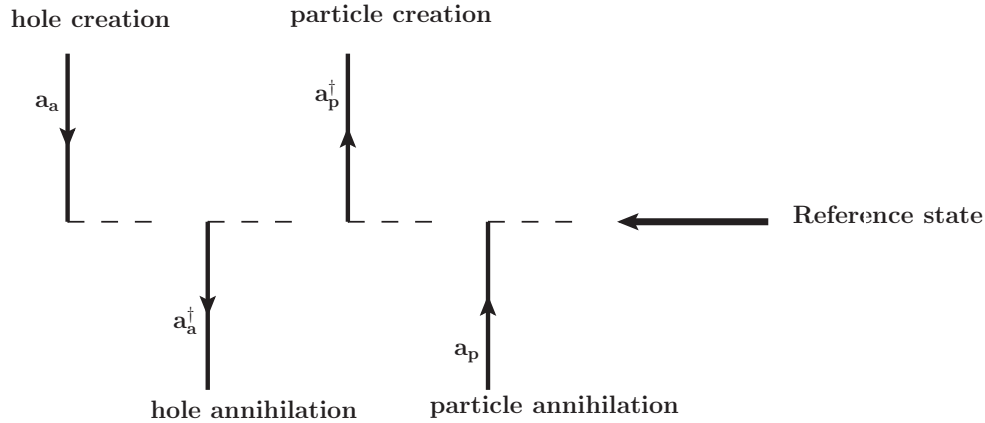


Figure 2.4: Diagrammatic representation of hole and particle creation and annihilation. Hole lines are denoted with downward arrows, and particle lines are denoted with upward arrows.

represented by solid arrows where a downward going arrow represents a core (hole) orbital and the upward arrow represents a particle orbital. The Graphical representation of the particle-hole formalism is shown in Fig. 2.4. One can use normal ordering to express the Hamiltonian in terms of the reference state $|\Phi_0\rangle$. In terms of the second quantization operator, the electronic Hamiltonian can be expressed as

$$H = \langle \Phi_0 | H | \Phi_0 \rangle + F_N + V_N, \quad (2.69)$$

where the subscript N denotes the normal ordering. F_N and V_N are the one-body and two-body terms resulting from the Wick's contraction. The possible diagrams are shown in Fig. 2.5. The term $\langle \Phi_0 | H | \Phi_0 \rangle$ is a scalar quantity, and it is called the DHF energy, E_{DHF} , or the self-consistent field energy E_{SCF} . Invoking Eq. 2.55, one can show that

$$\begin{aligned} E_{DHF} &= \langle \Phi_0 | H | \Phi_0 \rangle \\ &= \langle \Phi_0 | H_{DHF} + V_{res} | \Phi_0 \rangle \\ &= \langle \Phi_0 | H_{DHF} | \Phi_0 \rangle + \langle \Phi_0 | V_{res} | \Phi_0 \rangle \\ &= E_0 + E^{(1)}. \end{aligned} \quad (2.70)$$

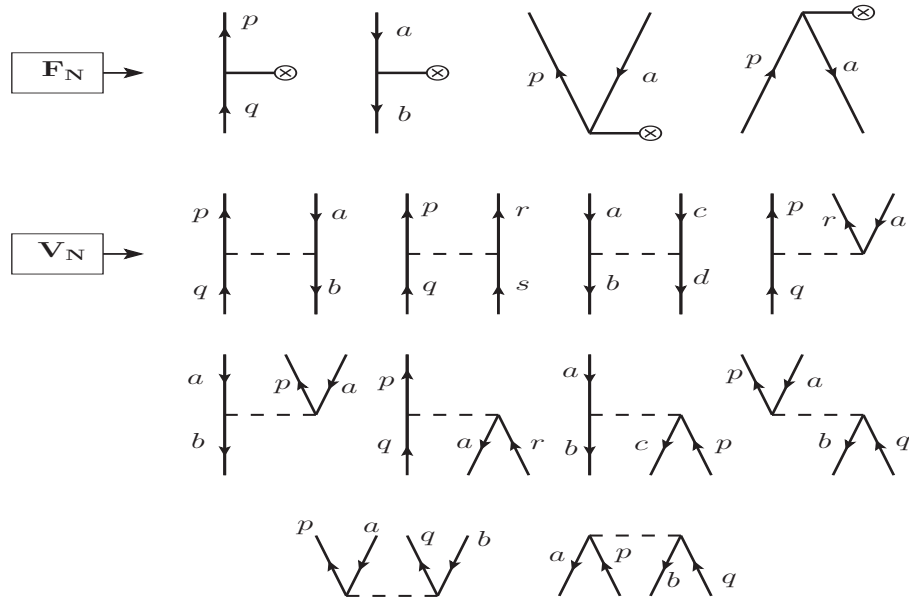


Figure 2.5: Graphical representations of normal-ordered one-body and two-body interactions operator.

So, the DHF energy is the sum of the eigenenergy of H_{DHF} and the first-order correction due to V_{res} .

2.9 Electron correlation effects

The DHF method incorporates a portion of electron-electron interactions into the mean-field approach but omits a significant chunk of dynamic electron correlation effects in its calculations. Essentially, the DHF method addresses the interaction between electrons in an averaged manner rather than an actual one. When striving for precise estimations of spectroscopic properties, in atomic systems, it becomes evident that the overlooked residual Coulomb interactions play a crucial role. As mentioned in the earlier section, the actual Hamiltonian can be written as,

$$H = H_{DHF} + V_{res}. \quad (2.71)$$

DHF method does not account for V_{res} , which is a part of the actual Hamiltonian. The physical effects that arise due to the residual Coulomb interactions are referred to as electron correlation effects, which are beyond the reach of the mean-field calculations.

The V_{res} can be expressed as

$$V_{res} = \frac{1}{2} \sum_{ijkl} a_i^\dagger a_j^\dagger a_l a_k \langle \phi_i \phi_j | h_2 | \phi_k \phi_l \rangle - \sum_{ij} a_i^\dagger a_j \langle \phi_i | u_{DHF} | \phi_j \rangle. \quad (2.72)$$

With the use of normal ordering of second quantization operators, V_{res} can be divided into normal ordered zero-, one- and two-body parts, i.e.

$$V_{res} = V_0 + V_1 + V_2, \quad (2.73)$$

where

$$V_0 = \frac{1}{2} \sum_{ab}^{core} [\langle \phi_a \phi_b | h_2 | \phi_a \phi_b \rangle - \langle \phi_a \phi_b | h_2 | \phi_b \phi_a \rangle] + \sum_a^{core} \langle \phi_a | -u_{DHF} | \phi_a \rangle, \quad (2.74)$$

$$V_1 = \sum_{ij} \left\{ a_i^\dagger a_j \right\} \langle \phi_i | v | \phi_j \rangle, \quad (2.75)$$

and

$$V_2 = \frac{1}{2} \sum_{ijkl} \left\{ a_i^\dagger a_j^\dagger a_l a_k \right\} \langle \phi_i \phi_j | h_2 | \phi_k \phi_l \rangle. \quad (2.76)$$

The matrix element $\langle \phi_i | v | \phi_j \rangle$ can be expressed as

$$\langle \phi_i | v | \phi_j \rangle = \sum_a [\langle \phi_i \phi_a | h_2 | \phi_j \phi_a \rangle - \langle \phi_a \phi_i | h_2 | \phi_j \phi_a \rangle] + \langle \phi_i | -u_{DHF} | \phi_j \rangle. \quad (2.77)$$

It can be shown that the effective potential v in the V_1 part vanishes in the DHF method. In this case, the correction in the actual state due to V_{res} comes from only the V_2 parts [1]. The actual energy of a state can be obtained using the equation

$$H|\Psi\rangle = E|\Psi\rangle, \quad (2.78)$$

where $|\Psi\rangle$ is the total wave function of the many-body system. The actual quantity that is calculated using many-body methods is $\Delta E_{corr} = E - E_{DHF}$, defined as the correlation energy. E_{DHF} can be evaluated with the knowledge of the DHF wave function. The commonly employed many-body methods for atomic calculations are the RMBPT, RCC, relativistic configuration interaction (RCI), multiconfiguration DHF (MCDHF) method, etc.

2.10 Summary

In this chapter, we have explored essential tools designed to simplify computational procedures for studying multi-electronic atomic systems. We began by addressing the inherent challenges posed by electron-electron repulsion terms in such systems. Due to presence of this two-body interaction term, one cannot solve the wave function of the multi-electronic atomic systems exactly. To solve this issue, we have replaced this two-body Coulombic repulsion potential with effective one-body DHF potential. The difference between the exact interaction and mean-field DHF interaction is defined as the V_{res} . This V_{res} term is addressed by many-body methods. In practical applications of many-body methods, essential tools are required to streamline the computational tasks involved in determining properties within atomic systems. In this context, we present the second-order quantization operator, normal ordering and Goldstone diagram. These tools provide a framework as well as a visual representation of interaction terms and correlations, facilitating the understanding of the many-body calculations.

Bibliography

- [1] I. Lindgren and J. Morrison, *Atomic Many-Body Theory*, edited by G. Ecker, P. Lambropoulos, and H. Walther, Springer-Verlag, Berlin (1985).
- [2] R. J. Bartlett, *Modern Electronic Structure Theory*, vol-II, p.1047, Ed. D. R. Yarkony, World Scientific, Singapore (1995).
- [3] I. Shavitt and R. Bartlett, *Many-Body Methods in Chemistry and Physics: MBPT and Coupled-Cluster Theory*, Cambridge Molecular Science, Cambridge University Press (2009).
- [4] F. Mandl and G. Shaw, *Quantum Field Theory*, A Wiley-Interscience Publication (1988).
- [5] R. P. Feynman, *Quantum Electrodynamics*, Benjamin/Cummings Company, California USA (1961).
- [6] M. E. Rose, *Elementary Theory of Angular Momentum*, John Wiley & Sons Inc., New York (1957).
- [7] A. R. Edmonds, *Angular Momentum in Quantum Mechanics*, Princeton, New Jersey Princeton University Press, Second Edition (1960).
- [8] D. M. Brink and G. R. Satchler, *Angular Momentum*, Clarendon Press, Oxford (1968).
- [9] I. Sobel'man, *Introduction to the Theory of Atomic Spectra*, International series of monographs in natural philosophy, Pergamon Press, (1972).

- [10] J. J. Sakurai, *Advanced Quantum Mechanics*, Addison-Wiley Publishing Company, Singapore (1967).
- [11] I. P. Grant, Proc. R. Soc. London Ser. A **262**, 555 (1961).
- [12] I. P. Grant, *Relativistic Atomic Structure Calculations*, Methods in Computational Chemistry, Plenum Press, New York (1988).
- [13] I. P. Grant, Adv. Phys. **19**, 747 (1970).
- [14] J. C. Slater, Phys. Rev. **34**, 1293 (1929).
- [15] E. U. Condon, Phys. Rev. **36**, 1121 (1930).
- [16] D. J. Griffiths, *An Introduction to Quantum Mechanics*, Pearson Edu. Asia Pte. Ltd., Singapore (2005).
- [17] R. K. Chaudhuri, P. K. Panda and B. P. Das, Phys. Rev. A **59**, 1187 (1999).
- [18] W. R. Johnson, *Atomic Structure Theory: Lectures on Atomic Physics*, Springer-Link: Springer e-Books (2007).
- [19] E. Clementi and G. Corongiu, Chem. Phys. Lett. **90**, 359 (1982).
- [20] A. Szabo and N. S. Ostlund, *Modern Quantum Chemistry: Introduction to Advanced Electronic Structure Theory*, Dover Publications Inc., New York (1996).
- [21] G. C. Wick, Phys. Rev. **80**, 268 (1950).

Chapter 3

Many-Body Methods: Integrating Electronic Correlation Effects

THE DHF method neglects the electron correlation effects that originate from the residual term V_{res} [1, 2]. Consequently, the application of many-body theory becomes imperative for accurate calculations of any atomic property. To incorporate the electron correlation effects, various relativistic many-body methods, such as RMBPT [3, 4, 5, 6], RPA [7, 8, 9, 10, 11], RCC [12, 13, 14], RCI [15, 16, 17], MCDHF [18, 19, 20] etc. have been utilized by various groups. As we will be using the RCC method to study the PV effects in ^{133}Cs atom, it is judicious that we first explore how the RCC method incorporates electron correlation effects into the calculation. In this context, we explore various many-body methods, namely, RMBPT, RPA, and RCC, and draw connections between these methods. This exercise will not only be useful to build a theoretical understanding of atomic calculation but also be helpful to support accuracy estimation for our RCC results that we are going to discuss later. A simple diagram depicting the general process of atomic property calculation is shown in Fig. 3.1.

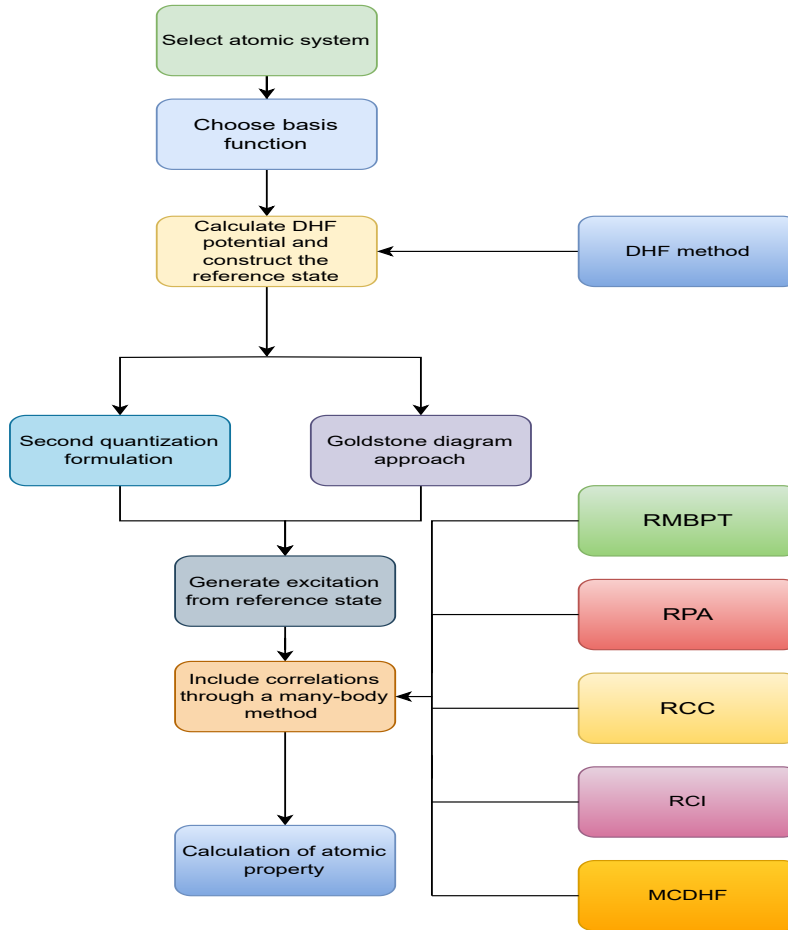


Figure 3.1: A flowchart depicting the procedure of atomic many-body calculation.

3.1 The RMBPT method

The RMBPT method offers a framework for addressing electron correlation effects within multi-electron systems, achieved through systematic expansions of energies and wave functions in successive orders [1, 2]. Herein, we discuss the Rayleigh-Schrödinger perturbation theory in the wave operator formalism. As outlined in the preceding chapter, we typically decompose the total Hamiltonian H into a mean-field component H_{DHF} and a residual part V_{res} using the DHF method.

Table 3.1: A comparative description of the RMBPT method formalism for the closed-shell and one-valence open-shell atomic systems. $|\Psi_c\rangle$ and $|\Psi_v\rangle$ are the exact wave function of the total Hamiltonian H . Ω_c represents the wave operator accounting for electron correlations only from the core orbitals, while Ω_v takes care of correlations from all electrons, including the valence electron. The subscript ‘linked’ means that only the linked diagrams will contribute to the wave operator [1]. The subscript ‘2’ in $\Omega_{2c}^{(1)}$ and $\Omega_{2v}^{(1)}$ corresponds to double excitation. a, b, p, q, r and v are the single electron orbitals (i.e., $|a\rangle \equiv |\phi_a\rangle$, $|p\rangle \equiv |\phi_p\rangle$, and so on) and $\epsilon_a, \epsilon_b, \epsilon_p, \epsilon_q, \epsilon_r$ and ϵ_v are the corresponding single particle orbital energies, respectively.

Parameter	Closed-shell	One-valence
Model space	$P_c = \Phi_c\rangle\langle\Phi_c $	$P_v = \Phi_v\rangle\langle\Phi_v $
Orthogonal space	$Q_c = \sum_{I \neq c} \Phi_I\rangle\langle\Phi_I $	$Q_v = \sum_{I \neq v} \Phi_I\rangle\langle\Phi_I $
Wave operator	$ \Psi_c\rangle = \Omega_c \Phi_c\rangle$	$ \Psi_v\rangle = \Omega^v \Phi_v\rangle,$ $\Omega^v = \Omega_c + \Omega_v$
Bloch equation	$[\Omega_c, H_{DHF}] P_c = [Q_c V_{res} \Omega_c P_c]_{linked}$	$[\Omega_v, H_{DHF}] P_v = [Q_v V_{res} (\Omega_c + \Omega_v) P_v - \Omega_v P_v V_{res} (\Omega_c + \Omega_v) P_v]_{linked}$
First-order wave operator	$\Omega_{2c}^{(1)} = \frac{1}{2} \sum_{abpq} a_p^\dagger a_q^\dagger a_b a_a \frac{\langle pq h_2 ab\rangle}{\epsilon_a + \epsilon_b - \epsilon_p - \epsilon_q}$	$\Omega_{2v}^{(1)} = \sum_{q,a,r} a_q^\dagger a_r^\dagger a_a a_v \frac{\langle qr h_2 va\rangle}{\epsilon_v + \epsilon_a - \epsilon_q - \epsilon_r}$

For an atomic system, we define $|\Phi_\alpha\rangle$ as the DHF wave function

$$H_{DHF} |\Phi_\alpha\rangle = E_\alpha |\Phi_\alpha\rangle \quad (3.1)$$

with E_α as the corresponding eigen energy. We treat this $|\Phi_\alpha\rangle$ and E_α as the zeroth-order wave function and energy, respectively. In this context, we divide the whole Hilbert space into two subspaces, which are generally known as model space (P_α) and the orthogonal space (Q_α) as described below

$$P_\alpha = |\Phi_\alpha\rangle\langle\Phi_\alpha| \quad (3.2)$$

and

$$Q_\alpha = \sum_{I \neq \alpha} |\Phi_I\rangle \langle \Phi_I|, \quad (3.3)$$

where $|\Phi_I\rangle$ s are also the eigenfunctions of H_{DHF} with energies E_I . As H_{DHF} is hermitian, its eigenfunctions follow the completeness theorem i.e.

$$P_\alpha + Q_\alpha = \sum_I |\Phi_I\rangle \langle \Phi_I| = \mathcal{I}. \quad (3.4)$$

As P_α and Q_α spans over the Hilbert space, the exact wave function $|\Psi_\alpha\rangle$ of total Hamiltonian H can be written as linear combinations of $|\Phi_\alpha\rangle$ and $|\Phi_I\rangle$ s. In wave operator formalism, we introduce a wave operator Ω_α as follows

$$|\Psi_\alpha\rangle = \Omega_\alpha |\Phi_\alpha\rangle. \quad (3.5)$$

This wave operator Ω_α generates excitations from the zeroth-order state $|\Phi_\alpha\rangle$ by operating the second quantization operator, thus constructing the Q_α space. The perturbative expansion of the wave operator has the form

$$\Omega_\alpha = 1 + \Omega_\alpha^{(1)} + \Omega_\alpha^{(2)} + \dots = 1 + \chi_\alpha, \quad (3.6)$$

where $\chi_\alpha = \Omega_\alpha^{(1)} + \Omega_\alpha^{(2)} + \dots$ is called the correlation operator and the superscripts indicate the order of correction. The amplitude of the wave operator can be derived from the Bloch's equation [1] given by

$$[\Omega_\alpha, H_{DHF}] P_\alpha = Q_\alpha V_{res} \Omega_\alpha P - \chi_\alpha P_\alpha V_{res} \Omega_\alpha P_\alpha. \quad (3.7)$$

Now, we discuss this RMBPT method in the context of closed-shell and one-valence open-shell atomic systems. We define $|\Phi_c\rangle$ as the zeroth-order wave function or the reference state for closed-shell atomic system and for one-valence atom $|\Phi_v\rangle$. To compute

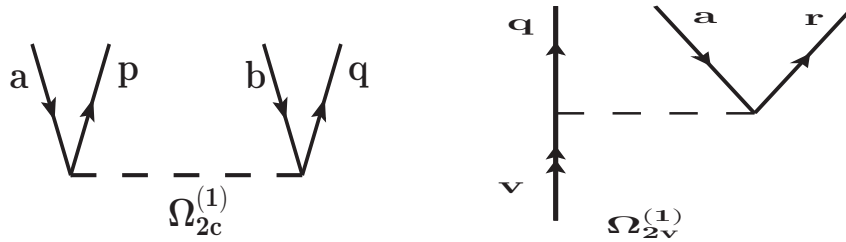


Figure 3.2: Diagrammatic representations of the $\Omega_{2c}^{(1)}$ and $\Omega_{2v}^{(1)}$ operators. The dotted line represents the V_{res} interaction term. The double arrow represents the valence orbital v .

the $|\Phi_v\rangle$, we first solve for the closed-core reference state $|\Phi_c\rangle$ in the V^{N_e-1} potential (N_e being the number of electrons) formalism. Subsequently, ground state or excited state configurations can be constructed by attaching an additional electron to $|\Phi_c\rangle$, i.e., $|\Phi_v\rangle = a_v^\dagger|\Phi_c\rangle$, where a_v^\dagger represents the addition of the valence orbital designated by v . The reason to choose V^{N_e-1} potential formalism is to be consistent with the various earlier works. Before discussing how one can calculate transitional matrix elements in the RMBPT method, we have given a general description of the method in the context of closed-shell and one-valence atomic systems in Table 3.1. We show the corresponding Goldstone diagrams for $\Omega_{2c}^{(1)}$ and $\Omega_{2v}^{(1)}$ in Fig. 3.2.

3.1.1 Calculation of transition matrix element

In this subsection, we will demonstrate the procedure for computing matrix elements within the RMBPT method, starting from the DHF approximation. Our focus is specifically on atoms containing a single valence electron. For an arbitrary one-body operator \mathcal{O} , the transition matrix element between the final (f) and initial (i) states at the DHF level is given by

$$\mathcal{O}_{fi}^{(1)} = \langle \Phi_f | \mathcal{O} | \Phi_i \rangle. \quad (3.8)$$

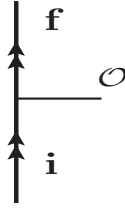


Figure 3.3: Zeroth-order transition matrix element of a general one-body operator \mathcal{O} .

This is also referred to as the zeroth-order matrix element. In a one-valence system, the states $|\Phi_{i/f}\rangle$ can be expressed as $|\Phi_{i/f}\rangle = a_{i/f}^\dagger |\Phi_c\rangle$. Utilizing this, we can simplify the above equation

$$\begin{aligned}
 \mathcal{O}_{fi}^{(1)} &= \langle \Phi_f | \mathcal{O} | \Phi_i \rangle \\
 &= \langle \Phi_c | a_f \mathcal{O} a_i^\dagger | \Phi_c \rangle \\
 &= \langle \Phi_c | a_f \sum_{l,m} a_l^\dagger a_m \langle l | o | m \rangle a_i^\dagger | \Phi_c \rangle \quad (\text{Using Eq. 2.15}) \\
 &= \langle \Phi_c | \Phi_c \rangle \langle f | o | i \rangle \\
 &= \langle f | o | i \rangle = o_{fi}.
 \end{aligned} \tag{3.9}$$

Here ‘ o ’ is the single-electron operator. We can readily utilize the single-particle DHF orbitals to compute the zeroth-order matrix element. The diagrammatic representation of the zeroth-order matrix element is shown in Fig. 3.3. However, we need to employ the wave operator to incorporate correlation into the calculation. The second-order corrected transition element is expressed as

$$\begin{aligned}
 \mathcal{O}_{fi}^{(2)} &= \frac{\langle \Psi_f | \mathcal{O} | \Psi_i \rangle}{N_{fi}^{(2)}} \\
 &= \frac{\langle \Phi_f | (1 + \Omega_c^{\dagger(1)} + \Omega_f^{\dagger(1)}) \mathcal{O} (1 + \Omega_c^{(1)} + \Omega_i^{(1)}) | \Phi_i \rangle}{N_{fi}^{(2)}} \\
 &= \frac{\langle \Phi_f | \mathcal{O} | \Phi_i \rangle + \langle \Phi_f | \mathcal{O} \Omega_i^{(1)} | \Phi_i \rangle + \langle \Phi_f | \Omega_f^{\dagger(1)} \mathcal{O} | \Phi_i \rangle}{N_{fi}^{(2)}}.
 \end{aligned} \tag{3.10}$$

Here, $N_{fi}^{(2)} = \sqrt{N_f^{(2)} N_i^{(2)}}$ with $N_f^{(2)}$ and $N_i^{(2)}$ are the normalization factors for the final and initial states respectively at the level of second-order perturbation. It is defined as $N_v^{(2)} = \langle \Phi_v | (1 + \Omega_c^{\dagger(1)} + \Omega_v^{\dagger(1)}) (1 + \Omega_c^{(1)} + \Omega_v^{(1)}) | \Phi_v \rangle$. The initial term in the numerator in the preceding equation corresponds to the zeroth-order element. The second-order correction arising from correlation stems from the last two terms. Fig. 3.4 illustrates all the Goldstone diagrams corresponding to second-order correction of the matrix element of the operator \mathcal{O} . The third-order corrected transition matrix element will be

$$\begin{aligned}
 \mathcal{O}_{fi}^{(3)} &= \frac{\langle \Psi_f | \mathcal{O} | \Psi_i \rangle}{N_{fi}^{(3)}} \\
 &= \frac{\langle \Phi_f | (1 + \Omega_c^{\dagger(1)} + \Omega_f^{\dagger(1)} + \Omega_c^{\dagger(2)} + \Omega_f^{\dagger(2)}) \mathcal{O} (1 + \Omega_c^{(1)} + \Omega_i^{(1)} + \Omega_c^{(2)} + \Omega_i^{(2)}) | \Phi_i \rangle}{N_{fi}^{(3)}} \\
 &= \frac{1}{N_{fi}^{(3)}} \left[\langle \Phi_f | \mathcal{O} + \overbrace{\mathcal{O} \Omega_i^{(1)} + \Omega_f^{\dagger(1)} \mathcal{O}}^{\text{second-order}} + \overbrace{\Omega_c^{(2)\dagger} \mathcal{O} + \mathcal{O} \Omega_c^{(2)} + \Omega_c^{(1)\dagger} \mathcal{O} \Omega_i^{(1)} + \Omega_f^{(2)\dagger} \mathcal{O} + \mathcal{O} \Omega_i^{(2)} + \Omega_c^{(1)\dagger} \mathcal{O} \Omega_c^{(1)} + \Omega_f^{(1)\dagger} \mathcal{O} \Omega_i^{(1)}}^{\text{third-order}} | \Phi_i \rangle \right]. \quad (3.11)
 \end{aligned}$$

$N_{fi}^{(3)}$ corresponds to the third-order normalization factor. In a similar fashion, one can get the corrections from the fourth order, fifth order, and so on to account for higher-order correlation effects in the calculation. However, including higher-order corrections in this approach comes with a very high computational cost. We will discuss the third- and higher-order corrections in the coming sections.

3.2 RPA

Despite the RMBPT method's formulation spanning over five decades, there remains a limited understanding of convergence of the RMBPT results as one progresses to higher orders. Moreover, a notable challenge arises when advancing beyond the second order, as a multitude of terms are generated, posing difficulties in computation. This is where the RPA proves invaluable. RPA terms naturally align with the second-order RMBPT

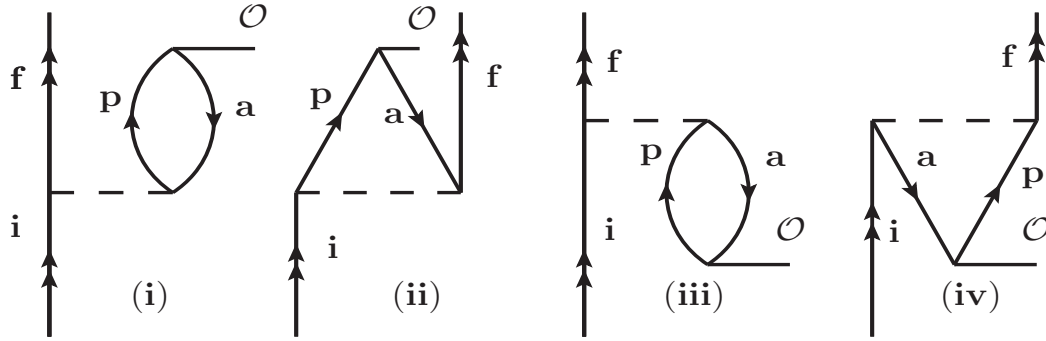


Figure 3.4: Diagrammatic representation of the second-order matrix element correction to the calculation of property denoted by a one-body operator \mathcal{O} .

(RMBPT(2)) terms, and we iteratively evaluate their contributions up to infinite order [7]. However, there are other terms that emerge in the third-order RMBPT theory (RMBPT(3)), which are also grouped accordingly. The third-order correction for matrix element can be categorized as $\mathcal{O}^{(RPA+3)} = \mathcal{O}^{RPA} + \mathcal{O}^{BO} + \mathcal{O}^{SR} + \mathcal{O}^{Norm}$. [9, 10, 21, 22, 23] Here, ‘BO’ represents Brückner orbitals, ‘SR’ denotes structural radiation terms, and ‘Norm’ stands for normalization.

3.2.1 Formulation of RPA

Recalling the previous discussions from the RMBPT method, we can write the second-order corrected to the matrix element

$$\begin{aligned}
 \mathcal{O}_{fi}^{(2)} &= \langle \Phi_f | \mathcal{O} | \Phi_i \rangle + \langle \Phi_f | \mathcal{O} \Omega_i^{(1)} | \Phi_i \rangle + \langle \Phi_f | \Omega_f^{\dagger(1)} \mathcal{O} | \Phi_i \rangle \\
 &= o_{fi} + \sum_{pa} \frac{o_{ap} [\langle fp | h_2 | ia \rangle - \langle fp | h_2 | ai \rangle]}{\epsilon_i + \epsilon_a - \epsilon_f - \epsilon_p} + \sum_{pa} \frac{[\langle fa | h_2 | ip \rangle - \langle fa | h_2 | pi \rangle] o_{pa}}{\epsilon_f + \epsilon_a - \epsilon_i - \epsilon_p}.
 \end{aligned}
 \tag{3.12}$$

The second and third terms correspond to the diagrams (i) and (ii), respectively, in Fig. 3.4, and the fourth and fifth terms correspond to the diagrams (iii) and (iv), respectively. In the RPA method, the effects of this particular class of diagrams from the RMBPT(2) method are included to all-order. In doing so, we can define a new operator Ω^{RPA} that

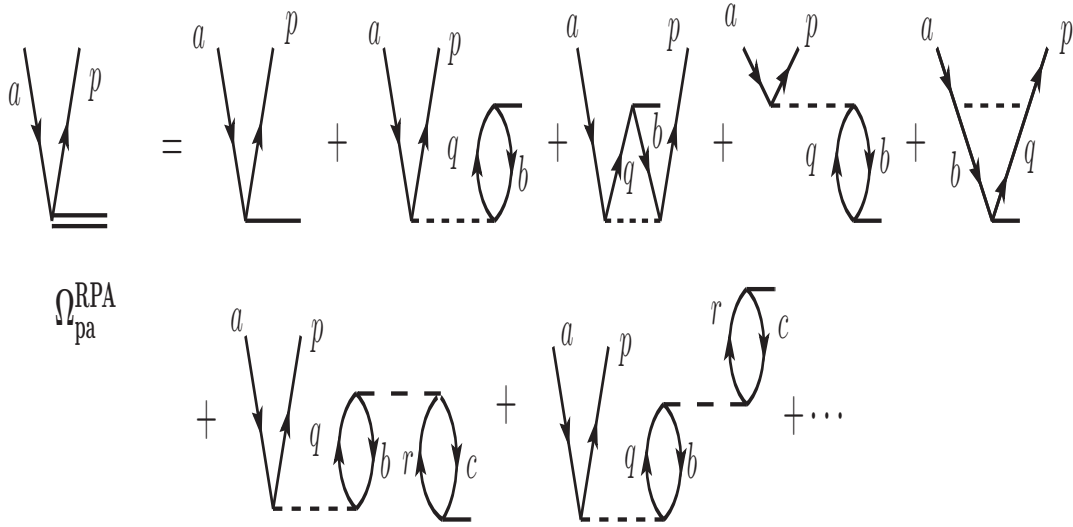


Figure 3.5: Diagrammatic representation of the RPA wave operator Ω_{pa}^{RPA} . The double line in the diagram implies that through the iterative scheme, the CP effects are included to all-orders.

includes correlation effects into the matrix elements from core states to virtual states to all-order. This wave operator can be evaluated using the following equations

$$\begin{aligned} \Omega_{pa}^{RPA} &= \Omega_{pa}^{RPA(0)} + \sum_{k=1}^{\infty} \sum_{bq} \frac{\langle pb|h_2|aq\rangle - \langle pb|h_2|qa\rangle}{\epsilon_b - \epsilon_q + \epsilon_f - \epsilon_i} \Omega_{qb}^{RPA(k-1)} \\ &+ \sum_{bq} \Omega_{bq}^{RPA(k-1)\dagger} \frac{\langle pq|h_2|ab\rangle - \langle pq|h_2|ba\rangle}{\epsilon_b - \epsilon_q + \epsilon_i - \epsilon_f}, \end{aligned} \quad (3.13)$$

where $\Omega_{pa}^{RPA(0)}$ is the zeroth-order matrix element o_{pa} . We use Eq. 3.13 to calculate the RPA wave operator iteratively. We present the diagrammatic representation of the RPA operator in 3.5. Once Ω^{RPA} has been calculated, one can use the following equation to calculate the matrix element in the RPA method

$$\mathcal{O}_{fi}^{RPA} = o_{fi} + \langle \Phi_f | \Omega^{RPA\dagger} \Omega_i^{(1)} | \Phi_i \rangle + \langle \Phi_f | \Omega_f^{\dagger(1)} \Omega^{RPA} | \Phi_i \rangle. \quad (3.14)$$

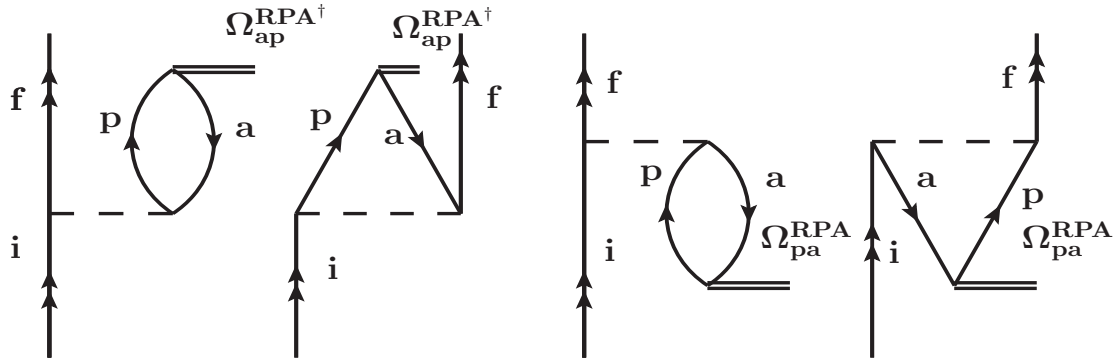


Figure 3.6: Diagrammatic representation of the all-order RPA diagrams. One can note the strong resemblance between the RPA and RMBPT(2) diagrams.

The RPA diagrams are illustrated in Fig. 3.6. Now we explain how RPA includes higher-order diagrams to the matrix elements calculation using a few examples. In Fig. 3.7, we have shown a diagram and its breakdown in terms of the RPA and RMBPT(3) wave operators. In the RPA method it is coming through $\Omega_f^{\dagger(1)}\Omega_{pa}^{RPA}$. We can express this in terms of the single electron orbitals as follows

$$\text{Diagram (i)} = \sum_{apbq} \frac{\langle fa|h_2|ip\rangle\langle pq|h_2|ab\rangle\langle b|o|q\rangle}{(\epsilon_a - \epsilon_p + \epsilon_f - \epsilon_i)(\epsilon_b - \epsilon_q + \epsilon_i - \epsilon_f)}. \quad (3.15)$$

But in the RMBPT method, this particular Goldstone diagram can come in two ways: (a) $\Omega_{2f}^{(1)\dagger}\mathcal{O}\Omega_{2c}^{(1)}$ and (b) $\mathcal{O}\Omega_{2i}^{(2)}$. In single orbitals, these can be written as

$$\text{Diagram (ii)} = \sum_{apbq} \frac{\langle fa|h_2|ip\rangle\langle pq|h_2|ab\rangle\langle b|o|q\rangle}{(\epsilon_a + \epsilon_b - \epsilon_p - \epsilon_q)(\epsilon_f + \epsilon_a - \epsilon_i - \epsilon_p)} \quad (3.16)$$

and

$$\text{Diagram (iii)} = \sum_{apbq} \frac{\langle fa|h_2|ip\rangle\langle pq|h_2|ab\rangle\langle b|o|q\rangle}{(\epsilon_a + \epsilon_b - \epsilon_p - \epsilon_q)(\epsilon_i + \epsilon_b - \epsilon_f - \epsilon_q)}. \quad (3.17)$$

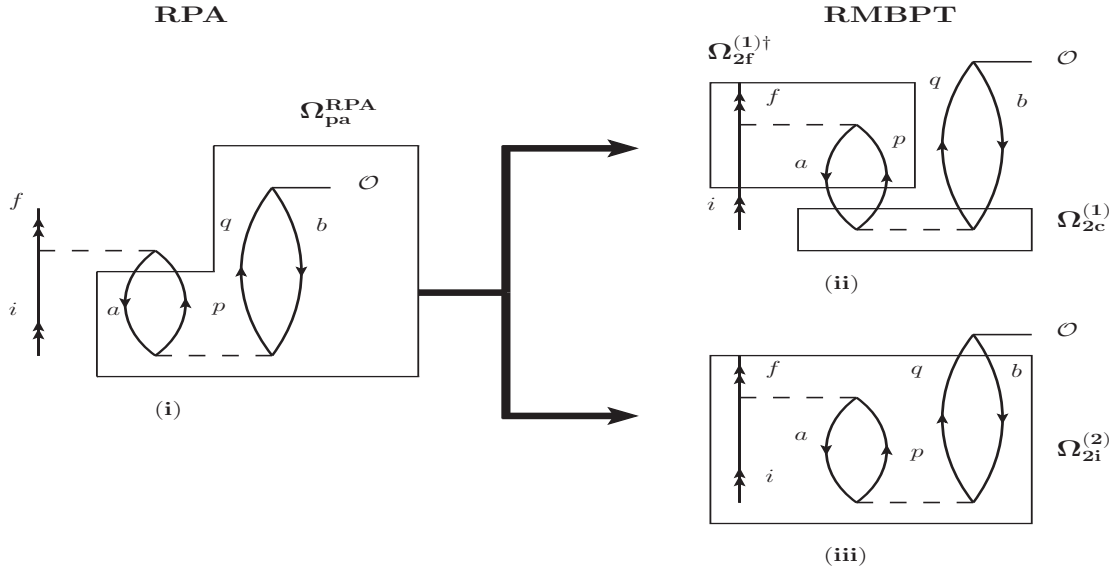


Figure 3.7: Equivalence between RPA and RMBPT: the shown RPA diagram effectively corresponds to two RMBPT(3) diagrams.

Now, adding diagram (ii) and diagram (iii), we get

$$\begin{aligned}
 \text{Diagram (ii)} + \text{Diagram (iii)} &= \sum_{apbq} \langle fa|h_2|ip\rangle \langle pq|h_2|ab\rangle \langle b|o|q\rangle \\
 &\times \left[\frac{1}{(\epsilon_a + \epsilon_b - \epsilon_p - \epsilon_q)(\epsilon_f + \epsilon_a - \epsilon_i - \epsilon_p)} \right. \\
 &\quad \left. + \frac{1}{(\epsilon_a + \epsilon_b - \epsilon_p - \epsilon_q)(\epsilon_i + \epsilon_b - \epsilon_f - \epsilon_q)} \right] \\
 &= \sum_{apbq} \frac{\langle fa|h_2|ip\rangle \langle pq|h_2|ab\rangle \langle b|o|q\rangle}{(\epsilon_a - \epsilon_p + \epsilon_f - \epsilon_i)(\epsilon_b - \epsilon_q + \epsilon_i - \epsilon_f)} \\
 &= \text{Diagram (i)}. \tag{3.18}
 \end{aligned}$$

So, this particular diagram from RPA corresponds to two RMBPT diagrams. We have shown another example in Fig. 3.8. This diagram contributes to the third-order correction of the matrix element. In terms of single electron orbitals, we can write

$$\text{Diagram (iv)} = \text{Diagram (v)} = \sum_{apbq} \frac{\langle fa|h_2|ip\rangle \langle pb|h_2|aq\rangle \langle q|o|b\rangle}{(\epsilon_a - \epsilon_p + \epsilon_f - \epsilon_i)(\epsilon_b - \epsilon_q + \epsilon_f - \epsilon_i)}. \tag{3.19}$$

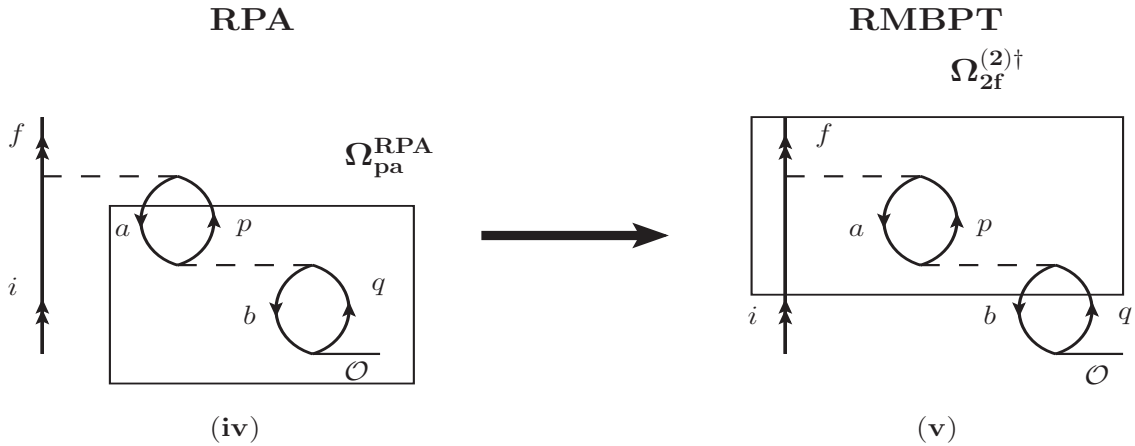


Figure 3.8: Equivalence between RPA and RMBPT: This particular RPA diagram corresponds to one RMBPT(3) diagram.

So, this RPA diagram corresponds to one RMBPT(3) diagram. These RPA diagrams, as shown in Fig. 3.6, bear a strong resemblance to the RMBPT(2) diagrams, but RPA incorporates correlation from these types of diagrams up to all-orders. There are other types of correlation effects, like BO and SR, that appear in third- and higher-order perturbation methods, but RPA is unable to capture them. To improve calculation, it is imperative to include these contributions. In the following part, we will discuss those diagrams that emerge in the RMBPT(3) method.

3.2.2 Correlation from BO

BO accounts for the pair-correlation (PC) effects, which refer to the distortion of the electron cloud surrounding the core electrons due to the interaction with the valence electrons [21, 22]. The diagrams shown in Fig. 3.9, along with their exchange diagrams, contribute to the third-order corrections to the transition matrix element. These BO diagrams come from the terms $\mathcal{O}\Omega_{1i}^{(2)}$ and $\Omega_{1f}^{(2)\dagger}\mathcal{O}$. We can express these diagrams in terms of the single electron orbitals

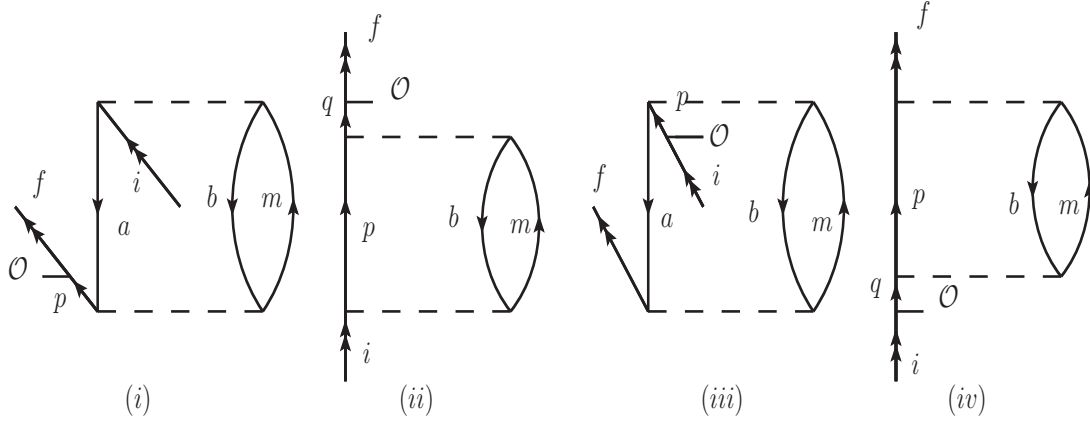


Figure 3.9: Direct diagrams of BO corrections to the transition matrix element. Diagrams (i) and (ii) correspond to the $\mathcal{O}\Omega_{1i}^{(2)}$ term, whereas (iii) and (iv) correspond to the $\Omega_{1f}^{(2)\dagger}\mathcal{O}$ term.

$$\text{Diagram (i)} = \langle \Phi_f | \mathcal{O} \Omega_{1i}^{(2)} | \Phi_i \rangle = - \sum_{abm, p \neq i} \frac{\langle f | o | p \rangle \langle pm | h_2 | ab \rangle \langle ab | h_2 | im \rangle}{(\epsilon_i - \epsilon_p)(\epsilon_a + \epsilon_b - \epsilon_p - \epsilon_m)},$$

$$\text{Diagram (ii)} = \langle \Phi_f | \mathcal{O} \Omega_{1i}^{(2)} | \Phi_i \rangle = \sum_{pbm, q \neq i} \frac{\langle f | o | q \rangle \langle qb | h_2 | pm \rangle \langle pm | h_2 | ib \rangle}{(\epsilon_i - \epsilon_q)(\epsilon_i + \epsilon_b - \epsilon_p - \epsilon_m)},$$

$$\text{Diagram (iii)} = \langle \Phi_f | \Omega_{1f}^{(2)\dagger} \mathcal{O} | \Phi_i \rangle = - \sum_{abm, p \neq i} \frac{\langle fm | h_2 | ab \rangle \langle ab | h_2 | pm \rangle \langle p | o | i \rangle}{(\epsilon_f - \epsilon_p)(\epsilon_a + \epsilon_b - \epsilon_p - \epsilon_m)}$$

and

$$\text{Diagram (iv)} = \langle \Phi_f | \Omega_{1f}^{(2)\dagger} \mathcal{O} | \Phi_i \rangle = \sum_{pbm, q \neq i} \frac{\langle fb | h_2 | pm \rangle \langle pm | h_2 | qb \rangle \langle q | o | i \rangle}{(\epsilon_f - \epsilon_q)(\epsilon_f + \epsilon_b - \epsilon_p - \epsilon_m)}. \quad (3.20)$$

3.2.3 Correlation from SR

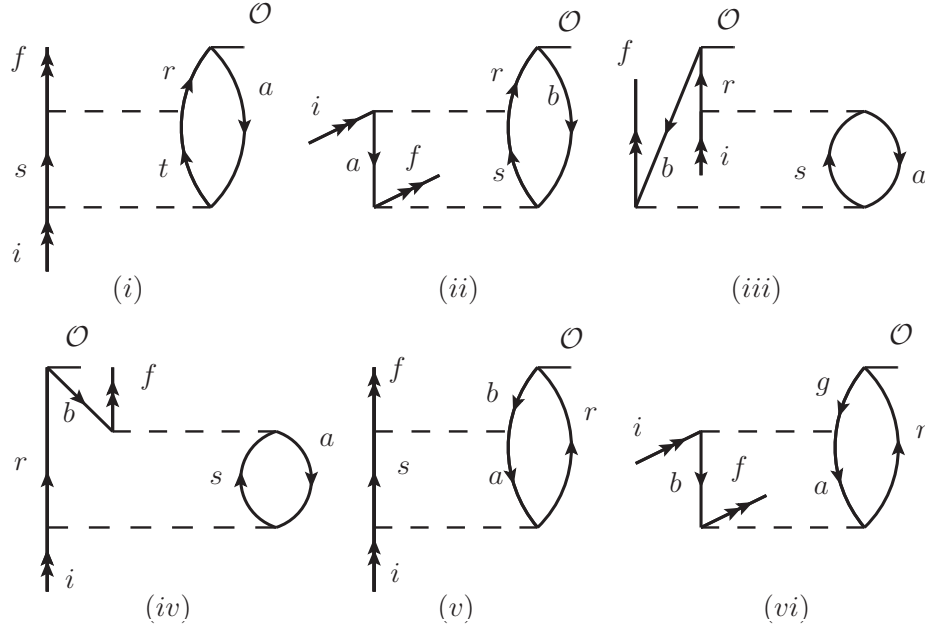
The SR terms account for the correlation effects due to virtual states. The virtual states are not true energy levels in the sense that as they are high-energy states, they are only mathematically considered for completeness to include the correlation in the electronic energy levels. We have presented the SR terms and their corresponding wave operators in Table 3.2. In terms of the single-particle orbitals, we can express these

Table 3.2: A description of the SR terms in terms of their corresponding wave operators. There are a total of 36 terms contributing to the SR correlation, including both direct and exchange terms.

Correlation type	Wave operator	No. of terms	Diagrammatic representation
SR	$\langle \Phi_f \mathcal{O} \Omega_{2i}^{(2)} \Phi_i \rangle$	12	see Fig. 3.10
	$\langle \Phi_f \Omega_{2f}^{(2)\dagger} \mathcal{O} \Phi_i \rangle$	12	see Fig. 3.11
	$\langle \Phi_f \Omega_{2f}^{(1)\dagger} \mathcal{O} \Omega_{2i}^{(1)\dagger} \Phi_i \rangle$	6	see Fig. 3.12
	$\langle \Phi_f \Omega_{2c}^{(1)\dagger} \mathcal{O} \Omega_{2c}^{(1)\dagger} \Phi_i \rangle$	6	see Fig. 3.12

terms as

$$\begin{aligned}
 \text{Diagram (i)} &= \langle \Phi_f | \mathcal{O} \Omega_{2i}^{(2)} | \Phi_i \rangle = \sum_{stra} \frac{\langle fr | h_2 | st \rangle \langle a | o | r \rangle \langle st | h_2 | ia \rangle}{(\epsilon_i + \epsilon_a - \epsilon_s - \epsilon_t)(\epsilon_i + \epsilon_a - \epsilon_r - \epsilon_f)}, \\
 \text{Diagram (ii)} &= \langle \Phi_f | \mathcal{O} \Omega_{2i}^{(2)} | \Phi_i \rangle = - \sum_{srab} \frac{\langle sf | h_2 | ba \rangle \langle b | o | r \rangle \langle ar | h_2 | is \rangle}{(\epsilon_i + \epsilon_b - \epsilon_r - \epsilon_f)(\epsilon_a + \epsilon_b - \epsilon_s - \epsilon_f)}, \\
 \text{Diagram (iii)} &= \langle \Phi_f | \mathcal{O} \Omega_{2i}^{(2)} | \Phi_i \rangle = - \sum_{srab} \frac{\langle sf | h_2 | ab \rangle \langle b | o | r \rangle \langle ar | h_2 | si \rangle}{(\epsilon_i + \epsilon_b - \epsilon_r - \epsilon_f)(\epsilon_a + \epsilon_b - \epsilon_s - \epsilon_f)}, \\
 \text{Diagram (iv)} &= \langle \Phi_f | \mathcal{O} \Omega_{2i}^{(2)} | \Phi_i \rangle = - \sum_{srab} \frac{\langle af | h_2 | sb \rangle \langle b | o | r \rangle \langle sr | h_2 | ai \rangle}{(\epsilon_i + \epsilon_b - \epsilon_r - \epsilon_f)(\epsilon_i + \epsilon_a - \epsilon_s - \epsilon_r)}, \\
 \text{Diagram (v)} &= \langle \Phi_f | \mathcal{O} \Omega_{2i}^{(2)} | \Phi_i \rangle = - \sum_{srab} \frac{\langle af | h_2 | bs \rangle \langle b | o | r \rangle \langle sr | h_2 | ia \rangle}{(\epsilon_i + \epsilon_b - \epsilon_r - \epsilon_f)(\epsilon_i + \epsilon_a - \epsilon_s - \epsilon_r)}, \\
 \text{Diagram (vi)} &= \langle \Phi_f | \mathcal{O} \Omega_{2i}^{(2)} | \Phi_i \rangle = \sum_{rabg} \frac{\langle rf | h_2 | ab \rangle \langle g | o | r \rangle \langle ab | h_2 | gi \rangle}{(\epsilon_a + \epsilon_b - \epsilon_r - \epsilon_f)(\epsilon_i + \epsilon_g - \epsilon_r - \epsilon_f)}, \\
 \text{Diagram (vii)} &= \langle \Phi_f | \Omega_{2f}^{(2)\dagger} \mathcal{O} | \Phi_i \rangle = \sum_{stra} \frac{\langle af | h_2 | sr \rangle \langle t | o | a \rangle \langle sr | h_2 | ti \rangle}{(\epsilon_f + \epsilon_a - \epsilon_i - \epsilon_t)(\epsilon_f + \epsilon_a - \epsilon_r - \epsilon_s)}, \\
 \text{Diagram (viii)} &= \langle \Phi_f | \Omega_{2f}^{(2)\dagger} \mathcal{O} | \Phi_i \rangle = - \sum_{srab} \frac{\langle fa | h_2 | rs \rangle \langle s | o | b \rangle \langle rb | h_2 | ia \rangle}{(\epsilon_f + \epsilon_b - \epsilon_i - \epsilon_s)(\epsilon_f + \epsilon_a - \epsilon_r - \epsilon_s)},
 \end{aligned}$$


 Figure 3.10: Direct diagrams of the SR correlations that appear via $\langle \Phi_f | \mathcal{O} \Omega_{2i}^{(2)} | \Phi_i \rangle$.

$$\text{Diagram (ix)} = \langle \Phi_f | \Omega_{2f}^{(2)\dagger} \mathcal{O} | \Phi_i \rangle = - \sum_{srab} \frac{\langle fa | h_2 | rs \rangle \langle r | o | b \rangle \langle sb | h_2 | ai \rangle}{(\epsilon_f + \epsilon_b - \epsilon_i - \epsilon_r)(\epsilon_f + \epsilon_a - \epsilon_r - \epsilon_s)},$$

$$\text{Diagram (x)} = \langle \Phi_f | \Omega_{2f}^{(2)\dagger} \mathcal{O} | \Phi_i \rangle = - \sum_{srab} \frac{\langle sf | h_2 | ar \rangle \langle r | o | b \rangle \langle ab | h_2 | si \rangle}{(\epsilon_a + \epsilon_b - \epsilon_i - \epsilon_s)(\epsilon_f + \epsilon_b - \epsilon_i - \epsilon_r)},$$

$$\text{Diagram (xi)} = \langle \Phi_f | \Omega_{2f}^{(2)\dagger} \mathcal{O} | \Phi_i \rangle = - \sum_{srab} \frac{\langle fs | h_2 | ar \rangle \langle r | o | b \rangle \langle ab | h_2 | is \rangle}{(\epsilon_a + \epsilon_b - \epsilon_i - \epsilon_s)(\epsilon_f + \epsilon_b - \epsilon_i - \epsilon_r)},$$

$$\text{Diagram (xii)} = \langle \Phi_f | \Omega_{2f}^{(2)\dagger} \mathcal{O} | \Phi_i \rangle = \sum_{abgr} \frac{\langle gf | h_2 | ab \rangle \langle r | o | g \rangle \langle ab | h_2 | ri \rangle}{(\epsilon_a + \epsilon_b - \epsilon_i - \epsilon_r)(\epsilon_f + \epsilon_g - \epsilon_i - \epsilon_r)},$$

$$\text{Diagram (xiii)} = \langle \Phi_f | \Omega_{2f}^{(1)\dagger} \mathcal{O} \Omega_{2i}^{(1)\dagger} | \Phi_i \rangle = \sum_{stra} \frac{\langle fa | h_2 | ts \rangle \langle t | o | r \rangle \langle sr | h_2 | ai \rangle}{(\epsilon_f + \epsilon_a - \epsilon_s - \epsilon_t)(\epsilon_i + \epsilon_a - \epsilon_r - \epsilon_s)},$$

$$\text{Diagram (xiv)} = \langle \Phi_f | \Omega_{2f}^{(1)\dagger} \mathcal{O} \Omega_{2i}^{(1)\dagger} | \Phi_i \rangle = \sum_{stra} \frac{\langle fa | h_2 | rt \rangle \langle t | o | s \rangle \langle sr | h_2 | ai \rangle}{(\epsilon_f + \epsilon_a - \epsilon_r - \epsilon_t)(\epsilon_i + \epsilon_a - \epsilon_r - \epsilon_s)},$$

$$\text{Diagram (xv)} = \langle \Phi_f | \Omega_{2f}^{(1)\dagger} \mathcal{O} \Omega_{2i}^{(1)\dagger} | \Phi_i \rangle = - \sum_{srab} \frac{\langle fb | h_2 | rs \rangle \langle a | o | b \rangle \langle sr | h_2 | ai \rangle}{(\epsilon_f + \epsilon_b - \epsilon_s - \epsilon_r)(\epsilon_i + \epsilon_a - \epsilon_r - \epsilon_s)},$$

$$\text{Diagram (xvi)} = \langle \Phi_f | \Omega_{2c}^{(1)\dagger} \mathcal{O} \Omega_{2c}^{(1)\dagger} | \Phi_i \rangle = - \sum_{srab} \frac{\langle fr | h_2 | ba \rangle \langle s | o | r \rangle \langle ba | h_2 | is \rangle}{(\epsilon_a + \epsilon_b - \epsilon_f - \epsilon_r)(\epsilon_a + \epsilon_b - \epsilon_i - \epsilon_s)},$$

$$\text{Diagram (xvii)} = \langle \Phi_f | \Omega_{2c}^{(1)\dagger} \mathcal{O} \Omega_{2c}^{(1)\dagger} | \Phi_i \rangle = \sum_{rabc} \frac{\langle fr | h_2 | bg \rangle \langle g | o | a \rangle \langle ba | h_2 | ir \rangle}{(\epsilon_a + \epsilon_b - \epsilon_i - \epsilon_r)(\epsilon_b + \epsilon_g - \epsilon_f - \epsilon_r)}$$

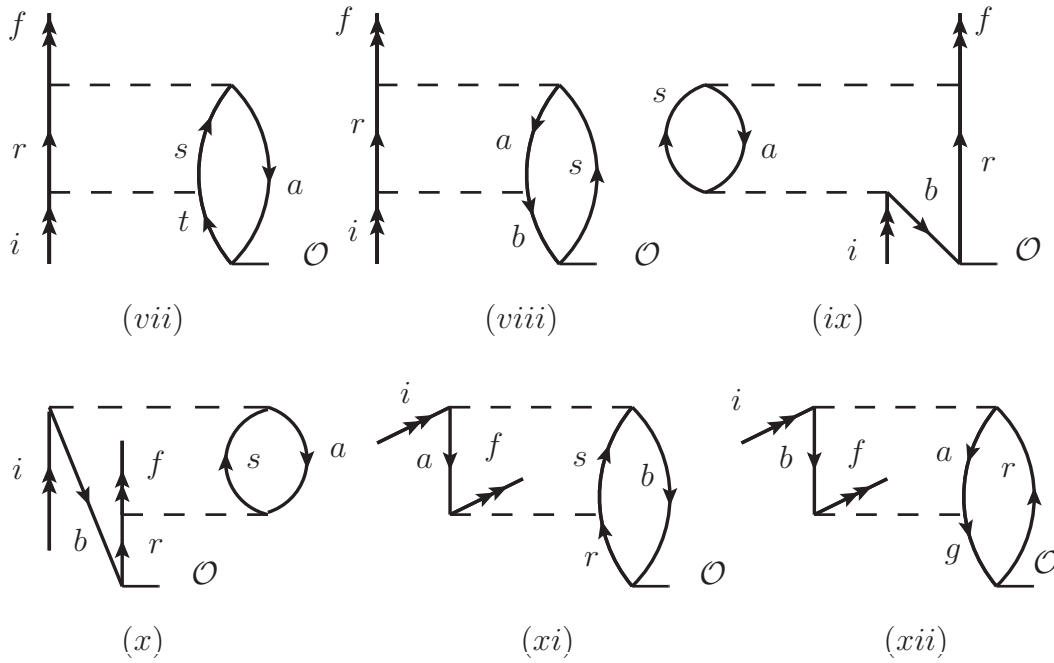


Figure 3.11: Direct diagrams of the SR correlations that correspond to the $\langle \Phi_f | \Omega_{2f}^{(2)\dagger} \mathcal{O} | \Phi_i \rangle$ term.

and

$$\text{Diagram (xviii)} = \langle \Phi_f | \Omega_{2c}^{(1)\dagger} \mathcal{O} \Omega_{2c}^{(1)\dagger} | \Phi_i \rangle = \sum_{rabc} \frac{\langle fr | h_2 | ab \rangle \langle a | o | g \rangle \langle gb | h_2 | ir \rangle}{(\epsilon_a + \epsilon_b - \epsilon_f - \epsilon_r)(\epsilon_b + \epsilon_g - \epsilon_i - \epsilon_r)}. \quad (3.21)$$

One can observe that the typical energy denominator for the BO term resembles $(\epsilon_i - \epsilon_p)(\epsilon_a + \epsilon_b - \epsilon_p - \epsilon_m)$, while that for the SR term resembles $(\epsilon_f + \epsilon_b - \epsilon_s - \epsilon_r)(\epsilon_i + \epsilon_a - \epsilon_r - \epsilon_s)$. Consequently, as long as the energy differences between core and valence states exceed the energy differences between different valence states, the BO terms will dominate over the SR terms [9].

3.2.4 Normalization correction

We must include the normalization factor to determine precise transition matrix element. The contribution from the normalization factor can be computed using the

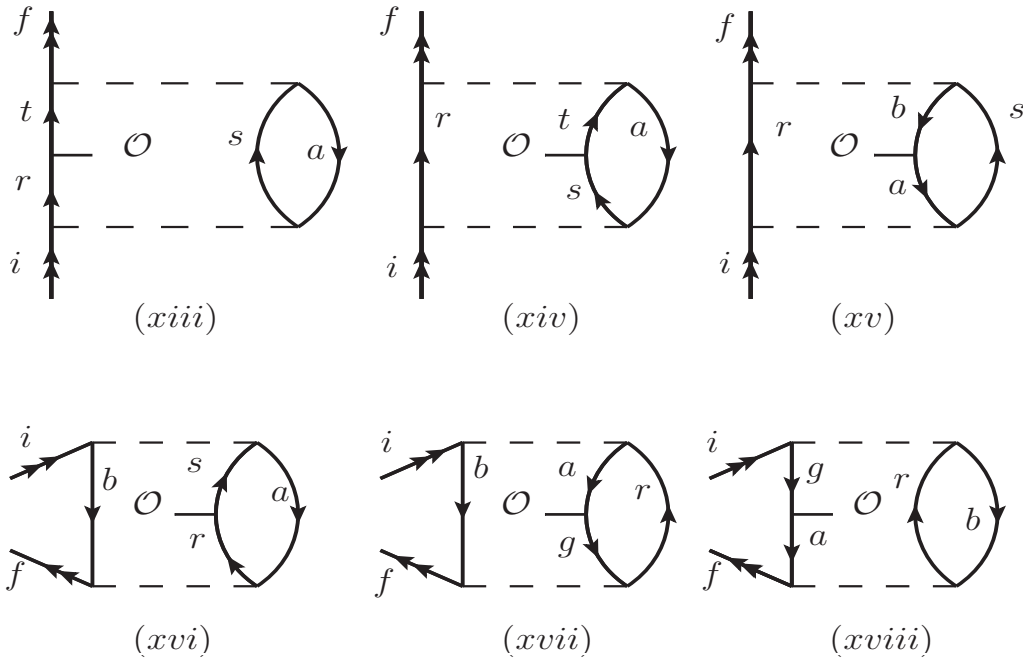


Figure 3.12: Direct diagrams of the SR correlation that appear through $\langle \Phi_f | \Omega_{2f}^{(1)\dagger} \mathcal{O} \Omega_{2i}^{(1)\dagger} | \Phi_i \rangle$ and $\langle \Phi_f | \Omega_{2c}^{(1)\dagger} \mathcal{O} \Omega_{2c}^{(1)\dagger} | \Phi_i \rangle$ terms. The first three diagrams correspond to the first term and the last three diagrams correspond to the later term.

following formula

$$\mathcal{O}^{Norm} = \left[\frac{\langle \Psi_f | \mathcal{O} | \Psi_i \rangle}{\sqrt{N_i N_f}} - \langle \Psi_f | \mathcal{O} | \Psi_i \rangle \right]. \quad (3.22)$$

We then add this correction to the $\langle \Psi_f | \mathcal{O} | \Psi_i \rangle$ calculation to present the final results. One important thing to note is that all these different correlation contributions from BO and SR have been taken into calculation through the RMBPT(3) method. To include all-order contributions, we need a higher-order many-body method which we are going to discuss next.

3.3 The RCC Theory

The RCC method has gained considerable attention for accurately incorporating electron correlation effects in various many-body systems, including nuclear, atomic, mo-

Table 3.3: A comparative description of the RCCSD method formalism for closed-shell and one-valence atomic systems. The operator, T , is applied only to excite the core electrons, and S_v corresponds to excitations that include the valence sector. The subscripts ('1' and '2') in T and S_v operators correspond to the level of excitation. H_N is the normal ordered Hamiltonian. Here, 'conn' stands for the connected terms and 'op' corresponds to the open part in $H_N e^T$ contraction. The term ΔE_v is known as the electron attachment energy or the electron affinity of the valence electron v . '*' denotes excited configuration with respect to $|\Phi_c\rangle$ or $|\Phi_v\rangle$ for closed-shell or one-valence atomic system respectively.

Parameter	Closed-shell	One-valence
Ansatz	$ \Psi_c\rangle = e^T \Phi_c\rangle$	$ \Psi_v\rangle = e^T \{1 + S_v\} \Phi_v\rangle$
Cluster Operator	$\Omega_c = e^T$ $T = T_1 + T_2$	$\Omega_c = e^T$; $\Omega_v = e^T S_v$ $S_v = S_{1v} + S_{2v}$
Diagrammatic representation	see Fig. 3.13	see Fig. 3.14
Correlation energy	$\Delta E_{corr} = \langle \Phi_c (H_N e^T)_{conn} \Phi_c \rangle$	$\Delta E_v = \langle \Phi_v (H_N e^T)_{op} \{1 + S_v\} \Phi_v \rangle$
Amplitude determining equation	$\langle \Phi_c^* (H_N e^T)_{conn} \Phi_c \rangle = 0$	$\langle \Phi_v^* (H_N e^T)_{op} \{1 + S_v\} \Phi_v \rangle = \Delta E_v \langle \Phi_v^* S_v \Phi_v \rangle$

lecular, and solid-state systems. It is often hailed as the gold standard of many-body theory due to its efficacy [1, 2, 25]. In contrast to other all-order quantum many-body methods like RCI and MCDHF, the fundamental appeal of this theory lies in its intrinsic properties of size extensivity and size consistency [2]. These characteristics stem from its basis as a purely linked diagram theory, ensuring accurate scaling relative to the total number of particles within a system. As mentioned earlier, the main focus of this chapter is to establish a connection between lower-order methods like RMBPT or RPA and the RCC method in order to examine how accurately RCC methods include all the contributions that appear in these methods up to all-orders. Before explicitly

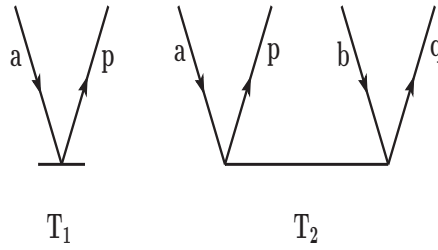


Figure 3.13: Goldstone diagrammatic representations of the T_1 and T_2 operators.

showing that, we briefly present an outline for the formulation of the RCC theory for closed-shell and one-valence open-shell atomic systems, just like it was defined for the RMBPT method. The current discourse on the RCC method revolves around a single reference function $|\Phi_\alpha\rangle$. In order to establish the equivalence between all-order RMBPT and RCC, we rewrite Eqs. 3.5 and 3.6 (dropping the subscript α)

$$|\Psi\rangle = \Omega|\Phi\rangle. \quad (3.23)$$

and

$$\Omega = 1 + \Omega^{(1)} + \Omega^{(2)} + \dots + \Omega^{(\infty)}. \quad (3.24)$$

Now, in terms of level of excitation, we can again segregate as follows

$$\begin{aligned} \Omega^{(1)} &= \Omega_1^{(1)} + \Omega_2^{(1)} + \dots + \Omega_{N_e}^{(1)}, \\ \Omega^{(2)} &= \Omega_1^{(2)} + \Omega_2^{(2)} + \dots + \Omega_{N_e}^{(2)}, \\ &\vdots \end{aligned}$$

and

$$\Omega^{(\infty)} = \Omega_1^{(\infty)} + \Omega_2^{(\infty)} + \dots + \Omega_{N_e}^{(\infty)}. \quad (3.25)$$

Note the difference between Ω_n and $\Omega^{(n)}$. Ω_n corresponds to the n -tuple excitation and $\Omega^{(n)}$ corresponds to the n -th order perturbation. In the RCC theory, the wave operator

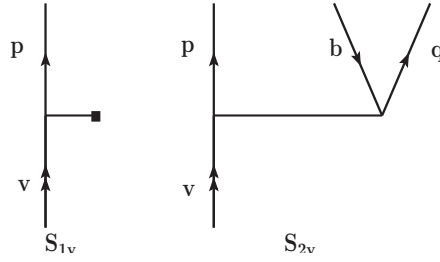


Figure 3.14: Goldstone diagrammatic representation of the S_{1v} and S_{2v} operators.

takes the exponential ansatz

$$|\Psi\rangle = e^T|\Phi\rangle. \quad (3.26)$$

So,

$$\Omega = e^T = 1 + T + \frac{T^2}{2!} + \frac{T^3}{3!} + \dots \quad (3.27)$$

T is called excitation operator or cluster operator. Depending upon the level of excitation from the reference state, we can write

$$T = T_1 + T_2 + T_3 + \dots + T_{N_e}. \quad (3.28)$$

So, using the above equations, we can write

$$\begin{aligned} \Omega_1 &= \Omega_1^{(1)} + \dots + \Omega_1^{(\infty)} = T_1, \\ \Omega_2 &= \Omega_2^{(1)} + \dots + \Omega_2^{(\infty)} = T_2 + \frac{T_1^2}{2!}, \\ \Omega_3 &= \Omega_3^{(1)} + \dots + \Omega_3^{(\infty)} = T_3 + T_1T_2 + \frac{T_1^3}{3!}, \\ &\vdots \end{aligned}$$

and so on. (3.29)

In the RCC method, when calculating T_1 , all single excitations contributing up to infinite-order perturbation are accounted for. This principle extends to T_2 , T_3 , and so forth. Another important thing to note here is that although T_1 corresponds to single excitation, one can generate higher-order excitations through non-linear terms of

T_1 , as T_1^2 corresponds to double excitation. Consequently, the RCC wave function for a many-electron atom encompasses the effects of electron correlation up to all-orders [24, 25, 26, 27, 28, 29, 30, 31]. We have presented a general description of the RCCSD method in Table 3.3 for closed-shell and one-valence atomic systems.

3.3.1 Calculation of transition matrix element

By changing the valence orbital ‘ v ’ we can get two states $|\Psi_i\rangle$ and $|\Psi_f\rangle$. Once we get these two states, the matrix element or the expectation value of an operator \mathcal{O} between these states can be evaluated using the following expression

$$\begin{aligned}
 \mathcal{O}_{fi}^{RCC} &= \frac{\langle \Psi_f | \mathcal{O} | \Psi_i \rangle}{\sqrt{\langle \Psi_f | \Psi_f \rangle \langle \Psi_i | \Psi_i \rangle}} \\
 &= \frac{\langle \Phi_f | \{1 + S_f^\dagger\} e^{T^\dagger} \mathcal{O} e^T \{1 + S_i\} | \Phi_i \rangle}{\langle \Phi_f | \{1 + S_f^\dagger\} e^{T^\dagger} e^T \{1 + S_i\} | \Phi_i \rangle} \\
 &= \frac{\langle \Phi_f | \{1 + S_f^\dagger\} \bar{\mathcal{O}} \{1 + S_i\} | \Phi_i \rangle}{\langle \Phi_f | \{1 + S_f^\dagger\} \bar{N} \{1 + S_i\} | \Phi_i \rangle}.
 \end{aligned} \tag{3.30}$$

Here, $\bar{\mathcal{O}} = e^{T^\dagger} \mathcal{O} e^T$ and $\bar{N} = e^{T^\dagger} e^T$. Several key Goldstone diagrams for the matrix element calculation are depicted in Fig. 3.15. If one compares the RCC diagrams with the RMBPT or the RPA method, one can see that the contribution from various RMBPT and RPA diagrams have been considered in the RCC diagrams. In Fig. 3.16, we have presented the breakdown of a few RCCSD diagrams in terms of RMBPT terms. As can be seen, terms like $\mathcal{O}\Omega_{1c}^{(2)}$, $\Omega_{2c}^{(1)\dagger}\mathcal{O}\Omega_{2c}^{(1)}$ have already been considered in the $\bar{\mathcal{O}}$ term in RCCSD method. Further, the contribution from BO and SR diagrams are coming from the $\bar{\mathcal{O}}S_{1i}$, $S_{1f}^\dagger\bar{\mathcal{O}}S_{1i}$, terms. Again, terms like $\bar{\mathcal{O}}S_{2i}$ captures the RPA contributions. So, the RCCSD method does not only include correlations from all these terms, but contributions from these terms have been made to all-orders, unlike the previously discussed methods. In order to show the superiority of the RCC method over RPA and RMBPT methods, we present the E1 matrix elements for different transitions in ^{133}Cs atom, obtained using different many-body methods, in Table 3.4. Additionally, we present a

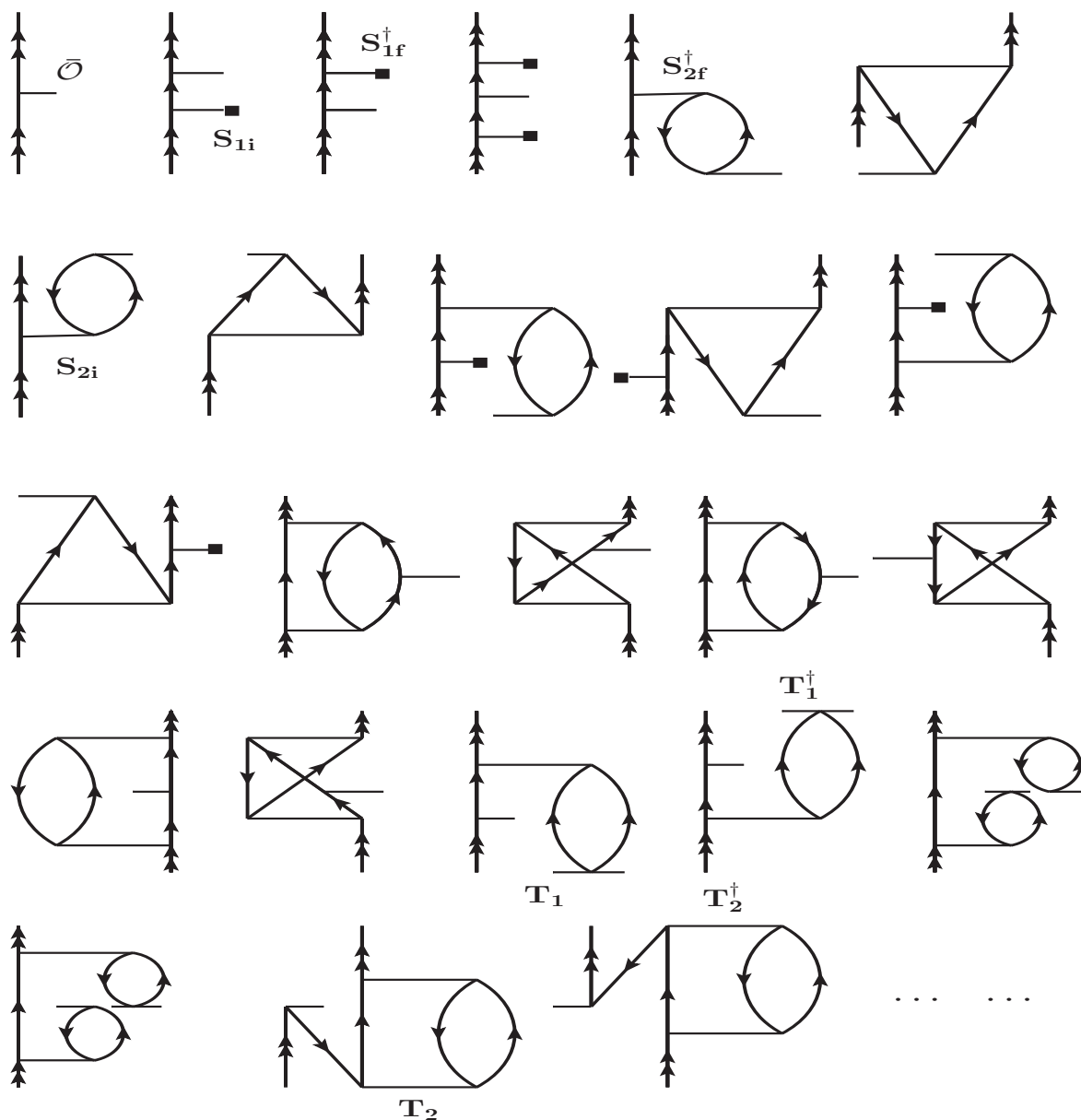


Figure 3.15: A few important matrix elements evaluating diagrams at the RCCSD level.

comparison in the same table with experimental values [32, 33, 34, 35, 36, 37]. When we compare our RCCSD results with experimental data, they align better with the measured values than the RMBPT(2) and RPA+BO+SR+Norm results. This superiority originates from the RCC method's more rigorous inclusion of electron correlation effects, as discussed previously.

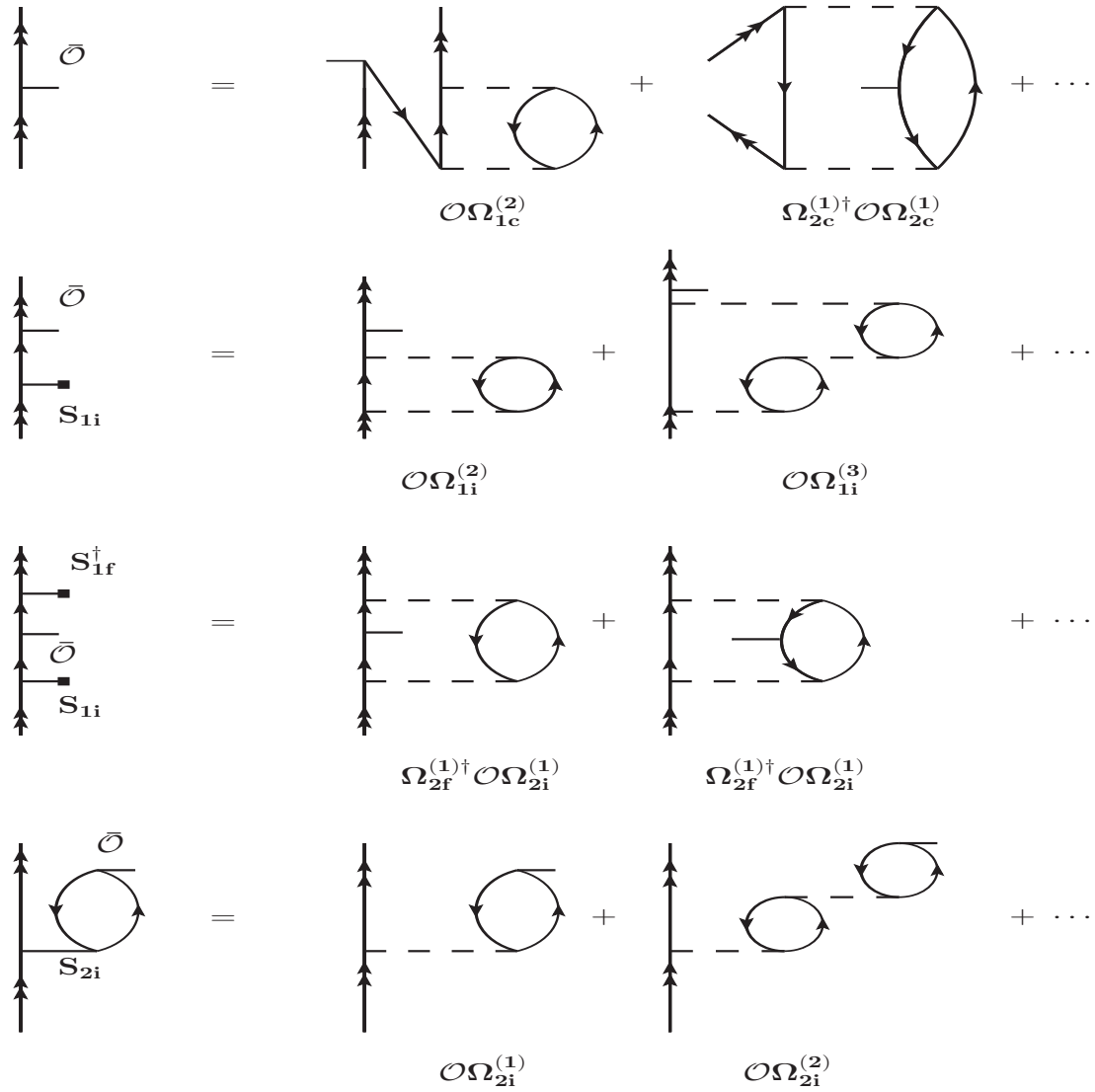


Figure 3.16: Breakdown of a few RCCSD property diagrams in terms of RMBPT diagrams. Below each diagram, the corresponding RMBPT terms have been mentioned.

3.4 Summary

In this chapter, we have discussed various many-body methods, including RMBPT, RPA, and RCC methods, and their incorporation of correlation effects from V_{res} . We have demonstrated that RMBPT(2) includes contributions from CP effects up to one-order, while the RPA method accounts for CP effects up to all-orders. Despite RPA's superiority over RMBPT(2), it neglects PC effects and contributions from SR terms

Table 3.4: Reduced E1 matrix elements in a.u. of ^{133}Cs atom from various many-body methods. We also compare our values with the experimental results.

Method	Transition For E1							
	$6P_{1/2} - 6S$	$7P_{1/2} - 6S$	$8P_{1/2} - 6S$	$9P_{1/2} - 6S$	$7S - 6P_{1/2}$	$7S - 7P_{1/2}$	$7S - 8P_{1/2}$	$7S - 9P_{1/2}$
DHF	5.2777	0.3717	0.1321	-0.0687	-4.4131	11.0121	0.9336	-0.3938
RMBPT(2)	4.9043	0.2225	0.0394	-0.0048	-4.4393	10.8914	0.8747	-0.3541
RPA	4.9747	0.2382	0.0489	-0.0128	-4.4499	10.9244	0.8818	-0.3584
RPA+BO	4.4103	0.3274	0.1015	-0.0426	-4.3481	10.0986	1.0200	-0.4214
RPA+BO+SR	4.4488	0.3460	0.1134	-0.0509	-4.3387	10.1007	1.0257	-0.4254
RPA+BO+SR+Norm.	4.3990	0.3430	0.1124	-0.0505	-4.3175	10.0823	1.0236	-0.4247
RCCSD	4.5487	0.3006	0.0914	-0.0388	-4.2500	10.2967	0.9492	-0.3867
Experiment	4.5097(74)[32] 4.5012(26) [33]	0.2825(20) [34] 0.27810(45)[35]			4.233(22)[36]	10.308(15)[37]		

that appear at the RMBPT(3) level. Furthermore, we have shown that the RCC method includes all these RPA and non-RPA correlation terms up to all-orders, as well as the correlation between RPA and non-RPA contributions. Finally, we have compared the E1 matrix elements calculated using these methods with available experimental values for the ^{133}Cs atom. The agreement of the RCC results with the experimental data demonstrates the superiority of the RCC method over the others.

Bibliography

- [1] I. Lindgren and J. Morrison, *Atomic Many-Body Theory*, edited by G. Ecker, P. Lambropoulos, and H. Walther, Springer-Verlag, Berlin (1985).
- [2] I. Shavitt and R. Bartlett, *Many-Body Methods in Chemistry and Physics: MBPT and Coupled-Cluster Theory*, Cambridge Molecular Science, Cambridge University Press (2009).
- [3] H. P. Kelly, Phys. Rev. **136**, B896 (1964).
- [4] I. Lindgren, J. Phys. B: Atom. Mol. Phys. **7**, 2441 (1974).
- [5] S. A. Blundell, W. R. Johnson and J. Sapirstein, Phys. Rev. A **37**, 2764 (1988); **38**, 2699 (1988); **42**, 1087 (1990).
- [6] C. Guet and W. R. Johnson, Phys. Rev. A **44**, 1531 (1991).
- [7] H. P. Kelly, Phys. Rev. **131**, 684 (1963).
- [8] A. L. Fetter and J. D. Walecka, *Quantum Theory of Many-Particle Systems*, McGraw–Hill, New York (1971).
- [9] S. A. Blundell, D. S. Guo, W. R. Johnson, and J. Sapirstein, At. Data Nucl. Data Tables **37**, 103 (1987).
- [10] W.R. Johnson, Z.W. Liu, and J. Sapirstein, At. Data Nucl. Data Tables **64**, 279 (1996).

- [11] I. M. Savukov and W. R. Johnson, Phys. Rev. A **62**, 052512 (2000).
- [12] J. Čížek, J. Chem. Phys. **45**, 4256 (1966); Adv. Chem. Phys. **14**, 35 (1969).
- [13] G. D. Purvis III and R. J. Bartlett, J. Chem. Phys. **86**, 7041 (1987).
- [14] Y. S. Lee, S. A. Kucharski and R. J. Bartlett, Theor. Chem. Phys. **81**, 5906 (1984).
- [15] A. W. Weiss, Phys. Rev. **122**, 1826 (1961).
- [16] F. Sasaki and M. Yoshimine, Phys. Rev. A **9**, 17 (1974).
- [17] M. H. Chen, K. T. Cheng, and W. R. Johnson Phys. Rev. A **47**, 3692 (1993).
- [18] Per E. M. Siegbahn, Jan Almlöf; Anders Heiberg, Björn O. Roos, J. Chem. Phys. **74**, 2384 (1981).
- [19] Björn O. Roos, Peter R. Taylor 1, Per E.M. Sigbahn, Chem. Phys. **48**, 157 (1980).
- [20] P Jönsson, C Froese Fischer and E Träbert, J. Phys. B: At. Mol. Opt. Phys. **31**, 3497 (1998).
- [21] K. A. Brueckner, Phys. Rev. **100**, 36 (1955).
- [22] P. O. Lowdin, J. Math. Phys. **3**, 1171 (1958).
- [23] V. A. Dzuba, V. V. Flambaum, P. G. Silvestrov and O. P. Sushkov, J. Phys. B: Atom. Mol. Phys. **20**, 1399 (1987).
- [24] J. Paldus, J. Čížek, and I. Shavitt, Phys. Rev. A **5**, 50 (1972).
- [25] R. F. Bishop and H. G. Kuemmel, Physics Today March issue, **52** (1987).
- [26] D. Mukherjee and S. Pal, Adv. Quantum Chem. **20**, 281 (1989).
- [27] M. S. Safronova, W. R. Johnson, and A. Derevianko, Phys. Rev. A **60**, 4476 (1999).
- [28] A-M. Mårtensson-Pendrill J. Phys. B: At. Mol. Opt. Phys. **35**, 917 (2002).

- [29] B. K. Sahoo, Phys. Rev. A **74**, 020501 (2006).
- [30] B. K. Sahoo, B. P. Das, R. K. Chaudhuri, D. Mukherjee, R. G. E. Timmermans, and K. Jungmann, Phys. Rev. A **76**, 040504 (2007).
- [31] D. Mukherjee, B. K. Sahoo, H. S. Nataraj, and B. P. Das, J. Phys. Chem. A **113**, 12549 (2009).
- [32] L. Young, W. T. Hill III, S. J. Sibener, S. D. Price, C. E. Tanner, C. E. Wieman and S. R. Leone, Phys. Rev. A **50**, 2174 (1994).
- [33] C. Amiot, O. Dulieu, R. F. Gutterres, and F. Masnou-Seeuws, Phys. Rev. A **66**, 052506 (2002).
- [34] A. A. Vasilyev, I. M. Savukov, M. S. Safronova and H. G. Berry, Phys. Rev. A **66**, 020101 (2002).
- [35] A. Damitz, G. Toh, E. Putney, C. E. Tanner, and D. S. Elliott, Phys. Rev. A **99**, 062510 (2019).
- [36] M.-A. Bouchiat, J. Guena, and L. Pottier, J. Phys. (Paris), Lett. **45**, 523 (1984).
- [37] S. C. Bennett, J. L. Roberts and C. E. Wieman, Phys. Rev. A **59**, R16 (1999).

Chapter 4

Electric Dipole Polarizability of Closed-Shell Atomic Systems

IN the previous chapter, we have shown that the RCC method encapsulates all the correlation effects that appear in the RMBPT and RPA methods up to all-orders.

In this chapter, we go one step further and introduce another perturbation along with V_{res} into the calculation. Herein, we present electric dipole polarizability (α_d) value for the ground state of singly charged Cs cation (Cs^+) and neutral zinc atom (Zn) due to the second-order dipole interaction. The aim of this chapter is to analyze the correlation trend of various many-body methods, namely RMBPT, RPA, and RCC for closed-shell atomic systems. We have chosen Zn alongside Cs^+ for this study because the static α_d value of the ground state of Zn has been accurately measured [1], whereas there are no experimental values available of α_d for Cs^+ . Further, various theoretical calculations based on sophisticated many-body methods are available for the Zn [1, 2, 3, 4, 5, 6]. This calculation of α_d will be helpful to demonstrate the validity of a theoretical approach by reproducing the experimental result. This polarizability calculation will be able to provide insights into the behavior of electron correlation effects in different many-body methods in the context of the calculation of perturbed properties. This will be helpful in supporting the accuracy of our calculations for PV studies.

4.1 Theory of static polarizability

Atomic orbitals are spherically symmetric, but their electric charge distribution can be deformed by stray electric fields [7, 8]. In the ground state of a closed-shell atomic system, the first-order energy shift due to a weak electric field is zero, and the primary contributions to the energy shifts come from second-order effects onwards [9]. These contributions are typically expressed as powers of the electric field strength and in terms of electric polarizabilities, which depend on the atomic state but are independent of the applied electric field strength [7]. In the presence of a weak electric field $\mathcal{E}(r)$ with strength \mathcal{E}_0 , the ground state energy level of an atomic system can be expressed in the perturbative approach as [1, 9, 10]

$$\begin{aligned} E_c &= E_c^{(0)} + E_c^{(1)} + E_c^{(2)} + \dots \\ &= E_c^{(0)} - \frac{1}{2}\alpha_d \mathcal{E}_0^2 + \dots \end{aligned} \quad (4.1)$$

Here $E_c^{(0)}$ is the ground state energy level and $E_c^{(n)}$ denotes n^{th} order correction to the energy. The first-order energy shift to the ground state is $E_c^{(1)} = 0$.

As the α_d value corresponds to second-order energy correction, we can evaluate this using perturbative analysis as [11]

$$\alpha_d = -\frac{2}{\langle \Psi_c^{(0)} | \Psi_c^{(0)} \rangle} \sum_{k \neq c} \frac{|\langle \Psi_c^{(0)} | D | \Psi_k^{(0)} \rangle|^2}{E_c^{(0)} - E_k^{(0)}}. \quad (4.2)$$

As mentioned in the earlier chapter, D is the electric dipole operator. $|\Psi_k^{(0)}\rangle$ and $E_k^{(0)}$ are the atomic wave functions and energies of the free atomic system, respectively, with k representing the level of a state. Since it is impractical to evaluate the complete set of $|\Psi_k^{(0)}\rangle$ for the evaluation of the above quantity, it can be determined conveniently by expressing as [12, 13, 14]

$$\alpha_d = 2 \frac{\langle \Psi_c^{(0)} | D | \Psi_c^{(d,1)} \rangle}{\langle \Psi_c^{(0)} | \Psi_c^{(0)} \rangle}, \quad (4.3)$$

where the first-order wave functions are defined as

$$|\Psi_c^{(d,1)}\rangle = \sum_{n \neq c} |\Psi_n^{(0)}\rangle \frac{\langle \Psi_c^{(0)} | D | \Psi_n^{(0)} \rangle}{E_c^{(0)} - E_n^{(0)}}. \quad (4.4)$$

Therefore, contributions from all the intermediate states in the sum-over-states to α_d can be accounted through the first-order wave function by determining it as the solution of the following inhomogeneous equation

$$(H - E_c^{(0)})|\Psi_c^{(d,1)}\rangle = -D|\Psi_c^{(0)}\rangle \quad (4.5)$$

in the *ab initio* framework with the electronic Hamiltonian H . In the approximation of $|\Psi_c^{(d)}\rangle \approx |\Psi_c^{(0)}\rangle + |\Psi_c^{(d,1)}\rangle$, it follows from the above expression

$$\alpha_d = \frac{\langle \Psi_c^{(d)} | D | \Psi_c^{(d)} \rangle}{\langle \Psi_c^{(d)} | \Psi_c^{(d)} \rangle} \equiv \langle D \rangle. \quad (4.6)$$

Here $|\Psi_c^{(d)}\rangle$ is the modified atomic wave function under the presence of D operator. So the dipole polarizability can be written as the expectation value of D in the modified atomic wave function.

4.2 Methodology

We start our calculation with the DHF method. Using DHF wave functions, we can evaluate the α_d value in the mean-field approach as

$$\alpha_d = 2\langle \Phi_c | D | \Phi_c^{(d,1)} \rangle, \quad (4.7)$$

where $|\Phi_c^{(d,1)}\rangle$ is the first-order perturbed wave function with respect to $|\Phi_c\rangle$. We can express these wave functions as

$$|\Phi_c^{(d,1)}\rangle = \sum_{I \neq c} |\Phi_I\rangle \frac{\langle \Phi_I | D | \Phi_c \rangle}{\mathcal{E}_c - \mathcal{E}_I}, \quad (4.8)$$

where $|\Phi_I\rangle$ are the intermediate states with mean-field energies \mathcal{E}_I . In the DHF method, the contribution from the V_{res} term has been neglected. To incorporate correlation effects, we first define unperturbed and perturbed wave functions as

$$|\Psi_c^{(0)}\rangle = \Omega_c^{(0)} |\Phi_c\rangle$$

and

$$|\Psi_c^{(d,1)}\rangle = \Omega_c^{(d,1)} |\Phi_c\rangle. \quad (4.9)$$

In the RMBPT method $\Omega_c^{(0)}$ and $\Omega_c^{(d,1)}$ are expressed [4, 15, 16, 17]

$$\Omega_c^{(0)} = \Omega_c^{(0,0)} + \Omega_c^{(1,0)} + \Omega_c^{(2,0)} + \dots \quad (4.10)$$

and

$$\Omega_c^{(d,1)} = \Omega_c^{(0,1)} + \Omega_c^{(1,1)} + \Omega_c^{(2,1)} + \dots, \quad (4.11)$$

where $\Omega_c^{(0,0)} = 1$ and $\Omega_c^{(n,m)}$ denotes inclusion of n^{th} and m^{th} order of V_{res} and D operators in the calculations. As mentioned in the last chapter, in the RMBPT method, the amplitudes of these wave operators can be determined using the generalized Bloch's equation. The Bloch equation for the unperturbed wave operator is given in the last chapter. For first-order perturbed wave operator we can write [4, 15, 17]

$$[\Omega_c^{(d,1)}, H_{DHF}] P_c = (D \Omega_c^{(0)} + V_{res} \Omega_c^{(d,1)}) P_c. \quad (4.12)$$

To understand how electron correlation effects propagate from the lower-order level to the higher-order level of perturbation in the determination of polarizabilities, we consider one- and two-orders of V_{res} in the RMBPT(2) and RMBPT(3) method respectively, and estimate α_d value. The expression of polarizability in the RMBPT(3) method is given by

$$\begin{aligned}
 \alpha_d &= \frac{2}{\mathcal{N}} \left\langle \Phi_c | [\Omega_c^{(0,0)} + \Omega_c^{(1,0)} + \Omega_c^{(2,0)}]^\dagger D [\Omega_c^{(0,1)} + \Omega_c^{(1,1)} + \Omega_c^{(2,1)}] | \Phi_c \right\rangle \\
 &= \frac{2}{\mathcal{N}} \left\langle \Phi_c | D\Omega_c^{(0,1)} + D\Omega_c^{(1,1)} + D\Omega_c^{(2,1)} + \Omega_c^{(1,0)\dagger} D\Omega_c^{(0,1)} + \Omega_c^{(2,0)\dagger} D\Omega_c^{(0,1)} \right. \\
 &\quad \left. + \Omega_c^{(1,0)\dagger} D\Omega_c^{(1,1)} | \Phi_c \right\rangle, \tag{4.13}
 \end{aligned}$$

where \mathcal{N} is the normalization constant. One can easily write the above expression for the RMBPT(2) method, by discarding terms $D\Omega_c^{(2,1)}$, $\Omega_c^{(2,0)\dagger} D\Omega_c^{(0,1)}$ and $\Omega_c^{(1,0)\dagger} D\Omega_c^{(1,1)}$. The RMBPT(2) and RMBPT(3) methods capture correlation effects up to finite order. In the RPA, one can capture the CP effects to all-orders in a very simple manner by extending the DHF expression. In RPA, the modified single particle DHF Hamiltonian for i th orbital $f_i^d = f_i + \lambda d$ can be written as

$$f_i^d |\tilde{i}\rangle = \tilde{\epsilon}_i |\tilde{i}\rangle \tag{4.14}$$

where the tilde symbol denotes the solution for f^d . Now expanding $|\tilde{i}\rangle = |i\rangle + \lambda|i^d\rangle + \mathcal{O}(\lambda^2)$ from Eq. 4.14 and retaining terms that are linear in λ , we can get

$$(f_i - \epsilon_i)|i^d\rangle = -d|i\rangle - u_i^d|i\rangle, \tag{4.15}$$

where

$$\begin{aligned}
 u_i^d|i\rangle &= \sum_b^{N_e} [\langle b|h_2|b\rangle|i^d\rangle - \langle b|h_2|i^d\rangle|b\rangle \\
 &\quad + \langle b^d|h_2|b\rangle|v\rangle - \langle b^d|h_2|i\rangle|b\rangle]. \tag{4.16}
 \end{aligned}$$

Both Eqs. 4.15 and 4.16 are solved iteratively to obtain the self-consistent solutions to account for CP effects up to all-orders. To make a comparison with the RMBPT method, we define wave operator $\Omega_c^{d,RPA} = \sum_{k=1}^{\infty} \sum_{a,p} \Omega_{a,p}^{(k,1)}$. The amplitude of this operator is given by

$$\begin{aligned} \Omega_{a,p}^{(k,1)} = & \Omega_a^p + \sum_{b,q} \left(\frac{[\langle pb|h_2|aq\rangle - \langle pb|h_2|qa\rangle]}{\epsilon_a - \epsilon_p} \Omega_{b,q}^{(k-1,1)} \right. \\ & \left. + \Omega_{b,q}^{(k-1,1)\dagger} \frac{[\langle pq|h_2|ab\rangle - \langle pq|h_2|ba\rangle]}{\epsilon_a - \epsilon_p} \right) \end{aligned} \quad (4.17)$$

To compute the amplitude of the above operator, we set $\Omega_{a,p}^{(0,1)} \approx \Omega_a^p = \frac{\langle p|d|a\rangle}{\epsilon_a - \epsilon_p} a_p^\dagger a_a$ in the beginning to initiate the iteration procedure from $k = 1$. We can present the RPA expression for α_d using the wave operators as

$$\alpha_d = 2\langle \Phi_c | D \Omega_c^{d,RPA} | \Phi_c \rangle. \quad (4.18)$$

The limitation of this method is that it incorporates CP effects only through singly excited configurations. Additionally, it approximates the bra state using the DHF wave function Φ_c , and it does not account for PC effects. In order to capture the RPA as well as all-order contributions from the non-RPA effects, we have to consider the RCC method [4, 17, 18]. In this work, we used the linear response RCC theory to estimate the polarizability values. We consider that the interaction operator D is a part of the atomic Hamiltonian and the total atomic Hamiltonian is given by

$$H_{at}^D = H + \lambda D, \quad (4.19)$$

where λ is introduced to keep track of the order of D in the calculations. The atomic wave function $|\Psi_c^{(d)}\rangle$ of the above Hamiltonian in the RCC theory can be given by

$$|\Psi_c^{(d)}\rangle = e^{\tilde{T}} |\Phi_c^{(d)}\rangle = e^T |\Phi_c\rangle, \quad (4.20)$$

where $|\Phi_c^{(d)}\rangle$ represents the modified DHF wave function constructed in the presence of D with the corresponding electron excitation operator \tilde{T} due to both V_{res} and D , while T is also the electron excitation operator due to both V_{res} and D but considering excitations from $|\Phi_c\rangle$. The expectation value of D can be written as

$$\begin{aligned}\langle D \rangle &= \frac{\langle \Psi_c^{(d)} | D | \Psi_c^{(d)} \rangle}{\langle \Psi_c^{(d)} | \Psi_c^{(d)} \rangle} \\ &= \frac{\langle \Phi_c | e^{T^\dagger} D e^T | \Phi_c \rangle}{\langle \Phi_c | e^{T^\dagger} e^T | \Phi_c \rangle}.\end{aligned}\quad (4.21)$$

Following Refs. [19, 20], the above expression yields

$$\langle D \rangle = \langle \Phi_c | e^{T^\dagger} D e^T | \Phi_c \rangle_{conn}, \quad (4.22)$$

Now expanding T in powers of λ as

$$T = T^{(0)} + \lambda T^{(d,1)} + \mathcal{O}(\lambda^2) \quad (4.23)$$

and retaining terms linear in λ in Eq. 4.21 we get

$$\langle D \rangle = 2 \frac{\langle \Phi_c | e^{T^{(0)\dagger}} D e^{T^{(0)}} T^{(d,1)} | \Phi_c \rangle}{\langle \Phi_c | e^{T^{(0)\dagger}} e^{T^{(0)}} | \Phi_c \rangle}. \quad (4.24)$$

Similarly expanding the cluster operator T in Eq. 4.22, it gives

$$\langle D \rangle = 2 \langle \Phi_c | e^{T^{(0)\dagger}} D e^{T^{(0)}} T^{(d,1)} | \Phi_c \rangle_{conn}. \quad (4.25)$$

Eqs. 4.24 and 4.25 are mathematically equivalent. Consequently following Eq. 4.6, the polarizability can be calculated using the expectation value evaluation approach in RCC theory as

$$\alpha_d = 2 \langle \Phi_c | e^{T^{(0)\dagger}} D e^{T^{(0)}} T^{(d,1)} | \Phi_c \rangle_{conn}. \quad (4.26)$$

Table 4.1: Calculated static dipole (α_d) polarizability values (in a.u.) of Zn and Cs⁺ using different many-body methods in the relativistic framework.

Method	Zn	Cs ⁺
	This work	
DHF	37.29	16.79
RMBPT(2)	43.50	13.70
RMBPT(3)	38.68	12.25
RPA	50.81	15.77
RCCSD	40.32	15.99

The amplitudes for the unperturbed operator $T^{(0)}$ are obtained by solving the usual RCC theory equations, as mentioned in the previous chapter. The first-order perturbed RCC operator amplitudes are determined as

$$\langle \Phi_c^* | (He^{T^{(0)}})_{conn} T^{(d,1)} | \Phi_c \rangle = -\langle \Phi_c^* | (De^{T^{(0)}})_{conn} | \Phi_c \rangle. \quad (4.27)$$

4.3 Results and Discussion

In Table 4.1, we present the results for α_d value for Zn and Cs⁺ obtained from our DHF, RMBPT(2), RMBPT(3), RPA and RCCSD methods. The correlation trends of the α_d values across different many-body methods are illustrated in Fig. 4.1. As shown in the table and figure, the value of α_d for neutral Zn atom increases in the RMBPT(2) method compared to the DHF method and then decreases again in the RMBPT(3) method. The RMBPT(2) method includes the lowest-order RPA terms, while the RMBPT(3) method incorporates the lowest-order non-RPA terms. The trend indicates that the RPA and non-RPA terms contribute with opposite signs in Zn, leading to a cancellation between these terms. This pattern is further confirmed by the RPA and RCCSD results. The RPA, which captures CP effects up to all-orders, produces a large value for α_d , whereas the RCCSD results are closer to the RMBPT(3) values. Subtracting the DHF values from the RCCSD results reveals that the difference is small for α_d . This suggests that the CP effects increase the magnitudes of α_d , while other

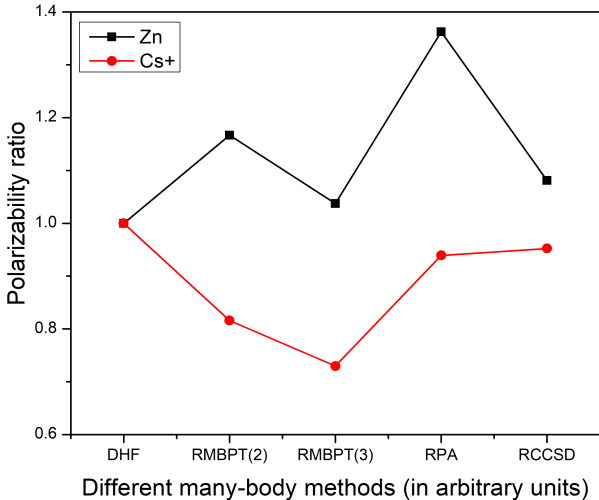


Figure 4.1: Ratios of dipole polarizability value of Zn and Cs⁺ from different many-body methods and their DHF values.

correlation effects contribute with opposite signs at the all-order perturbation level. The correlation trend α_d in Cs⁺ ion is quite different. The value of α_d decreases in RMBPT(2) and then again in RMBPT(3) level compared to the DHF method. This suggests that the RPA and non-RPA terms contribute with the same sign for Cs⁺ at lower order. In the RPA and RCCSD methods, the value of α_d increases again. The difference between the RCCSD and the DHF results is very small, suggesting there is a large cancellation among different correlation terms.

To better understand the RCCSD values, we present the results from individual terms in Table 4.2. In this table, we also compare the corresponding contributions to α_d of Zn from the RCCSD method previously reported in Refs. [4, 5]. Comparing the individual RCC term values from the earlier calculations [4, 5] with ours, we observe differences in the trends of various terms. The trends in our work are similar to those in Ref. [4] due to the identical implementation procedure of the RCC method. We utilized a much larger basis set with 40, 39, 38, 37, 36, and 35 GTOs for the *s*, *p*, *d*, *f*, *g*, and *h* orbitals, respectively, whereas Ref. [4] used only 35 GTOs for each symmetry up to *g* orbitals. When comparing the correlation trends through the individual RCC terms of Ref. [5] with our calculations, we find that the difference in the result from $DT_1^{(1)}$

Table 4.2: Comparison of contributions to α_d (in a.u.) of Zn and Cs⁺ from various RCCSD terms. We also compare the corresponding contributions from previously reported calculations using the RCCSD method for α_d of the Zn atom. Here, Norm denotes the difference between the contributions after and before normalizing the wave function with a normalization factor. NA stands for not applicable and Nonlin corresponds to the contributions from nonlinear terms.

Term	Zn			Cs ⁺	
	Ref. [5]	Ref. [4]	Ours	Term	Ours
$DT_1^{(1)}$	22.795	21.906	23.793	$DT_1^{(1)}$	8.790
$T_1^{(1)\dagger} D$	22.795	21.906	23.793	$T_1^{(1)\dagger} D$	8.790
$T_1^{(0)\dagger} DT_1^{(1)}$	-0.951	-1.229	-1.336	$T_1^{(0)\dagger} DT_1^{(1)}$	-0.091
$T_1^{(1)\dagger} DT_1^{(0)}$	-0.951	-1.229	-1.336	$T_1^{(1)\dagger} DT_1^{(0)}$	-0.091
$T_1^{(1)\dagger} DT_2^{(0)}$	-0.925	-2.643	-2.794	$T_1^{(1)\dagger} DT_2^{(0)}$	-1.014
$T_2^{(0)\dagger} DT_1^{(1)}$	-0.925	-2.643	-2.794	$T_2^{(0)\dagger} DT_1^{(1)}$	-1.014
$T_1^{(0)\dagger} DT_2^{(1)}$	0.041	NA	0.072	$T_1^{(0)\dagger} DT_2^{(1)}$	0.016
$T_2^{(1)\dagger} DT_1^{(0)}$	0.041	NA	0.072	$T_2^{(1)\dagger} DT_1^{(0)}$	0.016
$T_2^{(0)\dagger} DT_2^{(1)}$	0.673	1.024	1.025	$T_2^{(0)\dagger} DT_2^{(1)}$	0.262
$T_2^{(1)\dagger} DT_2^{(0)}$	0.673	1.024	1.025	$T_2^{(1)\dagger} DT_2^{(0)}$	0.262
Nonlin	NA	0.551	-1.200	Nonlin	0.064
Norm	-4.086	0.0	0.0	Norm	0.0

(along with its c.c. term) is small, but there are substantial differences among other RCC terms. Notably, the contribution from the normalization of the wave function (denoted as ‘Norm’ in Table 4.2) in Ref. [5] is quite large, even larger than the net correlation contributions (the difference between our DHF and final RCCSD results). Given this, we believe that implementing RCC theory, where only the connected terms are retained and the Norm factor does not appear in Eq. 4.22, is more credible. Unlike Zn, the α_d value for Cs⁺ was not previously evaluated using the linear response RCC theory. Therefore, we could not compare the contributions from our RCC terms with any earlier study.

We compare our RCCSD values for α_d with previously published results in Table

Table 4.3: Comparative table for α_d value (in a.u.) from different calculations using various many-body methods, experiments and scaling procedures.

Atomic system	Value	Method	Reference
Zn	40.32(71)	RCCSD	This work
	38.8(8)	Expt.+extrapol.	[1]
	42.79	CCSD	[1]
	41.69	CCSD(T)	[1]
	39.2(8)	CCSD(T)+scaling	[1]
	41.83	CCSD	[2]
	39.27	RCCSD	[2]
	40.55	CCSD(T)	[2]
	38.01	RCCSD(T)	[2]
	41.6	CCSD	[3]
	39.02	CCSD*	[3]
	40.39	CCSD(T)	[3]
	37.86	CCSD(T)*	[3]
	38.666(96)	CCSD _p T	[4]
	38.72	PRCC	[5]
	38.76	PRCC(T)	[5]
	35.33	MCDHF+scaling	[6]
38.92	Expt.+fitting	[21]	
Cs ⁺	15.99(10)	RCCSD	This work
	15.81	RPA	[22]
	15.8	RPA	[23]

*After considering quasi-relativistic corrections.

4.3. The RCCSD values are listed with the estimated uncertainties derived from our calculations. These uncertainties take into account contributions from higher-order Breit and QED interactions that were not taken into account in the many-body methods, as well as extrapolated contributions from higher-lying basis functions that were left out. Errors from extrapolated basis functions and relativistic effects are analyzed using the RMBPT and RPA methods. Results from the CC and RCC methods are presented using both the CCSD method and the CCSD method with contributions from partial triple excitations (CCSD(T)), along with their relativistic versions. The experimental value of α_d for Zn was measured using the Michelson twin interferometer technique

[1]. This value was later revised by fitting the data with improved numerical analyses [21]. There is approximately a 4% difference between our RCCSD values for α_d and the experimental value. Although our RMBPT(3) value for α_d is much closer to the experimental value, it is important to note that the RMBPT(3) method does not include correlations as rigorously as the RCCSD method. Furthermore, the convergence of the RMBPT(3) value is not guaranteed. Therefore, we recommend the RCCSD results over the RMBPT(3) values. The latest calculation of α_d for Zn uses a sum-over-states approach, combining only a few E1 matrix elements from the MCDHF method with experimental energies while estimating the remaining contributions using lower-order methods. This approach shows poor agreement with the experimental result [6]. The calculations reported in Refs. [4, 5] are equivalent to our RCCSD method, while those in Refs. [1, 2, 3] are based on the Finite Field approach using the non-relativistic CC method. Overall, there seems to be good agreement among all these calculations. It is noteworthy that in order to quote more accurate values, Refs. [1, 2, 3] have used scaled values. In the same table, we compare our RCCSD value for α_d for Cs^+ . Our result agrees well with the values that have been previously reported. This comparison proves that our implementation of the RCCSD method is correct and it is more capable of capturing the electron correlation effects than lower-order methods.

4.4 Summary

We have employed the RCC theory to determine the electric dipole polarizability of the Cs^+ ion. In V^{N_e-1} potential formalism, Cs^+ ion is the starting point of our calculation for the parity-violating amplitude in ^{133}Cs atom. By this polarizability result, we can assess the potential of our RCC method in determining the wave functions of the closed-shell Cs^+ ion. Since the experimental value of α_d for Cs^+ is not available in the literature, we have used another closed-shell atom, Zn, as a case study. Electric dipole polarizability of the ground state of Zn has been experimentally measured, providing a reliable benchmark for our theoretical methods. We have also presented values from

lower-order RMBPT(2), RMBPT(3), and RPA methods. We have compared our results with the earlier recommended values from various calculations. Our results from the RCC theory at the singles and doubles approximation match well with earlier reported values. This reinforces the validity of our computational approach and confirms that our implementation of the RCCSD method is accurate.

Bibliography

- [1] D. Goebel, U. Hohm, and G. Maroulis, Phys. Rev. A **54**, 1973 (1996).
- [2] M. Seth, P. Schwerdtfeger, and M. Dolg, J. Chem. Phys. **106**, 3623 (1997).
- [3] V. Kellö and A. J. Sadlej, Theor. Chim. Acta **91**, 353 (1995).
- [4] Y. Singh and B. K. Sahoo, Phys. Rev. A **90**, 022511 (2014).
- [5] S. Chattopadhyay, B. K. Mani and D. Angom, Phys. Rev. A **91**, 052504 (2015).
- [6] H. Kaur, N. Shukla, R. Srivastava, and B. Arora, Phys. Rev. A **104**, 012806 (2021).
- [7] K. D. Bonin and V. V. Kresin, *Electric Dipole Polarizabilities of Atoms, Molecules, and Clusters*, World Scientific, Singapore (1997).
- [8] H. Haken and H. C. Wolf, *Atoms in an Electric Field. In: The Physics of Atoms and Quanta*, Springer (Berlin, Heidelberg), pp. 251-279 (1996).
- [9] A. D. Buckingham, Adv. Chem. Phys. **12**, 107 (1967).
- [10] G. Maroulis and D. M. Bishop, Chem. Phys. Lett. **114**, 182 (1985).
- [11] W. Tenfen, M. V. Barp and F. Arretche, Phys. Rev. A **99**, 022703 (2019).
- [12] B. K. Sahoo, Chem. Phys. Lett. **448**, 144 (2007).
- [13] B. K. Sahoo, B. P. Das, R. K. Chaudhuri and D. Mukherjee, J. Comput. Methods Sci. Eng. **7**, 57 (2007).

- [14] B. K. Sahoo and B. P. Das, Phys. Rev. A **77**, 062516 (2008).
- [15] Y. Singh and B. K. Sahoo, Phys. Rev. A **91**, 030501(R) (2015).
- [16] I. Lindgren and J. Morrison, *Atomic Many-Body Theory*, Springer-Verlag Berlin Heidelberg (1986).
- [17] Y. Singh, B. K. Sahoo and B. P. Das, Phys. Rev. A **88**, 062504 (2013).
- [18] B. K. Sahoo, Y. Singh and B. P. Das, Phys. Rev. A **90**, 050501(R) (2014).
- [19] Rodney J. Bartlett and Monika Musiał, Rev. Mod. Phys. **79**, 291 (2007).
- [20] S. Pal, M. D. Prasad, and D. Mukherjee, Pramana **18**, 261 (1982).
- [21] L. W. Qiao, P. Li and K. T. Tang, J. Chem. Phys. **137**, 084309 (2012).
- [22] W.R. Johnson, D. Kolb, and K.-N. Huang, At. Data Nucl. Data Tables **28**, 333 (1983).
- [23] M. S. Safronova, W. R. Johnson, and A. Derevianko, Phys. Rev. A **60**, 4476 (1999).

Chapter 5

Unraveling NSI PV Amplitude Calculation in ^{133}Cs

EARLIER in the thesis, we have discussed the significance of precise calculations of the $E1_{PV}^{NSI}$ amplitude in testing the SM of particle physics. Consequently, numerous calculations have been conducted on a range of atomic systems [1, 2, 3, 4, 5, 6, 7, 8]. The most accurate calculations thus far have been performed for the $6s\ ^2S_{1/2} - 7s\ ^2S_{1/2}$ transition in the ^{133}Cs atom [9, 10, 11, 12]. However, controversies persist among these results. One of such high-precision calculations was carried out by Porsev *et al.* in 2010. They used the CCSDvT method to estimate the Main contributions, whereas the Core and Tail contributions were calculated through a blend of the many-body methods [9]. Later Dzuba *et al.* [10] refined the Core and Tail contributions of $E1_{PV}^{NSI}$ value using the TDHF+BO method. They used the Main contribution from the calculation of Porsev *et al.* This calculation yielded an opposite sign for the Core contribution to that of Porsev's. Both the studies claimed to achieve an accuracy below 0.5%, but their final results differ by 1%. Later Sahoo *et al.* [12] implemented the RCCSDT method to study $E1_{PV}^{NSI}$ in ^{133}Cs . The Core contribution in this approach aligned with Porsev's calculation. In this scenario, in order to test the SM and probe BSM physics it is necessary to find out the reason behind such disparity

among various high-precision studies. In this chapter, we are going to unravel the reason for these discrepancies. The objective of this chapter is to develop theoretical insights aimed at resolving the sign discrepancy in the Core contribution among different studies while shedding light on the constraints of the sum-over-states approach. Herein we have also discussed diverse methodologies within a general many-body framework for computing $E1_{PV}^{NSI}$ amplitude, illustrating how different many-body methods incorporate the correlation effects into the $E1_{PV}^{NSI}$ calculation.

5.1 Evaluation Procedures of $E1_{PV}^{NSI}$

In the presence NSI PV, the net atomic Hamiltonian is given by

$$H_{at} = H + H_{PV}^{NSI} = H + \lambda H_W, \quad (5.1)$$

where H contains contributions from em interactions and H_W is defined in order to treat $\lambda = \frac{G_F}{2\sqrt{2}}$ as a small parameter to include contributions from H_{PV}^{NSI} perturbatively through many-body methods. Using the wave functions of H_{at} , we determine $E1_{PV}^{NSI}$ of a transition between states $|\Psi_i\rangle$ and $|\Psi_f\rangle$ as

$$E1_{PV}^{NSI} = \frac{\langle \Psi_f | D | \Psi_i \rangle}{\sqrt{\langle \Psi_f | \Psi_f \rangle \langle \Psi_i | \Psi_i \rangle}}, \quad (5.2)$$

Following previous calculations of $E1_{PV}^{NSI}$ amplitude in ^{133}Cs , where atomic wave functions were determined by using the V^{N_e-1} potential, we generate both the ground and excited states of the ^{133}Cs atom using the Fock-space formalism. The reason for adopting this same formalism is to maintain consistency across various works, ensuring that the description of different correlation effects and the comparison of results remain coherent. For the same reason, we consider the wave functions to be in the electronic state $|JM_J\rangle$. Both $|\Psi_i\rangle$ and $|\Psi_f\rangle$ can be obtained by solving the EOM for H_{at} . However, parity cannot be considered a good quantum number for H_{at} . Consequently, it

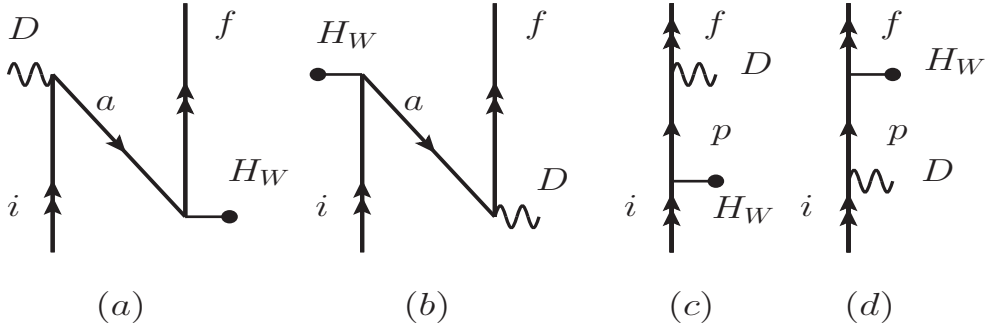


Figure 5.1: Goldstone diagrams representing Core (a and b) and Valence (c and d) contributions to $E1_{PV}^{NSI}$ in the V^{N_e-1} DHF potential of a one-valence atomic system. The operator D is shown with a curly line and H_W is shown in a line with a bullet point.

will relax one degree of freedom in describing atomic states, significantly increasing computational demands. As mentioned earlier in the thesis, the strength of H_{PV}^{NSI} is about one part of 10^{12} in comparison to H . Hence, it is only judicious to include contributions from H as much as possible in determining the aforementioned wave functions with available computational resources and account only for the first-order effect due to H_{PV}^{NSI} . Thus, we express atomic wave function $|\Psi_v\rangle$ of a general state with valence orbital v as

$$|\Psi_v\rangle = |\Psi_v^{(0)}\rangle + |\Psi_v^{(1)}\rangle. \quad (5.3)$$

We have absorbed λ in $|\Psi_v^{(1)}\rangle$. Substituting Eq. 5.3 in Eq. 5.2, we get

$$E1_{PV}^{NSI} \simeq \left[\frac{\langle \Psi_f^{(0)} | D | \Psi_i^{(1)} \rangle}{\mathcal{N}_{if}} + \frac{\langle \Psi_f^{(1)} | D | \Psi_i^{(0)} \rangle}{\mathcal{N}_{if}} \right], \quad (5.4)$$

where normalization factor $\mathcal{N}_{if} = \sqrt{N_f N_i}$ with $N_v = \langle \Psi_v^{(0)} | \Psi_v^{(0)} \rangle$. The contribution from the first term is referred to as the initial perturbed state contribution, whereas the contribution from the second term is referred to as the final perturbed state contribution in the above expression. In order to treat both the em and weak interaction

Hamiltonians on an equal footing and consider correlations between them, solutions of the unperturbed and first-order perturbed wave functions should satisfy

$$H|\Psi_v^{(0)}\rangle = E_v^{(0)}|\Psi_v^{(0)}\rangle \quad (5.5)$$

and

$$(H - E_v^{(0)})|\Psi_v^{(1)}\rangle = (E_v^{(1)} - H_W)|\Psi_v^{(0)}\rangle, \quad (5.6)$$

respectively, where $E_v^{(1)} = 0$ as H_W is odd parity operator. We can express $|\Psi_v^{(0)}\rangle$ and $|\Psi_v^{(1)}\rangle$ using the wave operator formalism

$$\begin{aligned} |\Psi_v^{(0)}\rangle &= \Omega^{v(0)}|\Phi_v\rangle \\ &= (\Omega_c^{(0)} + \Omega_v^{(0)})|\Phi_v\rangle, \end{aligned} \quad (5.7)$$

and

$$\begin{aligned} |\Psi_v^{(1)}\rangle &= \Omega^{v(1)}|\Phi_v\rangle \\ &= (\Omega_c^{(1)} + \Omega_v^{(1)})|\Phi_v\rangle, \end{aligned} \quad (5.8)$$

where $\Omega_c^{(0)}$ and $\Omega_v^{(0)}$ are the zeroth-order waver operator and $\Omega_c^{(1)}$ and $\Omega_v^{(1)}$ are the first-order perturbed wave operators. Substituting the wave operators, Eq. 5.4 can be expressed as

$$\begin{aligned} E1_{PV}^{NSI} &= \frac{\langle\Phi_f|(\Omega_c^{(0)} + \Omega_f^{(0)})^\dagger D(\Omega_c^{(1)} + \Omega_i^{(1)})|\Phi_i\rangle}{\mathcal{N}_{if}} \\ &+ \frac{\langle\Phi_f|(\Omega_c^{(1)} + \Omega_f^{(1)})^\dagger D(\Omega_c^{(1)} + \Omega_i^{(1)})|\Phi_i\rangle}{\mathcal{N}_{if}} \\ &= \frac{\langle\Phi_c|a_f(\Omega_c^{(0)} + \Omega_f^{(0)})^\dagger D(\Omega_c^{(1)} + \Omega_i^{(1)})a_i^\dagger|\Phi_c\rangle}{\mathcal{N}_{if}} \\ &+ \frac{\langle\Phi_c|a_f(\Omega_c^{(1)} + \Omega_f^{(1)})^\dagger D(\Omega_c^{(1)} + \Omega_i^{(1)})a_i^\dagger|\Phi_c\rangle}{\mathcal{N}_{if}} \end{aligned}$$

$$\begin{aligned}
 &= \frac{\langle \Phi_c | a_f [\Omega_c^{(0)\dagger} D \Omega_c^{(1)} + \Omega_c^{(1)\dagger} D \Omega_c^{(0)}] a_i^\dagger | \Phi_c \rangle}{\mathcal{N}_{if}} \\
 &+ \frac{\langle \Phi_c | a_f [\Omega_f^{(0)\dagger} D \Omega_c^{(1)} + \Omega_f^{(1)\dagger} D \Omega_c^{(0)}] a_i^\dagger | \Phi_c \rangle}{\mathcal{N}_{if}} \\
 &+ \frac{\langle \Phi_c | a_f [\Omega_c^{(0)\dagger} D \Omega_i^{(1)} + \Omega_c^{(1)\dagger} D \Omega_i^{(0)}] a_i^\dagger | \Phi_c \rangle}{\mathcal{N}_{if}} \\
 &+ \frac{\langle \Phi_c | a_f [\Omega_f^{(0)\dagger} D \Omega_i^{(1)} + \Omega_f^{(1)\dagger} D \Omega_i^{(0)}] a_i^\dagger | \Phi_c \rangle}{\mathcal{N}_{if}}. \tag{5.9}
 \end{aligned}$$

In the above expression, the contribution from the first term belongs to the ‘‘Core’’ correlation contribution, while the rest is termed as the ‘‘Valence’’ correlation contribution.

5.1.1 Sum-over-states approach

In the sum-over-states approach, the first-order wave function of a general state can be expressed as

$$|\Psi_v^{(1)}\rangle = \sum_{I \neq v} |\Psi_I^{(0)}\rangle \frac{\langle \Psi_I^{(0)} | H_W | \Psi_v^{(0)} \rangle}{(E_v^{(0)} - E_I^{(0)})}, \tag{5.10}$$

where $|\Psi_I^{(0)}\rangle$ are the zeroth-order intermediate states and $E_n^{(0)}$ is the unperturbed energy of the n^{th} level. Thus, Eq. 5.4 can be written as

$$\begin{aligned}
 E1_{PV}^{NSI} &= \sum_{I \neq i} \frac{\langle \Psi_f^{(0)} | D | \Psi_I^{(0)} \rangle \langle \Psi_I^{(0)} | H_W | \Psi_i^{(0)} \rangle}{(E_i^{(0)} - E_I^{(0)})} \\
 &+ \sum_{I \neq f} \frac{\langle \Psi_f^{(0)} | H_W | \Psi_I^{(0)} \rangle \langle \Psi_I^{(0)} | D | \Psi_i^{(0)} \rangle}{(E_f^{(0)} - E_I^{(0)})}. \tag{5.11}
 \end{aligned}$$

Correlations among the H and H_W that appear through Eq. 5.6 are omitted in the above expression. Further, there could be a conflict between the definitions of using Core, Main, and Tail contributions to $E1_{PV}^{NSI}$ with the definitions used in various first-principle based calculations. To understand how Core, Main, and Tail contributions

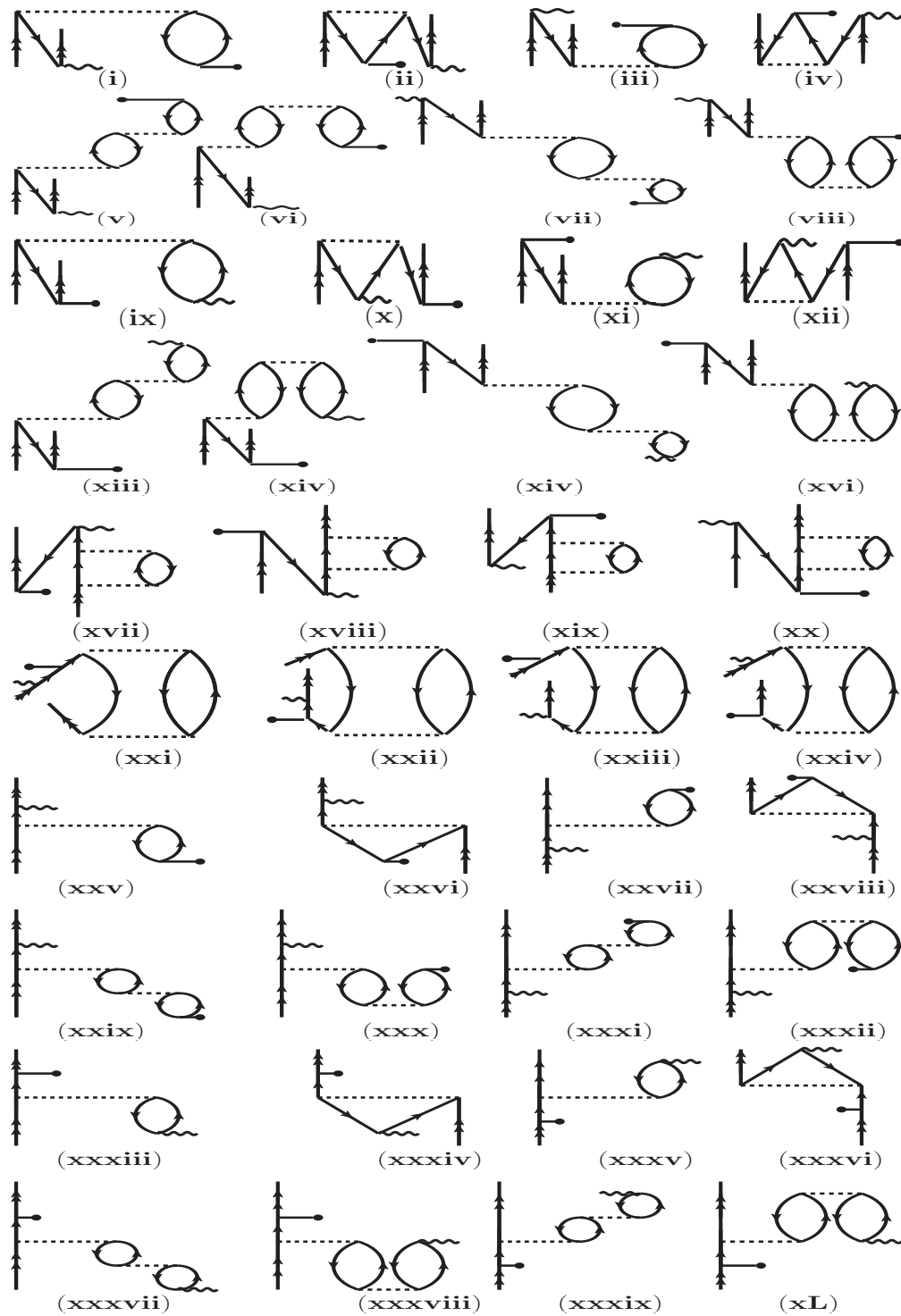


Figure 5.2: A few important electron correlation contributing diagrams to $E1_{PV}^{NSI}$ in the RMBPT(3) method.

have been defined in Ref. [9], we follow the work of Blundell *et al.* [13] where these terms were used for the first time in the context of estimating $E1_{PV}^{NSI}$. Division of the total $E1_{PV}^{NSI}$ value in this calculation was made as ‘‘Main’’, ‘‘Core’’ and ‘‘Tail’’ contributions based on the assumption that $|\Psi_i^{(0)}\rangle$, $|\Psi_f^{(0)}\rangle$ and $|\Psi_I^{(0)}\rangle$ can be expressed using only single Slater determinants like in the DHF method. Thus, the intermediate states $|\Psi_I^{(0)}\rangle$ are considered to have only the $np^2P_{1/2}$ configurations for the $6s^2S_{1/2} - 7s^2S_{1/2}$ transition. In such assumption, the Core (C), Main (V) and Tail (T) contributions to the $E1_{PV}^{NSI}$ amplitude of the above transition in ^{133}Cs were estimated as

$$\begin{aligned}
 E1_{PV}^{NSI}(C) &= \sum_{n \leq 5} \frac{\langle 7S_{1/2} | D | nP_{1/2} \rangle \langle nP_{1/2} | H_W | 6S_{1/2} \rangle}{(E_{6S_{1/2}}^{(0)} - E_{nP_{1/2}}^{(0)})} \\
 &+ \sum_{n \leq 5} \frac{\langle 7S_{1/2} | H_W | nP_{1/2} \rangle \langle nP_{1/2} | D | 6S_{1/2} \rangle}{(E_{7S_{1/2}}^{(0)} - E_{nP_{1/2}}^{(0)})}, \tag{5.12}
 \end{aligned}$$

$$\begin{aligned}
 E1_{PV}^{NSI}(V) &= \sum_{n=6-9} \frac{\langle 7S_{1/2} | D | nP_{1/2} \rangle \langle nP_{1/2} | H_W | 6S_{1/2} \rangle}{(E_{6S_{1/2}}^{(0)} - E_{nP_{1/2}}^{(0)})} \\
 &+ \sum_{n=6-9} \frac{\langle 7S_{1/2} | H_W | nP_{1/2} \rangle \langle nP_{1/2} | D | 6S_{1/2} \rangle}{(E_{7S_{1/2}}^{(0)} - E_{nP_{1/2}}^{(0)})} \tag{5.13}
 \end{aligned}$$

and

$$\begin{aligned}
 E1_{PV}^{NSI}(T) &= \sum_{n \geq 10} \frac{\langle 7S_{1/2} | D | nP_{1/2} \rangle \langle nP_{1/2} | H_W | 6S_{1/2} \rangle}{(E_{6S_{1/2}}^{(0)} - E_{nP_{1/2}}^{(0)})} \\
 &+ \sum_{n \geq 10} \frac{\langle 7S_{1/2} | H_W | nP_{1/2} \rangle \langle nP_{1/2} | D | 6S_{1/2} \rangle}{(E_{7S_{1/2}}^{(0)} - E_{nP_{1/2}}^{(0)})}, \tag{5.14}
 \end{aligned}$$

respectively. However, wave functions of multi-electron atomic systems are determined through a many-body method by expressing as a linear combination of many Slater determinants which can differ by either single or multiple excitations from the reference state. Consequently, contributions from cross-terms involving other Slater determinants, e.g., excited configuration $5p^56s7s$ of the intermediate state, cannot appear through the above breakup. One of such contributions is referred to as DCP effects which arise through the CPDF-RPA (or TDHF) method as described in the works of

Mårtensson [14] and Roberts [11, 15]. There are other contributions also that appear through the first-principle approach of the RCC method [16], which are neither part of BO contributions nor the CPDF-RPA method. These contributions are not negligible and call for an appropriate many-body method to account for their contributions at par with the $np\ ^2P_{1/2}$ intermediate states. This argument can be understood better with the following explanations. In the ^{133}Cs atom, the low-lying excited states have a common core $[5p^6]$ and differ by only a valence orbital. Thus, the DHF wave functions of these states can be expressed as $|\Phi_I\rangle = a_I^\dagger|\Phi_c\rangle$ and the exact wave functions can be defined as

$$\begin{aligned} |\Psi_I^{(0)}\rangle &= \Omega^{I(0)}|\Phi_I\rangle \\ &= (\Omega_c^{(0)} + \Omega_I^{(0)})|\Phi_I\rangle. \end{aligned} \quad (5.15)$$

Using these wave operators, we can express Eq. 5.11 as

$$\begin{aligned} E1_{PV}^{NSI} &= \sum_{I \neq i} \frac{\langle \Phi_c | a_f (\Omega_c^{(0)} + \Omega_f^{(0)})^\dagger D (\Omega_c^{(0)} + \Omega_I^{(0)}) a_I^\dagger | \Phi_c \rangle}{\mathcal{N}_{if}} \\ &\times \frac{\langle \Phi_c | a_I (\Omega_c^{(0)} + \Omega_I^{(0)})^\dagger H_W (\Omega_c^{(0)} + \Omega_i^{(0)}) a_i^\dagger | \Phi_c \rangle}{(E_i^{(0)} - E_I^{(0)})} \\ &+ \sum_{I \neq f} \frac{\langle \Phi_c | a_f (\Omega_c^{(0)} + \Omega_f^{(0)})^\dagger H_W (\Omega_c^{(0)} + \Omega_I^{(0)}) a_I^\dagger | \Phi_c \rangle}{\mathcal{N}_{if}} \\ &\times \frac{\langle \Phi_c | a_I (\Omega_c^{(0)} + \Omega_I^{(0)})^\dagger D (\Omega_c^{(0)} + \Omega_i^{(0)}) a_i^\dagger | \Phi_c \rangle}{(E_f^{(0)} - E_I^{(0)})}. \end{aligned} \quad (5.16)$$

Since the wave operators include linear combinations of configurations describing one-hole–one-particle, two-hole–two-particle, etc. excitations, it is evident that the higher-level excited configurations contributing to the intermediate states cannot be included in a sum-over-states approach.

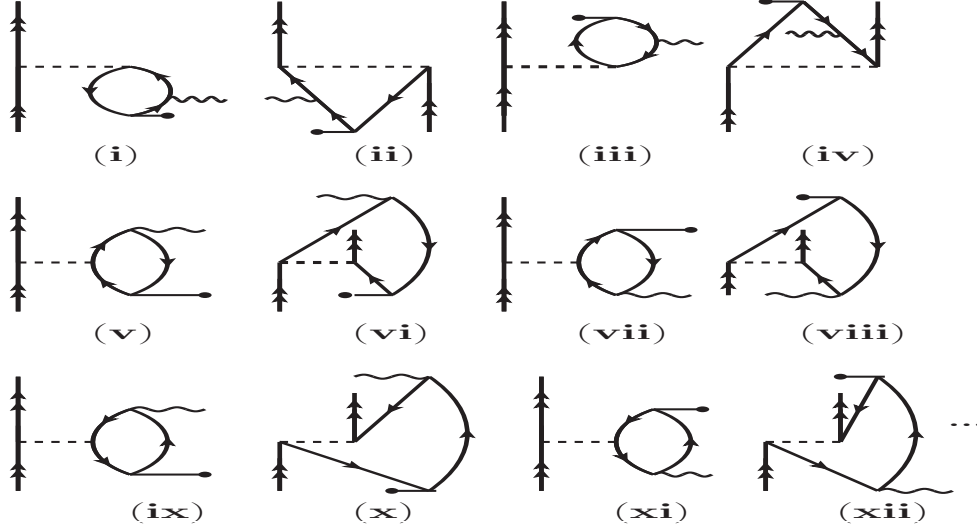


Figure 5.3: A few representative DCP diagrams from the RMBPT(3) method.

5.1.2 First-principle approach

Based on the above discussion, it is clear that in order to estimate the $E1_{PV}^{NSI}$ amplitudes accurately, it is imperative to use first principle approaches that account for contributions from all possible intermediate configurations. One can use either Eq. 5.4 or Eq. 5.9 for this purpose. In the former case, it is desirable to solve both Eqs. 5.5 and 5.6, while for the later approach, one needs to solve Bloch's equations for the unperturbed and perturbed wave operators. The amplitude solving Bloch's equations for the unperturbed operators $\Omega_c^{(0)}$ and $\Omega_v^{(0)}$ have been discussed earlier. The Bloch's equations for the first-order perturbed wave operators can be given by

$$[\Omega_c^{(1)}, H_{DHF}]P_c = (H_W\Omega_c^{(0)} + V_{res}\Omega_c^{(1)})P_c \quad (5.17)$$

and

$$\begin{aligned} [\Omega_v^{(1)}, H_{DHF}]P_v &= [H_W(\Omega_c^{(0)} + \Omega_v^{(0)}) + V_{res}(\Omega_c^{(1)} + \Omega_v^{(1)})P_v \\ &\quad - \Omega_v^{(1)}E_v^{(0)}. \end{aligned} \quad (5.18)$$

Now, we attempt to formulate several all-order methods, namely CPDF, RPA, CPDF-RPA, and RCC, using the wave operators. This would be helpful to make one-to-one connections among these methods, which will be beneficial in explaining the reason why there is a sign mismatch between the Core contributions to $E1_{PV}^{NSI}$ for the $6s\ ^2S_{1/2} - 7s\ ^2S_{1/2}$ transition in the ^{133}Cs atom [9, 10, 12].

We can rewrite Eq. 5.4 as

$$E1_{PV}^{NSI} = \frac{\langle \Psi_f^{(0)} | H_W | \tilde{\Psi}_i^{(1)} \rangle}{\mathcal{N}_{if}} + \frac{\langle \tilde{\Psi}_f^{(1)} | H_W | \Psi_i^{(0)} \rangle}{\mathcal{N}_{if}}. \quad (5.19)$$

This can be equivalently expressed by either

$$E1_{PV}^{NSI} = \frac{\langle \Psi_f^{(0)} | D | \Psi_i^{(1)} \rangle}{\mathcal{N}_{if}} + \frac{\langle \Psi_f^{(0)} | H_W | \tilde{\Psi}_i^{(1)} \rangle}{\mathcal{N}_{if}} \quad (5.20)$$

or

$$E1_{PV}^{NSI} = \frac{\langle \tilde{\Psi}_f^{(1)} | H_W | \Psi_i^{(0)} \rangle}{\mathcal{N}_{if}} + \frac{\langle \Psi_f^{(1)} | D | \Psi_i^{(0)} \rangle}{\mathcal{N}_{if}}. \quad (5.21)$$

In the above expressions, we define

$$|\tilde{\Psi}_i^{(1)}\rangle = \sum_{I \neq f} |\Psi_I^{(0)}\rangle \frac{\langle \Psi_I^{(0)} | D | \Psi_i^{(0)} \rangle}{(E_i^{(0)} - E_I^{(0)} + \omega)} \quad (5.22)$$

and

$$|\tilde{\Psi}_f^{(1)}\rangle = \sum_{I \neq i} |\Psi_I^{(0)}\rangle \frac{\langle \Psi_I^{(0)} | D | \Psi_f^{(0)} \rangle}{(E_f^{(0)} - E_I^{(0)} - \omega)} \quad (5.23)$$

with $\omega = E_f^{(0)} - E_i^{(0)}$ is the excitation energy between the initial and final states. It implies that Eqs. 5.4, 5.19, 5.20 and 5.21 are mathematically equivalent in an exact many-body method. Thus, any of these expressions can be used in the determination of the $E1_{PV}^{NSI}$ amplitude. We shall demonstrate later that the CPDF, RPA, CPDF-

RPA, and RCC methods use different formulas, as mentioned above. So, it is crucial to understand their relations and classifications of individual correlation contributions through the above methods. Since the level of approximations made to the unperturbed and perturbed wave functions are not same in these methods, it is obvious to guess that results from these methods can be very different unless electron correlation effects in an atomic system are negligibly small. It is also unclear whether classifications of Core and Tail contributions in these methods are uniquely defined or not. To understand the above points, let's find out the Core contributions from Eqs. 5.4 and 5.19 by expressing the perturbed wave function due to the D operator in terms of wave operators as

$$|\tilde{\Psi}_v^{(1)}\rangle = (\tilde{\Omega}_c^{(1)} + \tilde{\Omega}_v^{(1)})|\Phi_v\rangle. \quad (5.24)$$

With this, the Core contributing terms in both H_W and D perturbing approaches are given by

$$E1_{PV}^{NSI}(C) = \frac{\langle\Phi_c|a_f[\Omega_c^{(0)\dagger}D\Omega_c^{(1)} + \Omega_c^{(1)\dagger}D\Omega_c^{(0)}]a_i^\dagger|\Phi_c\rangle}{\mathcal{N}_{if}} \quad (5.25)$$

and

$$E1_{PV}^{NSI}(C) = \frac{\langle\Phi_c|a_f[\tilde{\Omega}_c^{(1)\dagger}H_W\Omega_c^{(0)} + \Omega_c^{(0)\dagger}H_W\tilde{\Omega}_c^{(1)}]a_i^\dagger|\Phi_c\rangle}{\mathcal{N}_{if}}. \quad (5.26)$$

It can be shown that the Core contributions arising through the wave operators $\Omega_c^{(1)}$ and $\tilde{\Omega}_c^{(1)}$ can be different. Similar arguments also hold for the Tail contributions arising through the perturbed valence operators $\Omega_v^{(1)}$ and $\tilde{\Omega}_v^{(1)}$. To get better inside of this argument, we can rewrite the sum-over-states formula given by Eq. 5.16 as

$$\begin{aligned} E1_{PV}^{NSI} &= \sum_{I \neq i} \frac{\langle\Phi_c|a_f\Omega_c^{(0)\dagger}D\Omega_c^{(0)}\Omega_c^{(0)\dagger}H_W\Omega_c^{(0)}a_i^\dagger|\Phi_c\rangle}{\mathcal{N}_{if}(E_f^{(0)} - E_I^{(0)} - \omega)} \\ &+ \sum_{I \neq i} \frac{\langle\Phi_c|a_f\Omega_f^{(0)\dagger}D\Omega_c^{(0)}\Omega_c^{(0)\dagger}H_W\Omega_i^{(0)}a_i^\dagger|\Phi_c\rangle}{\mathcal{N}_{if}(E_f^{(0)} - E_I^{(0)} - \omega)} \end{aligned}$$

$$\begin{aligned}
 & + \sum_{I \neq i} \frac{\langle \Phi_c | a_f \Omega_c^{(0)\dagger} D \Omega_c^{(0)} \Omega_c^{(0)\dagger} H_W \Omega_i^{(0)} a_i^\dagger | \Phi_c \rangle}{\mathcal{N}_{if}(E_f^{(0)} - E_I^{(0)} - \omega)} \\
 & + \sum_{I \neq i} \frac{\langle \Phi_c | a_f \Omega_f^{(0)\dagger} D \Omega_c^{(0)} \Omega_c^{(0)\dagger} H_W \Omega_c^{(0)} a_i^\dagger | \Phi_c \rangle}{\mathcal{N}_{if}(E_f^{(0)} - E_I^{(0)} - \omega)} \\
 & + \sum_{I \neq i} \frac{\langle \Phi_c | a_f \Omega_c^{(0)\dagger} D \Omega_I^{(0)} \Omega_I^{(0)\dagger} H_W \Omega_c^{(0)} a_i^\dagger | \Phi_c \rangle}{\mathcal{N}_{if}(E_f^{(0)} - E_I^{(0)} - \omega)} \\
 & + \sum_{I \neq i} \frac{\langle \Phi_c | a_f \Omega_f^{(0)\dagger} D \Omega_I^{(0)} \Omega_I^{(0)\dagger} H_W \Omega_i^{(0)} a_i^\dagger | \Phi_c \rangle}{\mathcal{N}_{if}(E_f^{(0)} - E_I^{(0)} - \omega)} \\
 & + \sum_{I \neq i} \frac{\langle \Phi_c | a_f \Omega_c^{(0)\dagger} D \Omega_I^{(0)} \Omega_I^{(0)\dagger} H_W \Omega_i^{(0)} a_i^\dagger | \Phi_c \rangle}{\mathcal{N}_{if}(E_f^{(0)} - E_I^{(0)} - \omega)} \\
 & + \sum_{I \neq i} \frac{\langle \Phi_c | a_f \Omega_f^{(0)\dagger} D \Omega_I^{(0)} \Omega_I^{(0)\dagger} H_W \Omega_c^{(0)} a_i^\dagger | \Phi_c \rangle}{\mathcal{N}_{if}(E_f^{(0)} - E_I^{(0)} - \omega)} \\
 & + \sum_{I \neq i} \frac{\langle \Phi_c | a_f \Omega_c^{(0)\dagger} D \Omega_I^{(0)} \Omega_c^{(0)\dagger} H_W \Omega_c^{(0)} a_i^\dagger | \Phi_c \rangle}{\mathcal{N}_{if}(E_f^{(0)} - E_I^{(0)} - \omega)} \\
 & + \sum_{I \neq i} \frac{\langle \Phi_c | a_f \Omega_f^{(0)\dagger} D \Omega_I^{(0)} \Omega_c^{(0)\dagger} H_W \Omega_i^{(0)} a_i^\dagger | \Phi_c \rangle}{\mathcal{N}_{if}(E_f^{(0)} - E_I^{(0)} - \omega)} \\
 & + \sum_{I \neq i} \frac{\langle \Phi_c | a_f \Omega_c^{(0)\dagger} D \Omega_I^{(0)} \Omega_c^{(0)\dagger} H_W \Omega_c^{(0)} a_i^\dagger | \Phi_c \rangle}{\mathcal{N}_{if}(E_f^{(0)} - E_I^{(0)} - \omega)} \\
 & + \sum_{I \neq i} \frac{\langle \Phi_c | a_f \Omega_f^{(0)\dagger} D \Omega_I^{(0)} \Omega_c^{(0)\dagger} H_W \Omega_c^{(0)} a_i^\dagger | \Phi_c \rangle}{\mathcal{N}_{if}(E_f^{(0)} - E_I^{(0)} - \omega)} \\
 & + \sum_{I \neq i} \frac{\langle \Phi_c | a_f \Omega_c^{(0)\dagger} D \Omega_c^{(0)} \Omega_I^{(0)\dagger} H_W \Omega_c^{(0)} a_i^\dagger | \Phi_c \rangle}{\mathcal{N}_{if}(E_f^{(0)} - E_I^{(0)} - \omega)} \\
 & + \sum_{I \neq i} \frac{\langle \Phi_c | a_f \Omega_f^{(0)\dagger} D \Omega_c^{(0)} \Omega_I^{(0)\dagger} H_W \Omega_i^{(0)} a_i^\dagger | \Phi_c \rangle}{\mathcal{N}_{if}(E_f^{(0)} - E_I^{(0)} - \omega)} \\
 & + \sum_{I \neq i} \frac{\langle \Phi_c | a_f \Omega_c^{(0)\dagger} D \Omega_c^{(0)} \Omega_I^{(0)\dagger} H_W \Omega_i^{(0)} a_i^\dagger | \Phi_c \rangle}{\mathcal{N}_{if}(E_f^{(0)} - E_I^{(0)} - \omega)} \\
 & + \sum_{I \neq f} \frac{\langle \Phi_c | a_f \Omega_c^{(0)\dagger} H_W \Omega_c^{(0)} \Omega_c^{(0)\dagger} D \Omega_c^{(0)} a_i^\dagger | \Phi_c \rangle}{\mathcal{N}_{if}(E_i^{(0)} - E_I^{(0)} - \omega)}
 \end{aligned}$$

$$\begin{aligned}
 & + \sum_{I \neq f} \frac{\langle \Phi_c | a_f \Omega_f^{(0)\dagger} H_W \Omega_c^{(0)} \Omega_c^{(0)\dagger} D \Omega_i^{(0)} a_i^\dagger | \Phi_c \rangle}{\mathcal{N}_{if}(E_i^{(0)} - E_I^{(0)} - \omega)} \\
 & + \sum_{I \neq f} \frac{\langle \Phi_c | a_f \Omega_c^{(0)\dagger} H_W \Omega_c^{(0)} \Omega_c^{(0)\dagger} D \Omega_i^{(0)} a_i^\dagger | \Phi_c \rangle}{\mathcal{N}_{if}(E_i^{(0)} - E_I^{(0)} - \omega)} \\
 & + \sum_{I \neq f} \frac{\langle \Phi_c | a_f \Omega_f^{(0)\dagger} H_W \Omega_c^{(0)} \Omega_c^{(0)\dagger} D \Omega_c^{(0)} a_i^\dagger | \Phi_c \rangle}{\mathcal{N}_{if}(E_i^{(0)} - E_I^{(0)} - \omega)} \\
 & + \sum_{I \neq f} \frac{\langle \Phi_c | a_f \Omega_c^{(0)\dagger} H_W \Omega_I^{(0)} \Omega_I^{(0)\dagger} D \Omega_c^{(0)} a_i^\dagger | \Phi_c \rangle}{\mathcal{N}_{if}(E_i^{(0)} - E_I^{(0)} - \omega)} \\
 & + \sum_{I \neq f} \frac{\langle \Phi_c | a_f \Omega_f^{(0)\dagger} H_W \Omega_I^{(0)} \Omega_I^{(0)\dagger} D \Omega_i^{(0)} a_i^\dagger | \Phi_c \rangle}{\mathcal{N}_{if}(E_i^{(0)} - E_I^{(0)} - \omega)} \\
 & + \sum_{I \neq f} \frac{\langle \Phi_c | a_f \Omega_c^{(0)\dagger} H_W \Omega_I^{(0)} \Omega_I^{(0)\dagger} D \Omega_i^{(0)} a_i^\dagger | \Phi_c \rangle}{\mathcal{N}_{if}(E_i^{(0)} - E_I^{(0)} - \omega)} \\
 & + \sum_{I \neq f} \frac{\langle \Phi_c | a_f \Omega_c^{(0)\dagger} H_W \Omega_I^{(0)} \Omega_c^{(0)\dagger} D \Omega_c^{(0)} a_i^\dagger | \Phi_c \rangle}{\mathcal{N}_{if}(E_i^{(0)} - E_I^{(0)} - \omega)} \\
 & + \sum_{I \neq f} \frac{\langle \Phi_c | a_f \Omega_f^{(0)\dagger} H_W \Omega_I^{(0)} \Omega_c^{(0)\dagger} D \Omega_i^{(0)} a_i^\dagger | \Phi_c \rangle}{\mathcal{N}_{if}(E_i^{(0)} - E_I^{(0)} - \omega)} \\
 & + \sum_{I \neq f} \frac{\langle \Phi_c | a_f \Omega_c^{(0)\dagger} H_W \Omega_I^{(0)} \Omega_c^{(0)\dagger} D \Omega_i^{(0)} a_i^\dagger | \Phi_c \rangle}{\mathcal{N}_{if}(E_i^{(0)} - E_I^{(0)} - \omega)} \\
 & + \sum_{I \neq f} \frac{\langle \Phi_c | a_f \Omega_f^{(0)\dagger} H_W \Omega_c^{(0)} \Omega_c^{(0)\dagger} D \Omega_c^{(0)} a_i^\dagger | \Phi_c \rangle}{\mathcal{N}_{if}(E_i^{(0)} - E_I^{(0)} - \omega)} \\
 & + \sum_{I \neq f} \frac{\langle \Phi_c | a_f \Omega_f^{(0)\dagger} H_W \Omega_c^{(0)} \Omega_I^{(0)\dagger} D \Omega_i^{(0)} a_i^\dagger | \Phi_c \rangle}{\mathcal{N}_{if}(E_i^{(0)} - E_I^{(0)} - \omega)} \\
 & + \sum_{I \neq f} \frac{\langle \Phi_c | a_f \Omega_c^{(0)\dagger} H_W \Omega_c^{(0)} \Omega_I^{(0)\dagger} D \Omega_c^{(0)} a_i^\dagger | \Phi_c \rangle}{\mathcal{N}_{if}(E_i^{(0)} - E_I^{(0)} - \omega)} \\
 & + \sum_{I \neq f} \frac{\langle \Phi_c | a_f \Omega_f^{(0)\dagger} H_W \Omega_c^{(0)} \Omega_I^{(0)\dagger} D \Omega_i^{(0)} a_i^\dagger | \Phi_c \rangle}{\mathcal{N}_{if}(E_i^{(0)} - E_I^{(0)} - \omega)} \\
 & + \sum_{I \neq f} \frac{\langle \Phi_c | a_f \Omega_c^{(0)\dagger} H_W c^{(0)} \Omega_I^{(0)\dagger} D \Omega_c^{(0)} a_i^\dagger | \Phi_c \rangle}{\mathcal{N}_{if}(E_i^{(0)} - E_I^{(0)} - \omega)}
 \end{aligned} \tag{5.27}$$

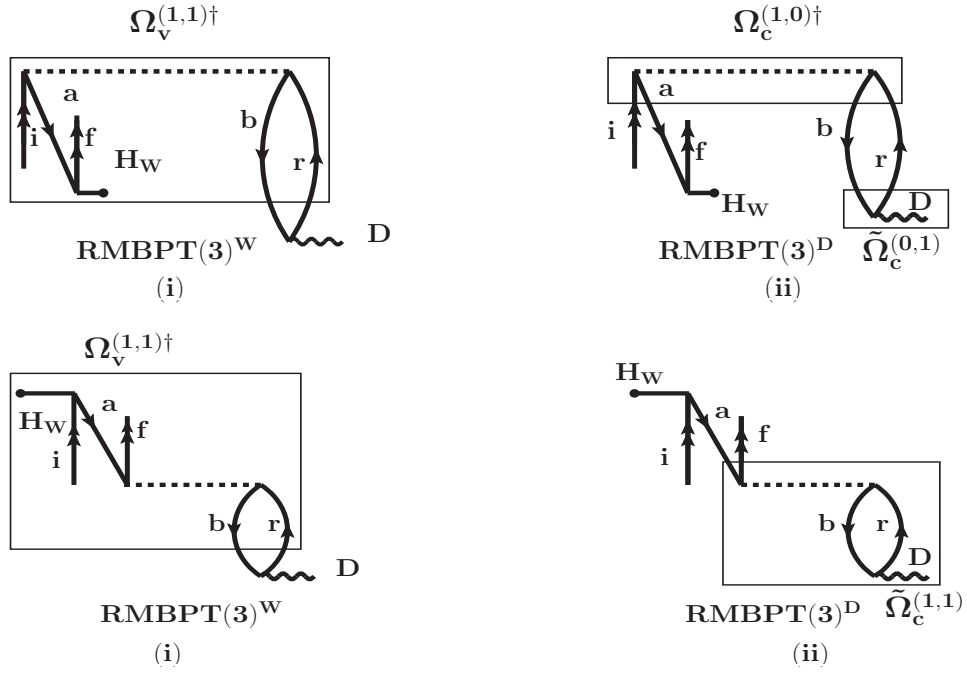


Figure 5.4: A few typical Goldstone diagrams of the RMBPT(3) method. It demonstrates how Valence contributions through $\Omega_v^{(1,1)\dagger} D$ in the RMBPT(3)^W method correspond to Core contributions through (a) $\Omega_c^{(1,0)\dagger} H_W \tilde{\Omega}_c^{(0,1)}$ and (b) $H_W \tilde{\Omega}_c^{(1,1)}$ in the RMBPT(3)^D method.

Both Eqs. 5.16 and 5.27 are equal, but they are written differently. These equations are nothing but the expanded forms of Eqs. 5.9 and 5.19 respectively. However, different terms are rearranged to place them under the categories of Core and Valence contributing terms in the respective formulas. Thus, we may now outline findings from the above discussions as follows

1. It is noteworthy that in the evaluation of $E1_{PV}^{NSI}$, both the H_W and D operators can be treated as perturbation. Thus, in an approximated method where correlation effects through both these operators are not incorporated equivalently, distinctions of “Core” and “Valence” contributions to $E1_{PV}^{NSI}$ cannot be defined uniquely. As a consequence, estimating both the “Core” and “Valence” contributions using a blend of many-body methods could mislead the final result.
2. Numerical stability to the calculation of $E1_{PV}^{NSI}$ can be verified by evaluating

expressions given by Eqs. 5.4, 5.19 and 5.20 simultaneously though it can be a strenuous procedure.

3. Scaling wave functions for estimating a part of contribution or using the experimental value of ω in an approximated method may not always imply that the result is improved. Rather, it could introduce further errors or numerical instability to the calculation.

The last point mentioned above can be understood through the following discussion. Let's use the experimental value for ω (shown as ω^{ex}) to define the first-order perturbed wave functions due to the D operator

$$|\tilde{\Psi}_i^{(1)}\rangle = \sum_{I \neq f} |\Psi_I^{(0)}\rangle \frac{\langle \Psi_I^{(0)} | D | \Psi_i^{(0)} \rangle}{(E_i^{(0)} - E_I^{(0)} + \omega^{ex})} \quad (5.28)$$

and

$$|\tilde{\Psi}_f^{(1)}\rangle = \sum_{I \neq i} |\Psi_I^{(0)}\rangle \frac{\langle \Psi_I^{(0)} | D | \Psi_f^{(0)} \rangle}{(E_f^{(0)} - E_I^{(0)} - \omega^{ex})}. \quad (5.29)$$

Substituting these wave functions in Eq. 5.11, the sum-over-states expression for $E1_{PV}^{NSI}$ can be given by

$$\begin{aligned} E1_{PV}^{NSI} &= \sum_{I \neq i} \frac{\langle \Psi_f^{(0)} | D | \Psi_I^{(0)} \rangle \langle \Psi_I^{(0)} | H_W | \Psi_i^{(0)} \rangle}{\mathcal{N}_{if}(E_i^{(0)} - E_I^{(0)} - \delta\omega)} \\ &+ \sum_{I \neq f} \frac{\langle \Psi_f^{(0)} | H_W | \Psi_I^{(0)} \rangle \langle \Psi_I^{(0)} | D | \Psi_i^{(0)} \rangle}{\mathcal{N}_{if}(E_f^{(0)} - E_I^{(0)} + \delta\omega)}, \end{aligned} \quad (5.30)$$

where $\delta\omega = \omega^{ex} - \omega$, with ω being the theoretical value, cannot be zero when ω is obtained using a particular many-body method. As can be seen, the introduction of ω^{ex} value affects contributions from the initial and final perturbed terms differently, leading to inconsistency in the evaluation of $E1_{PV}^{NSI}$. This can be better expressed

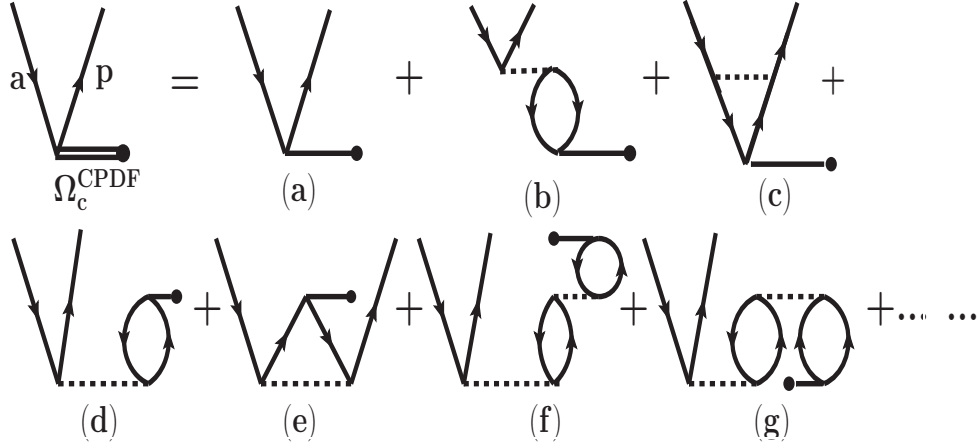


Figure 5.5: Goldstone diagrams contributing to amplitude determining equation of Ω_c^{CPDF} . Through an iterative scheme, these effects are included to all-orders.

through the following inequalities in an approximated many-body method

$$\begin{aligned}
 E1_{PV}^{NSI} &= \frac{\langle \Psi_f^{(0)} | D | \Psi_i^{(1)} \rangle}{\mathcal{N}_{if}} + \frac{\langle \Psi_f^{(1)} | D | \Psi_i^{(0)} \rangle}{\mathcal{N}_{if}} \\
 &\neq \frac{\langle \Psi_f^{(0)} | H_W | \tilde{\Psi}_i^{(1)} \rangle}{\mathcal{N}_{if}} + \frac{\langle \tilde{\Psi}_f^{(1)} | H_W | \Psi_i^{(0)} \rangle}{\mathcal{N}_{if}} \\
 &\neq \frac{\langle \Psi_f^{(0)} | D | \Psi_i^{(1)} \rangle}{\mathcal{N}_{if}} + \frac{\langle \Psi_f^{(0)} | H_W | \tilde{\Psi}_i^{(1)} \rangle}{\mathcal{N}_{if}} \\
 &\neq \frac{\langle \tilde{\Psi}_f^{(1)} | H_W | \Psi_i^{(0)} \rangle}{\mathcal{N}_{if}} + \frac{\langle \Psi_f^{(1)} | D | \Psi_i^{(0)} \rangle}{\mathcal{N}_{if}}.
 \end{aligned} \tag{5.31}$$

5.2 Many-body methods of $E1_{PV}^{NSI}$

The primary objective of the NSI PV study is to estimate the $E1_{PV}^{NSI}$ amplitude with sub-one percent accuracy from the standpoint of atomic many-body theory. Due to the complexities involved in considering various contributions, the calculation typically proceeds in multiple stages. The predominant contribution from H stems from electron correlation effects due to Coulomb interactions in the presence of PV interactions, while corrections from the Breit and QED interactions are treated separately. The corrections because of Breit and QED interactions on $E1_{PV}^{NSI}$ are minor; their estimated corrections

are generally consistent across different studies [3, 5, 8, 16, 17, 18, 19, 20]. Thus, our focus here is primarily on discussions involving the DC Hamiltonian for determining wave functions. Furthermore, our aim is to illustrate how various many-body methods incorporate the electron correlation effect into the calculation. This will help us to identify contributions that may arise from a specific many-body method but could be overlooked by another method. This exercise will pave the path to achieve highly accurate calculations of the $E1_{PV}^{NSI}$ amplitudes in ^{133}Cs by understanding the roles of Core and Valence correlations in these quantities. Starting with the DHF method, we discuss the calculations of $E1_{PV}^{NSI}$ amplitudes in ^{133}Cs using the various many-body methods, namely RMBPT, CPDF, RPA, CPDF-RPA, and RCC.

5.2.1 DHF method

Using wave functions from the DHF method, we can evaluate the $E1_{PV}^{NSI}$ amplitude in the mean-field approach as

$$E1_{PV}^{NSI} = \langle \Phi_f | D | \Phi_i^{(1)} \rangle + \langle \Phi_f^{(1)} | D | \Phi_i \rangle, \quad (5.32)$$

where $|\Phi_{n=i,f}^{(1)}\rangle$ is the first-order perturbed wave function with respect to $|\Phi_{n=i,f}\rangle$. We can express these wave functions as

$$|\Phi_n^{(1)}\rangle = \sum_I |\Phi_I\rangle \frac{\langle \Phi_I | H_W | \Phi_n \rangle}{\mathcal{E}_n - \mathcal{E}_I}, \quad (5.33)$$

where $|\Phi_I\rangle$ are the intermediate states with mean-field energies \mathcal{E}_I . Substituting this expression above, it yields

$$\begin{aligned} E1_{PV}^{NSI} &= \sum_{I \neq i} \frac{\langle \Phi_f | D | \Phi_I \rangle \langle \Phi_I | H_W | \Phi_i \rangle}{\mathcal{E}_i - \mathcal{E}_I} \\ &+ \sum_{I \neq f} \frac{\langle \Phi_f | H_W | \Phi_I \rangle \langle \Phi_I | D | \Phi_i \rangle}{\mathcal{E}_f - \mathcal{E}_I}. \end{aligned} \quad (5.34)$$

Using $H_W = \sum_i h_w(r_i)$ and $D = \sum_i d(r_i)$, and following the Slater-Condon rules, it gives

$$\begin{aligned}
 E1_{PV}^{NSI} &= \sum_a \frac{\langle f|d|a\rangle\langle a|h_w|i\rangle}{\epsilon_i - \epsilon_a} + \sum_a \frac{\langle f|h_w|a\rangle\langle a|d|i\rangle}{\epsilon_f - \epsilon_a} \\
 &+ \sum_{p \neq i} \frac{\langle f|d|p\rangle\langle p|h_w|i\rangle}{\epsilon_i - \epsilon_p} + \sum_{p \neq f} \frac{\langle f|h_w|p\rangle\langle p|d|i\rangle}{\epsilon_f - \epsilon_p}, \tag{5.35}
 \end{aligned}$$

where $|k = a, p\rangle$ denotes k^{th} single particle DHF orbital with energy ϵ_k . Contributions arising from the first two terms of the above expression are referred to as the lowest-order Core contributions while contributions from the later two terms are said to be Valence contributions that include the lowest-orders to both Main and Tail parts. In terms of wave operators, the DHF expression for $E1_{PV}^{NSI}$ can be given by

$$E1_{PV}^{NSI} = \langle \Phi_f | D \Omega^{i(0,1)} | \Phi_i \rangle + \langle \Phi_f | \Omega^{f(0,1)\dagger} D | \Phi_i \rangle \tag{5.36}$$

where $\Omega^{v(0,1)} = \Omega_c^{(0,1)} + \Omega_v^{(0,1)}$ and $\Omega_c^{(0,1)} \rightarrow \Omega_{1c}^{(0,1)} = \sum_{a,p} \frac{\langle p|h_w|a\rangle}{\epsilon_a - \epsilon_p} a_p^\dagger a_a \equiv \sum_{a,p} \Omega_a^p$ and $\Omega_v^{(0,1)} \rightarrow \Omega_{1v}^{(0,1)} = \sum_p \frac{\langle p|h_w|v\rangle}{\epsilon_v - \epsilon_p} a_p^\dagger a_v \equiv \sum_p \Omega_v^p$. Representing the wave operators in terms of the Goldstone diagrams, we show the Core and Valence contributions to $E1_{PV}^{NSI}$ in Fig. 5.1. Figs. 5.1 (a) and (b) correspond to Core contributing terms, while Figs. 5.1 (c) and (d) correspond to Valence contributing terms here.

5.2.2 RMBPT method

We employ the RMBPT method to estimate contributions only up to the third-order of perturbation (RMBPT(3) method) by considering two orders of V_{res} and one order of H_W ; i.e., the net Hamiltonian is expressed as

$$H_{at} = H_{DHF} + \lambda_1 V_{res} + \lambda_2 H_W, \tag{5.37}$$

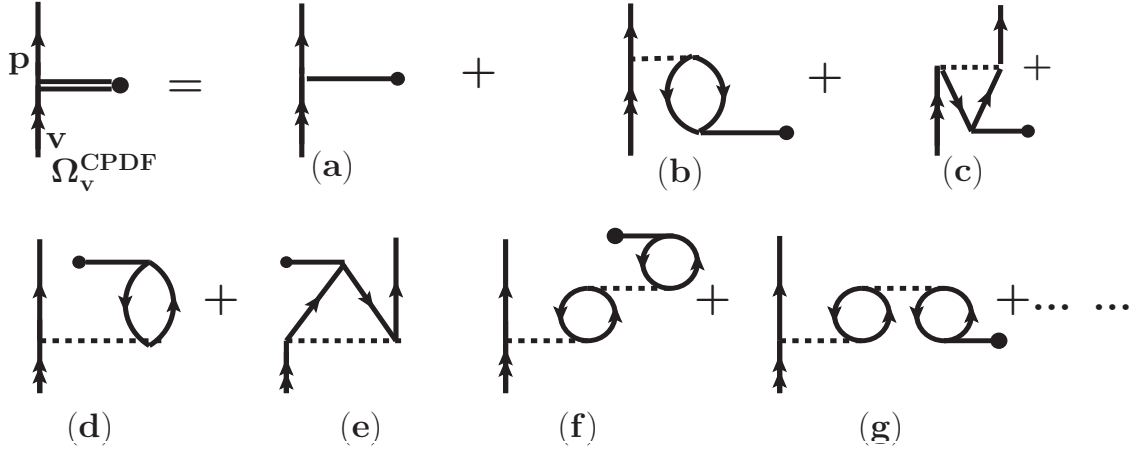


Figure 5.6: Diagrams denoting amplitude solving equation for Ω_v^{CPDF} . These core-polarization effects are included to all-orders in the CPDF method.

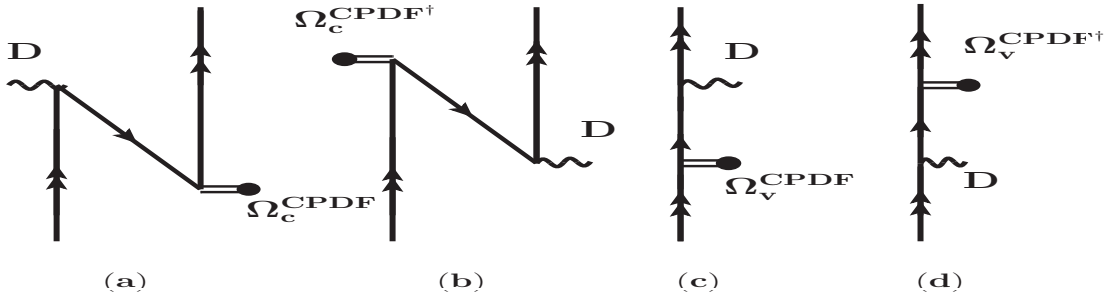


Figure 5.7: Property diagrams of the CPDF method. These diagrams are similar to the DHF method, but the H_W operators of the DHF diagrams are replaced by Ω_c^{CPDF} and Ω_v^{CPDF} .

where λ_1 and λ_2 are parameters introduced to count orders of V_{res} and H_W in the calculation. Here, we can calculate either the matrix element of D after perturbing wave functions by H_W or the matrix element of H_W after perturbing wave functions by D . We employ both approaches for two main reasons. Firstly, it helps in identifying lower-order contribution terms to the CPDF and RPA methods, facilitating a clearer understanding of their inclusion through the RCC method. Secondly, it offers insight into the classification of Core and Valence contributions. Amplitudes of the perturbed wave operators due to H_W can be evaluated by

$$[\Omega_c^{(k,1)}, H_{DHF}]P_c = Q_c H_W \Omega_c^{(k,0)} P_c + Q_c V_{res} \Omega_c^{(k-1,1)} P_c, \quad (5.38)$$

and

$$\begin{aligned}
 [\Omega_v^{(k,1)}, H_{DHF}]P_v &= Q_v V_{res}(\Omega_c^{(k-1,1)} + \Omega_v^{(k-1,1)})P_v \\
 &+ Q_v H_W(\Omega_c^{(k,0)} + \Omega_v^{(k,0)})P_v \\
 &- \sum_{m=1}^{k-1} \Omega_v^{(k-m,1)} E_v^{(m,0)}. \tag{5.39}
 \end{aligned}$$

For the case of considering D as the perturbing operator, Eqs. 5.38 and 5.39 can be again used to solve amplitudes of the $\tilde{\Omega}_c^{(1)}$, $\tilde{\Omega}_i^{(1)}$ and $\tilde{\Omega}_f^{(1)}$ operators in the RMBPT methods by replacing $\Omega_{a/v}^p$ by $\Omega_{a/v}^{p+} = \frac{\langle p|d|a\rangle}{\epsilon_{a/v} - \epsilon_p - \omega} a_p^\dagger a_{a/v}$ and $\Omega_{a/v}^{p\dagger}$ by complex conjugate of $\Omega_{a/v}^{p-} = \frac{\langle p|d|v\rangle}{\epsilon_{a/v} - \epsilon_p + \omega} a_p^\dagger a_{a/v}$. This follows, the n^{th} -order $E1_{PV}^{NSI}$ expression as

$$\begin{aligned}
 E1_{PV}^{NSI} &= \frac{1}{\sum_{l=0}^{n-1} N_{if}^l} \left[\sum_{k=0}^n \left(\langle \Phi_f | (\Omega_c^{(n-k,0)} + \Omega_f^{(n-k,0)})^\dagger D \right. \right. \\
 &\quad \left. \left. (\Omega_c^{(k,1)} + \Omega_i^{(k,1)}) | \Phi_i \rangle + \sum_{k=0}^n \left(\langle \Phi_f | (\Omega_c^{(k,1)} \right. \right. \right. \\
 &\quad \left. \left. \left. + \Omega_f^{(k,1)})^\dagger D (\Omega_c^{(n-k,0)} + \Omega_i^{(n-k,0)}) | \Phi_i \rangle \right) \right], \tag{5.40}
 \end{aligned}$$

where H_W is considered in the perturbation with $\mathcal{N}_{if}^k = [(\sum_l \langle \Phi_f | (\Omega_c^{(k-l,0)} + \Omega_f^{(k-l,0)})^\dagger (\Omega_c^{(l,0)} + \Omega_f^{(l,0)}) | \Phi_f \rangle) (\sum_m \langle \Phi_i | (\Omega_c^{(k-m,0)} + \Omega_i^{(k-m,0)})^\dagger (\Omega_c^{(m,0)} + \Omega_i^{(m,0)}) | \Phi_i \rangle)]^{1/2}$. In the case of D as perturbation, it yields

$$\begin{aligned}
 E1_{PV}^{NSI} &= \frac{1}{\sum_{l=0}^{n-1} N_{if}^l} \left[\sum_{k=0}^n \left(\langle \Phi_f | (\Omega_c^{(n-k,0)} + \Omega_f^{(n-k,0)})^\dagger H_W \right. \right. \\
 &\quad \left. \left. (\tilde{\Omega}_c^{(k,1)} + \tilde{\Omega}_i^{(k,1)}) | \Phi_i \rangle + \sum_{k=0}^n \left(\langle \Phi_f | (\tilde{\Omega}_c^{(k,1)} \right. \right. \right. \\
 &\quad \left. \left. \left. + \tilde{\Omega}_f^{(k,1)})^\dagger H_W (\Omega_c^{(n-k,0)} + \Omega_i^{(n-k,0)}) | \Phi_i \rangle \right) \right]. \tag{5.41}
 \end{aligned}$$

In Fig. 5.2, we show the important correlation contributing Goldstone diagrams to $E1_{PV}^{NSI}$ arising through the RMBPT(3) method. It should be noted that the lowest-order diagrams of the RMBPT(3) method are the same as the diagrams corresponding

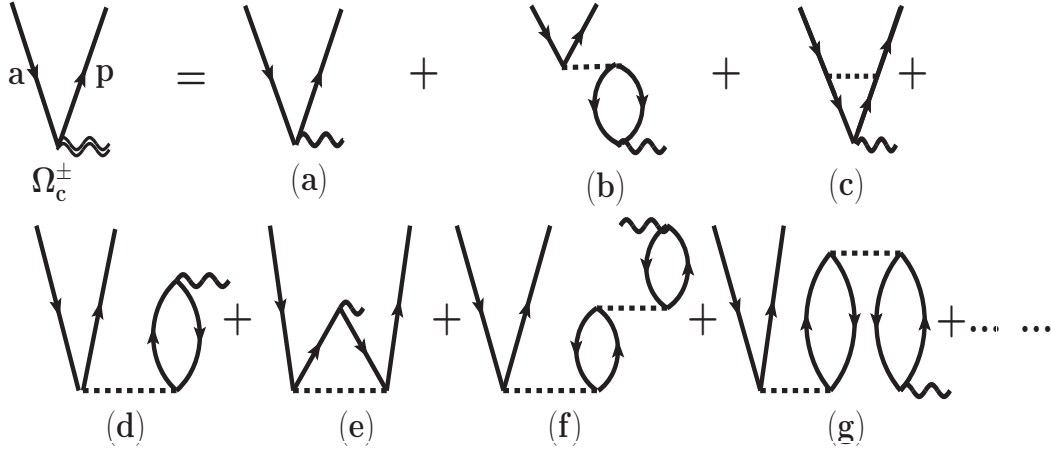


Figure 5.8: Graphical representation of Ω_c^\pm and its expansion in terms of lower-order perturbative method.

to the DHF method, and they are not shown here. In Fig. 5.3, we show a few DCP diagrams that arise in the RMBPT method. Since both Eqs. 5.40 and 5.41 are equivalent at a given level of approximation; the Goldstone diagrams are identical in both cases. Thus, the Core and Valence contributions arising through both expressions can be distinguished and quoted separately by adopting the definitions of the respective wave operators. This would help us identify lower-order Core and Valence correlation contributions to the CPDF, RPA, CPDF-RPA, and RCC methods that will be discussed next. In order to distinguish results while presenting from both the approaches, we use the notations $\text{RMBPT}(3)^W$ and $\text{RMBPT}(3)^D$ in place of $\text{RMBPT}(3)$ for the cases with H_W as the perturbation and with D as the perturbation respectively. We consider a few Goldstone diagrams in Fig. 5.4 that represent Valence (Main and Tail) contributions in the $\text{RMBPT}(3)^W$ method to demonstrate how they turn to Core contributing diagrams in the $\text{RMBPT}(3)^D$ method.

5.2.3 CPDF method

We now extend the $E1_{PV}^{NSI}$ calculation to all-orders in a very simple manner by extending the DHF expression and with much less computational effort compared to the $\text{RMBPT}(3)$ method. This can be derived by starting with the DHF expression, given

by

$$E1_{PV}^{NSI} = \langle f|d|i^{(1)}\rangle + \langle f^{(1)}|d|i\rangle, \quad (5.42)$$

where

$$|k^{(1)}\rangle = \sum_{I \neq k} |I\rangle \frac{\langle I|h_w|k\rangle}{\epsilon_k - \epsilon_I}. \quad (5.43)$$

In the CPDF method, the first-order perturbed single particle orbital $|k^{(1)}\rangle$ is obtained by including CP effects due to V_{res} to all-orders (denoted by $|k^{PV}\rangle$) by defining an effective potential in the presence of h_w . To arrive at this expression, we consider the net Hamiltonian H_{int} to define the modified single-particle DHF Hamiltonian $f_v^{PV} = f_v + \lambda_2 h_w$ and potential as

$$f_v^{PV}|\tilde{v}\rangle = \tilde{\epsilon}_v|\tilde{v}\rangle \quad (5.44)$$

and

$$\tilde{u}_v = \sum_b^{N_e} \left[\langle \tilde{b}|h_2^{bv}|\tilde{b}\rangle|\tilde{v}\rangle - \langle \tilde{b}|h_2^{bv}|\tilde{v}\rangle|\tilde{b}\rangle \right], \quad (5.45)$$

where the tilde symbol denotes solution for H_{int} in place of H . Now expanding $|\tilde{v}\rangle = |v\rangle + \lambda_2|v^{PV}\rangle + \mathcal{O}(\lambda_2^2)$ from Eq. 5.44 and retaining terms that are linear in λ_2 , we can get

$$(f_v - \epsilon_v)|v^{PV}\rangle = -h_w|v\rangle - u_v^{PV}|v\rangle, \quad (5.46)$$

where

$$u_v^{PV}|v\rangle = \sum_b^{N_e} \left[\langle b|h_2|b\rangle|v^{PV}\rangle - \langle b|h_2|v^{PV}\rangle|b\rangle \right. \\ \left. + \langle b^{PV}|h_2|b\rangle|v\rangle - \langle b^{PV}|h_2|v\rangle|b\rangle \right]. \quad (5.47)$$

Both Eqs. 5.46 and 5.47 are solved iteratively to obtain the self-consistent solutions to account for CP effects to all-orders. Using the above modified orbitals, $E1_{PV}^{NSI}$ can be evaluated as

$$E1_{PV}^{NSI} = \langle f|d|i^{PV} \rangle + \langle f^{PV}|d|i \rangle. \quad (5.48)$$

To make one-to-one comparison between contributions arising through the CPDF method and lower-order terms of the RMBPT(3) method, we can present the CPDF expression for $E1_{PV}^{NSI}$ using the wave operators as

$$E1_{PV}^{NSI} = \langle \Phi_f | D \Omega^{i,CPDF} | \Phi_i \rangle + \langle \Phi_f | \Omega^{f,CPDF\dagger} D | \Phi_i \rangle, \quad (5.49)$$

where $\Omega^{v,CPDF} = \Omega_c^{CPDF} + \Omega_v^{CPDF} = \sum_{k=1}^{\infty} \left[\sum_{a,p} \Omega_{a,p}^{(k,1)} + \sum_p \Omega_{v,p}^{(k,1)} \right]$. Amplitudes of these operators are given by

$$\begin{aligned} \Omega_{a,p}^{(k,1)} = & \Omega_a^p + \sum_{b,q} \left(\frac{[\langle pb|h_2|aq \rangle - \langle pb|h_2|qa \rangle]}{\epsilon_a - \epsilon_p} \Omega_{b,q}^{(k-1,1)} \right. \\ & \left. + \Omega_{b,q}^{(k-1,1)\dagger} \frac{[\langle pq|h_2|ab \rangle - \langle pq|h_2|ba \rangle]}{\epsilon_a - \epsilon_p} \right) \end{aligned} \quad (5.50)$$

and

$$\begin{aligned} \Omega_{v,p}^{(k,1)} = & \Omega_v^p + \sum_{b,q} \left(\frac{[\langle pb|h_2|vq \rangle - \langle pb|h_2|qv \rangle]}{\epsilon_v - \epsilon_p} \Omega_{b,q}^{(k-1,1)} \right. \\ & \left. + \Omega_{b,q}^{(k-1,1)\dagger} \frac{[\langle pq|h_2|vb \rangle - \langle pq|h_2|bv \rangle]}{\epsilon_v - \epsilon_p} \right), \end{aligned} \quad (5.51)$$

To compute amplitude of the above operators, we set $\Omega_{a,p}^{(0,1)} \approx \Omega_a^p$ and $\Omega_{v,p}^{(0,1)} \approx \Omega_v^p$ in the beginning to initiate the iteration procedure from $k = 1$. As can be followed here, only the effective singly excited configurations are contributing through the $\Omega^{v,CPDF}$ operators. Thus, it completely misses out PC contributions. The Goldstone diagrams that contribute to the amplitudes of Ω_c^{CPDF} are shown in Fig. 5.5. Similarly, the

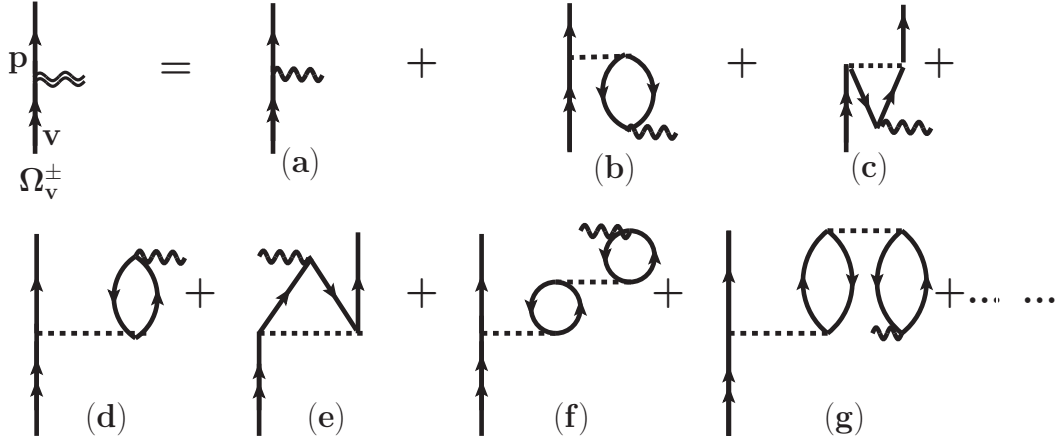


Figure 5.9: Graphical representation of Ω_v^\pm and its expansion in terms of lower-order perturbative method.

Goldstone diagrams contributing to the amplitudes of Ω_v^{CPDF} are shown in Fig. 5.6. Using these operators, we show the final Goldstone diagrams that contribute to $E1_{PV}^{NSI}$ in Fig. 5.7. By analyzing these diagrams in terms of the Goldstone diagrams shown in Figs. 5.5 and 5.6, it is easy to follow how the CP effects are included to all-orders through the CPDF method.

5.2.4 RPA method

The CPDF method captures correlation effects in the first-order wave functions only through the H_W operator but completely misses out on the correlation effects in the unperturbed state that arise through the D operator. The CPDF method is formulated based on Eq. 5.4. Therefore, proceeding with a similar manner based on Eq. 5.19, it can lead to capturing CP effects through the D operator, and the RPA is formulated exactly on the same line. To derive the RPA expression, we consider the net Hamiltonian $H_{int}^\pm = H + \lambda_3 D \mp \omega$ to define the modified single particle DHF Hamiltonian $f_v^\pm = f_v + \lambda_3 d \mp \omega$. Proceeding in similar manner we can get

$$(f_v - \epsilon_v \mp \omega)|v^\pm\rangle = -d|v\rangle - u_i^\pm|v\rangle, \quad (5.52)$$

where

$$u_v^\pm |v\rangle = \sum_b^{N_e} [\langle b|h_2|b\rangle |v^\pm\rangle - \langle b|h_2|v^\pm\rangle |b\rangle + \langle b^\mp|h_2|b\rangle |v\rangle - \langle b^\mp|h_2|v\rangle |b\rangle]. \quad (5.53)$$

Here also both Eqs. 5.52 and 5.53 are solved iteratively to obtain the self-consistent solutions. Using the above D operator modified orbitals, $E1_{PV}^{NSI}$ can be evaluated as

$$E1_{PV}^{NSI} = \langle \Phi_f | H_W \Omega^{i,+} | \Phi_i \rangle + \langle \Phi_f | \Omega^{f,-\dagger} H_W | \Phi_i \rangle, \quad (5.54)$$

where $\Omega^{v,\pm} = \Omega_c^\pm + \Omega_v^\pm = \sum_{k=1}^{\infty} [\sum_{a,p} \Omega_{a,p}^{\pm(k,1)} + \sum_p \Omega_{v,p}^{\pm(k,1)}]$. Amplitudes of these operators are given by

$$\begin{aligned} \Omega_{a,p}^{\pm(k,1)} &= \Omega_a^{p\pm} + \sum_{b,q} \left(\frac{[\langle pb|h_2|aq\rangle - \langle pb|h_2|qa\rangle]}{\epsilon_a - \epsilon_p \pm \omega} \Omega_{b,q}^{\pm(k-1,1)} \right. \\ &\quad \left. + \Omega_{b,q}^{\mp(k-1,1)\dagger} \frac{[\langle pq|h_2|ab\rangle - \langle pq|h_2|ba\rangle]}{\epsilon_a - \epsilon_p \pm \omega} \right) \end{aligned} \quad (5.55)$$

and

$$\begin{aligned} \Omega_{v,p}^{\pm(k,1)} &= \Omega_v^{p\pm} + \sum_{b,q} \left(\frac{[\langle pb|h_2|vq\rangle - \langle pb|h_2|qv\rangle]}{\epsilon_v - \epsilon_p \pm \omega} \Omega_{b,q}^{\pm(k-1,1)} \right. \\ &\quad \left. + \Omega_{b,q}^{\mp(k-1,1)\dagger} \frac{[\langle pq|h_2|vb\rangle - \langle pq|h_2|bv\rangle]}{\epsilon_v - \epsilon_p \pm \omega} \right), \end{aligned} \quad (5.56)$$

where we assume $\Omega_{a,p}^{\pm(0,1)} \approx \Omega_a^{p\pm}$ and $\Omega_{v,p}^{\pm(0,1)} \approx \Omega_v^{p\pm}$ initially for the iteration procedure.

We also intend to mention here is that in Eqs. 5.55 and 5.56, ω value can be used from the experiment while in the *ab initio* framework it is taken from the DHF method. Following the explanation in the previous section, it is obvious that the RPA wave operators will pick up CP correlations through the D operator to all-orders. Again based on the classification adopted in this thesis, the Goldstone diagrams contributing to the amplitude determining equation for Core operator are shown in Fig. 5.8, while

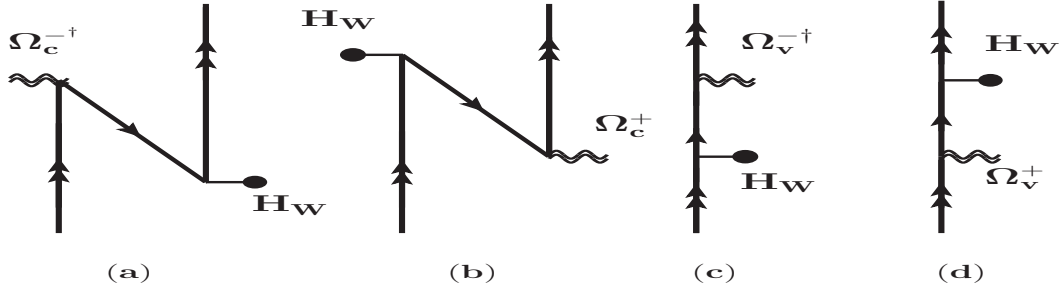


Figure 5.10: Property contributing diagrams of the RPA. These diagrams are similar to the CPDF diagrams, but the core-polarization effects are included through the D operator instead of H_W .

the diagrams contributing to the amplitudes of the Valence operator are shown in Fig. 5.9. Using the above operators, we show the final Goldstone diagrams that contribute to $E1_{PV}^{NSI}$ of RPA in Fig. 5.10. By analyzing these diagrams in terms of the Goldstone diagrams shown in Figs. 5.8 and 5.9, it can be followed how the CP effects are included through D to all-orders through the RPA. Though the number of Goldstone diagrams that appear in the RPA and the CPDF method are same, it can be noticed here that the Core correlations (excluding DHF contributions) arising in the RPA are distinctly different than those that appear via the CPDF method.

5.2.5 CPDF-RPA method

The CPDF method and the RPA include CP effects only through the first-order perturbed wave functions, but the unperturbed wave functions in both cases are used from the DHF method. In order to achieve CP effects through both states, it is necessary to include the H_W and D operators as perturbations. Keeping in view of the above, we define the total Hamiltonian as

$$\begin{aligned}
 H_t &= H + \lambda_2 H_W + \lambda_3 D \\
 &\equiv H_{int} + \lambda_3 D.
 \end{aligned}
 \tag{5.57}$$

Treating both the H_W and D operators perturbatively, the exact atomic wave function ($|\bar{\Psi}_v\rangle$) of H_t can be expressed as

$$\begin{aligned} |\bar{\Psi}_v\rangle &= |\Psi_v^{(0,0)}\rangle + \lambda_2 |\Psi_v^{(1,0)}\rangle + \lambda_3 |\tilde{\Psi}_v^{(0,1)}\rangle \\ &\quad + \lambda_2 \lambda_3 |\Psi_v^{(1,1)}\rangle + \dots \end{aligned} \quad (5.58)$$

$|\Psi_v^{(m,n)}\rangle$ represents consideration of m orders of H_W and n orders of D in the atomic wave function $|\Psi_v\rangle$ of H . In the wave operator formalism, it is given by

$$\begin{aligned} \bar{\Omega}_v |\Phi_v\rangle &= \Omega_v^{(0,0)} |\Phi_v\rangle + \lambda_2 \Omega_v^{(1,0)} |\Phi_v\rangle + \lambda_3 \tilde{\Omega}_v^{(0,1)} |\Phi_v\rangle \\ &\quad + \lambda_2 \lambda_3 \Omega_v^{(1,1)} |\Phi_v\rangle + \dots, \end{aligned} \quad (5.59)$$

where superscripts denote the same meaning as above. In this case, we can determine the $E1_{PV}^{NSI}$ amplitude as the transition amplitude of $O \equiv \lambda_2 H_W + \lambda_3 D$ between the initial perturbed state to the final unperturbed state or between the initial unperturbed state to the final perturbed state (see Eqs. 5.20 and 5.21). i.e.

$$\begin{aligned} E1_{PV}^{NSI} &= \langle \Psi_f^{(0,0)} | \Psi_i^{(1,1)} \rangle + \langle \Psi_f^{(0,0)} | D | \Psi_i^{(1,0)} \rangle \\ &\quad + \langle \Psi_f^{(0,0)} | H_W | \tilde{\Psi}_i^{(0,1)} \rangle \\ &= \langle \Phi_f | \Omega_f^{(0,0)\dagger} \Omega_i^{(1,1)} | \Phi_i \rangle + \langle \Phi_f | \Omega_f^{(0,0)\dagger} D \Omega_i^{(1,0)} | \Phi_i \rangle \\ &\quad + \langle \Phi_f | \Omega_f^{(0,0)\dagger} H_W \tilde{\Omega}_i^{(0,1)} | \Phi_i \rangle \end{aligned} \quad (5.60)$$

or

$$\begin{aligned} E1_{PV}^{NSI} &= \langle \Psi_f^{(1,1)} | \Psi_i^{(0,0)} \rangle + \langle \Psi_f^{(1,0)} | D | \Psi_i^{(0,0)} \rangle \\ &\quad + \langle \tilde{\Psi}_f^{(0,1)} | H_W | \Psi_i^{(0,0)} \rangle \\ &= \langle \Phi_f | \Omega_f^{(1,1)\dagger} \Omega_i^{(0,0)} | \Phi_i \rangle + \langle \Phi_f | \Omega_f^{(1,0)\dagger} D \Omega_i^{(0,0)} | \Phi_i \rangle \\ &\quad + \langle \Phi_f | \tilde{\Omega}_f^{(0,1)\dagger} H_W \Omega_i^{(0,0)} | \Phi_i \rangle, \end{aligned} \quad (5.61)$$

keeping terms that are of the order of $\lambda_2\lambda_3$. Note that in this approach, both H_W and D operators are treated symmetrically. Thus, definitions of both Core and Valence contributions to $E1_{PV}^{NSI}$ will be identical for both Eqs. 5.60 and 5.61. Also, it would be judicious to use both expressions to verify numerical uncertainty in the final result. However, if ω^{ex} (some earlier studies have done it through the scaling procedure) is used, then the results from both these equations may not agree with each other due to inconsistencies in the treatment of the intermediate states through these equations. We start by writing the modified single particle Hamiltonian for the corresponding Hamiltonian $H_t = H_{int} + \lambda_3 D$ in the CPDF-RPA method as $f_v^{PV\pm} = f_v^{PV} + \lambda_3 d \mp \omega$. It follows

$$f_v^{PV\pm}|\bar{v}\rangle = \bar{\epsilon}_v|\bar{v}\rangle \quad (5.62)$$

and

$$\bar{u}_v = \sum_b^{N_e} [\langle \bar{b}|h_2|\bar{b}\rangle|\bar{v}\rangle - \langle \bar{b}|h_2|\bar{v}\rangle|\bar{b}\rangle], \quad (5.63)$$

where the bar symbol denotes solution for H_t . By expanding, we get $|\bar{v}\rangle = |v^{PV}\rangle + \lambda_3|v^{PV\pm}\rangle + \mathcal{O}(\lambda_3^2)$. It gives

$$(f_v^{PV} - \epsilon_v^{PV} \mp \omega)|v^{PV\pm}\rangle = -d|v^{PV}\rangle - u_v^{PV(1)}|v^{PV}\rangle, \quad (5.64)$$

where

$$u_v^{PV(1)}|v^{PV}\rangle = \sum_b^{N_e} [\langle b^{PV}|h_2|b^{PV}\rangle|v^{PV\pm}\rangle - \langle b^{PV}|h_2|v^{PV\pm}\rangle|b^{PV}\rangle + \langle b^{PV}|h_2|b^{PV}\rangle|v^{PV\pm}\rangle - \langle b^{PV}|h_2|v^{PV\pm}\rangle|b^{PV}\rangle]. \quad (5.65)$$

Further expanding Eqs. 5.64 and 5.65, and retaining terms of the order of $\lambda_2\lambda_3$ we get

$$(f_v - \epsilon_v \mp \omega)|v^{PV\pm}\rangle = -d|v^{PV}\rangle - u_v^\pm|v^{PV}\rangle - h_w|v^\pm\rangle$$

$$-u_v^{PV}|v^\pm\rangle - u_v^{PV^\pm}|v\rangle, \quad (5.66)$$

where

$$\begin{aligned} u_v^{PV^\pm}|v\rangle = & \sum_b^{N_e} [\langle b^\mp|h_2|b^{PV}\rangle|v\rangle - \langle b^\mp|h_2|v\rangle|b^{PV}\rangle \\ & + \langle b^{PV}|h_2|b^\pm\rangle|v\rangle - \langle b^{PV}|h_2|v\rangle|b^\pm\rangle \\ & + \langle b|h_2|b^{PV^\pm}\rangle|v\rangle - \langle b|h_2|v\rangle|b^{PV^\pm}\rangle \\ & + \langle b^{PV^\mp}|h_2|b\rangle|v\rangle - \langle b^{PV^\mp}|h_2|v\rangle|b\rangle]. \end{aligned} \quad (5.67)$$

It can be further noted that in the CPDF method, the perturbed core DHF orbital ($|a^{PV}\rangle$) is orthogonal to the unperturbed core orbital ($|a\rangle$), and the same is also true in the RPA. i.e. $\langle a|a^{PV}\rangle = 0$ and $\langle a|a^\pm\rangle = 0$. However, $\langle a|a^{PV^\pm}\rangle \neq 0$ in the CPDF-RPA method [14]. This necessitates to use the orthogonalized core orbitals ($|a^{o^\pm}\rangle$) by imposing the condition

$$|a^{o^\pm}\rangle = |a^{PV^\pm}\rangle - \sum_b |b\rangle\langle b|a^{PV^\pm}\rangle. \quad (5.68)$$

In Fig. 5.11, we show the Goldstone diagrams contributing to the determination of the $|a^{PV^\pm}\rangle$ and also the extra diagrams that are subtracted to obtain $|a^{o^\pm}\rangle$.

Following the general formula given by Eq. 5.60, we can write

$$\begin{aligned} E1_{PV}^{NSI} &= \langle f|d + u_i^+|i^{PV}\rangle + \langle f|h_w + u_i^{PV}|i^+\rangle + \langle f|u_i^{PV^+}|i\rangle \\ &= \langle \Phi_f|D\Omega^{i,CPDF}|\Phi_i\rangle + \langle \Phi_f|H_W\Omega^{i,+}|\Phi_i\rangle \\ &\quad + \langle \Phi_f|\Omega^{CPDF+}|\Phi_i\rangle. \end{aligned} \quad (5.69)$$

Similarly, using the formula given by Eq. 5.61 we can get

$$\begin{aligned} E1_{PV}^{NSI} &= \langle f^{PV}|d + u_i^+|i\rangle + \langle f^-|h_w + u_i^{PV}|i\rangle + \langle f|u_f^{PV^-}|i\rangle \\ &= \langle f^{PV}|d + u_i^+|i\rangle + \langle f^-|h_w + u_i^{PV}|i\rangle + \langle f|u_i^{PV^+}|i\rangle \end{aligned}$$

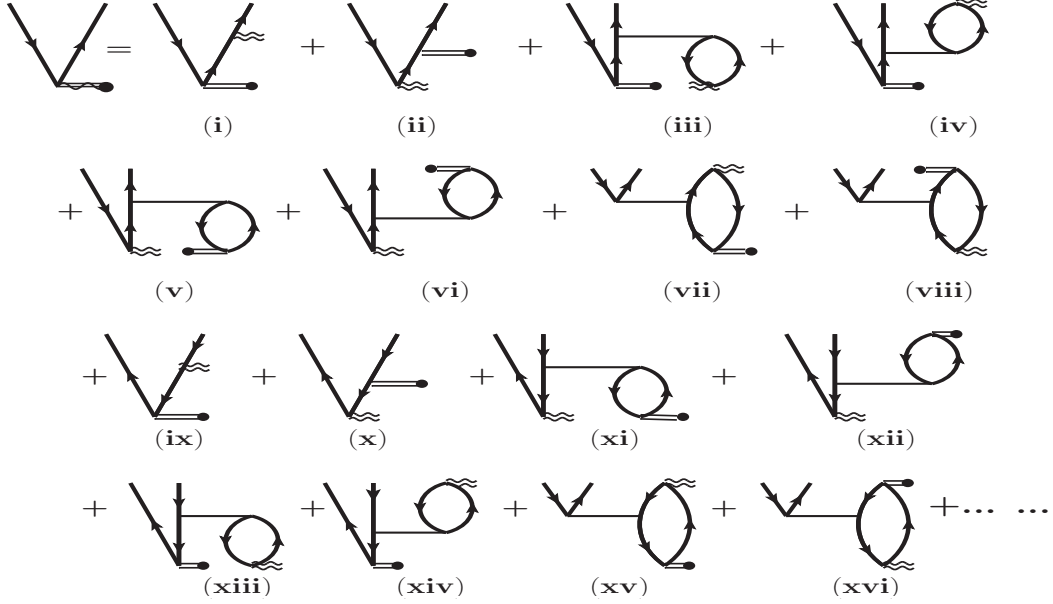


Figure 5.11: Goldstone diagrams representing terms of Eq. (5.66) representing the $u^{PV\pm}$ term that gives rise to DCP contributions in the CPDF-RPA method. Diagrams from (ix) to (xvi) along with their exchanges are coming due to the implementation of the orthogonalization condition.

$$\begin{aligned}
 &= \langle \Phi_f | \Omega^{f,CPDF+} D | \Phi_i \rangle + \langle \Phi_f | \Omega^{f-\dagger} H_W | \Phi_i \rangle \\
 &\quad + \langle \Phi_f | \Omega^{f,CPDF-} | \Phi_i \rangle.
 \end{aligned} \tag{5.70}$$

In the above expressions, we define

$$\begin{aligned}
 \Omega^{CPDF+} &= \sum_{i,j} (\langle f | u_i^+ | i^{PV} \rangle + \langle f | u_i^{PV} | i^+ \rangle \\
 &\quad + \langle f | u_i^{PV+} | i \rangle) a_j^\dagger a_i
 \end{aligned} \tag{5.71}$$

and

$$\begin{aligned}
 \Omega^{CPDF-} &= \sum_{i,j} (\langle f^{PV} | u_f^- | i \rangle + \langle f^- | u_f^{PV} | i \rangle \\
 &\quad + \langle f | u_f^{PV-} | i \rangle) a_j^\dagger a_i.
 \end{aligned} \tag{5.72}$$

It is noteworthy that some literature works omit the contribution from $\langle f | u_i^{PV+} | i \rangle$

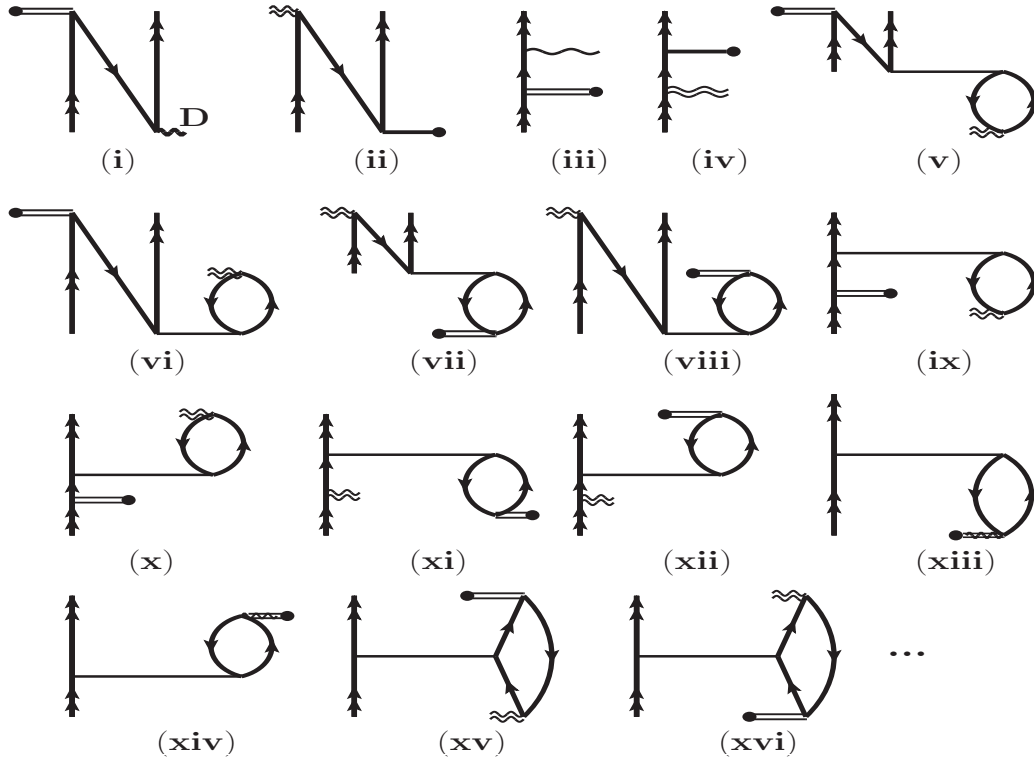


Figure 5.12: Goldstone diagrams contributing to the $E1_{PV}^{NSI}$ amplitude in the CPDF-RPA method.

in the CPDF-RPA method, with their contributions separately labeled as ‘DCP’ effects [10, 11]. In Fig. 5.12, we present the diagrams contributing to $E1_{PV}^{NSI}$ in the CPDF-RPA method, including the DCP effect. The CPDF-RPA method offers several advantages. It captures CP effects to all-orders, treats both the H_W and D operators equally, and includes DCP effects that the CPDF method or RPA misses. However, it overlooks numerous non-CP effects, such as PC contributions and correlations among CP and PC effects, in determining $E1_{PV}^{NSI}$. Additionally, the method manually incorporates the orthogonalization of perturbed occupied orbitals, lacking natural handling of this process. Some earlier calculations using the CPDF-RPA method neglected contributions from the DCP effects (see Ref. [11]). We denote those contributions as the CPDF-RPA*. Although we express the CPDF, RPA, and CPDF-RPA methods using wave operators, they cannot be derived using Bloch’s prescription. We have done this to establish a connection among the many-body methods. Consequently, these methods simply extend

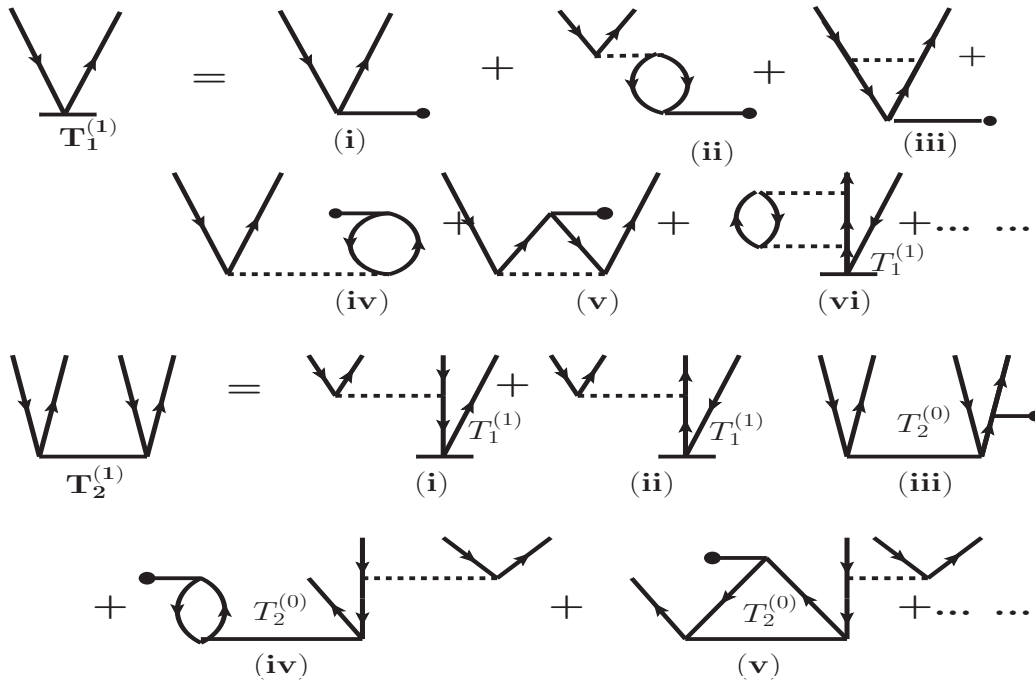


Figure 5.13: Goldstone diagrams showing breakdown of the $T^{(1)}$ operators in terms of lower-order perturbative excitations.

the DHF method and cannot account for effects neglected in generating single-particle orbitals. For example, the effects of V^{N_e} , V^{N_e-1} , V^{N_e-2} potentials used in determining wave functions via the Bloch equation, are managed through an effective Hamiltonian like $H_{eff} = P_v V_{res} \Omega_v^{(0)} P_v$, which appears in solving the amplitude of $\Omega_v^{(0)}$. However, the wave operator amplitude solving equations in the CPDF, RPA, and CPDF-RPA methods remains the same. Thus, the interaction of valence electrons neglected in the construction of the DHF potential (inactive valence orbital) is not rectified through these methods as in the RMBPT method. The RCC method will effectively address all these limitations of the CPDF-RPA method.

5.2.6 RCC method

Compared to the CPDF, RPA, and CPDF-RPA methods, implementation and computational efforts in the RCC method are extensively complex and expensive [21, 22, 23, 24]. But the RCC method not only accounts for correlations through both the H_W and

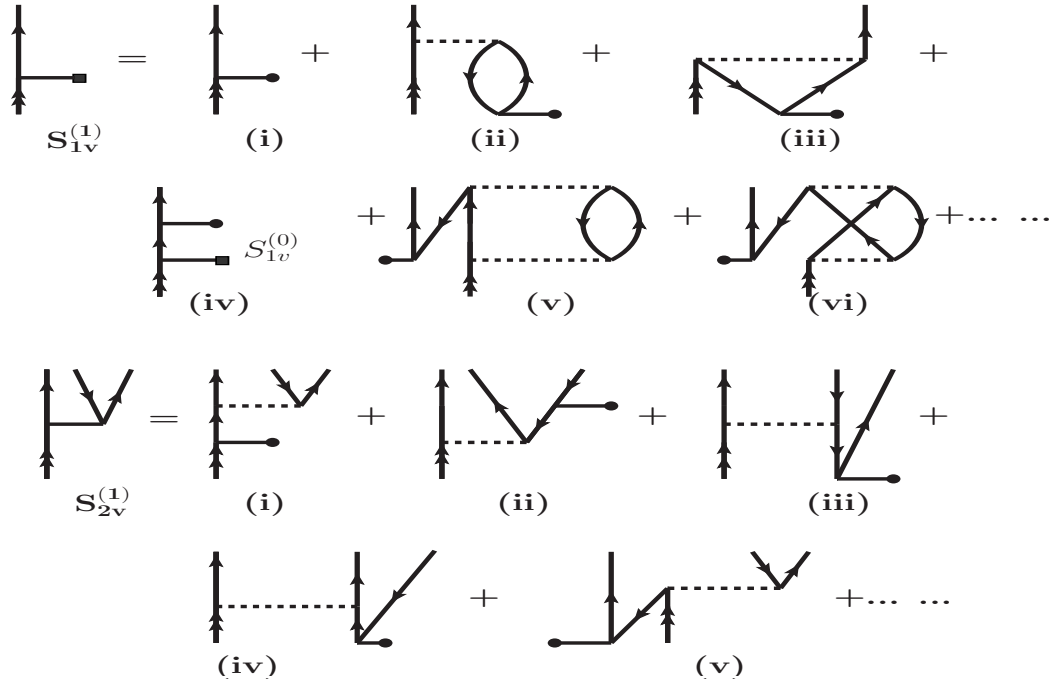


Figure 5.14: Goldstone diagrams showing breakdown of the $S_v^{(1)}$ operators in terms of lower-order perturbative excitations.

D operators to all-orders, but it also takes care of other shortcomings of the CPDF-RPA method. All CPDF-RPA effects, along with other effects like PC, inter-correlations among CP and PC effects, corrections due to choice of V^{N_e-1} DHF potential approximation, etc., are sub-summed within our RCC method. Here, we will consider the RCCSD method to demonstrate how it captures correlations of previously mentioned methods, including the appearance of orthogonalization of perturbed core orbitals in a natural fashion, all-order PC, DCP effects, and normalization of wave functions, etc., compared to a mixed many-body method. Since all these effects are present within the RCC theory and the wave functions are obtained through iterative scheme, all of these effects are inter-correlated. To evaluate $E1_{PV}^{NSI}$, we need to express the RCC operators in terms of both the unperturbed and first-order perturbed operators. We have three different options to obtain the $E1_{PV}^{NSI}$ amplitude in the RCC theory framework. First, by adopting the approach similar to the CPDF method, in which H_W is considered as external perturbation. Second, by treating D as the external perturbative operator as

in the RPA. The third approach would be along the lines of the CPDF-RPA method, in which both the H_W and D operators can be treated as external perturbations. The implementation of the third approach would be more challenging and computationally very expensive as it will demand storing amplitudes of four different types of perturbed RCC operators instead of storing only one type of perturbed amplitudes in the first case and two types in the second case. Among the first two approaches, computational efforts are almost similar, but implementation-wise, considering H_W as perturbation will be more natural and is easier to deal with its angular momentum couplings owing to its scalar form. Moreover, amplitudes of the perturbed operators due to H_W will converge faster than when D is treated as perturbation. Again, if needed, we can use experimental energies in the first approach to get semi-empirical results, which isn't possible in the second approach due to previously discussed reasons. .Therefore, we use the first approach to estimate the $E1_{PV}^{NSI}$ value.

We expand the T and S_v operators by treating H_W as the perturbation to separate out the solutions for the unperturbed and the first-order wave functions by expressing

$$T = T^{(0)} + \lambda_2 T^{(1)} \quad (5.73)$$

and

$$S_v = S_v^{(0)} + \lambda_2 S_v^{(1)}, \quad (5.74)$$

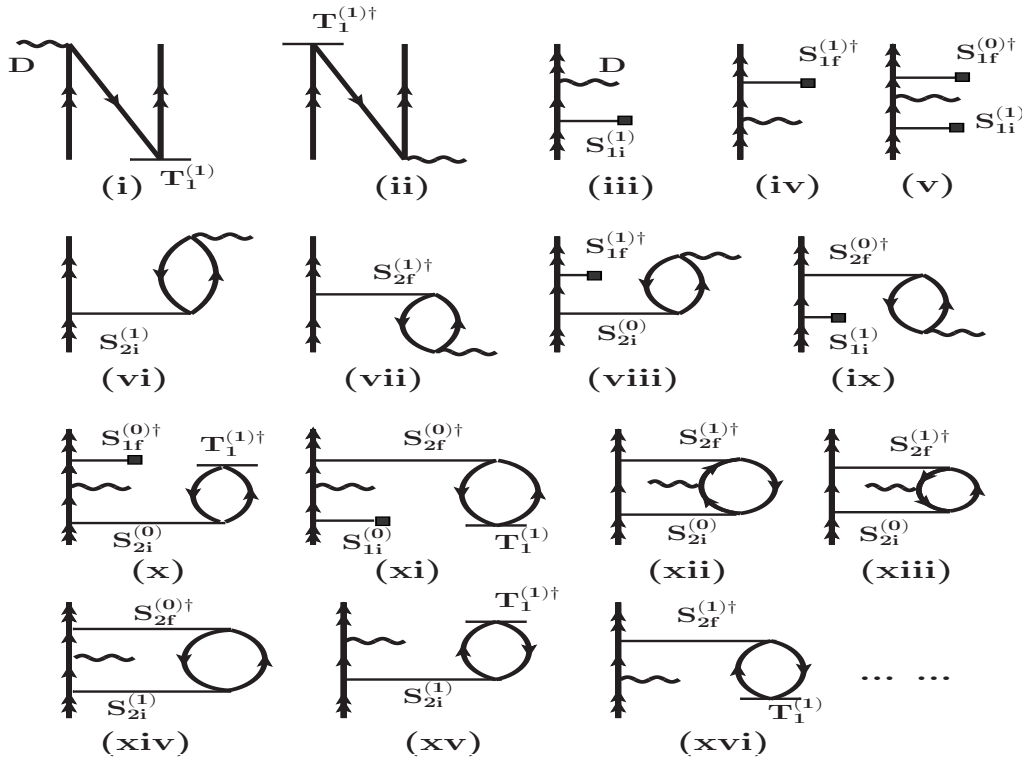
where the superscript meanings are same as specified earlier. This yields

$$|\Psi_v^{(0)}\rangle = (\Omega_c^{(0)} + \Omega_v^{(0)})|\Phi_v\rangle \quad (5.75)$$

and

$$|\Psi_v^{(1)}\rangle = (\Omega_c^{(1)} + \Omega_v^{(1)})|\Phi_v\rangle \quad (5.76)$$

with the definitions $\Omega_c^{(1)} = e^{T^{(0)}}T^{(1)}$ and $\Omega_v^{(1)} = e^{T^{(0)}}\{T^{(1)}S_v^{(0)} + S_v^{(1)}\}$. The unper-


 Figure 5.15: A few important $E1_{PV}^{NSI}$ evaluating diagrams in the RCCSD method.

turbed operator amplitudes are obtained by solving the usual RCC theory equations, as mentioned earlier. The first-order perturbed RCC operator amplitudes are determined as

$$\langle \Phi_c^* | (He^{T^{(0)}})_{conn} T^{(1)} | \Phi_c \rangle = -\langle \Phi_c^* | (H_W e^{T^{(0)}})_{conn} | \Phi_c \rangle \quad (5.77)$$

and

$$\begin{aligned} \langle \Phi_v^* | [(He^{T^{(0)}})_{conn} - E_v^{(0)}] S_v^{(1)} | \Phi_v \rangle = & -\langle \Phi_v^* | [(H_W e^{T^{(0)}})_{conn} \\ & + (He^{T^{(0)}})_{conn} T^{(1)}] \{1 + S_v^{(0)}\} | \Phi_v \rangle \end{aligned} \quad (5.78)$$

As can be seen, the exact calculated energy also enters into the amplitude determining equation of $S_v^{(1)}$ because of the V^{N_e-1} potential. This is one of the advantages of the RCC method over the CPDF-RPA method. In Figs. 5.13 and 5.14 we show some of the

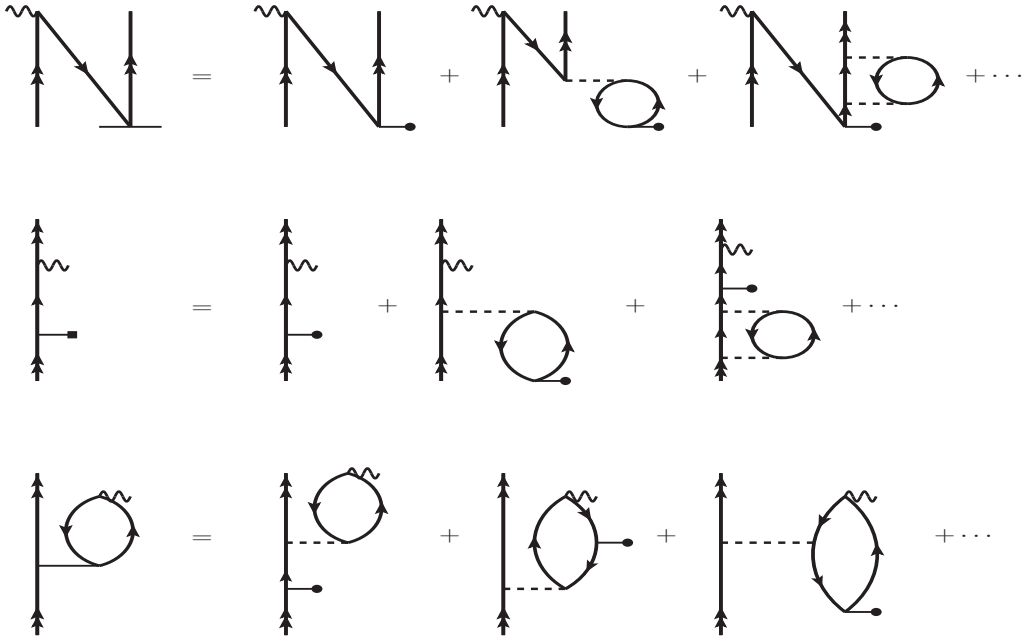


Figure 5.16: Breakdown of few RCCSD property diagrams in terms of lower-order RMBPT diagrams.

important Goldstone diagrams contributing to the $T_1^{(1)}$, $T_2^{(1)}$, $S_{1v}^{(1)}$ and $S_{2v}^{(1)}$ amplitudes. These diagrams can be compared with the CPDF-RPA wave operator amplitude determining diagrams in order to understand how they are embedded within the RCC operators irrespective of the fact that denominators in the RCC method will contain the exact energy of the state instead of the DHF energy in the CPDF-RPA method.

The $E1_{PV}^{NSI}$ expression between the states $|\Psi_i\rangle$ and $|\Psi_f\rangle$ in the RCC theory is given by

$$\begin{aligned}
 E1_{PV}^{NSI} = & \frac{\langle \Phi_f | \{ S_f^{(1)\dagger} + (S_f^{(0)\dagger} + 1) T^{(1)\dagger} \} \bar{D} \{ 1 + S_i^{(0)} \} | \Phi_i \rangle}{\langle \Phi_f | \{ S_f^{(0)\dagger} + 1 \} \bar{N} \{ 1 + S_i^{(0)} \} | \Phi_i \rangle} \\
 & + \frac{\langle \Phi_f | \{ S_f^{(0)\dagger} + 1 \} \bar{D} \{ T^{(1)} (1 + S_i^{(0)}) + S_i^{(1)} \} | \Phi_i \rangle}{\langle \Phi_f | \{ S_f^{(0)\dagger} + 1 \} \bar{N} \{ 1 + S_i^{(0)} \} | \Phi_i \rangle}, \quad (5.79)
 \end{aligned}$$

where $\bar{D} = e^{T^{(0)+}} D e^{T^{(0)}}$ and $\bar{N} = e^{T^{(0)+}} e^{T^{(0)}}$. Unlike the CPDF, RPA and CPDF-RPA methods, normalization factors appear explicitly in the RCC expression. Using the wave operator notations, one can easily identify which RCC terms contribute to the

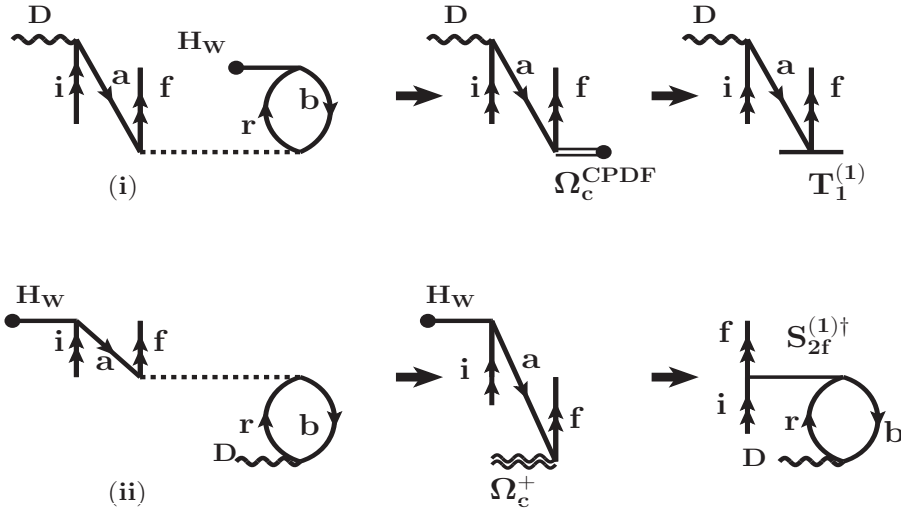


Figure 5.17: Relating Core contributing diagrams from (i) $D\Omega_c^{(1,1)}$ of the RMBPT(3)^W method and (ii) $H_W\tilde{\Omega}_c^{(1,1)}$ of the RMBPT(3)^D method to the Core contributing diagrams in the CPDF-RPA method. The former remains as a Core contributing diagram while the later turns out to be a Valence contributing diagram in the RCCSD method.

Core and Valence correlations in the evaluation of $E1_{PV}^{NSI}$. It means basically, any term is connected either with the $S_{n=i,f}^{(0/1)}$ operators or with their complex conjugate operators will be a part of the Valence correlation; otherwise, they will belong to the Core correlation. It can be further clarified that the definitions of Core and Valence correlation contributions to $E1_{PV}^{NSI}$ in our RCC theory are in line with the RMBPT(3)^W and CPDF methods and different than the RMBPT(3)^D, RPA and CPDF-RPA methods. In Fig. 5.15, we show a few important contributing Goldstone diagrams from the RCC method to Core and Valence correlations. Also, for better understanding, the Goldstone diagrams of the RCCSD method are further demonstrated as the sum of lower-order Goldstone diagrams of the RMBPT(3) method in Fig. 5.16. From these relations, it can be followed that the RCC method includes correlation effects from CP, PC, and DCP to all-orders. It is also obvious from the above diagrams that orthogonalization to core orbitals and extra DCP contributions also appear in a natural manner in our RCC theory.

At this point, we would like to demonstrate how some of the lower-order Core contribut-

ing diagrams of the RMBPT(3) W and RMBPT(3) D methods propagate to CPDF-RPA and RCCSD methods. For this purpose, we consider each representing diagram from the RMBPT(3) W and RMBPT(3) D methods as shown in Fig. 5.17 (i) and (ii), respectively. As can be seen from these figures, a Core contributing diagram from the $D\Omega_c^{(1,1)}$ term of the RMBPT(3) W method propagates as $D\Omega_c^{CPDF}$ in the CPDF-RPA method and as $DT_1^{(1)}$ in the RCCSD method. Since $T_1^{(1)}$ contains both CP and PC effects to all-orders, the Core contributions estimated using the RCCSD method are more rigorous than the CPDF-RPA method. Returning to the Core contributing diagram from the $H_W\tilde{\Omega}_c^{(1,1)}$ term of the RMBPT(3) D method, it becomes a part of the Core contributing term $H_W\Omega_c^+$ of the CPDF-RPA method. However, this is embedded within the $S_{2f}^{(1)\dagger}D$ term of the RCCSD method representing a part of the Valence correlation. This implies that the definitions of Core and Valence contributing terms in the considered CPDF-RPA and RCCSD methods are not unique and depend on how one chooses the perturbation operator.

5.3 Results and Discussions

After establishing a theoretical understanding of various many-body methods, here we discuss the results obtained from these diverse methods. As mentioned in the Introduction, Porsev *et al.* [9] claimed an accuracy of about 0.27% for the $E1_{PV}^{NSI}$ amplitude of the $6s\ ^2S_{1/2} - 7s\ ^2S_{1/2}$ transition in ^{133}Cs . However, the estimation of Core and Tail contributions still relied on a combination of many-body methods without specifying the precise physical effects considered in their evaluation. We collectively refer to these two contributions as the X-factor in this study. In an effort to improve the accuracy of the computed $E1_{PV}^{NSI}$ value, Dzuba *et al.* [10] assessed the X-factor contributions using their TDHF approach, revealing an opposite sign for the Core contribution compared to that reported by Porsev. To understand the source of this discrepancy, we have calculated $E1_{PV}^{NSI}$ for the aforementioned transition using various many-body methods. We have also illustrated the similarities and differences among various contributions to

Table 5.1: Excitation energies (in cm^{-1}) of the low-lying states of ^{133}Cs from the RCCSD method. Energies are compared with the experimental values. We also present H_W (in units of $10^{-11}i(-Q_W/N)|e|a_0)$ matrix elements from various many-body method. N is the neutron number.

Transition	Excitation Energy		H_W amplitude
	RCCSD	Experiment [26]	RCCSD
$6P_{1/2}-6S$	-11243.93	-11178.27	-1.2541
$7P_{1/2}-6S$	-21838.93	-21765.35	-0.7135
$8P_{1/2}-6S$	-25787.48	-25708.83	-0.4808
$9P_{1/2}-6S$	-27735.96	-27637.00	0.3471
$7S-6P_{1/2}$	7352.53	7357.26	0.6067
$7S-7P_{1/2}$	-3242.47	-3229.82	0.3445
$7S-8P_{1/2}$	-7191.02	-7173.31	0.2320
$7S-9P_{1/2}$	-9139.50	-9101.47	-0.1674

$E1_{PV}^{NSI}$ across these methods. To ensure the accuracy of our calculations, we validate our $E1_{PV}^{NSI}$ values from the DHF, CPDF, RPA, and CPDF-RPA methods by comparing them with earlier reported values by Mårtensson [14]. We also present the result of the $E1_{PV}^{NSI}$ value for the $6S-5D_{3/2}$ transition in ^{133}Cs to address a comment by Roberts and Ginges in Ref. [25], where they discuss the agreement of the sign of Core contribution to the $E1_{PV}^{NSI}$ value of an $S-D$ transition reported earlier using the RCCSD method [24], while noting a sign difference for the $6S-7S$ transition in ^{133}Cs .

5.3.1 Excitation energies and matrix elements

Before presenting results for $E1_{PV}^{NSI}$, in Table 5.1, we provide the excitation energies of some of the lower-lying valence orbitals of the ^{133}Cs atom. Additionally, we compare our RCCSD results with available experimental data [26]. We also showcase the H_W matrix elements obtained using the RCCSD methods. The RCCSD method matrix elements for the E1 operator have already been presented in Table 3.4.

5.3.2 Results for $E1_{PV}^{NSI}$ amplitude

In Table 5.2, we present the $E1_{PV}^{NSI}$ values for the $6S - 7S$ and $6S - 5D_{3/2}$ transitions in ^{133}Cs using the DC Hamiltonian derived from various methods, including the DHF method. The values highlighted in bold font in this table are claimed to be accurate within 0.5% by earlier studies. Nevertheless, a detailed examination reveals discrepancies of up to 1% among some values, suggesting potential issues with the estimation of accuracy in these calculations that call for further investigation. Results obtained from the sum-over-states approach, denoted as ‘Sum-over’ in the table, utilize scaled E1 matrix elements and energies from the CCSDvT method to estimate the Main contribution of $E1_{PV}^{NSI}$ for the $6S - 7S$ transition, while the X-factor is derived using a combination of many-body methods [9]. In another study [10], the same ‘Main’ contribution is adopted from Ref. [9], but Core and Tail contributions to the X-factor are estimated using the CPDF-RPA* method, referred to as RPA in the original paper, with PC effects estimated using the BO-correlation method. The results from these RPA+BO methods are listed under ‘Mixed-states’ in the table. The significant discrepancies observed in both sets of results stem from the X-factors estimated in Refs [9, 10]. If the total X-factors had been consistent between the two works but individual contributions had varied, then the discrepancy in the results could have been attributed to the distribution of contributions under the Core and Valence correlations in the approaches in both studies. However, the substantial differences observed between the X-factors for the $6S - 7S$ transition do not support such an explanation.

To investigate the origin of the significant discrepancies observed in various studies, we first examine the Main contribution to the $6S - 7S$ transition using properties calculated from our RCCSD method within the sum-over-states approach. We utilize the E1 matrix elements and energies from our calculations, as well as experimental data [26, 27, 28, 29, 30]. Table 5.3 presents the estimated Main contributions to $E1_{PV}^{NSI}$ for the $6S - 7S$ transition, categorized as follows: (a) results from *ab initio* calculations for E1 matrix elements and energies, (b) using experimental E1 values with calculated energies,

Table 5.2: $E1_{pV}^{NSI}$ values, in units $10^{-11}i(-Q_W/N)|e|a_0$, of the $6s\ ^2S_{1/2} - 7s\ ^2S_{1/2}$ and $6s\ ^2S_{1/2} - 5d\ ^2D_{3/2}$ transitions in ^{133}Cs from DC Hamiltonian reported by various works. The methods labeled as ‘Sum-over’ and ‘Mixed’ are derived using the sum-over-states approach and mixed many-body methods, respectively. Results highlighted in bold font are asserted to have an accuracy within 0.5% accuracy.

Method	This work	Others	This work	Others
	$6s\ ^2S_{1/2} - 7s\ ^2S_{1/2}$		$6s\ ^2S_{1/2} - 5d\ ^2D_{3/2}$	
DHF	0.7375	0.736 [14]	-2.3933	
RMBPT(3) ^W	1.0902		-2.4639	
CPDF	0.9226	0.924 [14]	-2.7989	
RPA	0.7094	0.707 [14]	-2.2362	
CPDF-RPA*	0.8876	0.8914 [10]	-3.1665	-3.80 [11]
		0.8923 [†] [10]		
		0.907 [11]		
CPDF-RPA	0.8859	0.886 [14]	-3.1071	-3.70 [31]
		0.9041 [8]		
RCCSD	0.8964	0.8961 [12]	-3.5641	-3.210[32]
RCCSDT		0.8967 [12]		
Sum-over		0.9053 [9]		-3.76 [33]
		0.8998 [†] [9]		
Mixed-states		0.8967 [10]		-3.62 [33]
		0.8938 [†] [10]		
		0.9083 [‡] [10]		

[†]Note: Scaled value.

[‡]Scaled value + borrowed contribution from Ref. [9].

(c) *ab initio* E1 values with experimental energies, and (d) employing experimental values for both the E1 matrix elements and energies. This analysis reveals that the result from (b) is larger than (a), while results from (c) and (d) are lower than (a). Thus, it suggests that the accuracy of energies in a given method influences the results more than the E1 matrix elements. Later, we explicitly demonstrate that using experimental energy alone of the initial or final state in first-principle calculations introduces errors to the $E1_{pV}^{NSI}$ estimation.

Now, we compare our calculation with earlier results in order to find the reason

Table 5.3: Estimated ‘Main’ contributions to the $E1_{PV}^{NSI}$ values, in units $10^{-11}i(-Q_W/N)|e|a_0$, of the $6s\ ^2S_{1/2} - 7s\ ^2S_{1/2}$ transition in ^{133}Cs using matrix elements involving $np\ ^2P_{1/2}$ intermediate states in the sum-over-states approach. Four cases are being considered: (a) *ab initio* result in which calculated values from Table 5.1 and 3.4 are used; (b) replacing calculated E1 matrix elements by their experimental values; (c) retaining calculated E1 matrix elements and using experimental energies; and (d) using experimental values for both E1 matrix elements and energies.

Approach	$\langle 7S D 6S^{PV} \rangle$	$\langle 7S^{PV} D 6S \rangle$	Total
(a)	-0.4461	1.3171	0.8710
(b)	-0.4373	1.3121	0.8748
(c)	-0.4522	1.3156	0.8634
(d)	-0.4434	1.3106	0.8672

for getting the opposite sign for the Core contribution for $6S - 7S$ transition in ^{133}Cs . Subtracting the *ab initio* value of Main from the final RCCSD result, we find the X-factor for $E1_{PV}^{NSI}$ of the $6S - 7S$ transition to be 0.0254, compared to 0.0175 and 0.0256 reported in Refs. [9] and [10], respectively, in units of $10^{-11}i(-Q_W/N)|e|a_0$. This shows a significant difference between the X-factor of Ref. [9] and our work, while the values nearly agree between Ref. [10] and our findings. Given the sign difference between the Core contribution from Ref. [10] and the RCCSD value this analysis implies that the discrepancy is primarily due to different definitions used for the Core contribution in both studies. To illustrate numerically how the definition of Core contribution changes depending on the chosen approach to estimate $E1_{PV}^{NSI}$, we present the Core and Valence contributions separately for the $6S - 7S$ and $6S - 5D_{3/2}$ transitions using both the RMBPT(3)^W and RMBPT(3)^D approaches in Table 5.4. For the purpose of demonstrating how the appearance of H_{eff} in the wave function determining equation due to the choice of V^{N_e-1} modifies the result, we provide RMBPT(3) outcomes considering the effect of H_{eff} (denoted as (a) in the table) and replacing it with the DHF energy, as done in the CPDF-RPA method (results indicated as (b) in the table). It is evident that the Core and Valence contributions from both the RMBPT(3)^W and RMBPT(3)^D approaches yield different results, while the final outcomes from both methods are nearly

Table 5.4: Core and Valence correlation contributions to the $E1_{PV}^{NSI}$ values, in units $10^{-11}i(-Q_W/N)|e|a_0$, for the $6s\ ^2S_{1/2} - 7s\ ^2S_{1/2}$ and $6s\ ^2S_{1/2} - 5d\ ^2D_{3/2}$ transitions in ^{133}Cs from the RMBPT(3) W and RMBPT(3) D approaches. Results (a) considering H_{eff} effect due to V^{N_e-1} potential and (b) using DHF orbital energies are shown for comparison.

Approach	RMBPT(3) W		RMBPT(3) D	
	Core	Valence	Core	Valence
		$6s\ ^2S_{1/2} - 7s\ ^2S_{1/2}$		
(a)	-0.00205	1.09220	-0.00003	1.24290
(b)	-0.00206	0.43938	-0.00031	0.43763
		$6s\ ^2S_{1/2} - 5d\ ^2D_{3/2}$		
(a)	-0.16391	-2.30000	-0.12208	-2.55427
(b)	-0.18267	-3.97004	-0.12513	-4.02758

similar. Additionally, significant changes in the results for both transitions are observed when H_{eff} is considered in the wave function-solving equation compared to when it is not.

To further investigate the discrepancies in the X-factors reported in various studies, we delineate the Core and Valence contributions to the $E1_{PV}^{NSI}$ values separately for both the $6S - 7S$ and $6S - 5D_{3/2}$ transitions through first-principle calculations in Table 5.5. Examination of the table reveals that the signs of Core contributions to $E1_{PV}^{NSI}$ for both transitions, obtained from the DHF method and various many-body methods at a given level of approximation, are consistent across different research groups. To further validate our results, we compare the Core and Valence contributions to the $6S - 7S$ transition in Table 5.6 from both the initial and final perturbed states using the DHF, CPDF, RPA, and CPDF-RPA* methods with values reported in a Comment by Roberts and Ginges [25] and by Mårtensson [14]. We find reasonably good agreement between our results and the earlier estimations. This consistency suggests that there are no issues with the implementation of these theories in our calculations.

We have shown the definition of Core and Valence contributions are not unique and change depending upon the choice of perturbation operator. However, the exact

Table 5.5: *Ab initio* contributions to Core and Valence parts of the $E1_{PV}^{NSI}$ values, in units $10^{-11}i(-Q_W/N)|e|a_0$, for the $6s\ ^2S_{1/2} - 7s\ ^2S_{1/2}$ and $6s\ ^2S_{1/2} - 5d\ ^2D_{3/2}$ transitions in ^{133}Cs from different methods considered in this work using the DC Hamiltonian. Available results from previous calculations are also given for comparison.

Method	This work		Others	
	Core	Valence	Core	Valence
<u>$6s\ ^2S_{1/2} - 7s\ ^2S_{1/2}$</u>				
DHF	-0.00173	0.73923	-0.00174 [25]	
RMBPT(3) ^W	-0.00205	1.09220		
RMBPT(3) ^D	-0.00003	1.24290		
CPDF	-0.00199	0.92454	-0.00201 [25]	
RPA	0.00028	0.70912		
CPDF-RPA*	0.00169	0.88591	0.00170 [25]	
CPDF-RPA	0.00169	0.88421		
RCCSD	-0.00197	0.89840	-0.0019 [12]	0.8980 [12]
<u>$6s\ ^2S_{1/2} - 5d\ ^2D_{3/2}$</u>				
DHF	-0.11684	-2.27646		
RMBPT(3) ^W	-0.16391	-2.3000		
RMBPT(3) ^D	-0.12208	-2.55427		
CPDF	-0.19122	-2.60768		
RPA	-0.12037	-2.11585		
CPDF-RPA*	-0.20786	-2.95860		
CPDF-RPA	-0.20786	-2.89923		
RCCSD	-0.14745	-3.41667		

reason for the discrepancy in the sign of the Core contribution to $E1_{PV}^{NSI}$ for the $6S - 7S$ transition in ^{133}Cs between Ref. [9] and Ref. [10] remains unclear as Ref. [9] does not explicitly mention the exact method(s) used for its estimation. By comparing the signs of Core contributions from various methods employed in our study, we infer that Ref. [9] likely estimates the Core contribution by treating H_W as the perturbation. In such a case, the Tail contributions to $E1_{PV}^{NSI}$ for the $6S - 7S$ transition in ^{133}Cs from Refs. [9] and [12], as well as from our RCCSD results, should closely align with each other.

Table 5.6: Comparison of contributions from the initial and final perturbed states to $E1_{PV}^{NSI}$ of the $6s\ ^2S_{1/2} - 7s\ ^2S_{1/2}$ transition of ^{133}Cs , in units $10^{-11}i(-Q_W/N)|e|a_0$, at different levels of approximation between the present work and that are reported in Refs. [14, 25].

Method	$\langle 7S^{PNC} D 6S \rangle$		$\langle 7S D 6S^{PNC} \rangle$	
	Ours	Ref. [14]	Ours	Ref. [14]
	<u>Total contribution</u>			
DHF	1.01168	1.010	-0.27418	-0.274
CPDF	1.26664	1.267	-0.34409	-0.344
RPA	1.02557	1.023	-0.31617	-0.316
CPDF-RPA*	1.27910	1.279	-0.39150	-0.391
	Ours	Ref. [25]	Ours	Ref. [25]
	<u>Core contribution</u>			
DHF	-0.02638	-0.02645	0.02465	0.02472
CPDF	-0.04298	-0.04319	0.04099	0.04119
RPA	-0.03536		0.03564	
CPDF-RPA*	-0.05794	-0.05822	0.05963	0.05992
	<u>Valence contribution</u>			
DHF	1.03806		-0.29883	
CPDF	1.30962		-0.38508	
RPA	1.06094		-0.35181	
CPDF-RPA*	1.33704		-0.45113	

The notable differences in the X-factors reported in Ref. [9] and our work indicate that the former work underestimates the Tail contribution. It should be noted that the Tail contributions are estimated without using sum-over-states approach, so the difference in these values is mainly due to different levels of approximation made in the many-body methods employed for their estimations. Now, let's explore the reason why Roberts and Ginges obtained the same sign for the Core contribution to $E1_{PV}^{NSI}$ of the $7S - 6D_{3/2}$ transition in Ra^+ using their RPA+BO method as reported in the RCC method in Ref. [24]. Since the correlation trends for $E1_{PV}^{NSI}$ of the $nS - (n-1)D_{3/2}$

transitions are comparable in Cs and Ra^+ , where n represents the ground state principal quantum number of each system, we can elucidate this point by analyzing the Core contributions to $E1_{PV}^{NSI}$ of the $6S - 5D_{3/2}$ transition from different methods and comparing their trends with the $6S - 7S$ transition of ^{133}Cs . Upon examining these contributions from Table 5.5, it becomes evident that there is an order of magnitude difference in the Core contribution to the $6S - 7S$ transition between the $\text{RMBPT}(3)^W$ and $\text{RMBPT}(3)^D$ methods, whereas there is a change in sign between these results from the CPDF method and the RPA. However, the disparities between the Core contributions from the $\text{RMBPT}(3)^W$ and $\text{RMBPT}(3)^D$ methods in the $6S - 5D_{3/2}$ transition are minor, and there is no difference in sign between the CPDF and RPA results. These trends can be rationalized as follows: In the $6S - 7S$ transition, the wave functions of both associated states exhibit significant overlap with the nucleus, while in the $6S - 5D_{3/2}$ transition, only the wave function of the ground state demonstrates substantial overlap with the nucleus. Consequently, strong CP effects contribute through both states in the former case. Additionally, the contribution from individual diagrams of the CPDF-RPA method is almost comparable in the $6S - 7S$ transition, whereas selective diagrams predominantly contribute in the $6S - 5D_{3/2}$ transition. Since CP effects induced by the D operator are stronger and exhibit opposite signs compared to those induced by H_W , the net Core contributions in the $S - S$ and $S - D$ transitions behave differently in the CPDF method and RPA, and this discrepancy extends to the CPDF-RPA*/CPDF-RPA method. As Core and Valence contributions are essentially redistributed in the CPDF-RPA* and RCCSD methods, the difference between the final values in Refs. [10] and [12], as well as in the present work, is minimal in the $6S - 7S$ transition, while it is slightly noticeable in the $6S - 5D_{3/2}$ transition (refer to Table 5.2 for the comparison of results from the Mixed-states and RCCSD methods).

We can estimate the DCP contributions from our calculations by taking the differences between the results from the CPDF-RPA* and CPDF-RPA methods. This difference for the $6S - 7S$ transition from our work is compared with the corresponding values from Refs. [14] and [11]. Through this comparison, we observe better agreement

between our result and Mårtensson than with Roberts. Our final CPDF-RPA result also aligns more closely with Ref. [14] than with Ref. [11]. It is worth noting that the CPDF-RPA* results in Refs. [10] and [25] are also scaled using $\omega^{ex} = 0.0844$ a. u. As explained in the preceding section, we have theoretically justified why such an approach could introduce errors in determining $E1_{PV}^{NSI}$ values. To illustrate this numerically, we provide results for both the $6S - 7S$ and $6S - 5D_{3/2}$ transitions from the CPDF-RPA method using Eqs. 5.69 and 5.70 in Table 5.7. We present these values using ω , ω^{ex} , and also ω^{ex} with experimental energies ($E_{i,f}^{expt}$) of the $6S$, $7S$, and $5D_{3/2}$ states. Upon comparing these results, an intriguing trend emerges. When both ω and energies of the atomic states are considered either from theory or experiment the results from both Eqs. 5.69 and 5.70 match each other. Otherwise, significant discrepancies arise in the results from these two equations. In methods like RMBPT, RPA, or CPDF-RPA, it is feasible to use ω^{ex} and experimental energies of the initial and final states concurrently in the $E1_{PV}^{NSI}$ evaluation. However, in more complex methods like the RCC method, one must choose between using ω^{ex} or ω^{ex} with the experimental energy of only the valence state (whose perturbed state wave function is evaluated). Since the energies of the double and triple excited configurations appear in the denominator of the RCC theory, their experimental energies cannot be employed in the wave function determining equations. Aligning this understanding with the above finding, it's evident that scaling the wave function using only the experimental energy of the valence state may not always yield accurate results; instead, it could introduce additional errors to the calculation. As elucidated in the earlier sections, this aspect can be theoretically grasped using Eq. 5.30. Nonetheless, it is noteworthy from Table 5.7 that our result with the ω^{ex} value from the CPDF-RPA* method doesn't correspond with the respective results from Refs. [10, 25] for the $6S - 7S$ transition. Regrettably, we are unable to discern the underlying reason for this discrepancy, although the results with the theoretical ω value from both works agree quite well.

In Table 5.8, we present the $E1_{PV}^{NSI}$ values for the $6S - 7S$ and $6S - 5D_{3/2}$ transitions in ^{133}Cs , focusing on individual RCCSD terms to provide a quantitative understanding

of the preceding discussion. By leveraging definitions of the T and S_v RCC excitation operators, we categorize the results into Core and Valence correlation contributions. By subtracting the Core contributions of the DHF method from the contributions of the $\bar{D}T_1^{(1)}$ and its complex conjugate (c.c.) term, the net Core correlation contributions to $E1_{PV}^{NSI}$ in the RCCSD method can be inferred. Similarly by subtracting the Valence contributions of the DHF method from the $\bar{D}S_{1i}^{(1)} + S_{1f}^{(1)\dagger}\bar{D}$ terms and adding contributions from other Valence correlation contributing terms, we can get the net Valence correlation contributions to $E1_{PV}^{NSI}$ in the RCCSD method. The Core correlations arising through $\bar{D}T_1^{(1)}$ and c.c. terms encompass contributions from both singly and doubly excited configurations. By analysing the RMBPT(3)^W diagrams contributing to the $T_1^{(1)}$ amplitude determining equation shown in Fig. 5.13, it can be understood that the $\bar{D}T_1^{(1)}$ and c.c. terms contain the Core contributions of the CPDF method, PC contributions of the RMBPT(3) method to all-orders and many more. However, they do not include Core contributions arising through the RPA and some contributions from the CPDF-RPA method. Likewise, the Valence correlation contributions from the CPDF method, RPA, and CPDF-RPA* method are included through the $\bar{D}S_{1i}^{(1)} + S_{1f}^{(1)\dagger}\bar{D}$ terms in the RCCSD method. Additionally, they encompass contributions from the BO-correlation technique and beyond. However, numerous correlation contributions to $E1_{PV}^{NSI}$ arise through other RCCSD terms, such as $\bar{D}S_{2i}^{(1)}$, $\bar{D}T_{1/2}^{(1)}S_{1/2i}^{(0)}$, $T_{1/2}^{(1)\dagger}\bar{D}S_{1/2i}^{(0)}$, such terms but replacing $S_{1/2i}^{(0/1)}$ operators with $S_{1/2f}^{(0/1)\dagger}$, $S_{1/2f}^{(0)\dagger}\bar{D}S_{1/2i}^{(1)}$, $S_{1/2f}^{(1)\dagger}\bar{D}S_{1/2i}^{(1)}$ etc. These contributions are not present in the CPDF-RPA* method, and many of them cannot be considered part of the BO-correlation method. Additionally, corrections to the entire correlation contributions, including those from the CPDF-RPA method due to wave function normalization (given as ‘Norm’), are quoted separately in the table and found to be significant. The most prominent DCP contributions are absorbed through the $\bar{D}S_{2i}^{(1)} + S_{2f}^{(1)\dagger}\bar{D}$ terms in the RCCSD method, which also include some Core contributions from the CPDF-RPA method (like the ones appears in the RPA). Moreover, non-linear terms like $\bar{D}T_{1/2}^{(1)}S_{2i}^{(0)}$, $T_2^{(1)\dagger}\bar{D}S_{1i}^{(0)}$, and their counterparts encompass additional Valence correlation contributions beyond the combined scope of

CPDF-RPA and BO-correlation methods. In Table 5.8, we provide contributions to $E1_{PV}^{NSI}$ for the $6S - 7S$ and $6S - 5D_{3/2}$ transitions from the RCCSD terms using scaled $S_v^{(0)}$ and $S_v^{(1)}$ amplitudes. We demonstrate the variation in results when scaling both the unperturbed and perturbed wave functions independently by: (a) Scaling only the amplitudes of the $S_v^{(0)}$ operators. (b) Scaling amplitudes of both the $S_v^{(0)}$ and $S_v^{(1)}$ operators. Significant differences are observed between both the scaled results. It is important to note that scaling the $T^{(0/1)}$ amplitudes is not appropriate as the orbitals used for their determination encounter the V^{N_e} potential, unlike the amplitude determining equations for the $S_v^{(0/1)}$ operators, where orbitals encounter the V^{N_e-1} potential. Thus, substituting the ω^{ex} value in the estimation of Core contribution may not be theoretically sound. Moreover, we can only substitute the energy of the valence state from outside in the wave function solving equations, while energies of the intermediate states are implicitly generated in the RCC theory. Consequently, evaluating the $E1_{PV}^{NSI}$ amplitudes through the scaling procedure using the RCC method may introduce numerical errors to the calculations. Nevertheless, comparing the semi-empirical results obtained by using experimental energies with the *ab initio* values of $E1_{PV}^{NSI}$ for both the $6S - 7S$ and $6S - 5D_{3/2}$ transitions reveals significant differences. These differences can be minimized by including higher-level excitations in the RCC theory. However, these higher-level excitations will not only improve the energy values but also alter the matrix elements of the H_W and D operators. As demonstrated by Sahoo *et al.* [12, 35], inclusion of triple excitations in the RCC theory modifies the energies and matrix elements of the H_W and D operators in a manner that the $E1_{PV}^{NSI}$ values from the RCCSD and RCCSDT methods remain nearly unchanged. Consequently, we cannot argue that the scaled $E1_{PV}^{NSI}$ values are more accurate than the *ab initio* values in the RCCSD method approximation. For completeness, we also estimate Q_W using the *ab initio* value of $E1_{PV}^{NSI}$ for the $6S \rightarrow 7S$ transition. By combining this with the experimental values for vector polarizability (β) from Ref. [36] and for the NSI PV amplitude ratio $E1_{PV}^{NSI}/\beta$ from Ref. [37], we obtain $Q_W = -73.74$.

5.4 Summary

We have investigated roles of Core and Valence correlation effects in the calculations of $E1_{PV}^{NSI}$ amplitudes of the $6S \rightarrow 7S$ and $6S \rightarrow 5D_{3/2}$ transitions in ^{133}Cs by using a variety of relativistic many-body methods at different levels of approximation, such as RPMBT(3), CPDF, RPA, combined CPDF-RPA and RCCSD methods. Through this analysis, we have addressed a longstanding issue regarding the opposite signs of the Core correlation contribution to the $E1_{PV}^{NSI}$ amplitude of the $6S \rightarrow 7S$ transition in ^{133}Cs . We have shown that the definition of Core and Valence contribution is not unique and depends on the choice of perturbation operator. In Porsev and Dzuba's calculation, different operators were chosen as perturbations, so the value of the Core contribution was different. Further we have also analyzed results from the sum-over-states approach and first-principles calculations using the RCCSD method to identify missing contributions in the former approach. The inclusion of these missing contributions through the combined CPDF-RPA method was compared with the RCCSD method. This comparison demonstrated that the first-principle approach using RCC theory incorporates electron correlation effects more rigorously than the other methods mentioned above for the evaluation of $E1_{PV}^{NSI}$ amplitude in the ^{133}Cs atom.

Section 5.4. Summary

Table 5.7: Contributions to Core and Valence parts from different terms to $E1_{PV}^{NSI}$ of the $6s\ ^2S_{1/2} - 7s\ ^2S_{1/2}$ and $6s\ ^2S_{1/2} - 5d\ ^2D_{3/2}$ transitions in ^{133}Cs , in units $10^{-11}i(-Q_W/N)|e|a_0$ from Eqs. 5.69 and 5.70 of the CPDF-RPA method, which are quoted under ‘Expression a’ and ‘Expression b’ respectively. Results are given using the calculated ω value, ω^{ex} and ω^{ex} with the experimental energies of the initial and final states (denoted by $E_{i,f}^{expt}$).

Contribution	Expression a			Expression b		
	$\langle 7s h_w 6s^+ \rangle$	$\langle 7s u_{6s}^{PV} 6s^+ \rangle$	$\frac{6s\ ^2S_{1/2} - 7s\ ^2S_{1/2}}{\text{Total}}$	$\langle 7s^{PV} d 6s \rangle$	$\langle 7s^{PV} u_{6s}^+ 6s \rangle$	Total
Core (ω)	-0.0357	-0.02257	-0.05794	-0.04299	-0.01495	-0.05794
Valence (ω)	1.06094	0.27610	1.33704	1.30962	0.02742	1.33704
Core (ω^{ex})	-0.03464	-0.02211	-0.05675	-0.04299	-0.01458	-0.05757
Valence (ω^{ex})	-0.19464	-0.04598	-0.24062	1.30962	0.02743	1.33705
Core ($E_{i,f}^{expt}$)	-0.03546	-0.02283	-0.05829	-0.04331	-0.01498	-0.05829
Valence ($E_{i,f}^{expt}$)	1.21721	0.31956	1.53677	1.53384	0.00293	1.53677
	$\langle 7s d 6s^{PV} \rangle$	$\langle 7s u_{6s}^+ 6s^{PV} \rangle$	Total	$\langle 7s^- h_w 6s \rangle$	$\langle 7s^- u_{6s}^{PV} 6s \rangle$	Total
Core (ω)	0.04099	0.01864	0.05963	0.03564	0.023399	0.05963
Valence (ω)	-0.38508	-0.06605	-0.45113	-0.35181	-0.09932	-0.45113
Core (ω^{ex})	0.04099	0.01915	0.06014	0.03651	0.02458	0.06109
Valence (ω^{ex})	-0.38508	-0.06644	-0.45152	-0.17081	-0.05022	-0.22103
Core ($E_{i,f}^{expt}$)	0.04210	0.01999	0.06209	0.03686	0.02523	0.06209
Valence ($E_{i,f}^{expt}$)	-0.12128	-0.05800	-0.17928	-0.13743	-0.04185	-0.17928
	$\langle 5d_{3/2} h_w 6s^+ \rangle$	$\langle 5d_{3/2} u_{6s}^{PV} 6s^+ \rangle$	$\frac{6s\ ^2S_{1/2} - 5d\ ^2D_{3/2}}{\text{Total}}$	$\langle 5d_{3/2}^{PV} d 6s \rangle$	$\langle 5d_{3/2}^{PV} u_{6s}^+ 6s \rangle$	Total
Core (ω)	0.0	-0.00616	-0.00616	-0.00451	-0.00165	-0.00616
Valence (ω)	0.0	-0.27386	-0.27386	-0.27878	0.00492	-0.27386
Core (ω^{ex})	0.0	-0.00612	-0.0612	-0.00451	-0.00164	-0.00615
Valence (ω^{ex})	0.0	-0.23287	-0.23287	-0.27878	0.00493	-0.27385
Core ($E_{i,f}^{expt}$)	0.0	-0.00628	-0.00628	-0.00459	-0.001087	-0.00628
Valence ($E_{i,f}^{expt}$)	0.0	-0.83936	-0.83936	-0.87962	0.04028	-0.83936
	$\langle 5d_{3/2} d 6s^{PV} \rangle$	$\langle 5d_{3/2} u_{6s}^+ 6s^{PV} \rangle$	Total	$\langle 5d_{3/2}^- h_w 6s \rangle$	$\langle 5d_{3/2}^- u_{6s}^{PV} 6s \rangle$	Total
Core (ω)	-0.19574	-0.00596	-0.20170	-0.12037	-0.08133	-0.20170
Valence (ω)	-2.88646	0.20172	-2.68474	-2.11585	-0.56889	-2.68474
Core (ω^{ex})	-0.19574	-0.00636	-0.20210	-0.12109	-0.08182	-0.20291
Valence (ω^{ex})	-2.88646	0.20201	-2.68445	-1.94829	-0.52407	-2.47236
Core ($E_{i,f}^{expt}$)	-0.20110	-0.00744	-0.20854	-0.12363	-0.08491	-0.20854
Valence ($E_{i,f}^{expt}$)	-2.02306	0.16022	-1.86284	-1.46451	-0.39833	-1.86284

Table 5.8: First-principle calculated $E1_{PV}^{NSI}$ values (in $-i(Q_W/N)|e|a_0 \times 10^{-11}$) of the $6s\ ^2S_{1/2} - 7s\ ^2S_{1/2}$ and $6s\ ^2S_{1/2} - 5d\ ^2D_{3/2}$ transitions in ^{133}Cs from different terms of the RCCSD method. Both *ab initio* and scaled values are given for comparison. We have used two different types of scaling: (a) only scaling amplitudes of the unperturbed $S_v^{(0)}$ operators and (b) scaling amplitudes of both the $S_v^{(0)}$ and $S_v^{(1)}$ operators. Here, contributions under ‘Norm’ represents the difference between the contributions after and before normalizing the RCCSD wave functions. ‘Others’ denotes contributions from those RCCSD terms that are not shown explicitly in this table.

RCC term	$6s\ ^2S_{1/2} - 7s\ ^2S_{1/2}$			$6s\ ^2S_{1/2} - 5d\ ^2D_{3/2}$		
	<i>Ab initio</i>	Scaled-a	Scaled-b	<i>Ab initio</i>	Scaled-a	Scaled-b
Core contribution						
$\overline{DT}_1^{(1)}$	-0.04161	-0.04161	-0.04161	-0.00062	-0.00062	-0.00062
$T_1^{(1)\dagger}\overline{D}$	0.03964	0.03964	0.03964	-0.17132	-0.17132	-0.17132
Others	-0.00005	-0.00005	-0.00005	0.01757	0.01757	0.01757
Norm	0.00005	0.00005	0.00005	0.00692	0.00670	0.00670
Valence contribution						
$\overline{DS}_{1i}^{(1)}$	-0.19363	-0.19363	-0.19688	-2.96310	-2.96310	-2.97589
$S_{1f}^{(1)\dagger}\overline{D}$	1.80382	1.80382	1.80263	-0.89993	-0.89993	-1.30760
$S_{1f}^{(0)\dagger}\overline{DS}_{1i}^{(1)}$	-0.23184	-0.23187	-0.23297	-0.06863	-0.06548	-0.06487
$S_{1f}^{(1)\dagger}\overline{DS}_{1i}^{(0)}$	-0.41826	-0.41895	-0.41942	0.10487	0.10502	0.14626
$\overline{DS}_{2i}^{(1)}$	-0.00039	-0.00039	-0.00039	0.00107	0.00107	0.00108
$S_{2f}^{(1)\dagger}\overline{D}$	0.00033	0.00033	0.00033	-0.00023	-0.00023	-0.00023
Others	-0.04040	-0.04222	-0.04025	0.24888	0.24806	0.27704
Norm	-0.02122	-0.01942	-0.02110	0.16040	0.15505	0.15309
Total	0.89643	0.89570	0.88998	-3.56412	-3.56721	-3.91879

Bibliography

- [1] B. P. Das, J. Andriessen, M. Vajed-Samii, S. N. Ray and T. P. Das, Phys. Rev. Lett. **49**, 32 (1982).
- [2] V. A. Dzuba, V. V. Flambaum, P.G. Silvestrov, O.P. Sushkov, J. Phys. B **20**, 3297 (1987).
- [3] M. G. Kozlov, S. G. Porsev, W. R. Johnson, Phys. Rev. A **64**, 052107 (2001).
- [4] V. A. Dzuba, V. V. Flambaum, P. G. Silvestrov, O.P. Sushkov, Europhys. Lett. **7**, 413 (1988).
- [5] V. A. Dzuba, V. V. Flambaum, O. P. Sushkov, Phys. Lett. A **141**, 147 (1989).
- [6] S. A. Blundell, W. R. Johnson and J. Sapirstein, Phys. Rev. Lett. **65**, 1411 (1990).
- [7] M. G. Kozlov, S. G. Porsev, V. V. Flambaum, J. Phys. B **29**, 689 (1996).
- [8] V. A. Dzuba, V. V. Flambaum and J. S. M. Ginges, Phys. Rev. D **66**, 076013 (2002).
- [9] S. G. Porsev, K. Beloy and A. Derevianko, Phys. Rev. D **82**, 036008 (2010).
- [10] V. A. Dzuba, J. C. Berengut, V. V. Flambaum and B. Roberts, Phys. Rev. Lett. **109**, 203003 (2012).
- [11] B. M. Roberts, V. A. Dzuba and V. V. Flambaum, Phys. Rev. A **88**, 042507 (2013).
- [12] B. K. Sahoo, B. P. Das and H. Spiesberger, Phys. Rev. D **103**, L111303 (2021).

- [13] S. A. Blundell, J. Sapirstein and W. R. Johnson, *Phys. Rev. D* **45**, 5 (1992).
- [14] A. -M. Mårtensson-Pendrill, *J. Phys.* **46**, 11 (1985).
- [15] B. M. Roberts, V. A. Dzuba and V. V. Flambaum, *Phys. Rev. A* **88**, 012510 (2013).
- [16] B. K. Sahoo, B. P. Das and H. Spiesberger, *Phys. Rev. D* **105**, 018302 (2022).
- [17] A. I. Milstein, O. P. Sushkov and I. S. Terekhov, *Phys. Rev. Lett.* **89**, 283003 (2002).
- [18] B. A. Brown, A. Derevianko and V. V. Flambaum, *Phys. Rev. C* **79**, 035501 (2009).
- [19] A. Derevianko, *Phys. Rev. Lett.* **85**, 1618 (2000); *Phys. Rev. A* **65**, 012106 (2001).
- [20] V. M. Shabaev, K. Pachucki, I. I. Tupitsyn and V. A. Yerokhin, *Phys. Rev. Lett.* **94**, 213002 (2005).
- [21] B. P. Das, B. K. Sahoo, G. Gopakumar, and R. K. Chaudhuri, *J. Mol. Str.* **768**, 141 (2006).
- [22] B. K. Sahoo, *J. Phys. B* **43**, 085005 (2010).
- [23] B. K. Sahoo, B. P. Das, *Phys. Rev. A* **84**, 010502(R) (2011).
- [24] L. W. Wansbeek, B. K. Sahoo, R. G. E. Timmermans, K. Jungmann, B. P. Das and D. Mukherjee, *Phys. Rev. A* **78**, 050501(R)(2008).
- [25] B. M. Roberts and J. S. M. Ginges, *Phys. Rev. D* **105**, 018301 (2022).
- [26] A. Kramida, Yu. Ralchenko, J. Reader and NIST ASD Team, NIST Atomic Spectra Database (ver. 5.6.1) (National Institute of Standards and Technology, Gaithersburg, MD, 2018).
- [27] L. Young, W. T. Hill III, S. J. Sibener, S. D. Price, C. E. Tanner, C. E. Wieman and S. R. Leone, *Phys. Rev. A* **50**, 2174 (1994).

- [28] A. A. Vasilyev, I. M. Savukov, M. S. Safronova and H. G. Berry, Phys. Rev. A **66**, 020101 (2002).
- [29] M.-A. Bouchiat, J. Guena, and L. Pottier, J. Phys. (Paris), Lett. **45**, 523 (1984).
- [30] S. C. Bennett, J. L. Roberts and C. E. Wieman, Phys. Rev. A **59**, R16 (1999).
- [31] B. M. Roberts, V. A. Dzuba and V. V. Flambaum, Phys. Rev. A **88**, 012510 (2013).
- [32] A. Kastberg, B. K. Sahoo, T. Aoki, Y. Sakemi and B. P. Das, Symmetry **12**, 974 (2020).
- [33] V. A. Dzuba, V. V. Flambaum and J. S. M. Ginges, Phys. Rev. D **63**, 062101 (2001).
- [34] B. K. Sahoo and B. P. Das, Phys. Rev. Letts. **120**, 203001 (2018).
- [35] B. K. Sahoo and B. P. Das, arXiv:2008.08941 [hep-ph] (2020) (Unpublished).
- [36] Jonah A. Quirk, Aidan Jacobsen, Amy Damitz, Carol E. Tanner and D. S. Elliott, Phys. Rev. Lett. **132**, 233201 (2024).
- [37] C. S. Wood *et al.*, Science **275**, 1759 (1997).

Chapter 6

Hyperfine Interaction Induced Electric Dipole Polarizability in ^{133}Cs

BERFORE studying NSD PV in ^{133}Cs atom, it is judicious to check the potential of the method to produce accurate results. In Chapter 4, we verified that the RCC method is better than the lower-order methods like RMBPT and RPA by calculating second-order electric dipole polarizability for closed-core atomic systems. In this chapter, we are extending this exercise by trying to calculate the E1 polarizabilities (α_{F,M_F}) of the $F = 3$ and $F = 4$ hyperfine levels of the ground state in ^{133}Cs . There are two primary reasons for choosing this property. First, like NSD PV amplitude, α_{F,M_F} depends on the wave function of the hyperfine level. Considering correction up to first-order from NSD parity-violating interaction, we can express the NSD PV amplitude between initial (i) and final (f) state as

$$\begin{aligned} E1_{PV}^{NSD} &= \langle \Psi_f^{(0),F} | D | \Psi_i^{(1),F} \rangle + \langle \Psi_f^{(1),F} | D | \Psi_i^{(0),F} \rangle \\ &= \sum_{I \neq i} \frac{\langle \Psi_f^{(0),F} | D | \Psi_I^{(0),F} \rangle \langle \Psi_I^{(0),F} | H_{PV}^{NSD} | \Psi_i^{(0),F} \rangle}{E_i^{(0),F} - E_I^{(0),F}} \end{aligned}$$

$$+ \sum_{I \neq f} \frac{\langle \Psi_f^{(0),F} | H_{PV}^{NSD} | \Psi_I^{(0),F} \rangle \langle \Psi_I^{(0),F} | D | \Psi_i^{(0),F} \rangle}{E_f^{(0),F} - E_I^{(0),F}}, \quad (6.1)$$

where $|\Psi_v^{(0),F}\rangle$ is the wave function of the hyperfine level due to em interaction which can be expressed as $|\Psi_v^{(0),F}\rangle = |(IJ)FM_F\rangle$ and $E_v^{(0),F}$ is the corresponding energy. $|\Psi_v^{(1),F}\rangle$ is the first-order perturbed wave function. In a similar way, the expression for the α_{F,M_F} can be written as

$$\begin{aligned} \alpha_{F,M_F} &= \langle \Psi_v^{(0),F} | D | \Psi_v^{(1),F} \rangle + \langle \Psi_v^{(1),F} | D | \Psi_v^{(0),F} \rangle \\ &= \sum_{I \neq v} \frac{\langle \Psi_v^{(0),F} | D | \Psi_I^{(0),F} \rangle \langle \Psi_I^{(0),F} | D | \Psi_v^{(0),F} \rangle}{E_v^{(0),F} - E_I^{(0),F}} \\ &\quad + \sum_{I \neq v} \frac{\langle \Psi_v^{(0),F} | D | \Psi_I^{(0),F} \rangle \langle \Psi_I^{(0),F} | D | \Psi_v^{(0),F} \rangle}{E_v^{(0),F} - E_I^{(0),F}}. \end{aligned} \quad (6.2)$$

The expressions for $E1_{PV}^{NSD}$ and α_{F,M_F} exhibit notable similarities. In case of $E1_{PV}^{NSD}$, the electronic component of the NSD PV Hamiltonian, $K^{(1)}$, is a rank one operator. Similarly, for α_{F,M_F} the perturbed operator, D , is a rank one operator. This suggests that the angular momentum coupling for $E1_{PV}^{NSD}$ and α_{F,M_F} calculations will be similar. Further, calculation of α_{F,M_F} depends on the magnetic dipole hyperfine interaction, which originates in the nucleus. The electronic component of this interaction is also a rank one operator. Secondly, our primary objective is to probe K_W by combining theoretical and experimental results for the NSD PV amplitude. As we are treating K_W as an unknown quantity, we cannot compare our calculated value of $E1_{PV}^{NSD}$ with the experimental result. In this scenario, calculation of the polarizability of the hyperfine level of ^{133}Cs will be useful to support the accuracy of our NSD PV calculations. As there are experimental and various theoretical results available for α_{F,M_F} , we can compare our polarizability results with the earlier studies and assess the potential of our method.

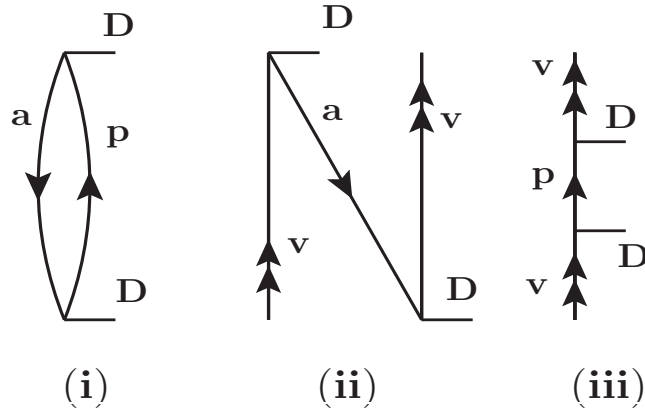


Figure 6.1: Goldstone diagrams representing the DHF contributions to the second-order E1 polarizability. The horizontal line represents the E1 operator D .

6.1 Prelude of earlier calculations

Beyond going verifying the precision of our NSD PV results, the accurate determination of these polarizability values is also important for high-precision experiments like atomic clocks, atom trapping and quantum computers [1, 2, 3, 4, 5, 6, 7]. The polarizability of the hyperfine levels of the ground state in the ^{133}Cs atom has been studied by a number of research groups [8, 9, 10, 11, 12, 13, 14]. Nonetheless, there exist disparities of around 10% across the calculated results for the differential static scalar E1 polarizability values estimated using various methods. Variations observed in various experimental results [15, 16, 17, 18, 19] exacerbate this discrepancy even more. Subsequently, it was claimed that these inconsistencies could be attributed to the neglected contributions of intermediate continuum states in certain calculations [13]. A similar disparity is observed for the tensor component of α_{F,M_F} between the theoretical and experimental results [20, 21, 22]. There exists roughly a 30% deviation between the experimental value and the theoretical result for the $F = 4$ level [23, 24]. More research on these quantities is necessary, given the significant differences in the scalar and tensor components of the static α_{F,M_F} values. We perform analyses of the static and dynamic α_{F,M_F} values of the hyperfine levels of the ground state in the ^{133}Cs atom at two wavelengths ($\lambda = 2\pi c/\omega$ with the speed of light c and angular frequency

ω), namely 936 nm and 1064 nm. We have chosen $\lambda = 936$ nm value as it is in close alignment with the magic wavelength [25, 26] for the $6S_{1/2} - 6P_{3/2}$ transition, which is used for cooling of the ^{133}Cs atoms. As high-power laser is not available at 936 nm, we choose the $\lambda = 1064$ nm ytterbium-doped fiber laser, which provides more than 50W of power.

6.2 Theory of dynamic polarizability

A uniform oscillating electric field with angular frequency ω at a given time t is given by

$$\vec{\mathcal{E}}_L(\omega, t) = \frac{1}{2}|\mathcal{E}_0|\vec{\varepsilon}e^{-i\omega t} + \frac{1}{2}|\mathcal{E}_0|\vec{\varepsilon}e^{i\omega t}, \quad (6.3)$$

where $|\mathcal{E}_0|$ denotes the strength of the field and $\vec{\varepsilon}$ is the degree of polarization. The interaction Hamiltonian can be written as

$$\begin{aligned} H_{int} &= -\vec{\mathcal{E}}_L(\omega, t) \cdot \vec{D} \\ &= -\frac{|\mathcal{E}_0|}{2} \left[\vec{\varepsilon} \cdot \vec{D}e^{-i\omega t} + \vec{\varepsilon}^* \cdot \vec{D}e^{i\omega t} \right]. \end{aligned} \quad (6.4)$$

The leading non-vanishing second-order energy shift in power of $|\mathcal{E}_0|$ in a hyperfine level $|FM_F\rangle$ can be given by

$$\Delta E_{\text{light}} = -\frac{1}{2}\alpha_{F,M_F}(\omega)\mathcal{E}_L^2(\omega), \quad (6.5)$$

where $\alpha_{F,M_F}(\omega)$ is known as the dynamic E1 polarizability. For $\omega = 0$, it corresponds to the static E1 polarizability. $\alpha_{F,M_F}(\omega)$ can be evaluated as expectation value of an effective operator

$$D_{eff}^{(2)} = \left[\vec{\varepsilon}^* \cdot \vec{D}R_F^+ \vec{\varepsilon} \cdot \vec{D} + \vec{\varepsilon} \cdot \vec{D}R_F^- \vec{\varepsilon}^* \cdot \vec{D} \right], \quad (6.6)$$

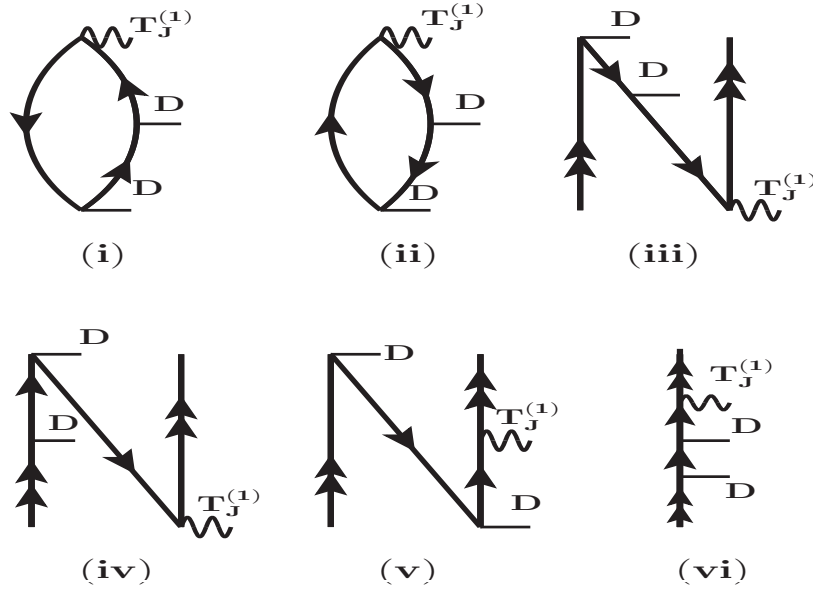


Figure 6.2: Diagrammatic representation of the top contribution to the third-order hyperfine interaction induced E1 polarizability. In addition to two interactions by the E1 operator D (represented by a horizontal line), each diagram includes a hyperfine interaction $\mathbf{T}_J^{(1)}$ (represented by a curly line).

where R_F^\pm are the resolvent operators, given by

$$R_F^\pm = \sum_{F', M_{F'}} \frac{|F' M_{F'}\rangle \langle F' M_{F'}|}{E_F - E_{F'} \pm \omega}. \quad (6.7)$$

Polarization vectors can be separated from the electronic operators in Eq. 6.6 by expressing

$$\vec{\varepsilon}^* \cdot \vec{D} R_F^\pm \vec{\varepsilon} \cdot \vec{D} = \sum_{L=0,1,2} (-1)^L (\vec{\varepsilon}^* \otimes \vec{\varepsilon})^L \cdot \left(\vec{D} \otimes R_F^\pm \vec{D} \right)^L. \quad (6.8)$$

Thus, the effective operator can be written as

$$D_{eff}^{(2)} = \sum_{L=0,1,2} (-1)^L (\vec{\varepsilon}^* \otimes \vec{\varepsilon})^L \cdot \left[\left(\vec{D} \otimes R_F^+ \vec{D} \right)^L + (-1)^L \left(\vec{D} \otimes R_F^- \vec{D} \right)^L \right], \quad (6.9)$$

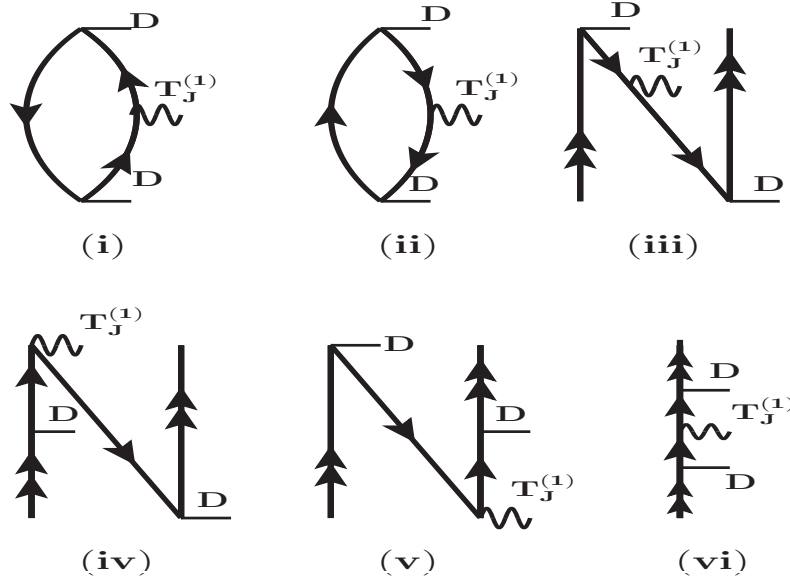


Figure 6.3: Diagrammatic representation of the center part of the third-order hyperfine interaction induced E1 polarizability. All notations are the same as the previous figure.

using which, we get the polarizability as

$$\begin{aligned}
 \alpha_{F,M_F} &= -\langle FM_F | D_{eff}^{(2)} | FM_F \rangle \\
 &= - \sum_{L=0,1,2} \sum_{Q=-L}^L (-1)^{L-Q} (\vec{\varepsilon}^* \otimes \vec{\varepsilon})_Q^L \\
 &\quad \times \langle FM_F | \left(\vec{D} \otimes R_F^+ \vec{D} \right)_Q^L \\
 &\quad + (-1)^L \langle FM_F | \left(\vec{D} \otimes R_F^- \vec{D} \right)_Q^L | FM_F \rangle. \tag{6.10}
 \end{aligned}$$

Using the polarization dependent factors, we can rewrite the aforementioned expression as

$$\begin{aligned}
 \alpha_{F,M_F} &= \alpha_F^S + \mathcal{A} \frac{M_F}{2F} \cos \theta_k \alpha_F^A \\
 &\quad + \frac{3M_F^2 - F(F+1)}{F(2F-1)} \frac{3 \cos^2 \theta_p - 1}{2} \alpha_F^T, \tag{6.11}
 \end{aligned}$$

where \mathcal{A} indicates the degree of polarization, θ_p is the polarization angle, and θ_k is the angle between the quantization axis and the wave vector. Furthermore, the scalar, axial-vector, and tensor components of α_{F,M_F} , which are M_F independent, are denoted by the terms α_F^S , α_F^A , and α_F^T and are given by

$$\begin{aligned} \alpha_F^S(\omega) &= -\frac{1}{3(2F+1)} \sum_{F'} |\langle F || \mathbf{D} || F' \rangle|^2 \\ &\quad \times \left[\frac{1}{E_F - E_{F'} + \omega} + \frac{1}{E_F - E_{F'} - \omega} \right], \end{aligned} \quad (6.12)$$

$$\begin{aligned} \alpha_F^A(\omega) &= -\sqrt{\frac{6F}{(F+1)(2F+1)}} \sum_{F'} (-1)^{F+F'+1} \\ &\quad \times \begin{Bmatrix} F & 1 & F \\ 1 & F' & 1 \end{Bmatrix} |\langle F || \mathbf{D} || F' \rangle|^2 \\ &\quad \times \left[\frac{1}{E_F - E_{F'} + \omega} - \frac{1}{E_F - E_{F'} - \omega} \right], \end{aligned} \quad (6.13)$$

and

$$\begin{aligned} \alpha_F^T(\omega) &= 2\sqrt{\frac{5F(2F-1)}{6(F+1)(2F+3)(2F+1)}} \\ &\quad \times (-1)^{F+F'+1} \begin{Bmatrix} F & 2 & F \\ 1 & F' & 1 \end{Bmatrix} |\langle F || \mathbf{D} || F' \rangle|^2 \\ &\quad \times \left[\frac{1}{E_F - E_{F'} + \omega} + \frac{1}{E_F - E_{F'} - \omega} \right]. \end{aligned} \quad (6.14)$$

It is exhausting to deal with the wave functions in the hyperfine coordinate system. In order to deal with this, we can approximate the $|FM_F\rangle$ levels with a good approximation considering up to the first-order perturbation as

$$|FM_F\rangle = |IM_I; JM_J\rangle + \sum_{J', M_{J'}} |IM_I; J'M_{J'}\rangle \frac{\langle IM_I; J'M_{J'} | H_{hf} | IM_I; JM_J \rangle}{E_J - E_{J'}}, \quad (6.15)$$

where I is the nuclear spin with azimuthal component M_I and J is the total angular

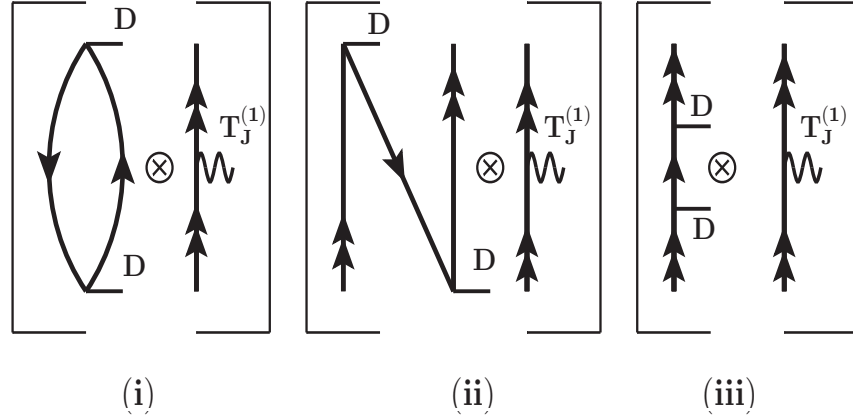


Figure 6.4: Diagrammatic representation of the normalization part of the third-order hyperfine interaction induced E1 polarizability.

momentum of the atomic state with azimuthal component M_J . The scalar hyperfine interaction Hamiltonian is denoted by H_{hf} , which can be defined as

$$H_{hf} = \sum_k T_J^{(k)} \cdot T_I^{(k)}, \quad (6.16)$$

where the electronic and nuclear components of H_{hf} with rank k of the multipole expansion are defined as $T_J^{(k)}$ and $T_I^{(k)}$, respectively, with $k = 1, 3, 5 \dots$ indicating contributions from the magnetic multipoles and $k = 2, 4, 6 \dots$ indicating contributions from the electric multipoles. Since the contributions of the other multipoles to these quantities are negligibly small, we only take into account the dominant $k = 1$ term in the calculation corresponding to the M1 hyperfine interaction for the purposes of this study [22, 23]. The $\langle IM_I; J'M_{J'} | H_{hf} | IM_I; JM_J \rangle$ matrix element can, then, be evaluated using the relation

$$\begin{aligned} \langle IM_I; J'M_{J'} | T_J^{(1)} \cdot T_I^{(1)} | IM_I; JM_J \rangle &= (-1)^{I+J+F} \begin{Bmatrix} J' & J & 1 \\ I & I & F \end{Bmatrix} \\ &\times \langle J' || \mathbf{T}_J^{(1)} || J \rangle \langle I || \mathbf{T}_I^{(1)} || I \rangle, \end{aligned} \quad (6.17)$$

Table 6.1: Calculated values of the second-order static and dynamic E1 polarizabilities (in a.u.) of the ground state of the Cs atom. Wavelengths are in nm.

Method	α_{6S}^S values			α_{6S}^A values	
	$\lambda = \infty$	$\lambda = 936$	$\lambda = 1064$	$\lambda = 936$	$\lambda = 1064$
This work					
DHF	662.6	-2303.2	7945.1	-459.7	20772.2
RCCSD	404.8	2684.0	1138.7	-1300.8	-196.8
RCCSDT	400.0	3094.3	1164.4	-1819.3	-206.3
Final	401.0(6)	3022.1(40)	1170.8(16)	-1599.5(59)	-201.8(18)
Others					
Theory [14]	400.80(97)				
Theory [31]	399.8				
Theory [32]	403.9				
Theory [33]	399.9(1.9)				
Experiment [30]	401.00(6)				

in which the nuclear coordinate part is converted to a factor as

$$\langle I || \mathbf{T}_I^{(1)} || I \rangle = \sqrt{I(I+1)(2I+1)} g_I \mu_N, \quad (6.18)$$

with $g_I = \mu_I/I$ for the M1 moment μ_I and nuclear Bohr magnetron μ_N . After substituting all the relations, we can express α_F^S , α_F^A and α_F^T components as

$$\alpha_F^S = \alpha_F^{S(2,0)} + \alpha_F^{S(2,1)}, \quad (6.19)$$

$$\alpha_F^A = \alpha_F^{A(2,0)} + \alpha_F^{A(2,1)}, \quad (6.20)$$

and

$$\alpha_F^T = \alpha_F^{T(2,0)} + \alpha_F^{T(2,1)}, \quad (6.21)$$

Table 6.2: Magnetic dipole hyperfine interaction induced E1 polarizabilities (in 10^{-10} Hz/(V/m) 2) of the hyperfine levels of the ground state of ^{133}Cs at various wavelengths (λ). Wavelengths are in nm. The unit Hz/(V/m) 2 can be converted into a.u. by multiplying 0.401878046×10^8 .

Quantity	Method	$F = 3$			$F = 4$		
		$\lambda = \infty$	$\lambda = 936$	$\lambda = 1064$	$\lambda = \infty$	$\lambda = 936$	$\lambda = 1064$
$\alpha_F^{S(2,1)}$	DHF	-3.1420	-49.5027	-2381.2965	2.4423	38.5007	1852.1969
	RCCSD	-2.5706	-153.5968	-26.5174	1.9993	119.4880	8.3956
	RCCSDT	-2.5586	-225.2741	-25.3313	1.9898	175.2118	19.6881
	Final	-2.559(11)	-201.1(17)	-25.3(13)	1.990(10)	156.4(14)	19.7(10)
	TDHF+BO [23]	-2.5419			1.9770		
	RCICP [14]	-34.248(7)			-29.598(7)		
$\alpha_F^{A(2,1)}$	DHF	0.0	8.6958	561.5658	0.0	9.0179	582.5113
	RCCSD	0.0	-132.2379	-9.0495	0.0	-137.1366	-9.2136
	RCCSDT	0.0	-238.6758	-11.0932	0.0	-247.5169	-11.5043
	Final	0.0	-185.59(51)	-9.70(7)	0.0	-192.47(53)	-10.06(7)
$\alpha_F^{T(2,1)}$	DHF	0.0344	0.4310	25.8040	-0.0639	-0.8044	-48.1693
	RCCSD	0.0183	6.0153	0.4561	-0.0339	-11.2287	-0.8888
	RCCSDT	0.0188	10.4966	0.5508	-0.0350	-19.5937	-1.0279
	Final	0.0185(8)	8.482(16)	0.5084(21)	-0.0342(15)	-15.834(30)	-0.9487(39)
	TDHF+BO [23]	0.0141			-0.0262		
	RCICP [14]	0.03051(6)			-0.05703(11)		
	Semi-empirical [21]				-0.0372(25)		
Experiment [24]				-0.0334(2) $_{stat}$ (25) $_{syst}$			

where $\alpha_F^{S/A/T(m,n)}$ means the components are including m -orders of E1 interactions and n -orders of M1 hyperfine interactions, respectively. The hyperfine interaction independent components can be estimated by using the relations

$$\begin{aligned}
 \alpha_F^{S(2,0)}(\omega) &= -\frac{1}{3(2J+1)} \sum_{J'} |\langle J || \mathbf{D} || J' \rangle|^2 \\
 &\quad \times \left[\frac{1}{E_J - E_{J'} + \omega} + \frac{1}{E_J - E_{J'} - \omega} \right] \\
 &\equiv \alpha_J^S(\omega),
 \end{aligned} \tag{6.22}$$

$$\begin{aligned}
 \alpha_F^{A(2,0)}(\omega) &= -\sqrt{\frac{6F(2F+1)}{(F+1)}} \begin{Bmatrix} J & F & I \\ F & J & 1 \end{Bmatrix} \\
 &\times \sum_{J'} (-1)^{F+J'+I+2J} \begin{Bmatrix} 1 & 1 & 1 \\ J & J & J' \end{Bmatrix} \\
 &\times \left[\frac{|\langle J||\mathbf{D}||J' \rangle|^2}{E_J - E_{J'} + \omega} - \frac{|\langle J||\mathbf{D}||J' \rangle|^2}{E_J - E_{J'} - \omega} \right] \\
 &= \sqrt{\frac{F(2F+1)(J+1)(2J+1)}{J(F+1)}} \\
 &\times (-1)^{I+J+F+1} \begin{Bmatrix} J & F & I \\ F & J & 1 \end{Bmatrix} \alpha_J^A(\omega), \tag{6.23}
 \end{aligned}$$

and

$$\begin{aligned}
 \alpha_F^{T(2,0)}(\omega) &= -\sqrt{\frac{20F(2F-1)(2F+1)}{6(F+1)(2F+3)}} \begin{Bmatrix} J & F & I \\ F & J & 2 \end{Bmatrix} \\
 &\times \sum_{J'} (-1)^{I+F+J'+2J} \begin{Bmatrix} 1 & 1 & 2 \\ J & J & J' \end{Bmatrix} \\
 &\times \left[\frac{|\langle J||\mathbf{D}||J' \rangle|^2}{E_J - E_{J'} + \omega} + \frac{|\langle J||\mathbf{D}||J' \rangle|^2}{E_J - E_{J'} - \omega} \right] \\
 &= -\sqrt{\frac{(J+1)(2J+3)(2J+1)F(2F-1)}{J(2J-1)(F+1)(2F+3)(2F+1)}} \\
 &\times (2F+1)(-1)^{I+J+F+1} \begin{Bmatrix} J & F & I \\ F & J & 2 \end{Bmatrix} \\
 &\times \alpha_J^T(\omega), \tag{6.24}
 \end{aligned}$$

where α_J^S , α_J^A and α_J^T are the components of atomic state E1 polarizabilities. It can be followed from the selection rules that α_J^T will not contribute to the states with

$J < 3/2$. Proceeding in the similar manner, we can express hyperfine interaction induced polarizability [13, 27]

$$\alpha_F^{\mathcal{K}(2,1)}(\omega) = W_F^{\mathcal{K}} [2T_F^{\mathcal{K}}(\omega) + C_F^{\mathcal{K}}(\omega) + R_F^{\mathcal{K}}(\omega)], \quad (6.25)$$

where the symbol \mathcal{K} denotes scalar, axial-vector, and tensor components for the integer values $K = 0, 1$ and 2 , respectively, as used below. Each component is further divided into contributions from three different terms defined as top ($T_F^{\mathcal{K}}$), center ($C_F^{\mathcal{K}}$), and residual (or normalization) ($R_F^{\mathcal{K}}$) that are expressed as

$$\begin{aligned} T_F^{\mathcal{K}}(\omega) &= \sqrt{(2K+1)I(I+1)(2I+1)} g_I \mu_N \\ &\times \sum_{J', J''} \left\{ \begin{matrix} I & I & 1 \\ J & J'' & F \end{matrix} \right\} \left\{ \begin{matrix} K & J'' & J \\ I & F & F \end{matrix} \right\} \\ &\times \left\{ \begin{matrix} K & J'' & J \\ J' & 1 & 1 \end{matrix} \right\} (-1)^{J+J''} \frac{\langle J || \mathbf{T}_J^{(1)} || J'' \rangle \langle J'' || \mathbf{D} || J' \rangle \langle J' || \mathbf{D} || J \rangle}{(E_J - E_{J''})} \\ &\times \left[\frac{1}{(E_J - E_{J'} + \omega)} + \frac{(-1)^K}{(E_J - E_{J'} - \omega)} \right], \end{aligned} \quad (6.26)$$

$$\begin{aligned} C_F^{\mathcal{K}}(\omega) &= \sqrt{(2K+1)I(I+1)(2I+1)} g_I \mu_N \\ &\times \sum_{J', J''} \sum_L \left\{ \begin{matrix} F & K & F \\ J & 1 & J'' \\ I & 1 & L \end{matrix} \right\} \left\{ \begin{matrix} I & J & F \\ 1 & J' & J'' \\ I & 1 & L \end{matrix} \right\} \\ &\times (-1)^{I+K-F+J} \langle J || \mathbf{D} || J'' \rangle \langle J'' || \mathbf{T}_J^{(1)} || J' \rangle \langle J' || \mathbf{D} || J \rangle \\ &\times \left[\frac{1}{(E_J - E_{J'} + \omega)(E_J - E_{J''} + \omega)} \right. \\ &\left. + \frac{(-1)^K}{(E_J - E_{J'} - \omega)(E_J - E_{J''} - \omega)} \right], \end{aligned} \quad (6.27)$$

and

$$\begin{aligned}
 R_F^{\mathcal{K}}(\omega) &= \sqrt{(2K+1)I(I+1)(2I+1)}g_{I\mu_N} \\
 &\times \sum_{J'} \left\{ \begin{matrix} I & I & 1 \\ J & J & F \end{matrix} \right\} \left\{ \begin{matrix} K & J & J \\ I & F & F \end{matrix} \right\} \left\{ \begin{matrix} K & J & J \\ J' & 1 & 1 \end{matrix} \right\} \\
 &\times (-1)^{(J+J'+1)} \langle J || \mathbf{T}_J^{(1)} || J \rangle | \langle J || \mathbf{D} || J' \rangle |^2 \\
 &\times \left[\frac{1}{(E_J - E_{J'} + \omega)^2} + \frac{(-1)^K}{(E_J - E_{J'} - \omega)^2} \right]. \tag{6.28}
 \end{aligned}$$

Also, the pre-angular factors are given by

$$W_F^S = \sqrt{\frac{(2F+1)}{3}}, \tag{6.29}$$

$$W_F^A = -\sqrt{\frac{2F(2F+1)}{(F+1)}}, \tag{6.30}$$

and

$$W_F^T = -\sqrt{\frac{2F(2F-1)(2F+1)}{3(F+1)(2F+3)}}. \tag{6.31}$$

6.3 Approaches for calculation

As can be inferred from the above discussion, in order to obtain an accurate estimate of the α_F values in ^{133}Cs , a large set of matrix elements of the D and $T_J^{(1)}$ operators is required. We start our calculation by considering the V^{N_e-1} potential (N_e denotes the number of electrons) in the DHF method to produce as many bound states as possible with a common core $[5p^6]$ but differing by a valence orbital v in ^{133}Cs . The DHF wave functions of the interested states can be expressed as

$$|\Phi_v\rangle = a_v^\dagger |\Phi_c\rangle, \tag{6.32}$$

Table 6.3: The presently calculated the second-order static and dynamic atomic E1 polarizabilities (in a.u.) of the ground state of Cs atom. E1 matrix elements used in the estimation of ‘Main’ contributions are given explicitly, where values shown with superscript ‘a’ are calculated using the RCCSDT method.

Transition	E1 matrix element	α_{6S}^S values			α_{6S}^A values	
		$\lambda = \infty$	$\lambda = 936 \text{ nm}$	$\lambda = 1064 \text{ nm}$	$\lambda = 936 \text{ nm}$	$\lambda = 1064 \text{ nm}$
Main						
$6S_{1/2} - 6P_{1/2}$	$4.5067(40)^a$	132.93	1536.35	453.54	-2936.77	-762.65
$6S_{1/2} - 6P_{3/2}$	$6.3403(64)$ [34]	250.67	1467.97	699.66	1336.78	560.48
$6S_{1/2} - 7P_{1/2}$	$0.27810(45)$ [35]	0.26	0.34	0.32	-0.34	-0.28
$6S_{1/2} - 7P_{3/2}$	$0.57417(57)$ [35]	1.10	1.44	1.35	0.70	0.58
$6S_{1/2} - 8P_{1/2}$	$0.0824(10)^a$	0.02	0.02	0.02	-0.02	-0.02
$6S_{1/2} - 8P_{3/2}$	$0.2294(15)^a$	0.15	0.18	0.17	0.08	0.06
$6S_{1/2} - 9P_{1/2}$	$0.0424(15)^a$	0.01	0.01	0.01	-0.01	~ 0.0
$6S_{1/2} - 9P_{3/2}$	$0.1268(11)^a$	0.04	0.05	0.05	0.02	0.02
Total		385.2(6)	3006.4(40)	1155.1(16)	-1599.5(59)	-201.8(18)
Tail		0.20	0.14	0.14	0.005	0.004
Core-valence		-0.35(5)	-0.35(5)	-0.35(5)	-0.01(1)	-0.01(1)
Core		15.99(10)	15.9(1)	15.9(1)	0.0	0.0

where $|\Phi_c\rangle$ is the DHF wave function of the closed-core $[5p^6]$. Using these wave functions, the dominant part of the $\alpha_J^S(\omega)$ and $\alpha_J^A(\omega)$ values of the ground state of ^{133}Cs atom can be determined. We show Goldstone diagrams of the DHF contributions for $\alpha_J^S(\omega)$ and $\alpha_J^A(\omega)$ in Fig. 6.1. As D is a one-body operator, only the intermediate states represented by single orbital excitations contribute to the DHF diagrams. These diagrams correspond to Figs. 6.1 (i), (ii) and (iii), respectively, and can therefore be categorized as core, core-valence, and valence orbital contributions. To improve these calculations for accurate E1 polarizability estimations, electron correlation effects resulting from other configurations overlooked by the DHF method must be incorporated. We also plan to reduce computational uncertainties by using the highly accurate experimental energies from the NIST database [28]. Similarly, whenever possible, we use very precise values for the E1 matrix elements, either from theory or experiments. First, we apply the RCC method to evaluate these E1 matrix elements. We use the

experimental results whenever we discover that they are more accurately available than our RCC results. It should be highlighted, though, the experimental E1 values lack the sign information that is necessary to determine the E1 polarizabilities that are induced by hyperfine interactions. Thus, we apply our computed E1 matrix elements to assign the sign to the experimentally determined E1 values. Again, we identify the valence contributions from low-lying bound states as the “Main” contributions to differentiate them in the analyses, while the contributions from high-lying continuum orbitals to the valence contributions are estimated using lower-order methods and reported as “Tail” contributions.

With the previously described strategy, only the valence contributions to $\alpha_J^S(\omega)$ and $\alpha_J^A(\omega)$ can be improved because the RCC method can only evaluate the E1 matrix elements involving the bound excited states. However, the correlation contributions to the core and core-valence Goldstone diagrams, represented as Figs. 6.1 (i) and (ii), that involve core excitations must be derived from first-principle calculations. To assess the core and core-valence contributions to $\alpha_J^S(\omega)$ and $\alpha_J^A(\omega)$, we have used RPA. In both cases, we rewrite the expressions for both $\alpha_J^S(\omega)$ and $\alpha_J^A(\omega)$ as

$$\alpha_J^{\mathcal{K}} = \langle \Phi_c | D | \Phi_c^{(\infty,1)+} \rangle + \langle \Phi_c | D | \Phi_c^{(\infty,1)-} \rangle, \quad (6.33)$$

where \mathcal{K} stands either for S (scalar) or for A (axial-vector) and $|\Phi_c^{(\infty,1)\pm}\rangle$ are the perturbation wave functions with respect to the DHF wave function $|\Phi_c\rangle$ for $\pm\omega$ values at the energy denominator. CP effects to all-orders and one order of external dipole interaction are present in these perturbative wave functions. Note that the corresponding angular factors for the scalar and axial-vector components are included in the above expression but are not displayed explicitly.

The ground state of ^{133}Cs has an experimentally determined $\alpha_J^S(0)$ value. Therefore, comparing our calculation with the experimental result will help in validating our calculations for the dynamic values of $\alpha_J^S(\omega)$ and $\alpha_J^A(\omega)$. Additionally, the test would be helpful in identifying third-order polarizabilities induced by hyperfine interaction. We

Table 6.4: Some of the important matrix elements (in a.u.) of the $\mathbf{T}_{\mathbf{J}}^{(1)}$ operator of ^{133}Cs . Numbers appearing as $a[b]$ mean $a \times 10^b$. See the text for explanation of how the experimental values for the off-diagonal matrix elements are inferred.

Transition	RCCSDT method	Experiment
$6S_{1/2}-6S_{1/2}$	5.817[-7]	5.797[-7] [36]
$6S_{1/2}-7S_{1/2}$	2.859[-7]	2.825[-7] [36, 37]
$6S_{1/2}-8S_{1/2}$	1.795[-7]	1.790[-7] [36, 38]
$6S_{1/2}-5D_{3/2}$	-1.674[-8]	
$6S_{1/2}-6D_{3/2}$	8.770[-9]	
$6P_{1/2}-6P_{1/2}$	7.341[-8]	7.364[-8] [39]
$6P_{1/2}-7P_{1/2}$	4.143[-8]	4.187[-8] [39, 40]
$6P_{1/2}-8P_{1/2}$	2.759[-8]	2.821[-8] [39, 41]
$6P_{1/2}-7P_{1/2}$	4.143[-8]	
$6P_{1/2}-9P_{1/2}$	-1.968[-8]	
$6P_{1/2}-6P_{3/2}$	-4.394[-9]	
$6P_{1/2}-7P_{3/2}$	-2.572[-9]	
$7P_{1/2}-7P_{1/2}$	2.371[-8]	2.381[-8] [40]
$7P_{1/2}-8P_{1/2}$	1.567[-8]	1.606[-8] [40, 41]
$7P_{1/2}-9P_{1/2}$	-11.177[-9]	
$7P_{1/2}-6P_{3/2}$	-2.402[-9]	
$7P_{1/2}-7P_{3/2}$	-1.417[-9]	
$8P_{1/2}-8P_{1/2}$	10.595[-9]	10.840[-9] [41]
$8P_{1/2}-9P_{1/2}$	-7.446[-9]	
$8P_{1/2}-6P_{3/2}$	-1.610[-9]	
$8P_{1/2}-7P_{3/2}$	-9.460[-10]	
$9P_{1/2}-9P_{1/2}$	5.313[-9]	
$6P_{3/2}-6P_{3/2}$	3.874[-8]	
$6P_{3/2}-7P_{3/2}$	2.214[-8]	
$6P_{3/2}-8P_{3/2}$	1.500[-8]	
$7P_{3/2}-7P_{3/2}$	12.648[-9]	

show all contributions to the DHF values of $\alpha_F^{S/A/T(2,1)}$ for the top, center, and normalization contributions, respectively, in Figs. 6.2, 6.3 and 6.4, using Goldstone diagrams. Although these contributions to α_{F,M_F} are much smaller than the second-order contributions, it is more difficult to evaluate them accurately. We designate contributions from Fig. 6.2 (i) and (ii) together as core, (iii) as core-core, (iv) as core-valence, (v)

Section 6.3. Approaches for calculation

Table 6.5: Breakdown of our calculated $\alpha_F^{S(2,1)}$, $\alpha_F^{A(2,1)}$ and $\alpha_F^{T(2,1)}$ values for the $F = 3$ and $F = 4$ levels of ^{133}Cs in terms of the valence, valence-core, core-valence, core-core and core contributions. Results are given for both the static and dynamic E1 polarizabilities (in 10^{-10} Hz/(V/m)²).

Polarizability	Contribution	$F = 3$			$F = 4$		
		$\lambda = \infty$	$\lambda = 936$ nm	$\lambda = 1064$ nm	$\lambda = \infty$	$\lambda = 936$ nm	$\lambda = 1064$ nm
$\alpha_F^{S(2,1)}$	Valence	-2.5584	-201.0945	-25.3858	1.9904	156.4064	19.7445
	Valence-Core	-0.0016	-0.0032	0.0601	0.0013	0.0025	-0.0467
	Core-Valence	0.0010	-0.0040	0.0402	-0.0008	0.0031	-0.0313
	Core-Core	-0.0009	-0.0009	-0.0009	0.0007	~ 0.0	0.0007
	Core	0.0010	0.0010	0.0010	-0.0015	-0.0015	-0.0015
$\alpha_F^{A(2,1)}$	Valence	0.0	-185.6502	-9.6217	0.0	-192.5270	-9.9781
	Valence-Core	0.0	0.0317	-0.0258	0.0	0.0329	-0.0268
	Core-Valence	0.0	0.0265	-0.0548	0.0	0.0275	-0.0569
	Core-Core	0.0	~ 0.0	~ 0.0	0.0	~ 0.0	~ 0.0
	Core	0.0	~ 0.0	~ 0.0	0.0	~ 0.0	~ 0.0
$\alpha_F^{T(2,1)}$	Valence	0.0165	8.4872	0.5794	-0.0308	-15.8428	-1.0815
	Valence-Core	0.0010	-0.0024	-0.0355	-0.0017	0.0045	0.0664
	Core-Valence	0.0010	-0.0024	-0.0355	-0.0017	0.0045	0.0664
	Core-Core	~ 0.0	~ 0.0	~ 0.0	~ 0.0	~ 0.0	~ 0.0
	Core	~ 0.0	~ 0.0	~ 0.0	~ 0.0	~ 0.0	~ 0.0

as valence-core and (vi) as valence contributions to make the various contributions to these quantities easier to understand. Diagrams in Fig. 6.3 have been divided similarly because of the striking similarities between 6.2 and 6.3. As in the case of the second-order E1 polarizabilities, diagram (i) is designated as core, diagram (ii) as valence-core and diagram (iii) as valence contributions in Fig. 6.4.

To estimate the valence contributions to $T^{\mathcal{K}}$, $C^{\mathcal{K}}$, and $R^{\mathcal{K}}$, we use similar procedures of evaluating the second-order E1 polarizabilities. A large number of matrix elements involving the $S_{1/2}$, $P_{1/2;3/2}$, and $D_{3/2}$ states are needed to estimate the valence contribution to $T^{\mathcal{K}}$, as Fig. 6.2 shows. The evaluation of $T^{\mathcal{K}}$ requires knowledge of the correct signs for the E1 and $T_J^{(1)}$ matrix elements, unlike the second-order polarizabilities. E1 matrix elements for transitions from the ground state to the $P_{1/2;3/2}$ states and $T_J^{(1)}$ matrix elements for transitions between the $P_{1/2;3/2}$ states are needed to evaluate

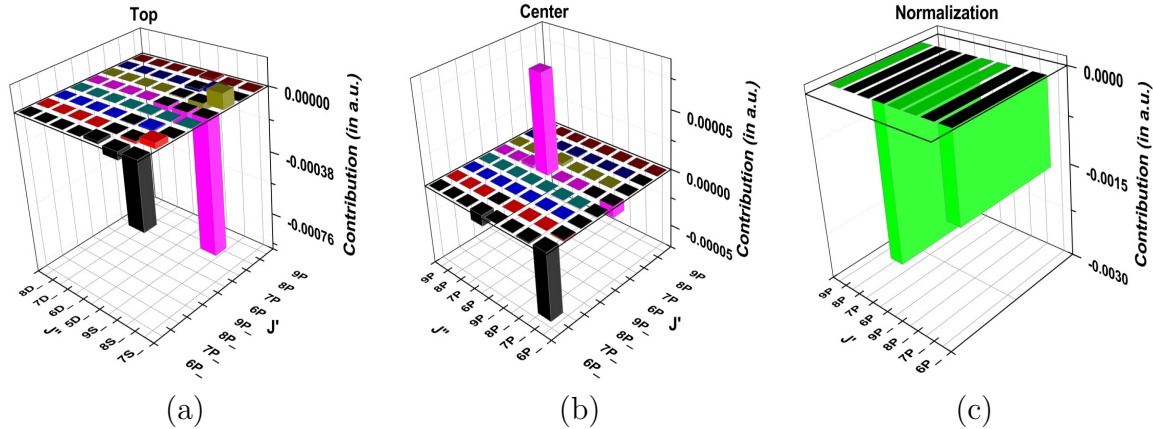


Figure 6.5: Demonstration of contributions from two different combinations of intermediate states (J' and J'') to the (a) top, (b) center and (c) normalization parts of the static $\alpha_F^{S(2,1)}$ value of the $F = 3$ level of ^{133}Cs . States with subscript $-$ symbol in the figure represent the lower angular momentum state of a fine-structure partner; i.e. P_- means $P_{1/2}$ and D_- denotes $D_{3/2}$, while P and D stand for the $P_{3/2}$ and $D_{5/2}$ states respectively.

the valence contribution to $C^\mathcal{K}$ in accordance with the parity and angular momentum selection rules. The valence contribution evaluation of $R^\mathcal{K}$ requires the same E1 matrix elements as in the case of the second-order E1 polarizabilities, in addition to the expectation value of $T_J^{(1)}$ in the ground state.

To achieve high accuracy in the third-order E1 polarizability calculations, reasonable consideration of the core, core-core, core-valence, and valence-core contributions to $T^\mathcal{K}$ and $C^\mathcal{K}$ is necessary. The methods previously discussed for the second-order E1 polarizabilities are applied to determine the core and valence-core contributions to $R^\mathcal{K}$. The core, core-core, core-valence and valence-core contributions to $T^\mathcal{K}$ and $C^\mathcal{K}$ require extremely careful estimation, in contrast to $R^\mathcal{K}$. The core contributions to these quantities necessitate matrix elements involving the core-core, core-virtual and virtual-virtual orbitals, as Figs. 6.2 and 6.3 indicate. It is clear that similar sets of matrix elements are needed for assessments of the core-valence and valence-core contributions. However, due to different angular momentum selection rules in both the expressions, different sets of core and virtual orbitals are involved in determining

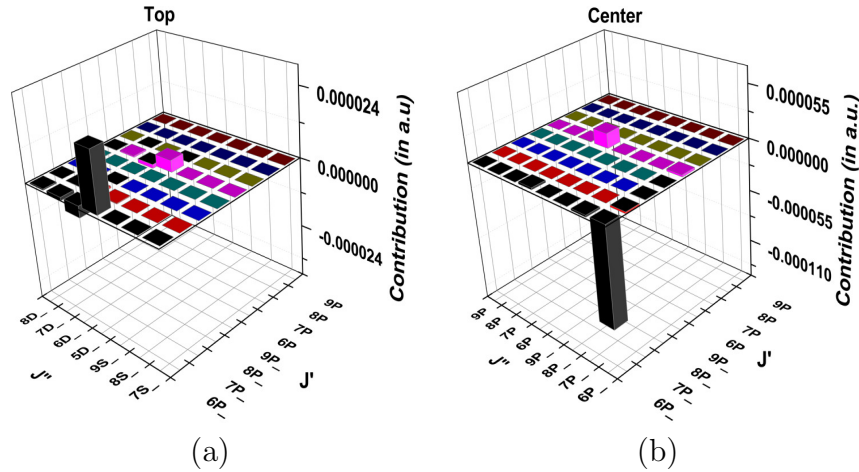


Figure 6.6: Contributions from different combinations of intermediate states (J' and J'') to the (a) top and (b) center parts of the static $\alpha_F^{T(2,1)}$ value of the $F = 3$ level of ^{133}Cs . The notation is same as in the previous figure.

the core and valence contributions to $T^\mathcal{K}$ and $C^\mathcal{K}$. Depending on how accurate they are, matrix elements between the bound states are either taken from the RCC theory or from experiments. Whenever possible, we also use the experimental energies in the denominator; if not, the calculated energies are used. The DHF method provides the E1 matrix elements between the core orbitals, while RPA provides the necessary elements between the virtual and core orbitals.

6.4 Results and Discussion

The α_J^S , α_J^A , $\alpha_F^{S(2,1)}$, $\alpha_F^{A(2,1)}$, and $\alpha_F^{T(2,1)}$ values of the $6S$ state of ^{133}Cs at various wavelengths are shown in Tables 6.1 and 6.2. For these assessments, we have utilized $g_I = 0.737885714$ with $I = 7/2$ from Ref. [29]. We have provided *ab initio* results from the DHF, RCCSD, and RCCSDT methods in the tables to understand the significance of the correlation effects and sensitivity of the results due to the use of the calculated and experimental energies. However, we provide our final recommended values from the semi-empirical approach. The recommended results, displayed in bold font in the tables, are compared with the experimental data that is currently available and a few

earlier computations from the literature. These tables show that the DHF values and the RCCSD results differ significantly from one another. This implies that the electron correlations are important for accurately determining both the second-order and third-order E1 polarizabilities. These differences are more prominent in the dynamic E1 polarizabilities. In fact, sign differences exist between the DHF and RCCSD values from the atomic polarizabilities, suggesting that these quantities exhibit large correlation contributions. Upon closely examining the DHF and RCCSD results, we find that the energy denominators are primarily responsible for the significant variations in these results. This explains why the use of experimental energies leads to noticeably better results. There are still significant differences between the RCCSDT and semi-empirical values for the dynamic polarizabilities, even though differences between the *ab initio* results and the semi-empirical values decrease when correlation effects through triple excitations are included in the calculations. Given that providing exact values for the E1 polarizabilities is our goal, the semi-empirical results are recommended for their future applications. We would like to make it clear at this point that the core, core-valence, and valence-core contributions are estimated from our calculations, while only the valence contributions are improved through the semi-empirical approach. Therefore, by incorporating higher-order correlation effects in the computation of the core, core-core, core-valence, and valence-core contributions, the calculated results can still be made more accurate. However, the semi-empirical values we quoted in Tables 6.1 and 6.2 have uncertainties that stem from the usual orders of magnitudes of these overlooked contributions.

Our recommended values agree perfectly with the measurements, as shown by a comparison of the static α_J^S and $\alpha_F^{T(2,1)}$ values with their experimental results [24, 30]. Our value is very close to the experimental result compared to the previous calculations of the static α_J^S values reported in Refs. [14, 31, 32, 33]. This is because, we have used a large number of precisely estimated E1 matrix elements from the most recent measurements [34, 35]. We anticipate that these results will also indicate the accuracy of our other calculated values, which include the dynamic polarizabilities at wavelengths of

Table 6.6: The ‘Main’ contributions of $T(\omega)$, $C(\omega)$ and $R(\omega)$ to the $\alpha_F^{S(2,1)}$, $\alpha_F^{A(2,1)}$, $\alpha_F^{T(2,1)}$ values of the $F = 3$ and $F = 4$ hyperfine levels of the ground state of ^{133}Cs at different wavelengths. All values are in a.u..

Contribution	$\lambda = \infty$			$\lambda = 936 \text{ nm}$			$\lambda = 1064 \text{ nm}$		
	$\alpha_F^{S(2,1)}$	$\alpha_F^{A(2,1)}$	$\alpha_F^{T(2,1)}$	$\alpha_F^{S(2,1)}$	$\alpha_F^{A(2,1)}$	$\alpha_F^{T(2,1)}$	$\alpha_F^{S(2,1)}$	$\alpha_F^{A(2,1)}$	$\alpha_F^{T(2,1)}$
For $F = 3$ level									
$T(\omega)$	-0.00121	0.0	0.00002	-0.00976	0.00145	0.00020	-0.00376	0.00012	0.00006
$C(\omega)$	0.00001	0.0	-0.00009	-0.01137	0.03754	-0.02486	-0.00031	0.00367	-0.00180
$R(\omega)$	-0.00376	0.0	0.0	-0.49459	0.18917	0.0	-0.05755	0.00794	0.0
For $F = 4$ level									
$T(\omega)$	0.00083	0.0	-0.00003	0.00670	0.00127	-0.00029	0.00258	0.00010	-0.00009
$C(\omega)$	-0.00001	0.0	0.00013	0.00780	0.03325	0.03703	0.00021	0.00325	0.00268
$R(\omega)$	0.00258	0.0	0.0	0.33926	0.16752	0.0	0.03948	0.00703	0.0

936 and 1064 nm. For the $F = 3$ and $F = 4$ levels, we were unable to find experimental results for $\alpha_F^{S(2,1)}$ and $\alpha_F^{A(2,1)}$ to compare directly with our estimated values. However, the results for $\alpha_F^{S(2,1)}$ agree reasonably with the calculation reported in Ref. [23], but they differ significantly for $\alpha_F^{T(2,1)}$. The authors of Ref. [23] used the BOs to estimate PC contributions and the combined TDHF+BO method to account for CP effects to all-orders. As discussed in the earlier chapters, PC and all RPA effects are implicitly included in the RCC method. We have found another semi-empirical calculation in which the values of $\alpha_F^{S(2,1)}$ and $\alpha_F^{T(2,1)}$ were calculated by the authors using the combined RCI and CP (RCICP) method [14]. Interestingly, there are notable differences between our computed results and theirs. We also found another semi-empirical result for $\alpha_F^{T(2,1)}$ for the $F = 4$ level [21]. In this calculation, the statistical Thomas-Fermi potential approach was used, and some of the matrix elements were scaled with experimental data. This approach resulted in an overestimated $\alpha_F^{T(2,1)}$ value compared to the experimental result and also differs from our calculation.

After discussing the final results, we want to examine each contribution to the

polarizability result and how it affects the accuracy of the second- and third-order E1 polarizabilities. Table 6.3 lists intermediate contributions to both $\alpha_J^S(\omega)$ and $\alpha_J^A(\omega)$ at various ω (λ) values. The E1 matrix elements of numerous significant transitions that contribute significantly to the valence part are listed; these are referred to as the “Main” elements. Refs. [34, 35] report precise measurements of lifetime or E1 polarizability in various atomic states, from which many of these E1 matrix elements are taken; others are derived from the current RCCSDT method. The “Tail” contributions to the valence part from the high-lying virtual states are estimated by using the E1 matrix elements from the DHF method and energies from the NIST database. RPA is used to estimate the contributions of the core and core-valence. It demonstrates that the accurate E1 matrix elements of the $6s\ ^2S_{1/2} \rightarrow 6p\ ^2P_{1/2;3/2}$ transitions and core contribution are the primary determinants of the precise estimate of the second-order E1 polarizabilities. Nonetheless, it is also crucial to take into account the contributions made by the E1 matrix elements of the $6s\ ^2S_{1/2} \rightarrow 7p\ ^2P_{1/2;3/2}$ transitions in order to increase the accuracy of the results.

Next, we talk about the contributions of $\alpha_F^{S(2,1)}$, $\alpha_F^{A(2,1)}$, and $\alpha_F^{T(2,1)}$ to the $F = 3$ and $F = 4$ hyperfine levels at various wavelengths. These calculations necessitate a large set of E1 and $T_J^{(1)}$ matrix elements, as was indicated in the previous section. Table 6.3 already provides a list of some of the dominantly contributing E1 matrix elements used in these computations. Many $T_J^{(1)}$ matrix elements that are crucial for evaluating $\alpha_F^{S(2,1)}$, $\alpha_F^{A(2,1)}$, and $\alpha_F^{T(2,1)}$ are listed in Table 6.4. With a few exceptions, where we use the exact values from the experiments [36, 37, 38, 39, 40, 41], the majority of these results are obtained using the RCCSDT method. Some of the off-diagonal matrix elements are estimated from the experimental values by using the relation

$$\langle J_f || T_J^{(1)} || J_i \rangle \simeq \sqrt{\langle J_f || T_J^{(1)} || J_f \rangle \langle J_i || T_J^{(1)} || J_i \rangle}. \quad (6.34)$$

We have also used the energies from the NIST database [28] in order to minimize uncertainties in the calculations.

In accordance with the discussion in the preceding section, these quantities are estimated by dividing their contributions into $T^{\mathcal{K}}$, $C^{\mathcal{K}}$, and $R^{\mathcal{K}}$. Moreover, there are contributions from the core, core-core, core-valence, valence-core, and valence in each of these. The individual contributions to the $\alpha_F^{S(2,1)}$, $\alpha_F^{A(2,1)}$, and $\alpha_F^{T(2,1)}$ values obtained by adding them from $T^{\mathcal{K}}$, $C^{\mathcal{K}}$, and $R^{\mathcal{K}}$ separately are shown in Table 6.5. These contributions come from the core, core-core, core-valence, valence-core, and valence parts. Table 6.5 clearly indicates that the valence contributions dominate the final values, while the contributions from the core, core-core, core-valence, and valence-core parts are small in $\alpha_F^{S(2,1)}$ and $\alpha_F^{A(2,1)}$. Notably, contributions to the tensor polarizabilities from the valence-core or core-valence correlations are non-negligible. The static $\alpha_F^{T(2,1)}$ value of the $F = 4$ level in ^{133}Cs has an experimental result available, which we plan to analyze in terms of various correlation contributions. Whereas the central value of the experimental result is $-3.34 \times 10^{-12} \text{ Hz}/(\text{V}/\text{m})^2$ [24], Table 6.5 indicates that the valence contribution to this quantity from our calculation is $-3.08 \times 10^{-12} \text{ Hz}/(\text{V}/\text{m})^2$. After ignoring their uncertainties, there is a discrepancy of approximately 8% between the two values. Minimizing uncertainty due to systematic effects in the measurement of $\alpha_F^{T(2,1)}$ would be extremely difficult, so it is important to figure out the roles of other physical contributions to the theoretical result in order to carry out future measurements more precisely. According to our analysis, the valence-core and core-valence contributions to the static $\alpha_F^{T(2,1)}$ value of the $F = 4$ level are quite significant, whereas the core and core-core contributions are negligibly small. The table shows that when these contributions are taken into account, the difference between the theoretical and experimental value drops to 2%. It is noteworthy that the contributions of valence-core and core-valence to the dynamic $\alpha_F^{T(2,1)}$ values at $\lambda = 936 \text{ nm}$ and $\lambda = 1064 \text{ nm}$ are remarkably insignificant in comparison to their respective valence contributions.

In contrast with the second-order E1 polarizabilities, the intermediate states' contributions are more difficult to show because their formulas have two summations (Eqs. 6.26 and 6.27). To demonstrate the significance of the contributions from different intermediate states, we, however, used an alternative approach. Three-dimensional plots

of contributions from two distinct sets of intermediate states to the valence parts of $T^{\mathcal{K}}$, $C^{\mathcal{K}}$, and $R^{\mathcal{K}}$ to the static $\alpha_F^{S(2,1)}$ and $\alpha_F^{T(2,1)}$ values are shown in Figs. 6.5 and 6.6, respectively. They are only displayed as a representative case for the $F = 3$ level. These figures demonstrate that the third-order E1 polarizabilities are primarily caused by matrix elements of a few selective transitions involving combinations of a few selective intermediate states. Acquiring this knowledge is crucial to further increasing the precision of these quantities. The intermediate states $7S_{1/2}$ and $6P_{1/2,3/2}$ contribute most to the top, center, and normalization parts of $\alpha_F^{S(2,1)}$, as Fig. 6.5 makes it apparent. As Fig. 6.6 shows, significant contributions to the top and center parts of $\alpha_F^{T(2,1)}$ originate from $5D_{3/2}$ and $6P_{1/2,3/2}$ states. Based on the sums of total contributions from all possible intermediate states in Table 6.6, we present the Main contributions to both static and dynamic $T^{\mathcal{K}}$, $C^{\mathcal{K}}$, and $R^{\mathcal{K}}$ values of $\alpha_F^{S(2,1)}$, $\alpha_F^{A(2,1)}$, and $\alpha_F^{T(2,1)}$. As can be seen from the table, the $R^{\mathcal{K}}$ component exhibits the dominant contribution to $\alpha_F^{S(2,1)}$ followed by $T^{\mathcal{K}}$ and then the $C^{\mathcal{K}}$ component. For $\alpha_F^{A(2,1)}$ also $R^{\mathcal{K}}$ contribution dominates, followed by the $C^{\mathcal{K}}$ part. In the case of $\alpha_F^{T(2,1)}$, the leading contribution comes from the $C^{\mathcal{K}}$ part, while the $R^{\mathcal{K}}$ component is zero. We compare our calculated Stark shift coefficient, $k_s = -\frac{1}{2}(\alpha_{F=4}^{S(2,1)} - \alpha_{F=3}^{S(2,1)})$, with the previously reported values in Table 6.7. The table shows that our result, $-2.274(10) \times 10^{-10} \text{ Hz}/(\text{V/m})^2$, is in good agreement with the most accurate measurement that has been found thus far, $-2.271(4) \times 10^{-10} \text{ Hz}/(\text{V/m})^2$ in Ref. [15]. The values in Refs. [16] and [17] also agree with it. On the other hand, it significantly differs from other measurements later reported in Refs. [18, 19]. We are unable to shed light on the differences between the experimental results. However, we have looked closely at and discussed the variations found in the theoretical outcomes. Our results are as accurate as the calculated value given in Ref. [13]; in comparison to other theoretical works [8, 9, 10, 11, 12, 14, 23], our result agrees better with the experiment [15]. Furthermore, our DHF value of $-2.792 \times 10^{-10} \text{ Hz}/(\text{V/m})^2$ of k_s agrees with the DHF value $-2.799 \times 10^{-10} \text{ Hz}/(\text{V/m})^2$ of Ref. [13]. Again, the authors of Ref. [13] have discovered that the continuum (Tail) contributes significantly to k_s . In this work, we also independently confirm this result

Table 6.7: Summary of the k_s value from different theoretical and experimental works in units of 10^{-10} Hz/(V/m)².

Reference	k_s value
This work	-2.274(10)
Theory [8]	-1.97(9)
Theory [9]	-2.06(1)
Theory [10]	-2.281(4)
Theory [11]	-2.28
Theory [12]	-2.26(2)
Theory [13]	-2.271(8)
Theory [14]	-2.324(5)
Theory [23]	-2.26(2)
Experiment [15]	-2.271(4)
Experiment [16]	-2.25(5)
Experiment [17]	-2.20(26)*
Experiment [18]	-1.89(12)*
Experiment [19]	-2.05(4)

* k_s calculated from BBR shift measurement.

and confirm that the k_s value equals -2.085×10^{-10} Hz/(V/m)² in the absence of the Tail contribution. By examining the different contributions listed in Tables 6.5 and 6.6, one can explicitly infer these Tail contributions from our calculations to the hyperfine interaction induced E1 polarizabilities. These tables show that the Tail contribution to k_s is 8% of the total contribution and that this part is primarily responsible for the largest uncertainty in our final k_s value.

6.5 Summary

In this chapter, we have conducted a detailed analysis of the electric dipole polarizability of the hyperfine levels of the ground state of ¹³³Cs using the RCC method. We have presented both the second-order atomic and third-order hyperfine interaction induced polarizability values. Our static values for both the second-order and third-order electric

dipole polarizabilities align well with the available experimental results. Additionally, we have identified the reasons for the discrepancies among experimental and earlier theoretical values for k_s and $\alpha_F^{T(2,1)}$. Previous studies overlooked the contributions from core and high-lying continuum orbitals. We have found that the contributions from these orbitals are significant, and their inclusion is necessary for precise calculation of polarizability values. This study also proves the superiority of the RCC theory over other methods like TDHF+BO and RCICP used in earlier studies. Given that methods similar to TDHF+BO were previously used to estimate the NSD PV amplitude in ^{133}Cs , our RCC calculations are expected to improve the result for $E1_{PV}^{NSD}$.

Bibliography

- [1] *The International System of Units (SI)*, edited by B. N. Taylor (U.S. GPO, Gaithersburg, MD) (2001).
- [2] A. W. Carr and M. Saffman, *Phys. Rev. Lett.* **117**, 150801 (2016).
- [3] N. Schlosser, G. Reymond, I. Protsenko, and P. Grangier, *Nature*, **411**, 1024 (2001).
- [4] C. P. Williams and S. H. Clearwater, *Explorations in Quantum Computing* (Springer-Verlag), New York, 1997).
- [5] D. P. DiVincenzo, *Fortschr. Phys.* **48**, 771 (2000).
- [6] A. Negretti, P. Treutlein, and T. Calarco, *Quantum Inf. Process.* **10**, 721 (2011).
- [7] M. G. Kozlov, M.S. Safronova, J.R. Crespo Lopez-Urrutia, and P.O. Schmidt, *Rev. Mod. Phys.* **90**, 045005 (2018).
- [8] S. Micalizio, A. Godone, D. Calonico, F. Levi, and L. Lorini, *Phys. Rev. A* **69**, 053401 (2004).
- [9] S. Ulzega, A. Hofer, P. Moroshkin, and A. Weis, arxiv physics/0604233 (Unpublished).
- [10] A. Weis and S. Ulzega *SPIE Proceedings* **6604**, 660408 (2007).
- [11] V. G. Palchikov, Y. S. Domnin, and A. V. Novoselov, *J. Opt. B* **5**, S131 (2003).

- [12] E. J. Angstmann, V. A. Dzuba, and V. V. Flambaum, Phys. Rev. Lett. **97**, 040802 (2006).
- [13] K. Beloy, U. I. Safronova, and A. Derevianko, Phys. Rev. Lett. **97**, 040801 (2006).
- [14] J. Jiang, X.J. Li, X. Wang, C.-Z. Dong, and Z. W. Wu, Phys. Rev. A **102**, 042823 (2020).
- [15] E. Simon, P. Laurent, and A. Clairon, Phys. Rev. A **57**, 436 (1998).
- [16] J. R. Mowat, Phys. Rev. A **5**, 1059 (1972).
- [17] A. Bauch and R. Schroder, Phys. Rev. Lett. **78**, 622 (1997).
- [18] F. Levi, D. Calonico, L. Lorini, S. Micalizio, and A. Godone, Phys. Rev. A **70**, 033412 (2004).
- [19] A. Godone, D. Calonico, F. Levi, S. Micalizio, and C. Calosso, Phys. Rev. A **71**, 063401 (2005).
- [20] P. G. H. Sandars, Phys. Rev. Lett. **19**, 1396 (1967).
- [21] S. Ulzega, A. Hofer, P. Moroshkin, and A. Weis, Europhys. Lett. **76**, 1074 (2006).
- [22] A. Hofer, P. Moroshkin, S. Ulzega, and A. Weis, Phys. Rev. A **77**, 012502 (2008).
- [23] V. A. Dzuba, V. V. Flambaum, K. Beloy, and A. Derevianko, Phys. Rev. A **82**, 062513 (2010).
- [24] C. Ospelkaus, U. Rasbach, and A. Weis, Phys. Rev. A **67**, 011402(R) (2003).
- [25] J. McKeever, J. R. Buck, A. D. Boozer, A. Kuzmich, H.-C. Nagerl, D. M. Stamper-Kurn, and H. J. Kimble, Phys. Rev. Lett. **90**, 133602 (2003).
- [26] B. Arora, M. S. Safronova, and C. W. Clark, Phys. Rev. A, **76**, 052509 (2007).
- [27] Y. M. Yu, B. K. Sahoo, Phys. Rev. A, **96**, 050502(R) (2017).

- [28] A. Kramida, Y. Ralchenko, and J. Reader, National Institute of Standards and Technology, Gaithersburg, MD (Available at: <http://physics.nist.gov/asd>) (2018).
- [29] N. Stone, *Atomic Data and Nuclear Data Tables*, **90**, 75–176 (2005).
- [30] J. M. Amini and H. Gould *Phys. Rev. Lett.*, **91**, 153001 (2003).
- [31] M. S. Safronova, W. R. Johnson, and A. Derevianko, *Phys. Rev. A* **60**, 4476 (1999).
- [32] S.H. Patil, K.T. Tang, *Chem. Phys. Lett.* **301**, 64 (1999).
- [33] A. Derevianko, W. R. Johnson, M. S. Safronova, and J. F. Babb, *Phys. Rev. Lett.* **82**, 3589 (1999).
- [34] L. Young, W. T. Hill, S. J. Sibener, S. D. Price, C. E. Tanner, C. E. Wieman, and S. R. Leone, *Phys. Rev. A* **50**, 2174 (1994).
- [35] A. Damitz, G. Toh, E. Putney, C. E. Tanner and D. S. Elliott, *Phys. Rev. A* **99**, 062510 (2019).
- [36] M. Allegrini, E. Arimondo, L. A. Orozco, *Journal of Phys. and Chem. Ref. Data* **51**, 4 (2022).
- [37] Guang Yang, Jie Wang, Baodong Yang, and Junmin Wang, *Laser Phys. Letts.* **13**, 085702 (2016).
- [38] P. Fendel, S. D. Bergeson, Th. Udem, and T. W. Hansch, *Opt. Lett.* **32**, 701 (2007).
- [39] D. Das and V. Natarajan, *J. Phys. B* **39**, 2013 (2006).
- [40] W. D. Williams, M. T. Herd, and W. B. Hawkins, *Laser Phys. Letts.* **15**, 095702 (2018).
- [41] W. Happer, *Atomic Physics 4*, edited by G. zu Putlitz, E. W. Weber, and A. Winnacker, (Plenum Press, New York) pp. 651-682 (1974).

Chapter 7

RCC calculations of NSD PV in ^{133}Cs

THE primary goal of studying NSD PV is to probe the NAM, a fundamental property of atomic nucleus. The NAM originates due to the presence of weak interaction among the nucleons. Although NAM is theoretically predicted, its existence is still under debate. The NAM value extracted in ^{133}Cs by combing high-precision PV measurements for the $6s\ ^2S_{1/2}$ - $7s\ ^2S_{1/2}$ transition [1] with atomic many-body calculations is at variance with the results from the nuclear shell model calculations and the nucleon-nucleon scattering experiments [2, 3, 4]. This discrepancy between atomic and nuclear results could be due to either (i) incomplete correlation in atomic many-body calculations, (ii) unknown systematic effects in the atomic experiment, or (iii) inappropriate approximations in nuclear calculations.

In this chapter, we focus on the first possibility. Herein we use various atomic many-body methods to calculate the NSD PV amplitudes among different hyperfine levels of the $6s\ ^2S_{1/2} \rightarrow 7s\ ^2S_{1/2}$ transition in ^{133}Cs . As mentioned earlier in Chapter 1, very few theoretical studies have been carried out to estimate the NAM in ^{133}Cs [2, 5, 6, 7]. In one of the early calculations, Flambaum and Dzuba *et al.* [5, 6] used the combined DHF and BO method to estimate the $E1_{PV}^{NSD}$ values between different

hyperfine levels of the $6s\ ^2S_{1/2} \rightarrow 7s\ ^2S_{1/2}$ transition in ^{133}Cs . Subsequently, Johnson *et al.* [7] employed RPA to compute these amplitudes through the inclusion of CP effect up to all-order. As we have already shown in the earlier chapters of the thesis, DHF or RPA cannot incorporate many correlation effects like PC and DCP. Thus, it is necessary to calculate the $E1_{PV}^{NSD}$ amplitudes in ^{133}Cs more accurately by including the correlation effects that were omitted earlier. Herein, we estimate the $E1_{PV}^{NSD}$ amplitudes among different hyperfine levels of the $6s\ ^2S_{1/2}$ and $7s\ ^2S_{1/2}$ states using the RCC theory, which captures these effects comprehensively. Further, to validate our analysis, we also present results from the DHF, CPDF, RPA, and CPDF-RPA methods.

7.1 Theory

Recalling Eq. 1.25, we can write the NSD PV Hamiltonian

$$H_{PV}^{NSD} = \frac{G_F}{\sqrt{2}} K_W \vec{\alpha}^D \cdot \vec{I}\rho(r). \quad (7.1)$$

One thing to note here is that the magnitude of K_W depends on the contributions from both NAM and NSD interactions within an atomic nucleus. As K_W is the quantity to be inferred by combining measurement with atomic calculation, we express the above Hamiltonian as

$$H_{PV}^{NSD} = K_W H^{NSD}, \quad (7.2)$$

so that calculations can be performed using H^{NSD} . Again, to simplify the calculations using the electronic component, we can express H^{NSD} , separating electronic and nuclear components, as

$$H^{NSD} = \frac{G_F}{\sqrt{2}} \vec{I}^{(1)} \cdot \vec{K}^{(1)}, \quad (7.3)$$

where $\vec{K}^{(1)}$ is the electronic component. Following the same approach as NSI PV amplitude calculation, we express $|\Psi_v\rangle^F$ as

$$|\Psi_v\rangle^F \simeq |\Psi_v^{F,(0)}\rangle + K_W |\Psi_v^{F,(1)}\rangle, \quad (7.4)$$

where $|\Psi_v^{F,(0)}\rangle$ is the hyperfine level wave function due to em interactions and $|\Psi_v^{F,(1)}\rangle$ is the first correction due to H^{NSD} . One important thing to note is that while K_W may not be small, H_{PV}^{NSD} is very small compared to the em interactions in the atomic systems. Therefore, K_W in the perturbative analysis does not indicate the strength of the interaction; rather, it simply indicates the order of perturbation. Keeping this in mind, the $E1_{PV}^{NSD}$ between two hyperfine levels $|\Psi_f\rangle^F \equiv |(IJ_f)F_f M_f\rangle$ and $|\Psi_i\rangle^F \equiv |(IJ_i)F_i M_i\rangle$, can be expressed using the Wigner-Eckart theorem as

$$E1_{PV}^{NSD} = (-1)^{F_f - M_f} \begin{pmatrix} F_f & 1 & F_i \\ -M_f & M_f - M_i & M_i \end{pmatrix} \times \langle F_f || D_{PV}^{NSD} || F_i \rangle, \quad (7.5)$$

where $\langle F_f || D_{PV}^{NSD} || F_i \rangle$ is the reduced matrix element and D_{PV}^{NSD} is the PV interaction induced E1 operator. From atomic calculation point of view, the actual quantity of interest from is $\mathcal{X}_{PV}^{NSD} = \langle F_f || D_{PV}^{NSD} || F_i \rangle / K_W$. In the sum-over-states approach, we can write \mathcal{X}_{PV}^{NSD} as

$$\begin{aligned} \mathcal{X}_{PV}^{NSD} &= \sum_{n \neq i} \frac{\langle F_f || D || F_n \rangle \langle F_n || H^{NSD} || F_i \rangle}{\mathcal{N}_F(E_{F_i}^{(0)} - E_{F_n}^{(0)})} + \sum_{n \neq f} \frac{\langle F_f || H^{NSD} || F_n \rangle \langle F_n || D || F_i \rangle}{\mathcal{N}_F(E_{F_f}^{(0)} - E_{F_n}^{(0)})} \\ &\simeq \sum_{n \neq i} \frac{\langle F_f || D || F_n \rangle \langle F_n || H^{NSD} || F_i \rangle}{\mathcal{N}_F(E_i^{(0)} - E_n^{(0)})} + \sum_{n \neq f} \frac{\langle F_f || H^{NSD} || F_n \rangle \langle F_n || D || F_i \rangle}{\mathcal{N}_F(E_f^{(0)} - E_n^{(0)})}, \end{aligned} \quad (7.6)$$

where $E_{F_n}^{(0)}$ and $E_n^{(0)}$ are the hyperfine and atomic energy values of the n^{th} state, respectively, and $\mathcal{N}_F = \sqrt{\langle \Psi_f^{(0)} | \Psi_f^{(0)} \rangle^F \langle \Psi_i^{(0)} | \Psi_i^{(0)} \rangle^F}$ is the normalization factor of the hyperfine levels. However, dealing with the wave functions in the hyperfine coordinate system is

challenging. To address this, we express the $|(IJ)FM_F\rangle$ levels in perturbation series as

$$\begin{aligned}
 |(IJ)FM_F\rangle &= |II; JM_J\rangle + \sum_{J', M_{J'}} |II; J'M_{J'}\rangle \\
 &\times \frac{\langle II; J'M_{J'} | H_{hf} | II; JM_J \rangle}{E_J - E_{J'}} + \dots .
 \end{aligned} \tag{7.7}$$

Here H_{hf} is the hyperfine interaction Hamiltonian. In this work, we consider only the first term $|II; JM_J\rangle$. Using this approximation and substituting the following relations [8]

$$\begin{aligned}
 \langle (I, J_n)F_n, M_n | \vec{K}^{(1)} \cdot \vec{I} | (I, J_i)F_i, M_i \rangle &= \delta_{F_n, F_i} \delta_{M_n, M_i} \times (-1)^{I+F_i+J_i} \sqrt{I(I+1)(2I+1)} \\
 &\times \begin{Bmatrix} J_n & J_i & 1 \\ I & I & F_i \end{Bmatrix} \langle J_n || K^{(1)} || J_i \rangle
 \end{aligned} \tag{7.8}$$

and

$$\begin{aligned}
 \langle (I, J_f)F_f, M_f | D | (I, J_n)F_n, M_n \rangle &= \sqrt{(2F_f+1)(2F_n+1)} \times (-1)^{F_f-M_f} \begin{pmatrix} F_f & 1 & F_n \\ -M_f & q & M_n \end{pmatrix} \\
 &\times (-1)^{I+F_n+J_f+1} \begin{Bmatrix} J_n & J_f & 1 \\ F_f & F_n & I \end{Bmatrix} \langle J_f || D || J_n \rangle
 \end{aligned} \tag{7.9}$$

in Eq. 7.6, it gives

$$\begin{aligned}
 \mathcal{X}_{PV}^{NSD} &= \mathcal{C} \left[\sum_{n \neq i} \begin{Bmatrix} J_n & J_i & 1 \\ I & I & F_i \end{Bmatrix} \begin{Bmatrix} J_n & J_f & 1 \\ F_f & F_i & I \end{Bmatrix} (-1)^{(J_f-J_i+1)} \right. \\
 &\times \frac{\langle J_f || D || J_n \rangle \langle J_n || K^{(1)} || J_i \rangle}{E_i^{(0)} - E_n^{(0)}} \\
 &+ \sum_{n \neq f} \begin{Bmatrix} J_n & J_f & 1 \\ I & I & F_f \end{Bmatrix} \begin{Bmatrix} J_n & J_i & 1 \\ F_i & F_f & I \end{Bmatrix} (-1)^{(F_f-F_i+1)} \\
 &\left. \times \frac{\langle J_f || K^{(1)} || J_n \rangle \langle J_n || D || J_i \rangle}{E_f^{(0)} - E_n^{(0)}} \right],
 \end{aligned} \tag{7.10}$$

where $\mathcal{C} = \frac{G_F}{\sqrt{2}} \sqrt{I(I+1)(2I+1)(2F_f+1)(2F_i+1)}$.

We can express \mathcal{X}_{PV}^{NSD} in terms of the final state ($|\Psi_f\rangle$) and initial state ($|\Psi_i\rangle$) atomic wave functions, as

$$\mathcal{X}_{PV}^{NSD} = \frac{1}{\mathcal{N}} \langle \Psi_f^{(0)} | \tilde{D}_f | \Psi_i^{(1)} \rangle + \langle \Psi_f^{(1)} | \tilde{D}_i | \Psi_i^{(0)} \rangle, \quad (7.11)$$

where $\mathcal{N} = \sqrt{\langle \Psi_f^{(0)} | \Psi_f^{(0)} \rangle \langle \Psi_i^{(0)} | \Psi_i^{(0)} \rangle}$ is the normalization factor of the atomic wave functions, \tilde{D}_i and \tilde{D}_f are the effective E1 operators which are explicitly given by

$$\tilde{D}_i = (-1)^{(F_f - F_i + 1)} \sum_n \langle J_n || D || J_i \rangle \times \begin{Bmatrix} J_n & J_f & 1 \\ I & I & F_f \end{Bmatrix} \begin{Bmatrix} J_n & J_i & 1 \\ F_i & F_f & I \end{Bmatrix} \quad (7.12)$$

and

$$\tilde{D}_f = (-1)^{(J_f - J_i + 1)} \sum_n \langle J_f || D || J_n \rangle \times \begin{Bmatrix} J_n & J_i & 1 \\ I & I & F_i \end{Bmatrix} \begin{Bmatrix} J_n & J_f & 1 \\ F_f & F_i & I \end{Bmatrix}. \quad (7.13)$$

Alternatively, following the discussion for $E1_{PV}^{NSI}$ in earlier chapter, we can express \mathcal{X}_{PV}^{NSD} amplitude between the states $|\Psi_f\rangle$ and $|\Psi_i\rangle$ as the second-order correction by considering D as an additional perturbation i.e.

$$\begin{aligned} \mathcal{X}_{PV}^{NSD} \simeq & \langle \Psi_f^{(0,0)} | \bar{D} | \Psi_i^{(1,0)} \rangle + \langle \Psi_f^{(0,0)} | \bar{K}^{(1)} | \Psi_i^{(0,1)} \rangle \\ & + \langle \Psi_f^{(0,0)} | \Psi_i^{(1,1)} \rangle, \end{aligned} \quad (7.14)$$

in which the superscripts (m, n) denotes m orders of $K^{(1)}$ and n orders of D . Eq. 7.6 is used in the RPA, CPDF and CPDF-RPA methods without considering the DCP effects. However, the DCP effects can be estimated in the CPDF-RPA method through the last term of Eq. 7.14. For the RCC theory, the DCP effects can be included by either adopting Eq. 7.6 or Eq. 7.14. As it is not convenient to determine the second-order perturbed wave function, $|\Psi_i^{(1,1)}\rangle$, using the formula given by Eq. 7.10, we give

here a more generic formula for \mathcal{X}_{PV}^{NSD} using the tensor product relations [8, 9] as

$$\begin{aligned}
 \mathcal{X}_{PV}^{NSD} = & \mathcal{C} \sum_{k=0,1,2} (2k+1) \left[\sum_{n \neq i} \begin{Bmatrix} J_f & J_i & k \\ I & I & 1 \\ F_f & F_i & 1 \end{Bmatrix} \begin{Bmatrix} J_f & k & J_i \\ 1 & J_n & 1 \end{Bmatrix} \right. \\
 & \times (-1)^{(J_f+J_i+1)} \frac{\langle J_f || D || J_n \rangle \langle J_n || K^{(1)} || J_i \rangle}{E_i^{(0)} - E_n^{(0)}} \\
 & + \sum_{n \neq f} \begin{Bmatrix} I & I & 1 \\ J_f & J_i & k \\ F_f & F_i & 1 \end{Bmatrix} \begin{Bmatrix} J_f & k & J_i \\ 1 & J_n & 1 \end{Bmatrix} \\
 & \left. \times (-1)^{(2J_f+F_f-F_i+1)} \frac{\langle J_f || K^{(1)} || J_n \rangle \langle J_n || D || J_i \rangle}{E_f^{(0)} - E_n^{(0)}} \right]. \quad (7.15)
 \end{aligned}$$

It can be shown that both Eqs. 7.10 and 7.15 are equivalent. However, in Eq. 7.15, F_i , F_f and J_n are not coupled through either $6j$ - or $9j$ -symbols as in the case for Eq. 7.10. This helps to implement the above expression in the CPDF-RPA method to compute \mathcal{X}_{PV}^{NSD} . \bar{D} and $\bar{K}^{(1)}$ can be defined as

$$\bar{D} = (-1)^{(J_f+J_i+1)} \sum_{k=0,1,2} (2k+1) \sum_n \begin{Bmatrix} J_f & J_i & k \\ I & I & 1 \\ F_f & F_i & 1 \end{Bmatrix} \begin{Bmatrix} J_f & k & J_i \\ 1 & J_n & 1 \end{Bmatrix} \langle J_f || D || J_n \rangle \quad (7.16)$$

and

$$\bar{K}^{(1)} = (-1)^{(2J_f+F_f-F_i+1)} \sum_{k=0,1,2} (2k+1) \sum_n \begin{Bmatrix} I & I & 1 \\ J_f & J_i & k \\ F_f & F_i & 1 \end{Bmatrix} \begin{Bmatrix} J_f & k & J_i \\ 1 & J_n & 1 \end{Bmatrix} \langle J_f || K^{(1)} || J_n \rangle. \quad (7.17)$$

Table 7.1: Estimated \mathcal{X}_{PV}^{NSD} values of the hyperfine transitions ($F_f - F_i$) among all possible hyperfine levels F_f and F_i of the $7s\ ^2S_{1/2}$ and $6s\ ^2S_{1/2}$ states, respectively, in ^{133}Cs from different methods. All the values are given in the units of $iea_0K_W \times 10^{-12}$. We also compare these values with the values reported in previous works at different levels of approximation in the many-body method.

Method	3 - 3	3 - 4	4 - 3	4 - 4
		This work		
DHF	1.9029	5.4663	4.7337	2.1665
CPDF	2.3345	7.0455	6.1470	2.6579
RPA	1.8305	5.6738	4.9689	2.0842
CPDF-RPA*	2.2456	7.2348	6.3707	2.5564
CPDF-RPA	2.0139	6.9891	6.2142	2.2928
RCCSD	2.3344	7.3943	6.4958	2.6575
		Other works		
DHF [7]	1.908	5.481	4.746	2.173
DHF [10]	2.011	5.774	5.000	2.289
RPA [7]	2.249	7.299	6.432	2.560
PRCC [†] [10]	2.274	6.313	5.446	2.589
SD [11]		7.948	7.057	

[†]The PRCC method of Ref. [10] is same as our RCCSD method.

As the matrix elements of both the $K^{(1)}$ and D operators and all the coupling angular factors are taken into account in the evaluation of $|\Psi_i^{(1,1)}\rangle$, any additional effective operator has not been defined for estimating \mathcal{X}_{PV}^{NSD} . We have implemented CPDF, RPA, CPDF-RPA and RCC methods to evaluate \mathcal{X}_{PV}^{NSD} . Because of the rank of the $K^{(1)}$ operator, the angular momentum coupling scheme for NSD PV is very complicated compared to NSI PV.

7.2 Results and Discussions

We present our results for \mathcal{X}_{PV}^{NSD} amplitudes between the $F = 3$ and $F = 4$ hyperfine levels of the $6s\ ^2S_{1/2} \rightarrow 7s\ ^2S_{1/2}$ transition in the ^{133}Cs atom in Table 7.1 using the DHF,

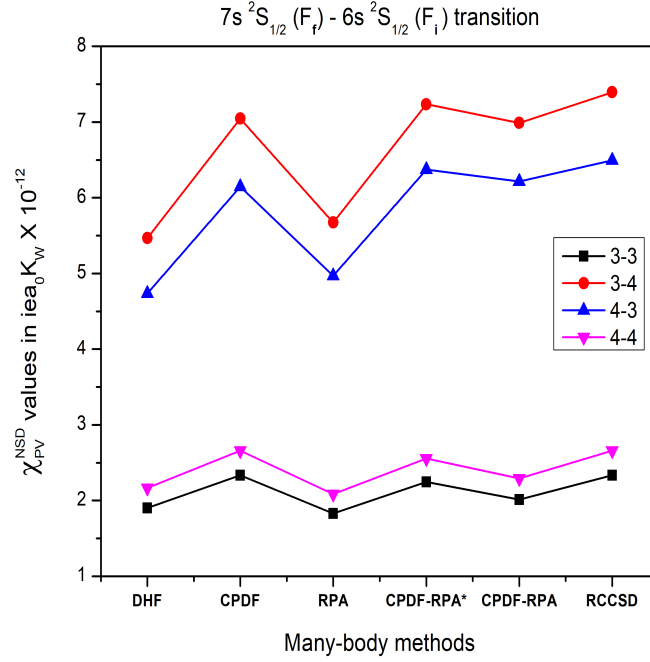


Figure 7.1: \mathcal{X}_{PV}^{NSD} values for the $F_f - F_i$ transitions of the $7s\ ^2S_{1/2}(F_f)$ and $6s\ ^2S_{1/2}(F_i)$ states in ^{133}Cs from different methods. The plotted values are presented in the same units as in Table 7.1.

CPDF, RPA, CPDF-RPA*, CPDF-RPA and RCCSD methods. The table shows that the value of the \mathcal{X}_{PV}^{NSD} values in the $F_i = 3 \rightarrow F_f = 3$ and $F_i = 4 \rightarrow F_f = 4$ transitions are smaller compared to the $F_i = 3 \rightarrow F_f = 4$ and $F_i = 4 \rightarrow F_f = 3$ transitions. In the same table, we also compare our results with earlier reported values in the literature [7, 10, 11]. We can conclude that CP effects arising through the $K^{(1)}$ are significantly stronger than those arising through the E1 operator by comparing the results obtained from the CPDF and RPA methods. Interestingly this correlation trend is more peculiar in the CPDF-RPA* method, in which results between the $F_i = 3 \rightarrow F_f = 4$ and $F_i = 4 \rightarrow F_f = 3$ hyperfine levels are larger than the CPDF values while they are smaller for the $F_i = 3 \rightarrow F_f = 3$ and $F_i = 4 \rightarrow F_f = 4$ hyperfine levels compared to the CPDF values. So from these results, it would not be clearly argued that the CP effects through the E1 operator always contribute with an opposite sign than the $K^{(1)}$ operator. Just like earlier in the case of the NSI PV study, the difference between CPDF-RPA*

and CPDF-RPA corresponds to DCP contribution. From the table, we can see that the DCP contributions are quite significant, and they reduce the values of \mathcal{X}_{PV}^{NSD} obtained using the CPDF-RPA* method. The results from the RCCSD method are seen to be larger than the CPDF-RPA method. As we have shown in the earlier chapter, the RCC method includes all correlation contributions from the CPDF-RPA method as well as contributions from PC effects and correlations among CP and PC effects to all-orders. Although results from the CPDF-RPA* and RCCSD methods appear to be very similar, one has to note that the RCCSD method includes DCP effects, whereas the CPDF-RPA* method does not. This suggests that the contributions from the PC effects play an important role in accurate determination of \mathcal{X}_{PV}^{NSD} values and cannot be neglected. To gauge the magnitudes of the \mathcal{X}_{PV}^{NSD} values quantitatively for the transitions between different hyperfine levels, we plot these values in Fig. 7.1.

As can be seen in Table 7.1, our calculations at the DHF level agree quite well with the calculations carried out in Ref. [7] but differ a little bit from Ref. [10]. A careful comparison shows the RPA values of Ref. [7] match well with our CPDF-RPA* results. From this analysis, we can assume that the RPA method of Ref. [7] is not exactly the same as our RPA method; rather, it considers the combined results from both the RPA and CPDF methods. However, it appears that in Ref. [7], DCP contributions were not included in the calculation. The calculations in Ref. [11] based on a sum-over-states approach in which E1 and $K^{(1)}$ matrix elements of a few low-lying transitions are explicitly evaluated using the linearized RCC theory (referred to as ‘SD’ in the original paper) and experimental energy values were used. Limitations of the sum-over-states approach have already been discussed in earlier chapter. The differences between the sum-over-states SD and *ab initio* RCCSD results could be attributed to the DCP effects and contributions from the Core and Tail contributions. The comparison between the results from the PRCC method of Ref. [10] and the RCCSD method of the present work shows large differences. This could be due to two reasons: the use of different size basis functions and the difference in the implementation of the method. Although GTOs are used in both works, different sets of parameters are being considered. Since

Table 7.2: The Core and Valence contributions to the \mathcal{X}_{PV}^{NSD} values in all the considered transitions among all possible hyperfine levels F_f and F_i of the $7s\ ^2S_{1/2}$ and $6s\ ^2S_{1/2}$ states, respectively, in ^{133}Cs from different methods. Same units as in Table 7.1 are used here.

Method	F_f	F_i	Core	Valence
DHF	3	3	-0.0046	1.9075
	3	4	-0.2031	5.6693
	4	3	-0.2014	4.9350
	4	4	-0.0051	2.1717
CPDF	3	3	-0.0049	2.3394
	3	4	-0.4417	7.4872
	4	3	-0.4396	6.5866
	4	4	-0.0056	2.6635
RPA	3	3	0.0007	1.8298
	3	4	-0.2814	5.9552
	4	3	-0.2821	5.2510
	4	4	0.0007	2.0835
CPDF-RPA*	3	3	0.0039	2.2417
	3	4	-0.6181	7.8529
	4	3	-0.6195	6.9902
	4	4	0.0039	2.5525
CPDF-RPA	3	3	0.0039	2.0100
	3	4	-0.6181	7.6072
	4	3	-0.6195	6.8337
	4	4	0.0039	2.2889
RCCSD	3	3	-0.0047	2.3392
	3	4	-0.3458	7.7401
	4	3	-0.3441	6.8399
	4	4	-0.0052	2.6627

our calculations at the DHF level agree with those of Ref. [7], we can presume that our basis functions are good enough for accurate estimation of \mathcal{X}_{PV}^{NSD} . It should be noted that Ref. [7] uses B-spline polynomials as basis functions. From the point of view of the method, both the PRCC and RCCSD methods are the singles and doubles

approximated RCC theory and obtain results in the first principle approach. However, the implementation procedures of these methods in Ref. [10] and in our work differ in dealing with the angular momentum couplings between the nuclear and electronic components. Following procedures adopted by other groups, we decouple nuclear and electronic angular factors and carry out calculations only on the electronic coordinate by expressing nuclear angular factors as prefactors. However, in Ref. [10], both the nuclear and electronic couplings are included together. We reproduced the CPDF-RPA method's results using the corresponding terms from the RCCSD method to ensure proper implementation of our approach. Additionally, we thoroughly investigated any additional contributions that resulted from the RCCSD method over the CPDF-RPA method. Based on this analysis, we conclude that our RCCSD calculations are more reliable.

In order to understand the roles of the Core and Valence correlation contributions in the evaluation of \mathcal{X}_{PV}^{NSD} , we showcase both these contributions from each method in Table 7.2. This table reveals an interesting phenomenon: the Valence contributions to the $F_i = 4 \rightarrow F_f = 4$ and $F_i = 3 \rightarrow F_f = 3$ transitions differ greatly, whereas the Core contributions to both transitions are comparable. The $F_i = 3 \rightarrow F_f = 4$ and $F_i = 4 \rightarrow F_f = 3$ transitions exhibit similar behaviour. This suggests that the resemblance of Core contributions to these transitions is not due to their angular and radial factors but rather represents an odd behavior of the property under investigation. Another interesting trend is that in contrast to the RPA, CPDF-RPA*, and CPDF-RPA methods, the signs of the Core contributions in the DHF, CPDF, and RCCSD are opposite for the $F_i = 3 \rightarrow F_f = 3$ and $F_i = 4 \rightarrow F_f = 4$ transitions, but they are the same for the $F_i = 3 \rightarrow F_f = 4$ and $F_i = 4 \rightarrow F_f = 3$ transitions. This implies that the Core contributions resulting from the CPDF-RPA* (or combined CPDF-RPA) approach are not equal to the total of the individual Core contributions from the CPDF and RPA methods taken together. From the analyses of the Valence contributions, we can see that, while their magnitudes vary greatly between methods, we do not find any sign differences among their values for any of the hyperfine transitions at different

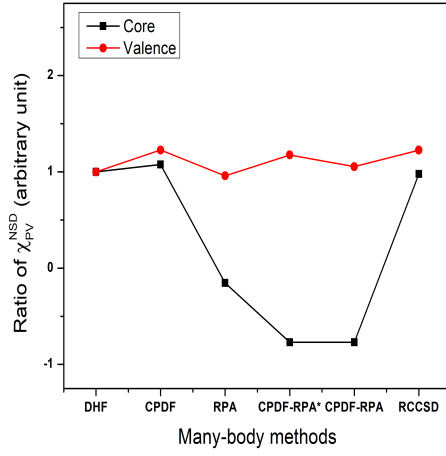
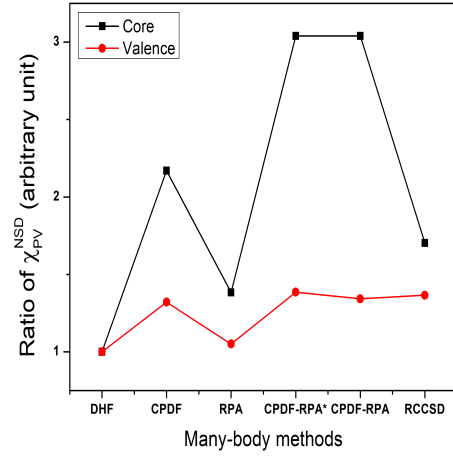
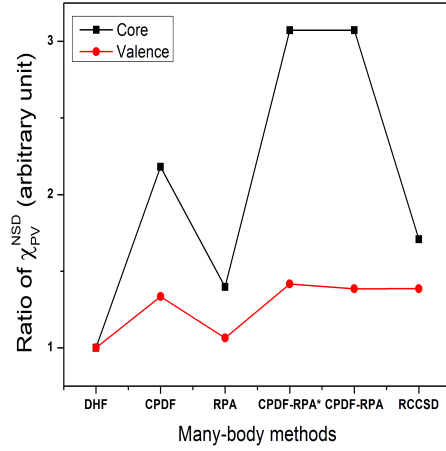
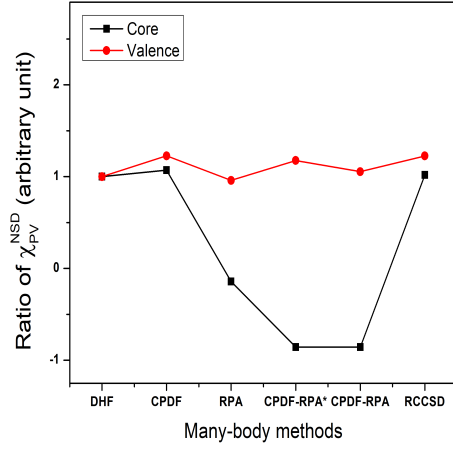

 (a) $F_f = 3 \rightarrow F_i = 3$

 (b) $F_f = 3 \rightarrow F_i = 4$

 (c) $F_f = 4 \rightarrow F_i = 3$

 (d) $F_f = 4 \rightarrow F_i = 4$

Figure 7.2: Ratios of the calculated \mathcal{X}_{PV}^{NSD} values for the $F_f - F_i$ transitions of the $7s \ ^2S_{1/2}$ and $6s \ ^2S_{1/2}$ states, respectively, in ^{133}Cs from different methods with respect to their DHF values.

levels of approximation in the methods. Compared to the $F_i = 3 \rightarrow F_f = 4$ and $F_i = 4 \rightarrow F_f = 3$ transitions, the differences in values obtained from the DHF method and other methods for the $F_i = 3 \rightarrow F_f = 3$ and $F_i = 4 \rightarrow F_f = 4$ transitions are comparatively smaller.

In order to gain a more quantitative understanding of the role of electron correlation effects in each many-body method, we plot the \mathcal{X}_{PV}^{NSD} values from each method with respect to the DHF values (by taking ratio of each calculation with respect to

Table 7.3: Comparison of contributions from the initial and final perturbed states to \mathcal{X}_{PV}^{NSD} among all possible hyperfine levels of the $7s\ ^2S_{1/2}(F_f) - 6s\ ^2S_{1/2}(F_i)$ transition in ^{133}Cs at different methods, in units of $iea_0K_W \times 10^{-12}$.

Method	F_f	F_i	$\langle 7S^{(0)} \tilde{D}_f 6S^{(1)} \rangle$	$\langle 7S^{(1)} \tilde{D}_i 6S^{(0)} \rangle$	Total
DHF	3	3	-0.7077	2.6106	1.9029
	3	4	0.9513	4.5150	5.4663
	4	3	1.2236	3.5101	4.7337
	4	4	-0.8057	2.9722	2.1665
CPDF	3	3	-0.8673	3.2018	2.3345
	3	4	1.2201	5.8254	7.0455
	4	3	1.5540	4.5930	6.1470
	4	4	-0.9873	3.6452	2.6579
RPA	3	3	-0.8158	2.6463	1.8305
	3	4	1.0969	4.5769	5.6738
	4	3	1.4108	3.5581	4.9689
	4	4	-0.9289	3.0131	2.0842
CPDF-RPA*	3	3	-0.9901	3.2357	2.2456
	3	4	1.3688	5.8660	7.2348
	4	3	1.7504	4.6203	6.3707
	4	4	-1.1277	3.6841	2.5564
CPDF-RPA	3	3	-0.9677	2.9816	2.0139
	3	4	1.3163	5.6728	6.9891
	4	3	1.6894	4.5248	6.2142
	4	4	-1.1018	3.3946	2.2928
RCCSD	3	3	-0.9807	3.3151	2.3344
	3	4	1.4815	5.9128	7.3943
	4	3	1.8590	4.6367	6.4958
	4	4	-1.1169	3.7744	2.6575

the corresponding DHF value) for each transition between the hyperfine levels in Fig. 7.2. As the figure clearly indicates, the correlation trends in the estimation of Core and Valence contributions at various approximations of the method differ. The net

magnitude of Core contribution is small, but they are pronounced in the estimation of Valence contribution. Because of this, results from previous reports that used a sum-over-states approach in which only the Valence contributions are estimated with greater rigor appear to be fairly accurate. Upon closer examination of the figure, it can be inferred that the CPDF-RPA method yields the largest correlation effects when compared to the other methods. In the $F_i = 3 \rightarrow F_f = 3$ and $F_i = 4 \rightarrow F_f = 4$ transitions, the CPDF method includes the smallest amount of correlation effects while in the $F_i = 3 \rightarrow F_f = 4$ and $F_i = 4 \rightarrow F_f = 3$ transitions the RPA method accounts for the smallest amount of correlation effects. Interestingly, even though the RCCSD method includes all effects included by the CPDF, RPA, and CPDF-RPA methods, the correlation effects arising through this method are the second smallest in all transitions. Thus, it implies that the PC effects that are absent from the other methods and included in the RCCSD method contribute nearly equally, albeit in opposite directions.

In Table 7.3, we present results from both the initial and final perturbed states separately for all the hyperfine level transitions using the methods employed in this work. As shown in the table, the final perturbed states predominantly contribute more than the initial perturbed states across all transitions, regardless of whether the $K^{(1)}$ or E1 operator is used as the perturbation. This trend is notably similar to the evaluation of the $E1_{PV}^{NSI}$ amplitude of the $6s\ ^2S_{1/2} - 7s\ ^2S_{1/2}$ transition in ^{133}Cs . Additionally, we observe that contributions to \mathcal{X}_{PV}^{NSD} from the initial and final states in the $F_i = 3 \rightarrow F_f = 3$ and $F_i = 4 \rightarrow F_f = 4$ transitions have opposite signs, whereas they have the same sign in the $F_i = 3 \rightarrow F_f = 4$ and $F_i = 4 \rightarrow F_f = 3$ transitions, resulting in an enhancement in the final result. We also analyze the contributions of the individual RCCSD terms to the \mathcal{X}_{PV}^{NSD} values in Table 7.4. Like in $E1_{PV}^{NSI}$, contributions arising through $\bar{D}T_1^{(1)}$ and its c.c. term correspond to the Core contributions, and the rest of the terms offer the Valence contributions. Upon closely examining the above table, it is evident that the corrections from $\bar{D}T_1^{(1)}$ and its c.c. term cancels in the $F_i = 3 \rightarrow F_f = 3$ and $F_i = 4 \rightarrow F_f = 4$ transitions, whereas they add up in the

Table 7.4: Contributions from different RCC terms to the \mathcal{X}_{PV}^{NSD} values (in units $iea_0 K_W \times 10^{-12}$) of the $7s \ ^2S_{1/2}(F_f) - 6s \ ^2S_{1/2}(F_i)$ transitions in ^{133}Cs . Here, contributions given under ‘Norm’ represent the corrections to results due to normalization factors of the wave functions. In this table \bar{D} denotes only the effective one-body part of $e^{T^{(0)\dagger}} D e^{T^{(0)}}$. Contributions from other non-linear terms of the RCCSD method are given together under “Others”.

RCC term	3 – 3	3 – 4	4 – 3	4 – 4
$\bar{D}T_1^{(1)}$	-0.1029	-0.1981	-0.1585	-0.1169
$T_1^{(1)\dagger} \bar{D}$	0.0983	-0.1501	-0.1879	0.1120
$\bar{D}S_{1i}^{(1)}$	-0.4487	0.6832	0.8561	-0.5110
$S_{1f}^{(1)\dagger} \bar{D}$	4.5384	8.0486	6.3017	5.1674
$S_{1f}^{(0)\dagger} \bar{D} S_{1i}^{(1)}$	-0.5575	0.8032	1.0178	-0.6349
$S_{1f}^{(1)\dagger} \bar{D} S_{1i}^{(0)}$	-1.0339	-1.8588	-1.4609	-1.1770
$\bar{D}S_{2i}^{(1)}$	-0.0577	0.1179	0.1403	-0.0658
$S_{2f}^{(1)\dagger} \bar{D}$	-0.0077	0.0273	0.0304	-0.0087
Others	-0.0389	0.0947	0.1090	-0.0452
Norm	-0.0549	-0.1736	-0.1522	-0.0624
Total	2.3344	7.3943	6.4958	2.6575

$F_i = 3 \rightarrow F_f = 4$ and $F_i = 4 \rightarrow F_f = 3$ transitions. The contribution from the $\bar{D}S_{1i}^{(1)}$ and $S_{1f}^{(1)\dagger} \bar{D}$ terms likewise exhibits a similar pattern. By drawing parallels to the $E1_{PV}^{NSI}$ calculation, it is evident that the RCCSD method includes all correlation contributions from the CPDF-RPA method and also includes PC and other non-RPA contributions that were not included in the CPDF-RPA method.

Now, to improve the accuracy of the \mathcal{X}_{PV}^{NSD} calculation, we first separate the Main contribution and the rest from our RCCSD calculation. Earlier results obtained using the sum-over-states approach estimated contributions from Core and Tail using lower-order methods without accounting for DCP. By dividing the RCCSD results into Main and the rest, the latter part corresponds to Core, DCP and Tail contributions together, thus improving accuracy over previous calculations. Next, we aim to improve the accuracy of the Main contribution obtained through the first-principle approach. In the previous calculations using the sum-over-states approach [11], the $np \ ^2P_{1/2,3/2}$ (with $n =$

Table 7.5: Calculated reduced $K^{(1)}$ matrix elements (in $iK_W \times 10^{-12}$) of the low-lying states of ^{133}Cs using the RCCSD method. These values have been used to estimate the ‘Main’ contributions to the \mathcal{X}_{PV}^{NSD} amplitudes.

Transition	$K^{(1)}$ amplitudes
$6P_{1/2} - 6S_{1/2}$	-2.0914
$7P_{1/2} - 6S_{1/2}$	-1.1801
$8P_{1/2} - 6S_{1/2}$	-0.7930
$9P_{1/2} - 6S_{1/2}$	0.5717
$6P_{3/2} - 6S_{1/2}$	0.0370
$7P_{3/2} - 6S_{1/2}$	0.0213
$8P_{3/2} - 6S_{1/2}$	0.0141
$9P_{3/2} - 6S_{1/2}$	0.0101
$7S_{1/2} - 6P_{1/2}$	1.0348
$7S_{1/2} - 7P_{1/2}$	0.5837
$7S_{1/2} - 8P_{1/2}$	0.3917
$7S_{1/2} - 9P_{1/2}$	-0.2823
$7S_{1/2} - 6P_{3/2}$	0.0167
$7S_{1/2} - 7P_{3/2}$	0.0094
$7S_{1/2} - 8P_{3/2}$	0.0067
$7S_{1/2} - 9P_{3/2}$	0.0050

6–9) intermediate bound states were used to estimate \mathcal{X}_{PV}^{NSD} . To maintain consistency with these calculations, we also consider these intermediate states to estimate the Main contributions to \mathcal{X}_{PV}^{NSD} . We first calculate the Main contribution using the calculated E1 matrix elements and energies from the RCCSD method. Then, we replace the calculated E1 matrix elements and energies with precisely known experimental values [12, 13, 14, 15, 16, 17, 18]. In Table 7.5, we have presented a list of the $K^{(1)}$ matrix elements from the RCCSD method. Since obtaining very accurate values of \mathcal{X}_{PV}^{NSD} is our primary goal, we use the sum-over-states approach to replace the *ab initio* Main contributions with the semi-empirical values. We give contributions to the \mathcal{X}_{PV}^{NSD} of different transitions involving the hyperfine levels of the $6s$ $^2S_{1/2}$ and $7s$ $^2S_{1/2}$ states from the *ab initio* and semi-empirical calculations in Table 7.6. Figure 7.3 illustrates the individual contributions from the np $^2P_{1/2,3/2}$ ($n = 6 - 9$) states to the Main contribution, highlighting their significance. The plots indicate that among all the bound states considered, the $6P_{1/2}$ and $7P_{1/2}$ states are the primary contributors to

Table 7.6: Estimated ‘Main’ Contributions to the \mathcal{X}_{PV}^{NSD} values, in units of $iea_0K_W \times 10^{-12}$, of the $7s\ ^2S_{1/2}(F_f) - 6s\ ^2S_{1/2}(F_i)$ transitions in ^{133}Cs using matrix elements involving the $np\ ^2P_{1/2,3/2}$ ($n = 6 - 9$) intermediate states from the RCCSD method in the sum-over-states approach. The values given by *ab initio* results. These values obtained after replacing some of the calculated E1 matrix elements and energies by their precisely known experimental values are given under semi-empirical results. These values are estimated for the initial perturbed and final perturbed states separately, then the final values are given after adding both the contributions.

F_f	F_i	$\langle 7S^{(0)} \tilde{D}_f 6S^{(1)} \rangle$	$\langle 7S^{(1)} \tilde{D}_i 6S^{(0)} \rangle$	Total
<i>Ab initio</i> results				
3	3	-1.1389	3.3557	2.2168
3	4	1.6080	6.0009	7.6089
4	3	2.0464	4.7093	6.7557
4	4	-1.2967	3.8206	2.5239
Semi-empirical results				
3	3	-1.1391	3.3376	2.1985
3	4	1.6078	5.9681	7.5759
4	3	2.0463	4.6834	6.7297
4	4	-1.2969	3.8000	2.5031

the Main contributions in all transitions, while contributions from the $nP_{3/2}$ states are minimal. In the $F_i = 3 \rightarrow F_f = 3$ and $F_i = 4 \rightarrow F_f = 4$ transitions, the $6P_{1/2}$ state contributes with opposite signs for the initial and final perturbed states, resulting in the $7P_{1/2}$ state being the dominant contributor. Conversely, in the $F_i = 3 \rightarrow F_f = 4$ and $F_i = 4 \rightarrow F_f = 3$ transitions, the $6P_{1/2}$ state contributes with the same sign for both the initial and final perturbed states, making it the dominant contributor over the $7P_{1/2}$ state. Additionally, there are significant cancellations among contributions from the intermediate states to both the initial and final perturbed states in all transitions. These cancellations are particularly strong in the initial perturbed state, explaining why contributions from the initial perturbed states are much smaller than those from the final perturbed states.

In Table 7.7, we present the recommended values for the Main, Core, DCP, and Tail contributions \mathcal{X}_{PV}^{NSD} , in units $iea_0K_W \times 10^{-12}$, as well as their estimated uncertainties

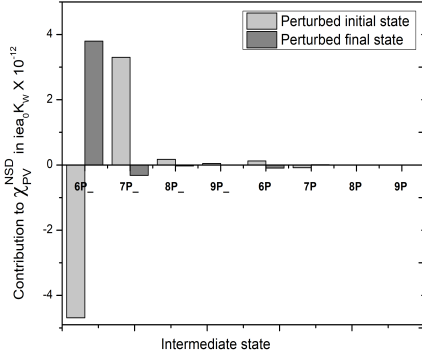
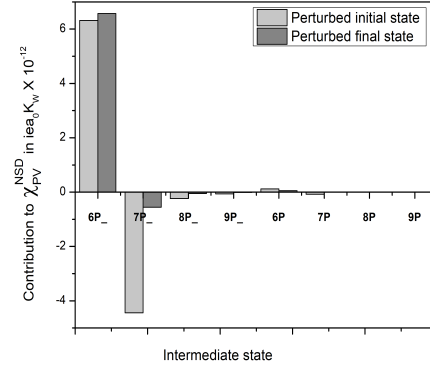
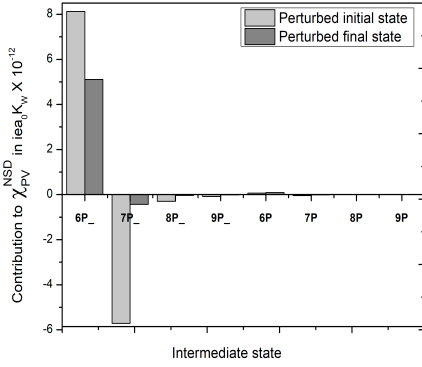
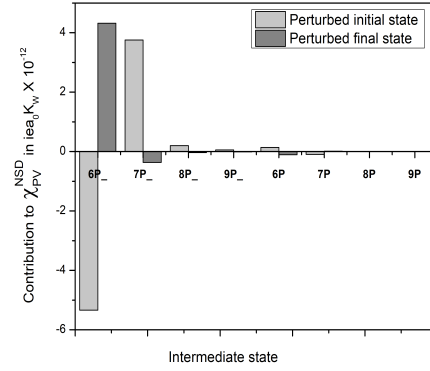

 (a) $F_f = 3 - F_i = 3$ transition

 (b) $F_f = 3 - F_i = 4$ transition

 (c) $F_f = 4 - F_i = 3$ transition

 (d) $F_f = 4 - F_i = 4$ transition

Figure 7.3: Contributions from different intermediate states to the χ_{PV}^{NSD} values for different $7s\ ^2S_{1/2}(F_f) - 6s\ ^2S_{1/2}(F_i)$ transitions in ^{133}Cs . P_- denotes $P_{1/2}$, and P denotes the $P_{3/2}$ state.

for all possible transitions among the hyperfine levels of the $6s\ ^2S_{1/2}$ and $7s\ ^2S_{1/2}$ states in ^{133}Cs by adopting the procedure discussed above. As the DCP and Tail contributions in our RCCSD method cannot be readily disengaged, they are presented collectively in the above table as DCP+Tail. The primary source of uncertainty in the Main contributions arises from the E1 matrix elements used in the experiments. Given the computational complexity of performing such analyses with the RCCSD method, we used the CPDF-RPA method to estimate uncertainties for the Core and DCP+Tail

Table 7.7: The final recommended Main, Core, DCP+Tail, Breit and QED contributions to the \mathcal{X}_{PV}^{NSD} values (in units of $iea_0K_W \times 10^{-12}$) of the $7s\ ^2S_{1/2}(F_f) - 6s\ ^2S_{1/2}(F_i)$ transitions in ^{133}Cs . Uncertainties are quoted within the parentheses.

F_f	F_i	Main	Core	DCP+Tail	+Breit	+QED	Total
3	3	2.1985(52)	-0.0047(2)	0.122(3)	-0.008	-0.008	2.300(6)
3	4	7.5759(73)	-0.3458(18)	0.131(2)	-0.008	-0.026	7.327(8)
4	3	6.7297(88)	-0.3441(18)	0.084(1)	-0.005	-0.023	6.442(9)
4	4	2.5031(56)	-0.0052(3)	0.139(3)	-0.009	-0.009	2.619(6)

contributions. We repeated the calculations by taking large sizes basis functions in the CPDF-RPA method with different combinations of high-lying s and p orbitals. From the variations in the \mathcal{X}_{PV}^{NSD} values, we assigned uncertainties to the Core and DCP+Tail contributions. We also included Breit and QED corrections using the RCCSD method to improve the accuracy of our results.

If we consider the next-order correction to $|(IJ)FM_F\rangle$ by the hyperfine interaction Hamiltonian, there can be another NSD contribution to $E1_{PV}$ due to the hyperfine-induced NSI interaction. As the contribution of this quantity is comparatively small, we neglect this correction in the present work. In Ref. [1], the quantity that was measured was the differential value of the NSD contribution to $E1_{PV}$. It was extracted by carrying out PV measurements between the $6s\ ^2S_{1/2}(F_i = 3) \rightarrow 7s\ ^2S_{1/2}(F_f = 4)$ transition and between the $6s\ ^2S_{1/2}(F_i = 4) \rightarrow 7s\ ^2S_{1/2}(F_f = 3)$ transition in ^{133}Cs . By assuming the net NSD contribution to $E1_{PV}$ arises only from $E1_{PV}^{NSD}$ then we can express the differential $E1_{PV}^{NSD}$ value between the above hyperfine levels F_i and F_f as [7]

$$\delta E1_{PV}^{NSD} = K_W \left[\left(\frac{\mathcal{X}_{PV}^{NSD}}{\mathcal{A}_{F_f, F_i}} \right)^{F_f, F_i} - \left(\frac{\mathcal{X}_{PV}^{NSD}}{\mathcal{A}_{F_i, F_f}} \right)^{F_i, F_f} \right], \quad (7.18)$$

where subscript and superscript F_f, F_i notations used in the above expression denote

Table 7.8: Numerical results for α and β values for 6S-7S transition in ^{133}Cs in a.u. We have used the experimental value of $\frac{\alpha}{\beta} = 9.905(11)$ from Ref. [21]. The error in the results is calculated from the uncertainty in the E1 matrix elements.

Method	α	β	
		From $\frac{\alpha}{\beta}$	Direct
		This work	
<i>Ab initio</i>	-280.13	28.28	27.23
Semi-empirical	-268.33(21)	27.09(4)	27.05(29)
		Others	
Sum-over-states [17]	-268.82(30)	27.139(42)	27.01(23)
Sum-over-states [23]	-266.31(23)	26.887(38)	27.023(114)
Experiment [19]			27.043(36)

the hyperfine levels for the transition $F_f \rightarrow F_i$ and

$$\mathcal{A}_{F_f F_i} = (-1)^{J_f + F_i + I + 1} \sqrt{6(2F_i + 1)(2F_f + 1)} \begin{Bmatrix} F_f & F_i & 1 \\ J_i & J_f & I \end{Bmatrix}.$$

In Ref. [1], the actual measured quantity is $\delta E1_{PV}^{NSD}/\beta = -0.077(11) \text{ mV/cm}$, where β represents the vector polarizability of the $6s \ ^2S_{1/2} \rightarrow 7s \ ^2S_{1/2}$ transition in ^{133}Cs . We infer $K_W = 0.117(16)$ by combining our calculated \mathcal{X}_{PV}^{NSD} values with the measurement of $\delta E1_{PV}^{NSD}/\beta$, using the recently reported value $\beta = 27.043(36)$ a.u. from Ref. [19]. Moreover, it produces $K_a = 0.103(16)$ by substituting $K_{NSD} = 0.0140$ from a nuclear model calculation [20]. Refs. [7] and [20] report values for K_a that are in good agreement with this.

7.2.1 Calculation for vector polarizability

It is clear from above that to estimate $E1_{PV}^{NSD}$ from the measurements of Ref. [1], it is necessary to know β . In the last three decades, various groups have tried different approaches to calculate the β value of ^{133}Cs for the $6s \ ^2S_{1/2} \rightarrow 7s \ ^2S_{1/2}$ transition. One method involves calculating the scalar polarizability α for the $6s \ ^2S_{1/2} \rightarrow 7s \ ^2S_{1/2}$ transition and then using the ratio $\frac{\alpha}{\beta}$ [21] to determine β . The other way to estimate

the vector polarizability β for the $6s\ ^2S_{1/2} \rightarrow 7s\ ^2S_{1/2}$ transition is from the ratio $\frac{M1_{hf}}{\beta}$, where $M1_{hf}$ is the hyperfine induced magnetic dipole transition between $6S$ and $7S$ state. Recently, Toh *et al.* [17] published their most accurate determination of β . They adopted the value of $\frac{\alpha}{\beta}$ and used the sum-over-states method to calculate α . Their calculation of α was carried out using experimentally and theoretically determined E1 matrix elements and energies. Their calculated values for α and β were $-268.82(30)$ and $27.139(42)$ a.u., respectively. Although the uncertainties of their calculation approach that of earlier calculation of Dzuba *et al.* [22] where they estimate β , using the $\frac{M1_{hf}}{\beta}$ ratio, to be $26.957(43)_{expt}(27)_{theory}$ a.u., their central values differ by 0.7%. In order to improve the calculation of α and β , the latest calculation was done by Tan *et al.* [23]. The value of α they obtained is $-266.31(23)$ a.u. Using the $\frac{\alpha}{\beta}$ ratio, they estimated β to be $26.887(38)$ a.u. Their results are in good agreement with those of Dzuba *et al.* [22], apparently resolving the discrepancies between the two methods of calculating β . But, recently, Quirk *et al.* [19] experimentally measured the β to be $27.043(36)$ a.u. One thing to note is that, in both Refs. [17, 23], only the ‘Main’ contribution has been calculated with high precision, while the Core-Valence and Tail parts have been estimated using lower-order many-body methods like RPA or DHF. In this scenario, additional investigations are needed to bring all of these values into better agreement. Based on the discussion in the previous chapter, the expression for the α and β can be written as [23]

$$\begin{aligned}
 \alpha &= \frac{1}{\sqrt{6}\sqrt{3(2J_i+1)}} \sum_{J_n} (-1)^{(J_i-J_n)} \langle J_f || D || J_n \rangle \langle J_n || D || J_i \rangle \\
 &\quad \times \left(\frac{1}{E_{J_f} - E_{J_n}} + \frac{1}{E_{J_i} - E_{J_n}} \right)
 \end{aligned} \tag{7.19}$$

and

$$\begin{aligned}
 \beta &= -\frac{1}{2} \sum_{J_n} \left\{ \begin{matrix} J_f & J_i & 1 \\ 1 & 1 & J_n \end{matrix} \right\} \langle J_f || D || J_n \rangle \langle J_n || D || J_i \rangle \\
 &\quad \times \left(\frac{1}{E_{J_f} - E_{J_n}} - \frac{1}{E_{J_i} - E_{J_n}} \right).
 \end{aligned} \tag{7.20}$$

Table 7.9: Breakdown of the semi-empirical results for α and β in terms of individual contribution. The results are in a.u.

Quantity	Core-Valence	Main	Tail+DCP
α	0.247	-268.358	-0.220
β	0.002	27.204	-0.151

Here, we have used the same procedure to estimate α and β as we did in the calculation of \mathcal{X}_{PV}^{NSD} . First, we calculate the α and β by the *ab initio* RCCSD method; then, we replace the ‘Main’ contribution from the $np\ ^2P_{1/2,3/2}$ ($n = 6 - 9$) states with the semi-empirical value. We present the results in Table 7.8. The primary reason behind the difference between our semi-empirical and *ab initio* results is the use of experimental energy and E1 matrix elements to estimate the Main part in the former approach. One can improve the *ab initio* results by considering corrections from triple excitations in the RCC method. In the same table, we also compare our results with the recent calculations. As can be seen, our semi-empirical calculations agree well with the experimental value in comparison with the others. This is because we have used the RCCSD method to estimate the contribution from core and high-lying orbitals. We also present a breakdown of the semi-empirical results in Table. 7.9. As the table indicates, to achieve high precision, it is necessary to estimate contributions from Core, Tail and DCP correlation.

7.3 Summary

In this chapter, we have presented the results of NSD PV amplitudes among different hyperfine levels of the $6s\ ^2S_{1/2} \rightarrow 7s\ ^2S_{1/2}$ transition in ^{133}Cs . To investigate the role of electron correlation effects, we have employed various many-body methods such as CPDF, RPA, CPDF-RPA and RCCSD. We found that the DCP contributions that were previously omitted in earlier studies are significant, contributing 3 to 12% to the NSD PV amplitudes across different hyperfine levels. We have also analyzed contributions from core and valence orbitals, demonstrating that contributions from core and

high-lying valence orbitals are crucial for precise determination of \mathcal{X}_{PV}^{NSD} . Given that the RCC method incorporates all types of correlation effects from lower-order methods, we consider our RCC results to be reliable. We further improved the accuracy of our RCC results using precise E1 amplitudes and energies from experiments in sum-over-states approach. Finally, by combining our calculation with measurement in ^{133}Cs , we have revised the limit on the magnitude of nucleon-nucleon parity-violating coupling constant. Our study indicates that the discrepancy between atomic and nuclear physics results is not due to uncertainties in different many-body calculations but may instead result from unknown systematic effects in the experiment or inappropriate approximations made in the nuclear calculations. Furthermore, we have also presented the scalar and vector transition polarizabilities using the RCCSD method. Our calculation for vector polarizability matches the recent experimental value.

Bibliography

- [1] C. S. Wood *et al.*, Science **275**, 1759 (1997).
- [2] W. C. Haxton and C. E. Wieman, Ann. Rev. Nuc. Part. Sc. **51**, 261 (2001).
- [3] W. S. Wilburn and J. D. Bowman, Phys. Rev. C **57**, 3425 (1998).
- [4] J. S. M. Ginges and V. V. Flambaum, Phys. Rep. **397**, 63 (2004).
- [5] V. V. Flambaum and D. W. Murray, Phys. Rev. C **56**, 1641 (1997).
- [6] V. A. Dzuba, V. V. Flambaum, P.G. Silvestrov and O. P. Sushkov, J. Phys. B **20** 3297 (1987).
- [7] W. R. Johnson, M. S. Safronova and U. I. Safronova Phys. Rev. A **67**, 062106 (2003).
- [8] I. Lindgren and J. Morrison, *Atomic Many-Body Theory*, edited by G. Ecker, P. Lambropoulos, and H. Walther, Springer-Verlag, Berlin (1985).
- [9] D. A. Varshalovich, A.N. Moskalev, and V. K. Khersonskii, *Quantum Theory Of Angular Momentum*, World Scientific Publishing Company, Singapore (1989).
- [10] B. K. Mani and D. Angom, arXiv:1104.3473 (2011) (Unpublished).
- [11] M. S. Safronova *et al.*, Nuc. Phys. A **827**, 411 (2009).
- [12] C. Amiot, O. Dulieu, R. F. Gutterres and F. Masnou Seeuws, Phys. Rev. A **66**, 052506 (2002).

- [13] A. Damitz, G. Toh, E. Putney, C. E. Tanner and D. S. Elliott, *Phys. Rev. A* **99**, 062510 (2019).
- [14] D. C. Morton, *Astrophys. J., Suppl. Ser.* **130**, 403 (2000).
- [15] L. Young, W. T. Hill, S. J. Sibener, S. D. Price, C. E. Tanner, C. E. Wieman and S. R. Leone, *Phys. Rev. A* **50** 2174 (1994).
- [16] G. Toh, A. Damitz, N. Glotzbach, J. Quirk, I. C. Stevenson, J. Choi, M. S. Safro-nova and D. S. Elliott, *Phys. Rev. A* **99**, 032504 (2019).
- [17] G. Toh, A. Damitz, C. E. Tanner, W. R. Johnson and D. S. Elliott, *Phys. Rev. Lett.* **123**, 073002 (2019).
- [18] A. Kramida, Yu. Ralchenko, J. Reader and NIST ASD Team, NIST Atomic Spec-
tra Database (ver. 5.6.1) (National Institute of Standards and Technology, Gaith-
ersburg, MD, (2018).
- [19] Jonah A. Quirk, Aidan Jacobsen, Amy Damitz, Carol E. Tanner and D. S. Elliott,
Phys. Rev. Lett. **132**, 233201 (2024).
- [20] W. C. Haxton, C. -P. Liu and M. J. Ramsey-Musolf, *Phys. Rev. Lett.* **86**, 5247
(2001).
- [21] D. Cho, C. S. Wood, S. C. Bennett, J. L. Roberts, and C. E. Wieman, *Phys. Rev.
A* **55**, 1007 (1997).
- [22] V. A. Dzuba and V. V. Flambaum, *Phys. Rev. A* **62**, 052101 (2000).
- [23] H. B. Tran Tan, D. Xiao, and A. Derevianko, *Phys. Rev. A* **108**, 022808 (2023).

Chapter 8

Summary and Future Directions

IN the past two decades, numerous high-precision atomic calculations have been reported for NSI parity violating amplitude for the $6S - 7S$ transition in ^{133}Cs . Despite the accuracy of these calculations being within 0.5%, there exists a discrepancy of approximately 1% among the final results from these studies. This inconsistency is further aggravated due to the opposite signs of the Core contributions in different NSI PV studies [1, 2, 3, 4]. Discrepancy exists in the results of NSD PV studies also. The results from atomic studies conflict with those from nuclear physics, necessitating a rigorous analysis of the NSD PV calculations [5, 6, 7]. In this study, we attempted to address these two issues by developing the earlier employed methods by different groups and analyzing their relations with the RCC methods as discussed in the previous chapters. This chapter summarises the steps undertaken to address the issues and outlines all the findings from the calculations carried out under this thesis. In the end, we conclude the work and provide future directions to improve the study further wherever possible.

8.1 Thesis summary

We commenced our work by introducing the fundamental tools of atomic many-body theory in Chapter 2. In the same chapter, second quantization operator, the Goldstone

diagram, and normal ordering have been discussed. Additionally, we introduced the DHF method and defined the residual interaction V_{res} . Subsequently, in Chapter 3, we examined various many-body theories, namely RMBPT, RPA, and RCCSD, and how these methods incorporate the correlation effects from V_{res} . The RPA method includes CP effects up to all-orders but neglects the PC effects and contributions from the SR terms that appear at the RMBPT(3) level. Furthermore, it has been shown that the RCCSD method includes all these RPA and non-RPA correlation effects simultaneously up to all-orders. We also compared the E1 matrix elements calculated from these methods with the available experimental values for ^{133}Cs atom. The RCCSD results are in good agreement with the measured values, establishing it as significantly superior to the RMBPT and RPA methods. In Chapter 4, we investigated the electric dipole polarizability of the closed-shell atomic systems Zn and Cs^+ . Numerous theoretical and experimental studies have been conducted on Zn's electric dipole polarizability, making it an ideal candidate for a case study to validate the accuracy of our calculations. Various methods such as RMBPT(2), RMBPT(3), RPA, and RCCSD have been used to calculate the α_d of the ground state of Cs^+ and Zn. Our calculations match well with the previously reported values.

After checking the implementation and potential of the RCCSD method, we addressed the aforementioned issue regarding the amplitude of NSI PV for the $6S - 7S$ transition in ^{133}Cs in Chapter 5. In this chapter, we explored various many-body methods, such as CPDF, RPA, CPDF-RPA, and RCCSD, which have been used in previous literature to study NSI PV. To examine the propagation of correlation in the Core and Valence contributions at an intermediate level, we also analyzed the results from $\text{RPMBT}(3)^W$ and $\text{RPMBT}(3)^D$ methods. The CPDF, $\text{RPMBT}(3)^W$, and RCCSD methods treat the PV operator H_W as perturbation, whereas the RPA, $\text{RPMBT}(3)^D$, and CPDF-RPA methods treat D as the perturbative operator. We explicitly showed that the definition of the Core and Valence contributions varies depending on the choice of the perturbative operator. Only at the DHF level one can uniquely identify the Core and Valence correlation. As previous studies employed various methods to investigate

the NSI PV amplitude for the $6S - 7S$ transition, the reported Core contributions differed. We also examined the utilization of experimental energy in *ab initio* theory. Our findings indicate that the use of experimental energy does not necessarily improve the precision of the calculations and may, in fact, introduce additional errors. Furthermore, importance of non-RPA contributions, such as DCP, which was omitted in earlier studies, has been demonstrated. We also showed that the RCCSD method effectively incorporates these contributions.

Before examining the NSD PV in ^{133}Cs , we first studied the electric dipole polarizability of the hyperfine levels of the ground state of the ^{133}Cs atom in Chapter 6. In this Chapter, we investigated both static and dynamic polarizabilities. We have also compared our results with previously reported experimental and theoretical studies. There were discrepancies among the experimental and theoretical values for the scalar Stark shift coefficient k_s and the tensor polarizability in earlier studies. We identified the source of these discrepancies as the neglect of contributions from the core and high-lying orbitals in the earlier studies. Previous studies primarily focused on the contributions from the low-lying valence orbitals. We showed that the contributions from core and continuum orbitals must be considered to estimate polarizability values accurately. In Chapter 7, the NSD PV amplitude of the $6S - 7S$ transition in ^{133}Cs has been explored. We employed several many-body methods within a relativistic framework, including CPDF, RPA, CPDF-RPA, and RCCSD to investigate the various roles of correlation effects in the calculations. Additionally, we analyzed results from the sum-over-states approach and first-principle calculations. We have also compared our RCCSD results with those from other methods. This comparison revealed that the RCCSD method incorporates electron correlation effects more rigorously than the other methods mentioned above when evaluating parity-violating electric dipole amplitudes in the ^{133}Cs atom. We have also revised the value of the NAM in ^{133}Cs . Furthermore, we presented the scalar and vector transition polarizabilities using the RCCSD method. Our calculation for vector polarizability matches the recent experimental value.

8.2 Novelty of the thesis

The key findings of the thesis are enumerated below

- The definition of Core and Valence contributions varies based on the choice of the perturbative operator in the many-body method. This variability explains the discrepancy in Core contributions reported by different groups in the study of NSI PV for the $6S - 7S$ transition in ^{133}Cs . Therefore, comparing individual Core or Valence contributions across different methods may not be appropriate. Thus, it is better to compare the final results.
- As shown in Chapter 5, using experimental energy in *ab initio* method like CPDF-RPA may not always improve the accuracy of calculations. Improper use of experimental energy values would lead to numerical instability in the results and introduce additional errors.
- As discussed in Chapters 6 and 7, while the contribution from low-lying valence orbitals is dominant in polarizability and PV amplitude calculations, the contributions from core and high-lying valence orbitals should not be neglected. Ignoring these contributions could lead to inaccurate results.
- It can now be concluded, based on the work conducted in this thesis, that the mismatch between atomic and nuclear results for NSD PV amplitude in ^{133}Cs is not due to the uncertainties associated with the atomic many-body calculations. To resolve this issue, additional APV experiments and theoretical studies are necessary.

The findings of this thesis will pave the path for improving the accuracy and precision of future atomic physics calculations.

8.3 Future directions

One of the main drawbacks of the current RCCSD method is the presence of non-terminating series in property calculating expressions like Eqs. 4.26 and 5.79. Truncating this series after finite terms may lead to inaccuracy in the calculations. Additionally, the RCCSD method does not comply with the Hellmann-Feynman theorem [8]. A simple solution to these problems at the same level of approximation would be to use the relativistic normal coupled-cluster (RNCC) theory [9, 10, 11, 12]. The RNCC method has several advantages over the RCC method, such as: (i) it avoids non-terminating series in property calculation, (ii) it adheres to the Hellmann-Feynman theorem, (iii) the normalization constant is unity, and (iv) it is derivable from the variational principle.

Here, we are going to discuss the brief formulation of the RNCC theory in the single and double excitation approximation (RNCCSD) for the closed-shell atomic system. We are also going to present the RNCCSD results for α_d of neutral Zn atom. First, we want to make it clear that we will approach in the same manner from Eq. 4.19 of RCC theory. In the RNCC theory the ket state $|\Psi_c^{(d)}\rangle$ is expressed as the ordinary RCC theory, but in place of $\langle\Psi_c^{(d)}|$ a new bra state $\langle\tilde{\Psi}_c^{(d)}|$ is defined such that both $\langle\Psi_c^{(d)}|$ and $\langle\tilde{\Psi}_c^{(d)}|$ have the same eigenvalue for H_{at}^D and it satisfies the biorthogonal condition [9, 10, 11, 12, 13]

$$\langle\tilde{\Psi}_c^{(d)}|\Psi_c^{(d)}\rangle = 1. \quad (8.1)$$

The bra state in the RNCC method is expressed as

$$\langle\tilde{\Psi}_c^{(d)}| = \langle\Phi_c|(1 + \Lambda)e^{-T}, \quad (8.2)$$

with a de-excitation operator Λ . It then follows that

$$\langle\tilde{\Psi}_c^{(d)}|\Psi_c^{(d)}\rangle = \langle\Phi_c|(1 + \Lambda)e^{-T}e^T|\Phi_c\rangle = \langle\Phi_c|\Phi_c\rangle = 1. \quad (8.3)$$

Table 8.1: Calculated static α_d value in a.u. of Zn using the RNCCSD method.

Method	α_d
RNCCSD	38.99(31)

It is imperative to impose the condition

$$\langle \Phi_c | \Lambda \bar{H}_{at}^D | \Phi_c \rangle = 0, \quad (8.4)$$

to ensure that both $\langle \Psi_c^{(d)} |$ and $\langle \tilde{\Psi}_c^{(d)} |$ have the same eigenvalue for H_{at}^D . One can see that $\bar{H}_{at}^D = e^{-T} H_{at}^D e^T = (H_{at}^D e^T)_{conn}$ is a terminating series. So the amplitude determining equation for the Λ operator can be written as

$$\langle \Phi_c | \Lambda \bar{H}_{at}^D | \Phi_c^* \rangle = 0, \quad (8.5)$$

where $|\Phi_c^*\rangle$ is an excited state determinant with respect to $|\Phi_c\rangle$. Now, adopting the perturbative approach, we can expand

$$\Lambda = \Lambda^{(0)} + \lambda \Lambda^{(d,1)} + \mathcal{O}(\lambda^2). \quad (8.6)$$

Consequently, the RNCC expressions for α_d can be expressed as

$$\alpha_d = \langle \Phi_c | (1 + \Lambda^{(0)}) \tilde{D} T^{(d,1)} + \Lambda^{(d,1)} \tilde{D} | \Phi_c \rangle, \quad (8.7)$$

where $\tilde{D} = (D e^{T^{(0)}})_{conn}$ is a terminating series. We present the RNCCSD result for α_d in Table 8.1. Comparing the RNCCSD value for α_d with the previously reported values in Table 4.3 shows that the RNCCSD value agrees more closely with the experimental result than the RCCSD value. Therefore, implementing the RNCC method for one-valence atomic systems will greatly improve the precision of atomic calculations.

This approach is also applicable to APV calculations. Extending beyond RCC with single and double excitations would require reformulating computational techniques

to calculate the cluster amplitudes. A simpler approach for improving the accuracy of atomic calculations is to implement the RNCC method, which offers certain advantages over the standard RCC method. Obtaining more accurate bounds on the weak interaction parameter requires extremely high-precision APV experiments on other transitions in ^{133}Cs and in different atoms. On the experimental side, advanced techniques like trapping atoms in a two-dimensional optical lattice with each site optimized for PV detection [14, 15] could potentially surpass the accuracy achieved by Wood *et al* [16]. A promising transition for high-precision measurement in the $6S - 5D_{3/2}$ transition of ^{133}Cs , where the PV amplitude is approximately four times larger than the $6S - 7S$ transition. This approach of using an optical lattice with optimized detection points is broadly applicable and not specific to any one species, making it effective for other alkali atoms like Fr as well [15, 17]. Additionally, there is improvement in the direct measurement of the nuclear anapole moment using Raman interactions [18, 19]. Precise atomic calculation can help reduce uncertainty in this sector.

Bibliography

- [1] S. G. Porsev, K. Beloy and A. Derevianko, *Phys. Rev. D* **82**, 036008 (2010).
- [2] V. A. Dzuba, J. C. Berengut, V. V. Flambaum and B. Roberts, *Phys. Rev. Lett.* **109**, 203003 (2012).
- [3] B. M. Roberts, V. A. Dzuba and V. V. Flambaum, *Phys. Rev. A* **88**, 042507 (2013).
- [4] B. K. Sahoo, B. P. Das and H. Spiesberger, *Phys. Rev. D* **103**, L111303 (2021).
- [5] W. C. Haxton and C. E. Wieman, *Ann. Rev. Nuc. Part. Sc.* **51**, 261 (2001).
- [6] W. S. Wilburn and J. D. Bowman, *Phys. Rev. C* **57**, 3425 (1998).
- [7] J. S. M. Ginges and V. V. Flambaum, *Phys. Rep.* **397**, 63 (2004).
- [8] R. P. Feynman, *Phys. Rev.* **56**, 340 (1939).
- [9] J. S. Arponen, *Ann. Phys.* **151**, 311 (1983).
- [10] R. F. Bishop and J. S. Arponen, *Int. J. Quant. Chem. Symp.* **24**, 197 (1990).
- [11] R. F. Bishop, *Theor. Chim. Acta* **80**, 95 (1991).
- [12] B. K. Sahoo and Yan-mei Yu, *Phys. Rev. A* **98**, 012513 (2018).
- [13] B. K. Sahoo and B. P. Das, *Phys. Rev. Lett.* **120**, 203001 (2018).

- [14] A. Kastberg, T. Aoki, B. K. Sahoo, Y. Sakemi, and B. P. Das, *Phys. Rev. A* **100**, 050101(R) (2019).
- [15] A. Kastberg, B. K. Sahoo, T. Aoki, Y. Sakemi and B. P. Das, *Symmetry* **12**, 974 (2020).
- [16] C. S. Wood *et al.*, *Science* **275**, 1759 (1997).
- [17] N. Fortson, *Phys. Rev. Lett.* **70**, 2383 (1993).
- [18] J. Choi and D. S. Elliott, *Phys. Rev. A* **93**, 023432 (2016).
- [19] A. Damitz, J. A. Quirk, C. E. Tanner, and D. S. Elliott, *Phys. Rev. A* **109**, 032810 (2024).